

Transactions of the ASME®

FLUIDS ENGINEERING DIVISION

Editor

JOSEPH KATZ (2005)

Assistant to the Editor

LAUREL MURPHY (2005)

Associate Editors

MALCOLM J. ANDREWS (2006)

S. BALACHANDAR (2005)

STEVEN L. CECCIO (2004)

ISMAIL CELIK (2003)

WILLIAM W. COPENHAVER (2004)

THOMAS B. GATSKI (2003)

FERNANDO F. GRINSTEIN (2005)

HAMID JOHARI (2006)

JINKOOK LEE (2006)

JEFFREY S. MARSHALL (2003)

M. VOLKAN ÖTÜGEN (2004)

MICHAEL W. PLESNIAK (2004)

AJAY K. PRASAD (2003)

DENNIS SIGNER (2005)

KYLE D. SQUIRES (2005)

YOSHINOBU TSUJIMOTO (2005)

BOARD ON COMMUNICATIONS

Chair and Vice-President

OZDEN OCHOA

OFFICERS OF THE ASME

President, **REGINALD VACHON**

Exec. Director

V. R. CARTER

Treasurer

R. E. NICKELL

PUBLISHING STAFF

Managing Director, Engineering

THOMAS G. LOUGHLIN

Director, Technical Publishing

PHILIP DI VIETRO

Managing Editor, Technical Publishing

CYNTHIA B. CLARK

Manager, Journals

JOAN MERANZE

Production Coordinator

JUDITH SIERANT

Production Assistant

MARISOL ANDINO

Transactions of the ASME, Journal of Fluids Engineering (ISSN 0098-2202) is published bimonthly (Jan., Mar., May, July, Sept., Nov.) by The American Society of Mechanical Engineers, Three Park Avenue, New York, NY 10016. Periodicals postage paid at New York, NY and additional mailing offices.

POSTMASTER: Send address changes to Transactions of the ASME, Journal of Fluids Engineering, c/o THE AMERICAN SOCIETY OF MECHANICAL ENGINEERS, 22 Law Drive, Box 2300, Fairfield, NJ 07007-2300.

CHANGES OF ADDRESS must be received at Society headquarters seven weeks before they are to be effective. Please send old label and new address.

STATEMENT from By-Laws. The Society shall not be responsible for statements or opinions advanced in papers or ... printed in its publications (B7.1, Par. 3).

COPYRIGHT © 2003 by the American Society of Mechanical Engineers. Authorization to photocopy material for internal or personal use under those circumstances not falling within the fair use provisions of the Copyright Act, contact the Copyright Clearance Center (CCC), 222 Rosewood Drive, Danvers, MA 01923, tel: 978-750-8400, www.copyright.com. Request for special permission or bulk copying should be addressed to Reprints/Permission Department.

INDEXED by Applied Mechanics Reviews and Engineering Information, Inc. Canadian Goods & Services Tax Registration #126148048.

Journal of Fluids Engineering

Published Bimonthly by The American Society of Mechanical Engineers

VOLUME 125 • NUMBER 4 • JULY 2003

TECHNICAL PAPERS

- 605 Entrainment Characteristics of Transient Turbulent Round, Radial and Wall-Impinging Jets: Theoretical Deductions
Lijun Song and John Abraham
- 613 The Discharge Coefficient of a Planar Submerged Slit-Jet
S. K. Ali and J. F. Foss
- 620 Entrainment Velocity in an Axisymmetric Turbulent Jet
Anthony M. Falcone and Joseph C. Cataldo
- 628 Concentration Probe Measurements in a Mach 4 Nonreacting Hydrogen Jet
D. R. Buttsworth and T. V. Jones
- 636 Modeling of Turbulent Fluid Flow Over a Rough Wall With or Without Suction
G. Grégoire, M. Favre-Marinet, and F. Julien Saint Amand
- 643 Numerical Study of Sheet Cavitation Breakoff Phenomenon on a Cascade Hydrofoil
Yuka Iga, Motohiko Nohmi, Akira Goto, Byeong Rog Shin, and Toshiaki Ikehagi
- 652 Influence of Roughness on the Two-Phase Flow Structure of Sheet Cavitation
B. Stutz
- 660 An Evaluation of a Two-Fluid Eulerian-Liquid Eulerian-Gas Model for Diesel Sprays
Venkatraman Iyer and John Abraham
- 670 Effect of Reynolds Number and Surface Roughness on the Efficiency of Centrifugal Pumps
J. F. Gülich
- 680 A Criterion to Define Cross-Flow Fan Design Parameters
A. Lazzaretto
- 684 A Systematic Experimental Approach to Cross-Flow Fan Design
A. Lazzaretto, A. Toffolo, and A. D. Martegani
- 694 Fluid Dynamic Aspects of Electrostatic Precipitators: Turbulence Characteristics in Scale Models
Aldo Coghe, Michele Mantegna, and Giorgio Sotgia
- 701 Experimental Study of the Flow in a Compact Heat Exchanger Channel With Embossed-Type Vortex Generators
F. Dupont, C. Gabillet, and P. Bot
- 710 The Forced Oscillations of Submerged Bodies
Angel Sanz-Andrés, Gonzalo Tevar, and Francisco-Javier Rivas
- 716 Analysis of Transient Flow in Pipes With Expanding or Contracting Sections
Adam Adamkowski
- 723 Application of an Angular Momentum Balance Method for Investigating Numerical Accuracy in Swirling Flow
H. Nilsson and L. Davidson

(Contents continued on inside back cover)

This journal is printed on acid-free paper, which exceeds the ANSI Z39.48-1992 specification for permanence of paper and library materials. ©™
♻️ 85% recycled content, including 10% post-consumer fibers.

TECHNICAL BRIEFS

- 731 Conservatism of the Grid Convergence Index in Finite Volume Computations on Steady-State Fluid Flow and Heat Transfer
Patrick J. Roache
- 732 Criticisms of the "Correction Factor" Verification Method
Patrick J. Roache
- 733 Some Observations on Uncertainties and the Verification and Validation of a Simulation
Hugh W. Coleman
- 736 Water Hammer Phenomena in Gas-Water Two-Phase Bubbly Flow Through a 90-Degree Bend Tube
Wang Shuli and Li Zhuo
- 738 On the Linear Encroachment in Two-Immiscible Fluid Systems in a Porous Medium
Kambiz Vafai and Bader Alazmi
- 740 2003 Fluids Engineering Calendar

ANNOUNCEMENTS AND SPECIAL NOTES

- 742 2004 ASME Heat Transfer/Fluids Engineering Summer Conference—Call for Papers
- 746 Information for Authors

The ASME Journal of Fluids Engineering is abstracted and indexed in the following:

Applied Science & Technology Index, AMR Abstracts Database, Chemical Abstracts, Chemical Engineering and Biotechnology Abstracts (Electronic equivalent of Process and Chemical Engineering), Civil Engineering Abstracts, Computer & Information Systems Abstracts, Corrosion Abstracts, Current Contents, Ei EncompassLit, Electronics & Communications Abstracts, Engineered Materials Abstracts, Engineering Index, Environmental Engineering Abstracts, Environmental Science and Pollution Management, Excerpta Medica, Fluidex, Index to Scientific Reviews, INSPEC, International Building Services Abstracts, Mechanical & Transportation Engineering Abstracts, Mechanical Engineering Abstracts, METADEX (The electronic equivalent of Metals Abstracts and Alloys Index), Petroleum Abstracts, Process and Chemical Engineering, Referativnyi Zhurnal, Science Citation Index, SciSearch (The electronic equivalent of Science Citation Index), Shock and Vibration Digest, Solid State and Superconductivity Abstracts, Theoretical Chemical Engineering

Entrainment Characteristics of Transient Turbulent Round, Radial and Wall-Impinging Jets: Theoretical Deductions

Lijun Song

Graduate Research Assistant

John Abraham¹

Professor,

e-mail: jabraham@ecn.purdue.edu

Maurice J. Zucrow Laboratories,
School of Mechanical Engineering,
Purdue University,
West Lafayette, IN 47907-2014

Expressions for the mass entrained in transient turbulent radial and wall-impinging jets are derived by employing scaling laws derived for quasi-steady jets. Quantitative values of the mass entrained in these jets are compared with that in the round jet through an analytical study. In the case of the round jet, the expression has been derived and reported in the literature. It is shown that the ratio of mass entrained in transient radial and round jets for the same mass and momentum flow rates has a constant value with respect to time. In the case of the wall-impinging jet, it is shown that the ratio of the mass entrained in the jet to that in the round jet is a function of the impinging distance and time. The increase in entrained mass with increase in jet penetration in the fully developed region is slower in the wall-impinging jet than in the round jet. [DOI: 10.1115/1.1593707]

Introduction

The study of transient turbulent jets is relevant in the context of several engineering applications. These include direct-injected internal combustion engines, fans, mixers, and various spraying devices. In some of these applications, for example in the engines, the jets may interact with the wall. Such interactions may influence heat, mass and momentum transfer rates. Jet-wall interactions have been a subject of research in diesel engines where the interactions have been shown to affect the fuel-air mixing process and the formation and oxidation of pollutants, [1–4]. Our work is motivated by our interest in impinging jets in diesel engines.

In this work, axisymmetric transient turbulent round jets, radial jets and wall-impinging jets will be studied. Figure 1 shows schematics of the three jets. The different regions of each jet are indicated. In the case of the round jet (see Fig. 1(a)), there are the developing region of the jet which may extend to about 10 effective diameters from the orifice, the fully developed region and the transient head vortex region. The developing and fully developed regions are quasi-steady and the developed region shows self-similar properties, [5–7]. The transient head-vortex region of the jet may occupy about 25% of the total length of the jet, [8]. Similar characteristics are shown by the radial jet (see Fig. 1(b)), [9–11]. In the case of the wall-impinging jet (see Fig. 1(c)), the region upstream of the impingement point typically behaves like a free jet. Where the jet impinges on the wall, a stagnation flow region is formed. The wall jet region has a fully developed quasi-steady region which shows self-similar behavior and a transient head vortex region, [12,13]. The objective of our work is to derive expressions for entrained mass in the transient jets and compare them. The approach involves employing relationships in the quasi-steady region of the jet to derive the expressions for the transient jets. There are assumptions employed in this approach and their validity will be discussed in the paper.

Figure 1(a) also shows the velocity profile and jet half-width, $y_{1/2}$, in the fully developed region of the round jet. The half-width in any axial plane is defined as the radial distance from the centerline to the position where the velocity is half its centerline value. For the round jet emerging from a nozzle into a stagnant

fluid, the width of the jet is proportional to the axial penetration distance, x , and the centerline velocity is proportional to x^{-1} in the developed region where the jet displays self-similar behavior. According to the hypothesis of Prandtl for free turbulent flows, the turbulent diffusivity can be assumed to be a product of the maximum difference in the time-mean velocities in the direction of the jet and a length proportional to the jet width. With this hypothesis, the turbulent diffusivity will be assumed to be constant and the velocity profile can be derived by solving the boundary layer equations, [5]. Much attention has been paid to velocity profiles and entrainment rates of round jets, [5,8,14–16]. The entrainment constant, k , is a variable that is employed to relate the entrained flow rate to the orifice diameter and density ratio, at any axial location, x , through the following equation:

$$\frac{\dot{m}(x) - \dot{m}_i}{\dot{m}_i} = k \left(\frac{x}{D} \right) \left(\frac{\rho_a}{\rho_i} \right)^{1/2} \quad (1)$$

where D is the orifice diameter, \dot{m}_i is the injected mass flow rate, the term $(\dot{m}(x) - \dot{m}_i)$ is the entrained mass flow rate, and ρ_a/ρ_i is the ratio of the ambient density to the injected density. $D(\rho_i/\rho_a)^{1/2}$ is also defined as the effective diameter, D_e . The greater the entrainment constant, the greater the mass entrained. A review by Abraham [15] showed that the measured entrainment constant, as reported in the literature, varied in the range of 0.2 to 0.457. This variation is likely to arise from differences in measurement techniques and in differences in the region of the jet where the measurement are carried out. Integrated measurements are likely to reflect changes in the values of the entrainment constant with axial distance. Studies of near-field entrainment rate constants show that the values of the constant in the near-field are lower than the values in the self-similar region of the jet with the values increasing monotonically from the orifice to the self-similar region, [8,16].

Figure 1(b) shows a schematic of a radial jet generated by the radial flux of fluid from a point source. Radial jets have received attention in the literature not only because of their practical applications but also because they are well-structured fundamental free turbulent flows. In the internal combustion engines, a hollow-cone jet that is generated by a pintle nozzle with 180-deg included angles can be regarded as a radial jet. The limiting case when the number of orifices in the Diesel injector is increased, with a spray orientation of zero degree with respect to the engine head, may also approximate a radial jet. Poreh and Cermak [17] used a

¹To whom correspondence should be addressed.

Contributed by the Fluids Engineering Division for publication in the JOURNAL OF FLUIDS ENGINEERING. Manuscript received by the Fluids Engineering Division October 6, 2001; revised manuscript received January 22, 2003. Associate Editors: J. Bridges and J. Katz.

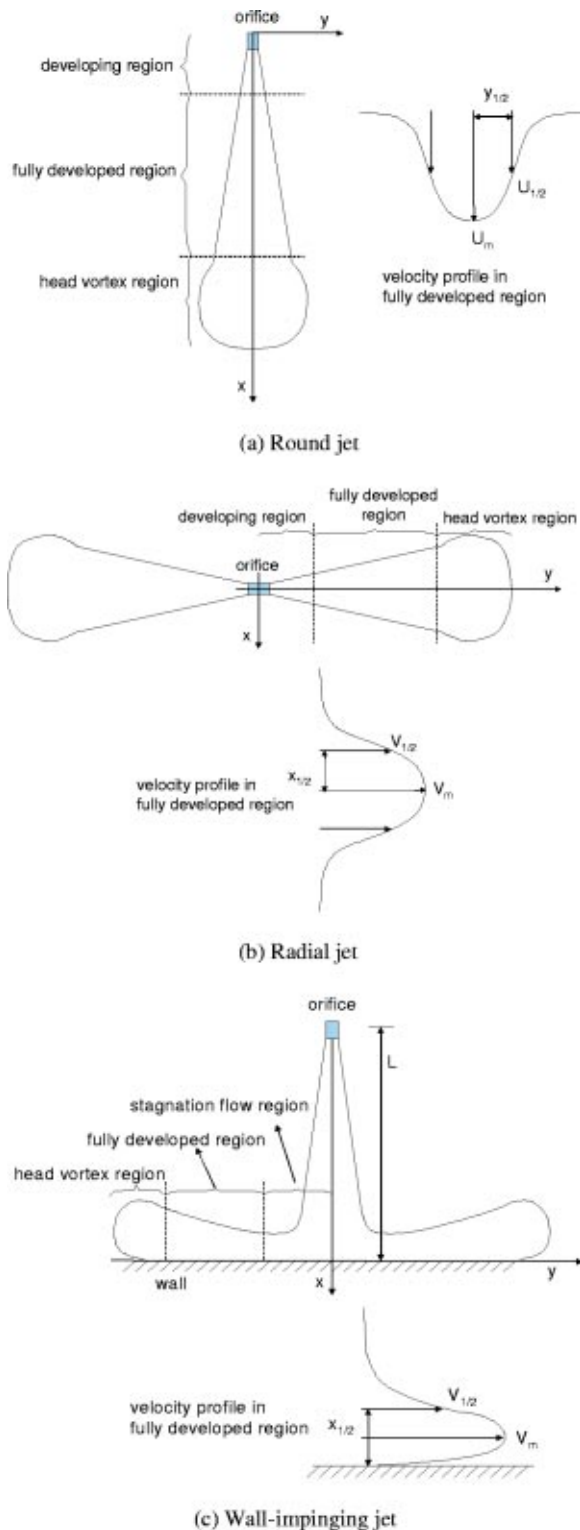


Fig. 1 Schematics of round, radial, and wall-impinging jets

simple turbulent diffusivity model which followed the hypothesis of Prandtl and derived a solution for the radial jet velocity profile. The velocity distribution that they obtained along the direction of the flow is similar to that for plane jets which are generated by fluid flux from a plane nozzle. Hunt and Ingham [10] considered the effect of nozzle geometry and obtained an analytical solution for the velocity profile in the region near the origin of the jet and in the far-field region at large distance along the jet axis from the

orifice. The asymptotic solutions for the velocities in the two regions were matched in the intermediate region. The theoretical prediction showed good agreement with measurements. Witze and Dwyer [18] presented a review of turbulent radial jets and also made measurements of the mean velocity and turbulence intensity distributions in the jet. In their measurements, radial jets were generated by the impingement of two axisymmetric jets. Following impingement, a radial jet resulted. When the two injectors were relatively close to each other, the resulting jet was found to have the same spreading rate as that of radial jets. The spreading rate of the jet is commonly defined as the rate of growth of the half-width. When the injectors were further apart, the resulting jet did not show the expected characteristics of a radial jet. Computational studies carried out by several workers for radial jets show that the $k-\epsilon$ turbulence model predicts a spreading rate of the jet within the range of measured values, [19–22].

Figure 1(c) shows a schematic of a wall-impinging jet. The radial wall jet can be generated by a central source of mass and momentum on the wall and the fluid spreading radially outwards or by the impingement of a round jet on a flat plate. In the case of an impinging jet, the presence of the wall has no apparent effect on the shape of the jet until just prior to contact, [4,23,24]. A radial wall jet will be formed after the stagnation zone. Glauert [12] carried out the first analytical study of the wall jet. The flow field was divided into two distinct regions. The inner region close to the wall, where the effects of the wall are dominant, was assumed to follow the empirical formula of Blasius based on a study of turbulent pipe flow and the $1/7$ power-law velocity profile was employed. The outer region, characterized by the features of free turbulent flows, was assumed to follow the mixing length hypothesis due to Prandtl and a constant turbulent diffusivity was employed across the region. The resulting expressions obtained for the maximum radial velocity and jet half-width were in the form of $V_m \propto y^m$, $x_{1/2} \propto y^n$, where y is the radial distance from the origin. The exponents differ about 10% from unity and depend on the local Reynolds number. But the variation of the exponents with radial distance is very small and within experimental error. The matched solution of the velocity profile agrees well with measurements, [13,25–27].

Poreh et al. [25] carried out measurements in the wall jet region of an impinging jet and considered effects of jet Reynolds number on the velocity distribution perpendicular to the wall at several radial distances from the point of impingement. Orifice diameters, D , of 2.54, 5.08, and 7.60 cm were employed in their measurements. The jet orifice was placed at a distance, L , of about 61 cm from the wall giving nondimensional distances, L/D , of 8 to 24 from the flat surface for the different orifice diameters. Mean velocities and turbulence intensities were measured with a constant-temperature hot-wire anemometer at radial distances that were at 4 cm to about 175 cm from the point of impingement. These distances, when nondimensionalized by the impinging distance, L , correspond to values of 0.4 to 2.9. The jet Reynolds number based on the mean injection velocity, orifice diameter, and air diffusivity varied from 1.2×10^5 to 3.3×10^5 . The measured maximum radial velocity and half-width were shown to fit power laws just as in the measurements of Bakke [13].

Witze and Dwyer [26] also employed an impinging jet and measured the maximum radial velocity and half-width. The distance, L , from the orifice to the flat plate was 9.53 cm. The nozzle diameter, D , was 0.3 cm giving a nondimensional impinging distance, L/D , of 31.7. The velocities were obtained at nondimensional radial distances from 0.1 to 1.0. The jet Reynolds number was about 1.8×10^5 . The measured constants in the expressions of maximum radial velocity and half-width were shown to be close to those of Bakke [13] and Poreh et al. [25].

The measurements of Tanaka and Tanaka [27] considered effects of nozzle dimensions on the flow structure by injecting gas from annular nozzles with various openings. The nozzle diameter, D , varied from 6 cm to 12 cm. The impinging distance, L , varied

from 0.6 cm to 0.8 cm. In their cases, the impinging distances are small such that the round free jet regions were not present. Mean velocities were measured with hot-wire anemometer at nondimensional radial distances of 2 to 100 for Reynolds number of 8.5×10^4 to 2.3×10^5 . The rates of decay of maximum radial velocity and growth of half-width were found close to the results from Bakke [13] and Poreh et al. [25].

The Contribution of This Work

In this study, expressions for the penetration rates and mass entrainment rates of transient turbulent radial and wall-impinging jets are derived. These expressions are compared with each other and with those for round jets. In deriving these expressions, theoretical velocity profiles in the fully developed quasi-steady region of the jets, where self-similar velocity profiles are achieved, are employed. The validity of this assumption and possible inaccuracies are discussed. It is shown that multiplying constants are required in the expressions to achieve agreement of predicted and measured jet penetration. In the next section of this paper, the expressions for penetration and entrainment rate of round jets are summarized and those for radial and wall-impinging jets are derived. In the following section, the expressions are compared to each other with the objective of relating the entrainment rate of wall-impinging jets to those of round jets and radial jets. This paper closes with summary and conclusions.

Analysis

1 Round Jet. The axial velocity as a function of radial and axial distances in a round jet can be derived by assuming a self-similar velocity profile and by employing conservation of momentum, [5]. In the case of a transient jet, by defining the position of the jet tip as the point where the instantaneous centerline velocity has reached a certain fraction, C_f , of the local steady centerline velocity, expressions for the tip velocity, U_{tip} , tip position, x_{tip} , and entrained mass, M_e , can be derived, [15]. Here, we rewrite the relations as a function of K, x , and t .

$$U_{tip} = \frac{C_f 3}{8 \pi C_t} \left(K \frac{\rho_i}{\rho_a} \right)^{1/2} \frac{1}{x} \quad (2)$$

$$x_{tip}^2 = \frac{2 C_f 3}{8 \pi C_t} \left(K \frac{\rho_i}{\rho_a} \right)^{1/2} t \quad (3)$$

$$M_e = \frac{1}{C_f} \left(\frac{8 \pi}{3} \right)^2 C_t^2 \rho_a x_{tip}^3 = 2^{3/2} C_f^{1/2} \left(\frac{8 \pi C_t}{3} \right)^{1/2} \rho_a \left(K \frac{\rho_i}{\rho_a} \right)^{3/4} t^{3/2} \quad (4)$$

where K is the kinematic momentum flux of the round jet leaving the orifice, x is the axial distance, t is the time after start of injection, and ρ_a/ρ_i is the ratio of injected density to ambient density. The constant C_t relates the jet diffusivity to the jet kinematic momentum. Schlichting [5] selected a value of 0.0161 by fitting experimental spreading rate. This choice of C_t corresponds to an entrainment constant of 0.457 in Eq. (1). Abraham [15] in a review showed that the measured entrainment constant varied in the range of 0.2 to 0.457 in the far field and that the precise value of C_t appears to be known only within a factor of about 2.

Comments on the Validity of the Approach. As mentioned earlier, the expressions for entrainment rates are derived by employing self-similar properties which exist only in the fully developed quasi-steady region of the jet. The expression for tip penetration is derived with the assumption that the tip velocity is some fraction, C_f , of the quasi-steady centerline velocity. This approach has been employed in prior works, [15,28,29]. Figure 2 shows measured and predicted penetration for a round transient gas jet. The measurements are those of Fujimoto et al. [24]. Acetylene was injected with a velocity of 6×10^3 cm/s through an orifice of diameter 0.16 cm into air at standard atmospheric conditions. The

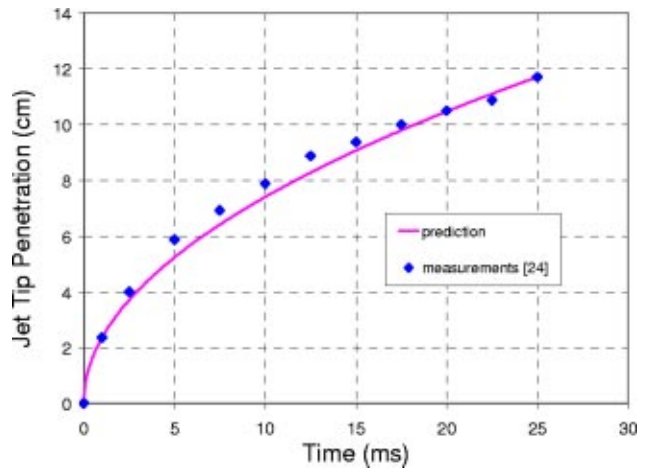


Fig. 2 Measured, [24], and predicted tip penetrations of a round jet

injected to chamber density ratio is approximately 1.0. The predicted curve is obtained by employing Eq. (3). It may be seen from Eq. (3) that different combination of C_f and C_t will give identical expressions for penetration. We employed $C_t=0.0113$ and $C_f=0.305$ to achieve the agreement shown in Fig. 2. In this case, $C_f/C_t=27.0$. A value of 0.0113 for C_t corresponds to $k=0.32$ in Eq. (1). This value of k has been widely quoted in the literature, [8,14,15]. It is interesting to note that Iyer and Abraham [29] employed $C_t=0.0161$ and $C_f=0.40$ to achieve agreement of measured and predicted penetrations for vaporizing diesel sprays for a wide range of injection velocities and density ratios. $C_t=0.0161$ is the value proposed by Schlichting [5]. In this case, $C_f/C_t=24.8$. What these results show is that it is possible to predict transient turbulent round jet penetration with the assumptions made. This does not imply, however, that the approach can achieve the same level of accuracy when predicting entrained mass.

As pointed out earlier, the self-similar behavior of the jet is not shown in the developing region of the jet which may extend to about ten effective diameters downstream of the orifice, [30]. It is also not shown in the unsteady head vortex region. This unsteady head vortex region may occupy about 25% of the total penetration of the jet, [8]. Furthermore, in a transient starting jet, self-similar behavior is not achieved for an initial period of time after start of injection. This time period may be about 100 nondimensional time units, [8,31]. The nondimensionalization parameter for time is D_e/U_0 where D_e is the effective orifice diameter and U_0 is the injection velocity. We can conclude from this discussion that there is a period of time after start of injection where the approach adopted here to estimate mass entrained will not be valid. This period is probably much longer than 100 nondimensional time units. Beyond this period of time, inaccuracies are likely to arise because self-similarity is not applicable for the entire length of the jet. Whether the constants, C_f and C_t , which appear in Eq. (4) are adequate to compensate for these inaccuracies is not known. It is not apparent that there should not be an additional correction factor that may depend on time. We will discuss this further below.

2 Radial Jet. We follow the same approach as for the round jet in deriving the expressions for transient penetration and entrained mass. From the simplified boundary layer equations which describes the flow field in a radial jet, with the assumption of a constant turbulent viscosity, the self-similar velocity profile of a radial jet in the developed region can be expressed by the following equation, [17]:

$$V(x,y) = \frac{2 v_t}{y} \alpha^2 \operatorname{sech}^2 \left(\alpha \frac{x}{y} \right) \quad (5)$$

where V is the radial velocity, y is the radial distance from the origin, and x is the axial distance from the origin, ν_t is the turbulent diffusivity and α is a constant of integration. We employ the conservation of momentum by assuming the gas density in the developed region is the same as the ambient density. The kinematic momentum, K , may then be expressed as

$$K = \frac{\rho_a}{\rho_i} 2\pi y \int_0^\infty V^2 dx = \frac{32\pi \nu_t^2 \alpha^3}{3}. \quad (6)$$

The constant α can be expressed as

$$\alpha = \left(\frac{3K}{32\pi \nu_t^2} \frac{\rho_i}{\rho_a} \right)^{1/3}. \quad (7)$$

We then substitute the above expression for α into Eq. (5) and obtain the following expression for velocity distribution:

$$V(x, y) = \frac{2\nu_t}{y} \left(\frac{3K}{32\pi \nu_t^2} \frac{\rho_i}{\rho_a} \right)^{2/3} \operatorname{sech}^2 \left(\left(\frac{3K}{32\pi \nu_t^2} \frac{\rho_i}{\rho_a} \right)^{1/3} \frac{x}{y} \right). \quad (8)$$

This expression is consistent with that given by Schwarz [9] who obtained the similarity solution to the equations of motion with boundary layer approximations for the incompressible radial jet. Equation (8) is only valid in the fully developed region where the self-similar velocity profile has been established. The velocity characteristics of the near-field are related to the injection condition and have to be studied separately. The measured spreading rate, which is the ratio of jet half-width, $x_{1/2}$, to radial distance, y , where the velocity is half its centerline value, varies from 0.098 to 0.115 with an average value of 0.107 according to a review by Wood and Chen [19]. Here we take the value of 0.106 from the measurements of Witzke and Dwyer [18]. With this value of spreading rate, if we assume that the virtual origin of the similarity velocity is at the orifice, then an expression for the half-width, $x_{1/2}$, is

$$x_{1/2} = 0.106y. \quad (9)$$

From the velocity distribution derived in Eq. (8) and the jet half-width growth rate in Eq. (9), the following relationship can be found at the jet half-width:

$$\left(\frac{3K}{32\pi \nu_t^2} \frac{\rho_i}{\rho_a} \right)^{1/3} 0.106 = 0.881. \quad (10)$$

Hence we have the following relationship between the turbulent diffusivity and the kinematic momentum:

$$\nu_t = C_t \left(K \frac{\rho_i}{\rho_a} \right)^{1/2}, \quad (11)$$

where $C_t = 0.0072$ when the spreading rate value of 0.106 is employed. The value of the constant C_t for the radial jet will be different, and varies about $\pm 5\%$, if other measured spreading rates (0.098–0.115) are considered.

Defining the position of the tip as the point where the instantaneous centerline velocity has reached a certain fraction, C_f , of the local steady centerline velocity (i.e., at $x=0$), the tip velocity becomes

$$V_{\text{tip}} = 2C_f C_t \left(\frac{3}{32\pi C_t^2} \right)^{2/3} \left(K \frac{\rho_i}{\rho_a} \right)^{1/2} \frac{1}{y}. \quad (12)$$

This equation can be integrated to show the relation for the jet tip position.

$$y_{\text{tip}}^2 = 4C_f C_t \left(\frac{3}{32\pi C_t^2} \right)^{2/3} \left(K \frac{\rho_i}{\rho_a} \right)^{1/2} t. \quad (13)$$

The volume flow rate at a distance y from the origin is given by

$$\dot{Q}_e = 2\pi y \int_{-\infty}^{\infty} V dx = 8\pi C_t \left(\frac{3}{32\pi C_t^2} \right)^{1/3} \left(K \frac{\rho_i}{\rho_a} \right)^{1/2} y. \quad (14)$$

Since the entrained mass flow rate can be related to the volume flow rate as

$$\dot{M}_e = \rho_a \dot{Q}_e, \quad (15)$$

after an integration, the entrained mass in the jet as a function of time can then be obtained as

$$M_e = \frac{4\pi}{3C_f} \left(\frac{3}{32\pi C_t^2} \right)^{-1/3} \rho_a y_{\text{tip}}^3 = C_f^{1/2} C_t^{1/6} \left(\frac{32\pi}{3} \right)^{1/3} \rho_a \left(K \frac{\rho_i}{\rho_a} \right)^{3/4} t^{3/2}. \quad (16)$$

3 Wall-Impinging Jet. The expressions for the maximum radial velocity and half-width of the wall jet that were derived by Glauert [12] had proportionality constants that had to be fitted with measured data. Poreh et al. [25] carried out a dimensional analysis of the variables and obtained a nondimensional form of the velocity profile in the following form:

$$\frac{V_m L}{\sqrt{K}} = F_m \left(\frac{\sqrt{K}}{\nu} \right) \left(\frac{y}{L} \right)^m \quad (17)$$

$$\frac{x_{1/2}}{L} = F_n \left(\frac{\sqrt{K}}{\nu} \right) \left(\frac{y}{L} \right)^n \quad (18)$$

where ν is the kinematic viscosity of the gas. L is selected to be the distance between the geometrical origin of similarity of the circular jet and the wall and can be approximated as the impinging distance as shown in Fig. 1(c). The nozzle diameter is not considered as an independent variable for the wall jet. This assumption is valid when the jet reaches its developed state before it impinges on the wall.

In order to account for the difference in density between the injected and the ambient gas, we substitute $K(\rho_i/\rho_a)$ instead of the kinematic momentum itself into Eqs. (17) and (18). Defining the position of the jet tip as the point where the instantaneous centerline velocity has reached a certain fraction, C_f , of the local steady centerline velocity, the tip velocity of a wall-impinging jet can be expressed as

$$V_{\text{tip}} = C_f F_m \left(K \frac{\rho_i}{\rho_a} \right)^{1/2} L^{-(1+m)} y^m. \quad (19)$$

This equation may be integrated to show the jet tip position as

$$y_{\text{tip}}^{1-m} = (1-m) C_f F_m \left(K \frac{\rho_i}{\rho_a} \right)^{1/2} L^{-(1+m)} t. \quad (20)$$

The velocity profile at a radial location, y , can be assumed to follow that from Glauert [12] as

$$\frac{V}{V_m} = f(\eta) \quad (21)$$

where η is the distance from the wall nondimensionalized by the local jet half-width

$$\eta = \frac{x}{x_{1/2}}. \quad (22)$$

The variation of the volume flux of the jet with the radial distance may be calculated from Eqs. (19) and (20) assuming the velocity profile of Glauert [12],

$$\begin{aligned} \dot{Q}_e &= 2\pi y V_m x_{1/2} \int_0^\infty f(\eta) d\eta \\ &= (1.092) 2\pi y V_m x_{1/2} \\ &= (1.092) 2\pi y \left(K \frac{\rho_i}{\rho_a} \right)^{1/2} F_m F_n \left(\frac{y}{L} \right)^{m+n}, \end{aligned} \quad (23)$$

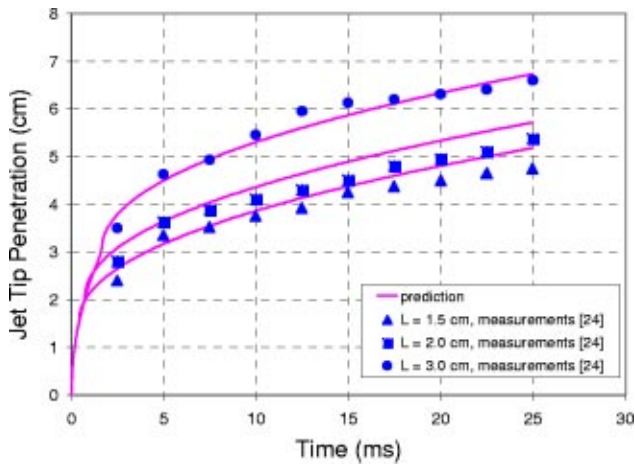


Fig. 3 Measured, [24], and predicted tip penetrations of wall-impinging jets for three impinging distances (L)

where 1.092 is value of integration of the nondimensionalized velocity term when a typical wall jet velocity profile, [12], is employed.

Then Eqs. (19) and (23) can be used to get the expression of the total entrained mass as a function of K and t .

$$M_e = \rho_a \frac{2\pi(1.092)}{C_f} \frac{F_n}{n+2} L^{1-n} y_{tip}^{2+n}$$

$$= \rho_a 2\pi(1.092) C_f^{(1+m+n)/(1-m)} \frac{F_n}{n+2} L^{(1+3m+2n)/(m-1)}$$

$$\times \left[(1-m) F_m \left(K \frac{\rho_i}{\rho_a} \right)^{1/2} t \right]^{(2+n)/(1-m)} \quad (24)$$

As we did in the case of the round jet, we will now show comparisons of measured and predicted tip penetrations of wall-impinging jets. The measurements are those of Fujimoto et al. [24] which we discussed earlier. Figure 3 shows the measured and predicted tip penetrations for three impinging distances, L : 1.5 cm, 2.0 cm, and 3.0 cm. Other conditions employed in the measurements were given earlier when we discussed the round jet measurements. In this figure, the tip penetration of the wall impinging jet after impingement is defined as the summation of the impinging distance, L , and the distance from the tip of the wall jet to the point where the centerline of the free jet meets the wall. Predicted and measured tip penetrations agree within 10% for the three cases. The constants employed in Eq. (20) to achieve this agreement are $F_m = 1.11$, $m = -1.12$, and $C_f = 0.305$. $F_m = 1.11$ and $m = -1.12$ are constants of Witze and Dwyer [26]. However, identical predictions may be obtained with $F_m = 1.32$, $m = -1.10$, and $C_f = 0.25$ where these values of F_m and m are the measured ones of Poreh et al. [25]. We will discuss these constants and entrainment predictions in the next section.

Comparison of Entrainment Characteristics of Round, Radial, and Wall-Impinging Jets

In this section, we compare the entrainment characteristics of the jets with the same injected momentum. Quantitative comparisons are made at the same time after start of injection for the round and radial jets and after start of impingement for a wall-impinging jet. Values of the constants which have been obtained by fitting the analytical expressions to measured data are employed.

The values of C_t are taken as 0.0113 for the round jet and 0.0072 for the radial jet, respectively. We assume that the two jets have the same values of C_f and $C_f = 0.305$. With these values for

Table 1 Measured constants in wall-impinging jets

Experimental reference	F_m	F_n	M	n
Poreh et al. [25]	1.32	0.098	-1.10	0.90
Witze and Dwyer [26]	1.11	0.0946	-1.12	1.01
Tanaka and Tanaka [27]	1.52	0.095	-1.09	0.97

the constants, the ratio of penetration of the radial jet to the round jet can be shown to be a constant from Eqs. (3) and (13):

$$\frac{y_{tip,radial}}{x_{tip,round}} = 0.31. \quad (25)$$

The ratio of entrained mass in the radial jet to that in the round jet can be shown from Eqs. (4) and (16) to be

$$\frac{M_{e,radial}}{M_{e,round}} = 1.63. \quad (26)$$

It is reasonable that the penetration is less and entrained mass is more for the radial jet than the round jet because the radial jet spreads circumferentially from the orifice and has greater surface area.

The wall-impinging jet may be approximated as a half of a radial jet. The difference between the two arises from momentum loss at the wall for the wall-impinging jet. It is interesting to compare the penetration and entrained mass of a half-radial jet with that of a round jet. The momentum of the half-radial jet is kept to be that of the round jet for this comparison. This would imply that in Eqs. (20) and (24) the momentum flow rate has to be doubled for the radial jet so that the half-radial jet has the same momentum flow rate as the round jet. In this case it may be shown that

$$\frac{y_{tip,half-radial}}{x_{tip,round}} = 0.37 \quad (27)$$

$$\frac{M_{e,half-radial}}{M_{e,round}} = 1.37 \quad (28)$$

The derivations of Eqs (20) and (24) employ measured velocity profiles in wall-impinging jets and hence they would include the effect of wall momentum loss. In this case, from Eqs. (3) and (20) and Eqs. (4) and (24), respectively, the expressions for the ratios of penetration and entrained mass of the wall-impinging jet to the corresponding parameters of the round jet can be shown to be related to the jet momentum and time. The results can also be expressed in terms of the ratio of the penetration to the impinging distance, L . The time t in the expressions is after start of injection for the round jet, and after start of impingement for the wall-impinging jet.

$$\frac{y_{tip,wall}}{x_{tip,round}} = \left(\frac{(1-m)C_{f,wall}F_m}{3C_{f,round}} \right)^{1/2} \left(\frac{y_{tip,wall}}{L} \right)^{(1+m)/2} \quad (29)$$

$$\frac{M_{e,wall}}{M_{e,round}} = \frac{C_{f,wall}^{1/2} 2\pi(1.092) \frac{F_n}{n+2}}{C_{f,round}^{1/2} C_t^2 \left(\frac{8\pi}{3} \right)^2}$$

$$\times \left(\frac{(1-m)F_m}{3} \right)^{3/2} \left(\frac{y_{tip,wall}}{L} \right)^{3(1+m)/2 + n - 1} \quad (30)$$

The constants employed for the velocity in the expressions of Eqs. (17) and (18) can be obtained from measurements. Table 1 summarizes the measured constants given in the literature, [25–27]. The flow structure of the jet in the experiments of Tanaka and

Table 2 Ratios of tip penetration and entrained mass of wall-impinging jets to round jets

Experimental reference	$\frac{y_{tip,wall}}{x_{tip,round}}$	$\frac{M_{e,wall}}{M_{e,round}}$
Poreh et al. [25]	$0.33 \left(\frac{y_{tip,wall}}{L} \right)^{-0.05}$	$1.12 \left(\frac{y_{tip,wall}}{L} \right)^{-0.25}$
Witze and Dwyer [26]	$0.33 \left(\frac{y_{tip,wall}}{L} \right)^{-0.06}$	$0.90 \left(\frac{y_{tip,wall}}{L} \right)^{-0.17}$

Tanaka [27] is not strictly that of a wall-impinging jet, since the impinging distances were small compared to the nozzle diameter such that a round jet was not present prior to impingement. In the case of their results, the characteristic length scale in the expressions is selected as \sqrt{A} , where A is the exit area of the nozzle slot, instead of the impinging distance.

With these constants from measurements, we can obtain quantitative expressions for the ratios of penetration and entrained mass of the wall-impinging jet to those of the round jet. These expressions are summarized in Table 2. As indicated earlier, $C_f = 0.25$ and $C_i = 0.305$ are employed with measured constants of Poreh et al. [25] and Witze and Dwyer [26], respectively. We employed values of $C_f = 0.305$ and $C_i = 0.0113$ for the round jet which corresponds to an entrainment constant of $k = 0.32$ in Eq. (1), [8]. Similar expressions can be obtained with the measured constants of Tanaka and Tanaka [27] if the value of C_f is determined by comparing predicted and measured penetrations.

Comparing the expressions in Table 2 with Eqs. (27) and (28), it may be seen that the primary difference is the presence of the terms involving $y_{tip,wall}/L$ for the wall-impinging jet. At relatively small values of $y_{tip,wall}$, the ratios of penetration and entrained mass of the wall jet to the half-radial jet are close to 1.0. However, as $y_{tip,wall}$ increases in value, i.e., as the jet penetrates further, the tip penetration of the wall-impinging jet and the mass entrained in the wall-impinging jet become smaller than the corresponding quantities in the half-radial jet. This is due to the loss of momentum to the wall in the wall-impinging jet.

Figure 4 shows the ratio of the penetrations of the half-radial jet and the wall-impinging jet to that of the wall-impinging jet, i.e., $y_{tip}/x_{tip,round}$, as a function of $y_{tip,wall}/L$ for the same momentum

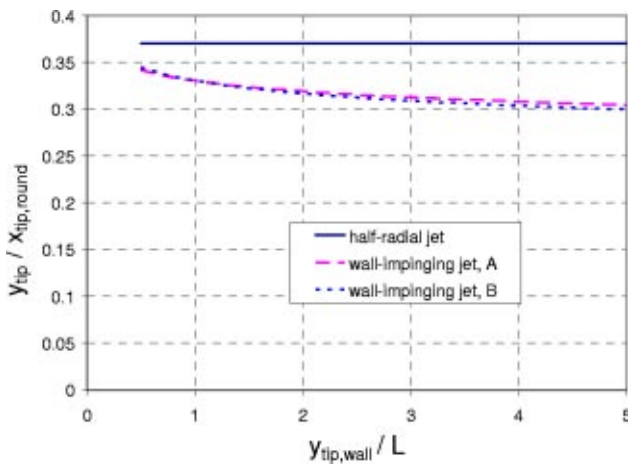


Fig. 4 Ratios of tip penetrations of half-radial and wall-impinging jets to that of the round jet. ($C_f = 0.305$, $C_i = 0.0113$ for the round jet; $C_f = 0.305$, $C_i = 0.0072$ for the half-radial jet; $C_f = 0.25$, $F_m = 1.32$, $F_n = 0.098$, $m = -1.10$, $n = 0.90$ for curve A; $C_f = 0.305$, $F_m = 1.11$, $F_n = 0.0946$, $m = -1.12$, $n = 1.01$ for curve B).

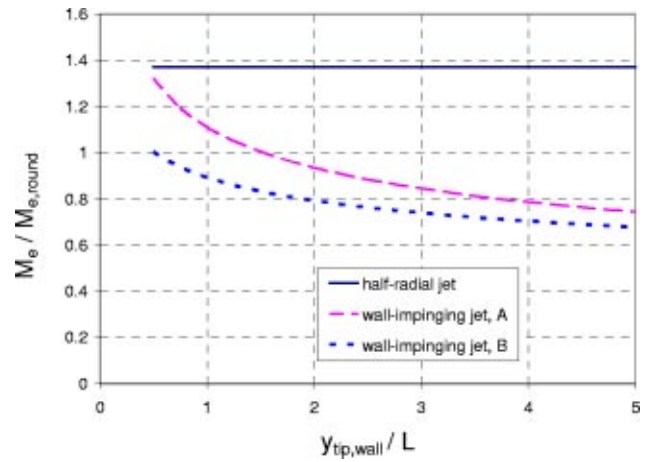


Fig. 5 Ratios of entrained mass of half-radial and wall-impinging jets to that of the round jet. ($C_f = 0.305$, $C_i = 0.0113$ for the round jet; $C_f = 0.305$, $C_i = 0.0072$ for the half-radial jet; $C_f = 0.25$, $F_m = 1.32$, $F_n = 0.098$, $m = -1.10$, $n = 0.90$ for curve A; $C_f = 0.305$, $F_m = 1.11$, $F_n = 0.0946$, $m = -1.12$, $n = 1.01$ for curve B).

flow rate. In generating this figure and also Figs. 5 and 6 below, it is assumed that the round jet, half-radial jet, and wall-impinging jet are starting jets. $y_{tip,wall} = 0$ corresponds to start of injection for the round and half-radial jets. In the case of the wall-impinging jet, it starts out as a wall jet from the impingement point. Notice that the ratio of tip penetration of the half-radial jet to the round jet is a constant given by Eq. (27) and is shown only for reference. Tip penetrations of wall-impinging jets based on the constants derived from the measurements of Poreh et al. [25] and Witze and Dwyer [26] are shown as curves A and B, respectively. The ratio of the tip penetration of the wall-impinging jet to that of the round jet decreases with increasing wall jet penetration as a result of momentum loss to the wall. Results are shown for nondimensional impinging distances greater than 0.5. For shorter distances, the ratio increases sharply as the distance decreases. The factor $(y_{tip,wall}/L)^{(1+m)/2}$ on the right hand side of Eq. (29) increases in value when $y_{tip,wall}$ goes to zero as $m < -1.0$. In any case, the expressions are unlikely to be valid in the stagnation region. Fig-

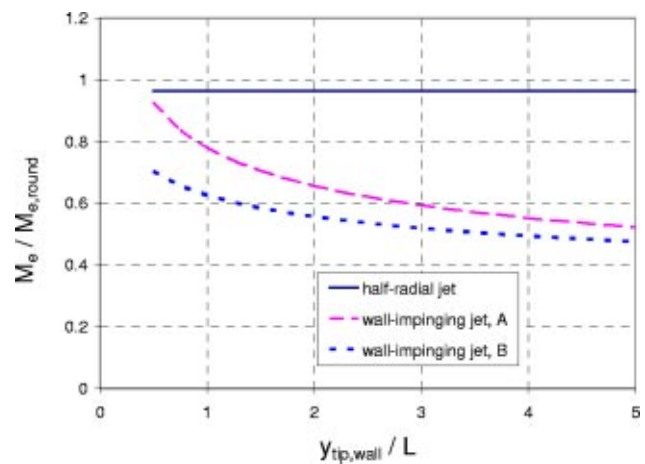


Fig. 6 Ratios of entrained mass of half-radial and wall-impinging jets to that of the round jet. ($C_f = 0.434$, $C_i = 0.0161$ for the round jet; $C_f = 0.305$, $C_i = 0.0072$ for the half-radial jet; $C_f = 0.25$, $F_m = 1.32$, $F_n = 0.098$, $m = -1.10$, $n = 0.90$ for curve A; $C_f = 0.305$, $F_m = 1.11$, $F_n = 0.0946$, $m = -1.12$, $n = 1.01$ for curve B).

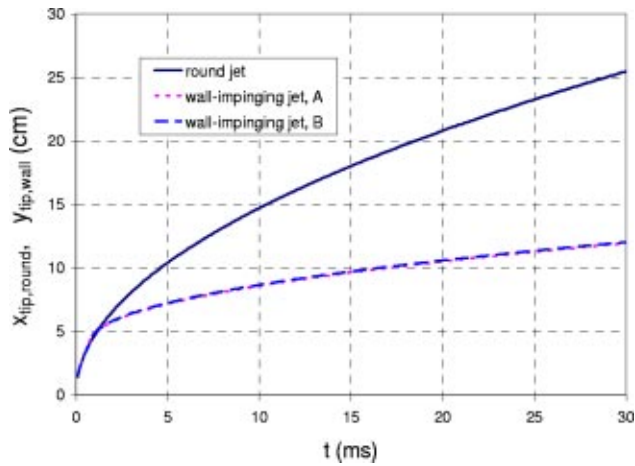


Fig. 7 Tip penetrations of the round and wall-impinging jets as a function of time. ($C_f=0.305$, $C_t=0.0113$ for the round jet; $C_f=0.25$, $F_m=1.32$, $F_n=0.098$, $m=-1.10$, $n=0.90$ for curve A; $C_f=0.305$, $F_m=1.11$, $F_n=0.0946$, $m=-1.12$, $n=1.01$ for curve B).

ure 5 shows the variation of the ratio of entrained mass of the half-radial jet and wall-impinging jet to that of the round jet. Again, the result for the half-radial jet is shown for reference only as it has no dependence on $y_{tip,wall}/L$. The effect of the different values of the constants on the results is reflected in this figure as well just as it was in Fig. 4. The consistent trend to note is the decrease in the ratio of entrained mass as the penetration increases.

As pointed out earlier, we have employed $C_f=0.305$ and $C_t=0.0113$, corresponding to $k=0.32$ in Eq. (1), for the round jet. We may consider a different set of values for these constants. If the values, $C_f=0.434$ and $C_t=0.0161$ are selected such that $k=0.457$ for the round jet, the ratios of entrained mass will decrease by about 30%, respectively, with the second set of constants relative to the first set. Figure 6 show the variations in ratios of entrained mass of the jets with the second set of constants for the round jet.

A challenging and interesting question at this point is: Which jet entrains more—the round jet or the wall-impinging jet? We will provide some insight by considering two extreme cases. We consider two jets that start out as round free jets at $t=0$ and one of the two jets impinges on a wall at time $t=t_0$. The mass entrained in the jet that impinges is determined differently. In one case (Case I), it is assumed that the wall-impinging jet starts as a starting wall jet from $t=t_0$ after impingement. In the other case (Case II), it is assumed that the wall-impinging jet starts from a wall jet that had already developed from time $t=0$ to $t=t_0$. We will consider conditions where the ratio of injected density to ambient density, ρ_i/ρ_a , is 4. The orifice diameter is 0.02 cm. The impinging distance is 4 cm. The injection velocity is 3.0×10^4 cm/s. The impinging distance and injection velocity are comparable to those in diesel engines.

Figure 7 shows the tip penetration, $x_{tip,round}$ for the round jet and y_{tip} for the wall-impinging jet as a function of time t . The tip penetration of the wall impinging jet after impingement is defined as the summation of the impinging distance, L , and the distance from the tip of the wall jet to the impingement point. In the case of the wall-impinging jet, the two sets of constants employed in Figs. 4 and 5 are again employed. It may be seen that impingement occurs at about 0.73 ms. Subsequent to this impingement, it is assumed that the wall-impinging jet develops as a starting wall jet (Case I). As pointed out in earlier discussions, identical penetrations are obtained with the two set of constants. Figure 8 shows the mass entrained in the round jet and in the wall-impinging jet as a function of time when it is assumed that after

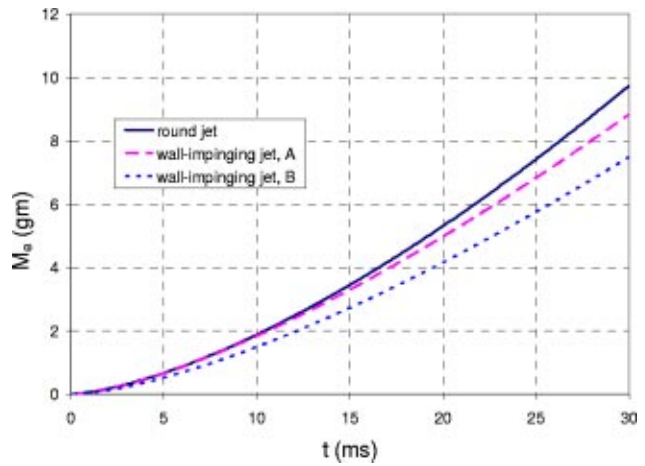


Fig. 8 Entrained mass of the round and wall-impinging jets as a function of time ($C_f=0.305$, $C_t=0.0113$ for the round jet; $C_f=0.25$, $F_m=1.32$, $F_n=0.098$, $m=-1.10$, $n=0.90$ for curve A; $C_f=0.305$, $F_m=1.11$, $F_n=0.0946$, $m=-1.12$, $n=1.01$ for curve B).

impingement, the jet starts out as a starting wall jet (Case I above). In this case, the mass entrained in the wall-impinging jet is defined as

$$M_e = M_{e,round}(t_0) + M_{e,wall}(t - t_0) \quad (31)$$

where t_0 is the time of impingement. Both curves A and B show that immediately after about $t=10$ ms, the wall-impinging jet entrains less than the round jet which is because of the momentum loss of the wall-impinging jet and also because of less time for the development of the wall-impinging jet compared to the round jet.

Figure 9 shows the mass entrained in the round jet and in the wall-impinging jet as a function of time in Case II. In this case, the mass entrained in the wall-impinging jet is defined as

$$M_e = M_{e,round}(t_0) + M_{e,wall}(t) - M_{e,wall}(t_0). \quad (32)$$

Curve A shows that for a certain time period, i.e., $t < 17$ ms, the wall-impinging jet entrains more air than the round jet. Recall that in this case, we are assuming that the wall-impinging jet starts from a wall jet that had already developed from time $t=0$ to $t=t_0$. It is also seen that as the jet penetrates beyond a certain distance, the rate of increase of mass entrained is slower for the

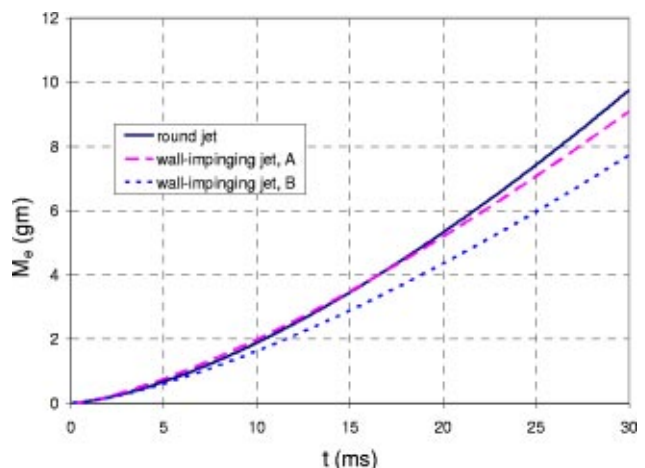


Fig. 9 Entrained mass of the round and wall-impinging jets as a function of time. ($C_f=0.305$, $C_t=0.0113$ for the round jet; $C_f=0.25$, $F_m=1.32$, $F_n=0.098$, $m=-1.10$, $n=0.90$ for curve A; $C_f=0.305$, $F_m=1.11$, $F_n=0.0946$, $m=-1.12$, $n=1.01$ for curve B).

wall-impinging jet relative to the round jet. The region of uncertainty leading to these different estimates is the stagnation region where the jet impinges on the wall (see Fig. 1(c)).

Summary and Conclusions

Theoretical expressions for the penetration rates and entrained mass of transient turbulent radial and wall-impinging jets are presented. In deriving these expressions, theoretical velocity profiles in the fully developed, quasi-steady region of the jets, where self-similar velocity profiles are achieved, are employed. This assumption is likely to lead to inaccurate answers, in particular for estimates of entrainment. The validity of the assumption and inaccuracies are discussed. It is shown that multiplying constants are required in the expressions to achieve agreement of predicted and measured jet penetration. For the radial jet, a constant that relates the turbulent diffusivity to the kinematic momentum is estimated from the measured spreading rate. For the wall-impinging jet, the jet maximum radial velocity and the spreading rate employed are obtained from measurements, and the similarity velocity profile is obtained from the analytical solution. With a selected set of constants, predicted and measured tip penetration of transient round jets and wall-impinging jets agree with 10% for a range of condition. With the selected constants, it is shown that the penetration of a wall-impinging jet smaller than that of a half radial jet because of momentum loss at the wall. The entrained mass of a starting wall jet is higher than that of a starting round jet for relatively smaller values of wall jet tip penetration and lower for higher values of tip penetration. The higher entrainment is due to a greater surface area for the wall jet relative to the round jet. However, as the jet penetrates beyond a certain value, the wall momentum loss overwhelms this greater surface area effect.

It is shown that it is difficult to reach a firm conclusion regarding the relative magnitude of entrained mass in round free and wall-impinging jets as our theoretical work does not clarify the structure of the jet immediately following impingement, i.e., in the stagnation region. However, it can be firmly said that the rate of increase of entrained mass in the fully developed region is slower than that in the fully developed round jet.

Acknowledgments

The authors acknowledge the support of Cummins Engine Company for this work. The authors thank the anonymous reviewers of this paper for their critical comments.

Nomenclature

A	= exit area of the nozzle slot
C_f	= constant, Eqs. (2)–(4), (12), (13), (16), (19), (20), and (24)
C_t	= constant, Eqs. (2)–(4), (11)–(14), and (16)
D	= orifice diameter
D_e	= effective orifice diameter
F_m	= function of Reynolds number, Eq. (17)
F_n	= function of Reynolds number, Eq. (18)
k	= entrainment constant, Eq. (1)
K	= kinematic momentum
L	= impinging distance
M_e	= entrained mass
\dot{m}	= mass flow rate
m	= constant, Eq. (17)
n	= constant, Eq. (18)
t	= time after start of injection
U	= axial velocity
U_0	= injection velocity
V	= radial velocity
V_m	= maximum radial velocity
x	= axial distance
$x_{1/2}$	= half-width for radial and wall-impinging jets

x_{tip}	= jet tip penetration in the x direction
y	= radial distance
y_{tip}	= jet tip penetration in the y direction
α	= constant, Eqs. (5)–(7)
ν_t	= turbulent diffusivity, Eq. (5)
ν	= kinematic viscosity, Eqs. (17) and (18)
ρ_i	= injected fluid density
ρ_a	= ambient fluid density
η	= nondimensional distance from the wall, Eq. (22)

References

- [1] Arcoumanis, C., Cutter, P., and Whitelaw, D. S., 1998, "Heat Transfer Process in Diesel Engines," *Trans. Inst. Chem. Eng.*, **76**, Part A, pp. 124–132.
- [2] Abraham, J., Khan, A., and Magi, V., 1999, "Jet-Jet and Jet-Wall Interactions of Transient Jets From Multi-Hole Injectors," SAE Paper 1999-0-0513.
- [3] Song, L., and Abraham, J., 2001, "Effect of Injector Hole Size, Number and Orientation on Diesel Engine Emissions," *Proceedings of the Second Joint Meeting of the US Sections of the Combustion Institute*, Oakland, CA, The Combustion Institute, Pittsburgh, PA.
- [4] Dec, J. E., and Tree, D. R., 2001, "Diffusion-Flame/Wall Interactions in a Heavy-Duty DI Diesel Engine," SAE Paper 2001-01-1295.
- [5] Schlichting, H., 1968, *Boundary Layer Theory*, McGraw-Hill, New York.
- [6] Rajaratnam, N., 1976, *Turbulent Jets*, Elsevier, New York.
- [7] Abramovich, G. N., 1963, *The Theory of Turbulent Jets*, MIT Press, Cambridge, MA.
- [8] Post, S., Iyer, V., and Abraham, J., 2000, "A Study of Near-Field Entrainment in Gas Jets and Sprays Under Diesel Conditions," *ASME J. Fluids Eng.*, **122**, pp. 385–395.
- [9] Schwarz, W. H., 1963, "The Radial Free Jet," *Chem. Eng. Sci.*, **18**, pp. 779–786.
- [10] Hunt, G. R., and Ingham, D. B., 1998, "Laminar and Turbulent Radial Jets," *Acta Mech.*, **127**, pp. 25–38.
- [11] Heskestad, G., 1966, "Hot-Wire Measurements in a Radial Turbulent Jet," *ASME J. Appl. Mech.*, **33**, pp. 417–424.
- [12] Glauert, M. B., 1956, "The Wall Jet," *J. Fluid Mech.*, **1**, Part 6, pp. 625–643.
- [13] Bakke, P., 1957, "An Experimental Investigation of a Wall Jet," *J. Fluid Mech.*, **2**, pp. 467–472.
- [14] Ricou, F., and Spalding, D., 1961, "Measurements of Entrainment by Axisymmetrical Turbulent Jets," *J. Fluid Mech.*, **11**, pp. 21–32.
- [15] Abraham, J., 1996, "Entrainment Characteristics of Transient Gas Jets," *Numer. Heat Transfer, Part A*, **30**, pp. 347–364.
- [16] Andriani, R., Coghe, A., and Cossali, G. E., 1996, "Near-Field Entrainment in Unsteady Gas Jets and Diesel Sprays: A Comparative Study," *Proceedings of the Combustion Institute*, **26**, The Combustion Institute, Pittsburgh, PA, pp. 2549–2556.
- [17] Poreh, M., and Cermak, J. E., 1959, "Flow Characteristics of a Circular Submerged Jet Impinging Normally on a Smooth Boundary," *Proceedings of the Sixth Midwestern Conference on Fluid Mechanics*, University of Texas, Austin, TX, American Physical Society, Ridge, NY, pp. 198–212.
- [18] Witze, P. O., and Dwyer, H. A., 1976, "The Turbulent Radial Jet," *J. Fluid Mech.*, **75**, Part 3, pp. 401–417.
- [19] Wood, P. E., and Chen, C. P., 1985, "Turbulence Model Predictions of Radial Jet—A Comparison of $k-\epsilon$ models," *Can. J. Chem. Eng.*, **63**, pp. 117–182.
- [20] Rubel, A., 1985, "On the Vortex Stretching Modification of the $k-\epsilon$ Turbulence Model: Radial Jets," *AIAA J.*, **23**, pp. 1129–1130.
- [21] Malin, M. R., 1988, "Prediction of Radially Spreading Turbulent Jets," *AIAA J.*, **26**, pp. 181–191.
- [22] Wilcox, D. C., 1998, *Turbulence Modeling for CFD*, DCW Industries, Inc. CA.
- [23] Beltaos, S., and Rajaratnam, N., 1974, "Impinging Circular Turbulent Jets," *J. Hydraul. Div., Am. Soc. Civ. Eng.*, **100**, pp. 1313–1328.
- [24] Fujimoto, H., Nogami, M., Hyun, G., Hirakawa, K., Asai, T., and Senda, J., 1997, "Characteristics of Free and Impinging Gas Jets by Means of Image Processing," SAE Paper 970045.
- [25] Poreh, M., Tsuei, Y. G., and Cermak, J. E., 1967, "Investigation of A Turbulent Radial Wall Jet," *ASME J. Appl. Mech.*, **34**, pp. 457–463.
- [26] Witze, P. O., and Dwyer, H. A., 1977, "Impinging Axisymmetric Turbulent Flows: The Wall Jet, the Radial Jet and Opposing Free Jets," *Proceedings of the 1st Symposium on Turbulent Shear Flows*, Springer-Verlag, New York, pp. 2.33–2.39.
- [27] Tanaka, T., and Tanaka, E., 1977, "Experimental Studies of a Radial Turbulent Jet (2nd Report, Wall Jet on a Flat Smooth Plate)," *Bull. JSME*, **20**, pp. 209–215.
- [28] Kuo, T. W., and Bracco, F. V., 1982, "On the Scaling of Transient Laminar, Turbulent, and Spray Jets," SAE Paper 820133.
- [29] Iyer, V., and Abraham, J., 1997, "Penetration and Dispersion of Transient Gas Jets and Sprays," *Combust. Sci. Technol.*, **130**, pp. 315–334.
- [30] Wygnanski, I., and Fiedler, H., 1969, "Some Measurements in the Self-Preserving Jets," *J. Fluid Mech.*, **38**, pp. 577–612.
- [31] Sangras, R., Kwon, O. C., and Faeth, G. M., 2002, "Self-Preserving Properties of Unsteady Round Nonbuoyant Turbulent Starting Jets and Puffs in Still Fluids," *ASME J. Heat Transfer*, **124**, pp. 460–469.

The Discharge Coefficient of a Planar Submerged Slit-Jet

S. K. Ali

Visteon Corporation,
Rawsonville Plant,
10300 Textile Road,
Ypsilanti, MI 48197
e-mail: sali5@visteon.com

J. F. Foss

Department of Mechanical Engineering,
Michigan State University,
East Lansing, MI 48824
e-mail: foss@egr.msu.edu

The discharge coefficient, C_D , of a planar, submerged slit-jet has been determined experimentally over a relatively wide range of Reynolds number values: $Re = 100-6500$, where the slit width (w) and the average streamwise velocity ($\langle U \rangle$) at the exit plane are used to define the Reynolds number. The C_D values exhibit a strong dependence on Re for $Re < 800$. For $Re > 3000$, C_D achieves an apparent asymptotic value of 0.687 for the present nozzle design. This value is about 12% higher than the potential flow value. In contrast, the velocity distribution along the centerline was in excellent agreement with that of the potential flow solution. The experimental techniques that were used to evaluate the $C_D(Re)$ values, their numerical values, the corresponding uncertainties, and the possible influence of the geometrical design of the nozzle on the results are presented.

[DOI: 10.1115/1.1593712]

Introduction

The discharge coefficient, C_D , of a nozzle or other constriction is a characteristic of practical significance. For low-subsonic flows, C_D depends both on the flow-field geometry and flow Reynolds number. Blevins [1] provides representative values. The discharge coefficient of a planar, or quasi-two-dimensional, submerged slit-jet is considered in the present communication. A two-dimensional slit-jet, which can be easily simulated using a large aspect ratio: $B_N/w \gg 1$, opening in the wall of a plenum, has been analyzed using potential flow methods; see Birkhoff and Zaranonello [2] and Vallentine [3]. The analytical value of the discharge coefficient of a slit-jet, which delivers an inviscid fluid from an “infinite” plenum, is 0.611. The effect of a finite plenum width (H), for a two-dimensional orifice, has been analytically evaluated by Ali [4] using potential flow methods. These calculations show that $C_D(H/w \gg 10)$ is negligibly different from $C_D(H/w = \infty)$. The minimum value of H/w for the present study was selected as 18 which removes the influence of this parameter on the C_D value.

The development of a vena-contracta, with the corresponding contraction of the separating streamlines and the acceleration of the centerline fluid elements to the maximum velocity magnitude U_0 , is a distinctive feature of both circular and planar (as studied herein) sharp-edged orifices. For the flow of an inviscid fluid through a slit jet, the separating streamlines continue to contract, and the vena-contracta is asymptotically approached. However, for a physical submerged jet, the vena-contracta has been found to occur at about one slit-width downstream from the exit plane; see Ali [4]. Physical jets also exhibit natural instabilities which result in the formation of symmetric and “two-dimensional” vortices along the shear layers. These vortex motions have been studied by Beavers and Wilson [5], Clark and Kit [6], Foss and Korschelt [7], and Ali [4].

For a slit-jet, the discharge coefficient C_D is defined as

$$C_D = \frac{\int_A \mathbf{V}(0,y,z) \cdot \mathbf{i} dA}{U_0 A_j}, \quad (1)$$

where $\mathbf{V}(0,y,z)$ is the time-mean velocity vector at the exit plane of the jet, \mathbf{i} is the unit vector in the streamwise (x) direction, U_0 is the maximum velocity on the centerline ($\bar{u}(x,0) \rightarrow U_0$ for $x \approx w$

and for sufficiently large Re values), and A_j is the area of the orifice given by the product: ($w \times B_N$), where B_N denotes the breadth of the nozzle. In terms of the spatial average velocity, $\langle U \rangle$, which is defined as

$$\langle U \rangle = \frac{1}{A_j} \int_A \mathbf{V}(0,y,z) \cdot \mathbf{i} dA, \quad (2)$$

the discharge coefficient becomes

$$C_D = \frac{\langle U \rangle}{U_0}. \quad (3)$$

The measurement techniques to determine $\langle U \rangle$ and U_0 are described in the following section.

The purpose of this paper is to

- present the experimentally determined values of the discharge coefficient C_D of the present submerged slit-jet over the Reynolds number range: $100 \leq Re \leq 6500$,
- compare the experimental results with the potential flow solution of the slit-jet flow field emanating from a finite width (H) plenum as shown in Fig. 1,
- discuss the influence of the nozzle plate geometry—as expressed by its thickness (t_N) and the inclination angle (α_N) of the relieved surface (see Fig. 1)—on the value of C_D , and
- present an explanation for the differences (as well as the elements of agreement) between the experimental results and the corresponding quantities in the potential flow solution.

Experimental Configuration

Figure 1 is a schematic representation of the flow facility that was used in this investigation. It was designed with $H/w > 10$, so that the influence of the “outer” side walls on the development of the jet is minimal. Water or a water-sugar mixture were used as the working liquids in this finite duration, gravity driven, “steady” flow facility. (This unique experimental facility has been fully described by Ali and Foss [8]). As shown in Fig. 1, the present flow facility is comprised of two major units: (i) a glass tank (A), and (ii) a clear plastic structure called the nozzle housing (NH) which is given the code description “C” in Fig. 1. The two nozzle plates with beveled edges are supported at right angles to the jet-axis by the NH; the nozzle plates form the planar slit-jet. The tank is filled with a working liquid such that its level is above the nozzle plates under the conditions of static equilibrium. The liquid-filled space above the nozzle plates is designated “the plenum;” the space below is called “the receiver.” The portion of the enclosed space above the nozzle plates, that is not liquid filled, is

Contributed by the Fluids Engineering Division for publication in the JOURNAL OF FLUIDS ENGINEERING. Manuscript received by the Fluids Engineering Division June 19, 2000; revised manuscript received February 28, 2003. Associate Editors: B. Schiavello.

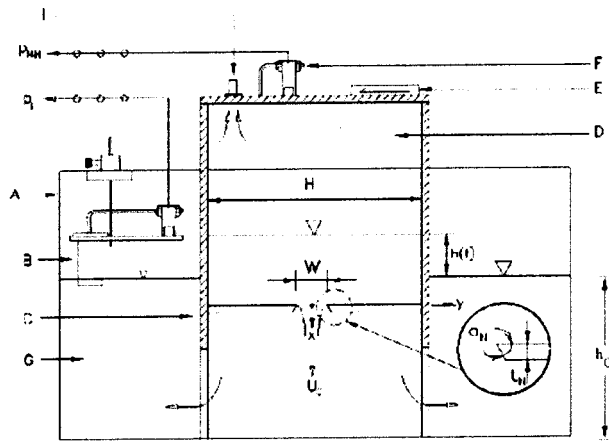


Fig. 1 Schematic representation of the operational features of the flow facility. A: 0.2 cubic meter (80 gal.) glass tank; B: volume flow sensor (VFS); C: nozzle housing (NH); D: low pressure cavity ($p_{NH}(t)$); E: bleed valve; F: pressure transducer; G: receiver; I: connection to vacuum tank. —→ pointer, —→ velocity (flow), —○—○— signal, ——— free surface

termed the “low pressure cavity (D).” The NH has partially open sides below the plane of the nozzle plates (see the outflow to the receiver in Fig. 1) and an air tight cover plate (above the nozzle plates) which supports a bleed valve (E). There are two additional openings in the cover plate: (i) a pressure tap connected to a pressure transducer (F), and (ii) a vacuum tank connection (I). The latter is used to lower the pressure in D thus raising the liquid head (h) in the NH. The slit-jet flow is caused by allowing atmospheric air to enter at a controlled rate through the bleed valve. This valve is operated by a computer controlled stepper motor to ensure a satisfactory approximation to a time steady exit flow from the plenum during the data acquisition period. Specifically, the pressure in D is linearly increased with respect to time in order to compensate for the linear decrease in the differential elevation, h , between the plenum and the receiver. In combination, the net effect is $dU_0/dt=0$ during the period of data acquisition.

Concurrent measurements were made over a wide range of Re (100–6500) to determine the two velocities, $\langle U \rangle$ and U_0 . Specifically, a single channel laser Doppler velocimeter (LDV) was used to measure the time average velocity on the centerline, U_0 , at $x/w \cong 2$. The spatial-average velocity $\langle U \rangle$ was determined by using a novel device, a volume flow sensor (VFS), as shown by “B” on the left-hand side of Fig. 1. The air, that is trapped in the inverted cup, is pressurized as the water level in the receiver tank is increased during the “run time” of the experiment. Since a precise relationship, as described in the next section, can be experimentally established between water level and the pressure in the inverted cup, and since the water level in the receiver increases slowly, the air pressure: $p_I(t)$, value from the cup provides a reliable measure of the time-dependent volume of fluid in the receiver and, hence, its time derivative that is equal to the discharge flow rate, $\int \int u(x=0, y, z, t) dy dz$.

Ideally the nozzle plates should be very thin. However, for practical reasons of strength, the nozzle plates were fabricated using $t_N=12.7$ mm stock. The plates were beveled at an angle $\alpha_N=60$ deg with respect to the plane of the nozzle plates, see Fig. 1 for the definition of α_N . Two values were used for the width, w , of the slit-jet: 12.7 mm and 25.4 mm. Hence, the ratio t_N/w was 1 and 0.5, respectively. The aspect ratio, B_N/w , was equal to 21.7 and 10.8, respectively.

Evaluation of C_D

The companion paper, Ali and Foss [8], provides a detailed description of the flow control process that provides a steady-state slit-jet flow for an elapsed time that is sufficient to record statis-

tically stationary centerline velocity $\bar{u}(x/w=2,0)=U_0$ and the jet exit average velocity $\langle U \rangle$. These values represent the flow behavior at a given Re and t_N/w .

The LDV measurements of $u(x/w=2,0,t)$ are averaged over the same time period, Δt , as that for $\langle U \rangle$ to yield U_0 . In this manner, the $C_D(Re, t_N/w)$ values can be obtained as shown in Eq. (3). The evaluation of the $\langle U \rangle$ and the U_0 values, that are to be used in establishing $C_D=C_D(Re, t_N/w)$, are the essence of the present contribution. As such, considerable care will be taken in identifying the source of these values including the bases for their uncertainty estimates. These considerations are given in the following subsections.

Evaluation of U_0

A Thermo Systems Inc., 35 mW He-Ne LDV system (primitive by today’s standards but adequate for the task at the time of its execution and for the required purpose of providing $u(x/w=2,0,t)$ as an accurately determined quantity) was used in this study. A counter-system (Model TSI 1980) was used to determine the Doppler shift frequency of the small particles that reliably follow the fluid velocity in this benign ($U_0 \partial U_0 / \partial x = 0$) environment. The fixed volume of liquid in the glass tank identified by A in Fig. 1, made it a relatively simple matter to obtain a densely seeded environment; polyvinyltoluene particles with a mean diameter of 2μ were used to provide the scattering centers. Hence, the preset counter output frequency: 308 Hz was readily met with updated velocity values. For reference, at a Re value of 3000 and jet width $w=12.7$ mm, this sample rate nominally provides a measured velocity value each 0.77 mm or 0.06 w . For the same Re value and $w=25.4$ mm, the spacing is 0.38 mm or 0.015 w .

Individual $u(x,0,t)$ measurements are, in principle, subject to the LDV phenomenon of velocity bias (where high-speed fluid elements have a larger probability of being “captured” by the instrument); see, e.g., Adrian [9]. This effect is, of course, exacerbated if the velocity variation at a given location exhibits a “wide” probability density function (pdf) and if there are significant time delays between data samples. The above discussion shows that the latter effect is not a factor in these measurements. The measured intensities (Ali [4]) were of order 0.1 ($=\bar{u}/U_0$) at the $x/w=2$ measurement location. Hence, velocity bias effects in the present experiment will not influence the integrity of the U_0 measurements.

Evaluation of $\langle U \rangle$

A single device, the volume flow sensor (VFS), was used to determine $\langle U \rangle$ for the present experiments. The VFS takes advantage of two intrinsic attributes of this experiment: (i) the receiving reservoir (G of Fig. 1) is characterized by an area: A_r , that is $31 \times A_j$ for $w=25.4$ mm (or, $62 \times A_j$ for $w=12.7$ mm), and (ii) air, at low-pressure rise values, is incompressible. Hence, the VFS of Fig. 1, will remain void of liquid as the liquid level around it is raised in the experiment. The air pressure, however, will be increased in proportion to the increasing submerged depth, h_j , of the VFS. This correlation between the rise in the liquid level and the rise in the pressure in the inverted cup was used to calibrate the VFS. The calibration method is described below:

Consider that the nozzle opening is blocked for a condition where the initial water level: $h_o(1)$, in “G” is known. If a controlled amount of water (M_c) is added to the reservoir G, then the water level rise ($h_o(2)-h_o(1)$) can be correlated with the added water. The inverted cup of the VFS will be slightly submerged for the condition: $h_o=h_o(1)$. There will be a corresponding voltage ($E_p(1)$) from the pressure transducer. Following the addition of the water, the voltage increment

$$\Delta E_p(1)=[E_p(2)-E_p(1)] \quad (4a)$$

$$=C_p \rho g [h_o(2)-h_o(1)] \quad (4b)$$

Table 1 Estimates of errors in the width w , span B_N , and the area of the jet A_j for the two jets

w m	δw m	B_N m	δB_N m	A_j m ²	δA_j m ²
0.0127	4×10^{-5}	0.275	5×10^{-4}	3.4836×10^{-3}	3.4644×10^{-5}
0.0254	6×10^{-5}	0.275	5×10^{-4}	6.9946×10^{-3}	6.8416×10^{-5}

will be recorded as the output from the pressure transducer; here, C_p is the calibration constant for the pressure transducer. Hence, the first controlled mass of water: $M_c(1)$, will be proportional to the increment in E_p as

$$M_c(1) \sim \Delta E_p(1). \quad (4c)$$

This provides a calibration technique:

$$M_c \sim \Delta E_p. \quad (4d)$$

If the confining walls of the glass tank are vertical, then

$$\Delta E_p = C_m \rho A_r \Delta h_o. \quad (4e)$$

This calibration procedure included measurement of the density of water using a picnometer. For M_c , a top-loading weighing scale was used to measure water in amounts of 15 pounds (6.8 kg), or 30 pounds (13.6 kg) at a time to pour into the tank G . The height of the water in the four corners of G was measured using a steel rule, and the laboratory computer was used to digitize E_p . An average height, h_G , of the water in the tank was found for each addition of M_c . Using the measured density of the water, the volume of water poured, V_C , was determined from M_C for each case; V_C was then used to determine the area of the receiver $A_r(h_G)$ at each height h_G . The average value of A_r was found to be 0.2136 square meter with standard deviation equal to 0.0004 square meter or nominally 0.2% of the mean area.

A linear regression analysis between the measured voltage E_p and the average height h_G yielded

$$h_G = \beta_0 + \beta_1 E_p \quad (5)$$

where β_0 and β_1 are the coefficients of the linear regression. The estimates of β_0 and β_1 were 0.03255 mm and 25.2201 mm/volt, respectively, and the corresponding estimates of standard error were found to be 7.933E-3 mm and 3.572E-3 mm/volt.

In a given experiment, the voltage increase ΔE_p , corresponding to the pressure rise in the cup, was measured over a given time interval Δt , which is the same as the interval for which the centerline velocity data $u(x=2w, y=0, t)$ were acquired using the LDV system described above. Using $\Delta(E_p)/\Delta(t)$ in the calibration equation yielded the average rate of rise of water in the receiver V_r :

$$V_r = \Delta h_G / \Delta t = \beta_1 \Delta E_p / \Delta t. \quad (6)$$

The use of the continuity equation to equate the outflow from the plenum to the receiver-inflow yielded the temporal/spatial average velocity of the jet $\langle U \rangle$, which is expressed as

$$\langle U \rangle = \beta_1 \frac{A_r}{A_j} \frac{\Delta E_p}{\Delta t}. \quad (7)$$

Uncertainty Analysis

A conservative estimate of relative uncertainty in C_D , $\delta C_D / C_D$, can be obtained from the general error propagation formula:

$$\delta C_D / C_D = [(\delta \langle U \rangle / \langle U \rangle)^2 + \delta(U_0 / U_0)^2]^{1/2}, \quad (8)$$

where $\delta \langle U \rangle / \langle U \rangle$ and $\delta U_0 / U_0$ are the relative uncertainties in the spatial/temporal average velocity and the maximum centerline velocity of the jet, respectively. It will be shown at the end of this section that the uncertainty in $\langle U \rangle$ is the dominant term and represents the uncertainty in C_D .

The relative uncertainty in $\langle U \rangle$: $\delta \langle U \rangle / \langle U \rangle$, was determined using the general error propagation formula applied to Eq. (7). It is expressed as

$$\frac{\delta \langle U \rangle}{\langle U \rangle} = \left[\left(\frac{\delta(\Delta E_p)}{\Delta E_p} \right)^2 + \left(\frac{\delta(\Delta t)}{\Delta t} \right)^2 + \left(\frac{\delta A_r}{A_r} \right)^2 + \left(\frac{\delta A_j}{A_j} \right)^2 + \left(\frac{\delta \beta_1}{\beta_1} \right)^2 \right]^{1/2}. \quad (9)$$

The first term, of the five terms on the right-hand side of Eq. (10), is the largest. It depends upon the execution of the experiment at a given Re, and the characteristic of the pressure transducer used. For the present work, the first term was evaluated from the characteristic of the Validyne DP15-22 pressure transducer and the measured voltage difference ΔE_p in the cup for each experiment. More specifically, the estimate of error $\delta(\Delta E_p)$ was obtained from the linearity specification: 0.2% of the full scale of the pressure transducer; this translated to ± 0.01016 volt. A conservative estimate: 0.0212 volt was used for $\delta(\Delta E_p)$, for evaluation.

The time: $\Delta t = 13.3$ seconds, was used in all measurements for $Re < 4000$. For higher Re values, Δt was reduced to shorter times of about eight seconds to accommodate the height of the inverted cup. Specifically, the larger flow rates required a shorter elapsed time for the given volumetric restriction imposed by the inverted cup. The influence of this reduction in time is discussed later in this section. The error in Δt , related to the error in computer clock timing, is negligibly small in all cases.

The estimate of standard deviation found in the area of the receiver, A_r (see section titled "Evaluation of $\langle U \rangle$ ") was used as the estimate of the error δA_r , namely, $\delta A_r = 0.0004 \text{ m}^2$ and $A_r = 0.2136 \text{ m}^2$. The normalized error $(\delta A_r / A_r)$ remained constant for jets of both widths. The error in the area of the jet, δA_j , was determined from conservative estimates of errors in the span B_N , and the width, w of the jet. The jet widths were measured carefully several times during the course of this investigation. The estimates of standard deviation of the measured values were determined and used as estimates of error δw . Table 1 lists the values of δw for the two jets. The span B_N was common for both jets; a conservative value of $\delta B_N = 0.5$ mm has been used to determine δA_j in each case. Extreme combinations of B_N and w were used to compute the estimate of error δA_j . Table 1 also lists the estimates of the areas A_j and the corresponding error estimates δA_j .

The last term in the error propagation formula (Eq. (9)) relates to the error in the coefficient of linear regression used in the correlation of the VFS voltage E_p and the head of water column h_G in the reservoir G . The corresponding estimates of standard error were determined using the method described by Beck and Arnold [10], p. 43, for both coefficients: β_0 and β_1 . The estimate of standard error were determined. The estimate of standard error in β_1 was used for $\delta \beta_1$; the values were: $\beta_1 = 25.22$ mm/volt and $\delta \beta_1 = 3.5719 \times 10^{-3}$ mm/volt.

Figure 2 presents the estimates of relative uncertainty in the measurements of $\langle U \rangle$ made in jets with $w = 12.7$ mm and 25.4 mm using water and water-sugar mixture. A similar, and strong dependence on Re is evident for both water jets. The beneficial effect of using the more viscous water-sugar mixture over water is also observed for low Re cases. Around $Re = 1000$, the relative uncertainty in $\langle U \rangle$ for a water jet is about twice the corresponding value for a water-sugar jet; this factor increases with decreasing Re. For

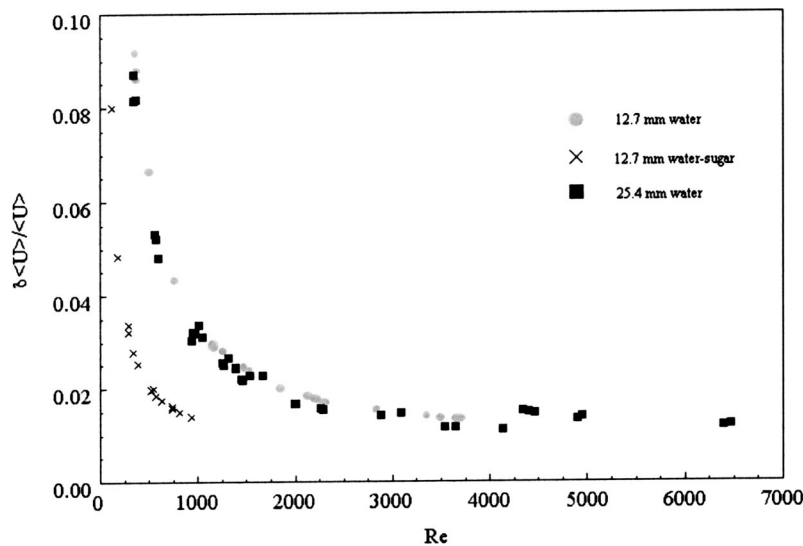


Fig. 2 The relative uncertainty in the measurements of $\langle U \rangle$ as a function of Re

a given Re , the high viscosity water-sugar mixture has to be run at a higher velocity $\langle U \rangle$ as compared with a water jet at the same Re . For a given jet width w and run time Δt , the higher velocity water-sugar jet results in a higher volume flow from the jet resulting in a higher voltage difference ΔE_p . This reduces the relative uncertainty in $\langle U \rangle$. In addition, the higher density of the water-sugar jet causes a higher hydrostatic pressure as compared with a water jet thus producing a favorable condition of reducing measurement uncertainty.

Figure 2 shows that the estimates of relative uncertainty in $\langle U \rangle$, with increasing Re , tend to assume an asymptotic value of about 1%; however, an increase to nominally 1.5% is observed at $Re > 4200$. This is caused by the reduction in the run time Δt discussed earlier in this section. (This shows that the relative uncertainty at low Re could have been reduced by regulating the run time Δt .)

Regarding the uncertainty in the measurement of the velocity on the centerline of the jet, $\delta(U_0)/U_0$, it is noted that U_0 was measured using a laser Doppler velocimeter (LDV). This device, unlike other instruments, is not required to undergo calibration. However, in order to gain confidence that all elements of the LDV system were functioning as expected. The system was checked by measuring the linear velocity of a clear plastic wheel mounted on a speed regulated DC motor. The velocities reported by the LDV measuring system compared quite well with the velocities of the disk.

Hence, considering Eq. (9), the uncertainty in $\delta \langle U \rangle / \langle U \rangle$ is taken to represent the uncertainty in $\delta C_D / C_D$.

Results and Discussion

Laser Doppler velocimetry measurements along the centerline of the jet: $\bar{u}(x,0)$, as described by Ali [4] have been executed for $500 \leq Re \leq 2900$. The experimental protocol for these measurements produced one time series of $u(x,y=0,t_k)$ values for each experiment at each x location and each sample time (t_k) for the LDV measurement. Hence, there are corresponding uncertainties in the \bar{u} , the $\langle U \rangle$, and the x locations for each data set. The uncertainties in the two velocities have been discussed in the previous section. The agreement between $\bar{u}(x,0)$ for the experimental and the potential flow cases is considered to be quite strong as shown in Fig. 3; the reported values are the best estimates of the results with a 95% confidence and with a nominal uncertainty of the

order of 1%. The strong agreement shown in Fig. 3 between the experimental and the potential flow results does not extend to the C_D values as noted below.

Figure 4 presents the values of discharge coefficient, C_D , as a function of Re . The relative uncertainty in the determination of C_D has been estimated in the previous section to vary from 1% to nominally 9% for the lowest Re values with a confidence interval of 95%. At low values of Re (< 800), C_D shows a strong Re dependence in which C_D increases as Re decreases. Given the results of the uncertainty analysis presented in the previous section, especially for $Re < 1000$, it is important to consider the influence of uncertainty on the trend of C_D just described. For Re between 300 and 1000, the plot in Fig. 4 contains data from three independent jets. The uncertainties for water as the working fluid and for both widths were relatively large: 3%–9%. However, the uncertainty for the water-sugar jet was significantly lower 1.5%–2.5%, as shown in Fig. 2. In contrast, the C_D data (see Fig. 4) in the same range of Re exhibited similar values for jets of both liquids and both widths. In other words, even though the uncertainty estimates of C_D for the low Re data are relatively high, the trends shown by the C_D values for the three independent jet widths are in quite good agreement.

The observation that C_D depends strongly on Re for $Re < 800$, can be made rational by noting that the boundary layer thickness, at the separation lip, will increase as the Re value is decreased. Since the fluid near the nozzle wall will have less inertia than that of the unshered fluid, and since the physical extent of the former will be increased as the Reynolds number is decreased, the near wall fluid will be able to execute a curved path with a smaller radius of curvature as the Reynolds number is decreased. In this regard, it can be expected that the jet width at the vena-contracta will be larger for smaller Re values. This interpretation of the physics of the flow is compatible with the observed increase in the C_D values as the Re value is decreased below a nominal value of 800. By extension, this physical reasoning would suggest that the value of C_D would approach 0.611, the value of C_D for a slit jet flow of an inviscid fluid, in the limit as the Re value becomes large. This expectation was not, however, supported by the measurements. As shown in Fig. 4, C_D apparently achieves an asymptotic value of 0.687 for $Re \geq 2000$ and for the $t_N/w = 0.5$ nozzle configuration. The C_D values for $t_N/w = 1.0$ configuration are larger (for $Re \geq 1500$) and the limited Re range does not permit a corresponding limiting value to be confidently inferred, al-

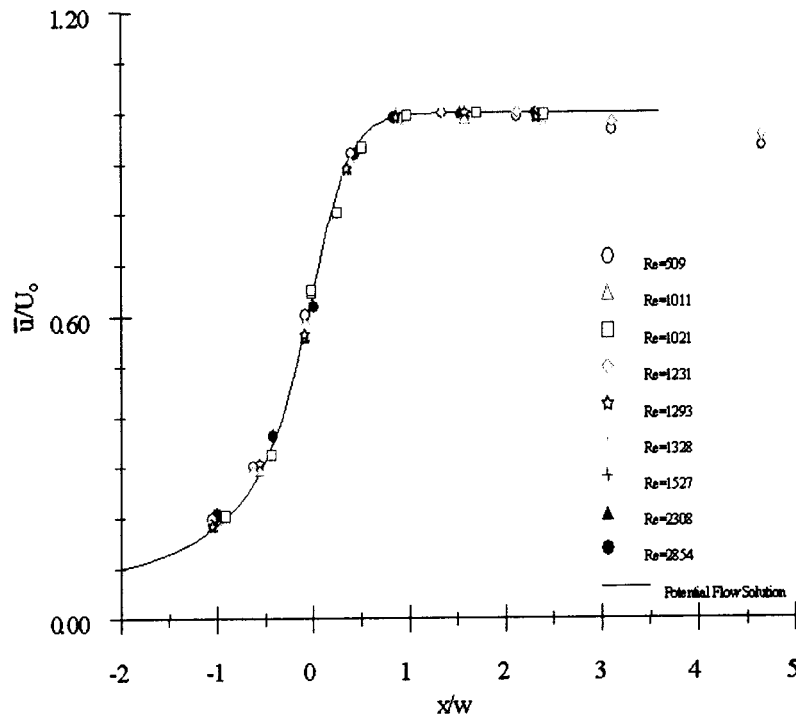


Fig. 3 Normalized mean velocity distribution along the centerline of the jet. The solid line represents the potential flow velocity distribution. The accuracy of the measured velocity is estimated to be within $\pm 1\%$.

beit a value of 0.717 is suggested by the trend of the available data. This suggests that the contraction of the jet is greater for $t_N/w = 0.5$ than in the case of $t_N/w = 1$. The 0.687 value is about 12% larger than the 0.611 value predicted by the potential flow analysis.

Idelchik [11] quotes, without further attribution, a range of discharge coefficients: 0.598–0.609, for a thin slit-jet (t_N less than or equal to $0.03 w$) that separates an upstream plenum from a down-

stream receiver. For the reasons stated above, the present authors consider the potential flow value: $C_D = 0.611$, to be the minimum possible value for this geometric configuration. It is, therefore, inferred that: (i) the Idelchik values represent a bias error in the experimental procedure (unspecified) that was used to obtain them, or (ii) the orifice was not sharp edged.

The apparent asymptotic approach to 0.687 in Fig. 4 suggests the presence of a geometry-dependent effect on the C_D values.

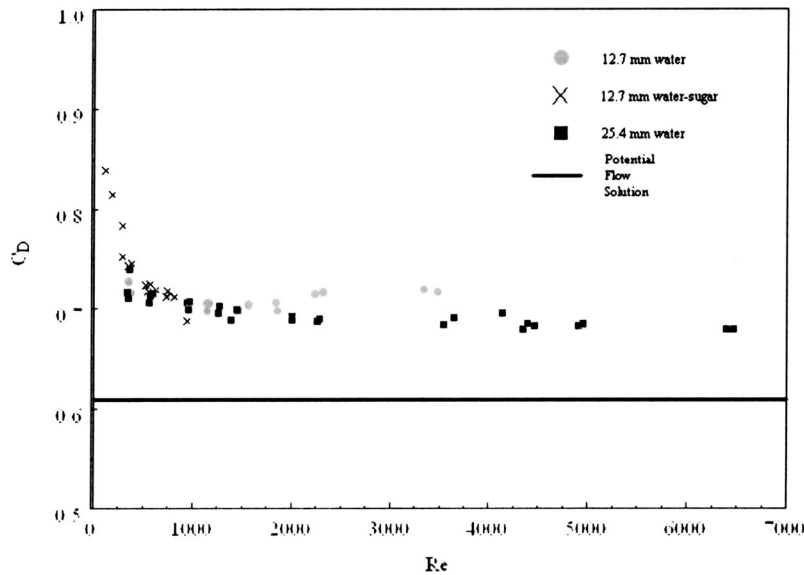


Fig. 4 Distribution of discharge coefficient C_D as a function of Re in jets with two different nozzle configurations: $[w, t_N/w, B_N/w]$ [12.7 mm, 1, 21.7] and [25.4 mm, 0.5, 10.8]. Note that two different working liquids were used for the jet with $w = 12.7$ mm. See Fig. 2 for the corresponding estimates of uncertainty in C_D . The solid line represents the potential flow solution for C_D .

Specifically, it is inferred that the values are influenced by the thickness, t_N , of the nozzle plate, and by the wedge angle α_N , for this relatively thick nozzle. See Fig. 1 for the t_N and α_N definitions. (This latter value is 60° in the present study and it is apparent that this angle will influence the C_D value as $\alpha_N \rightarrow 90$ deg.) Support for the inference of the (t_N/w) effect is provided by the C_D data in which two different slit-widths were used.

The influence of the nozzle-plate geometry on $V(0,y \approx \pm w/2,z)$ for $Re > 1500$ was suspected to be caused by an alteration of the entrainment path in the near-field of the jet. In the case of the relatively thicker nozzle plate ($t_N/w \approx 1$), there will be more obstruction to the entrainment flow than in the case of the relatively narrower nozzle plate ($t_N/w \approx 0.5$). Variations in the entrainment flow can alter the pressure field in the vicinity of the jet exit which, it is inferred, allows the relatively thicker nozzle plate flow to contract less at its vena-contracta as compared to the flow contraction associated with relatively thinner nozzle plate. The overlapping of the C_D values, for the two jets, below $Re \approx 1500$ suggests that for these values of Re the viscous effects are dominant, and therefore, the near-field is less sensitive to the geometry of the nozzle. The present results suggest that the flow field for $Re < 1500$ may be “universal” in nature, i.e., free from geometry-dependent effects. This inference has not been experimentally evaluated.

The inference, that t_N/w is the causal factor for the experimental C_D values to be larger than the potential flow value, is given support by the thickness constraint quoted by Idelchik [11]. Namely, the present experimental thickness values: 0.5w and 1.0w, are significantly larger than the largest acceptable value: 0.03w, given in that reference.

It is known from the previous studies, [4–7], that the submerged jet becomes unstable and develops symmetric (and spanwise) vortex motions for Re values greater than 250. Figure 4, however, shows a continuous decrease in the C_D values with increasing Re without a marked variation around $Re \approx 250$. It is therefore inferred that the formation of the vena-contracta is influenced only by the development of the boundary layers on the nozzle plates and not by the formation of vortices downstream of the exit plane.

Reference was made at the beginning of this section to the excellent agreement between the calculated and the measured (over a sixfold range of Re) values of $\bar{u}(x/w, y/w=0)/U_0$; see Fig. 3. The velocity field: $u(x,0,t)$, that is time-averaged to obtain these observed values, can be reliably described by the Euler “s” equation since the conditions of “inviscid flow behavior” and “incompressible flow” are clearly valid from the upper plenum to the vena-contracta. The third constraint: steady flow, that would be required for the derivation of the Bernoulli equation is not strictly valid for this flow condition given the presence of the vortex motions. The Bernoulli equation, for this flow, would be

$$p_k(x,0) + \rho \frac{\bar{u}^2}{2}(x,0) = p_k(\text{plenum}) \quad (10)$$

where $p_k = p + \rho g x$ is the “kinetic pressure” introduced by Potter and Foss [12] as an appropriate variable that combines the local static pressure and the gravitational body force effect in the differential momentum equation.

The LDV data of Ali [4] show that the velocity fluctuation (\bar{u}) levels are nominally: $(\bar{u})/U_0 = 0.041$ at $x/w = 1$. Hence, it is reasonable that the experimental data show qualitative agreement with the “steady-state” conditions of Eq. (10).

Considering the good agreement (shown in Fig. 3) between the calculated and the measured longitudinal velocity distribution over the Re range 500–2900, the strong dependence of C_D on Re over the same Re range shows that the influence of shear effects (development of boundary layers) on the nozzle plates is offset by some other physical effect. The Euler- n equation relates the centerline pressure, $p_k(x,y=0)$, to the radius of curvature, R , and the velocity, V , along a curved path “ n ” which is everywhere normal

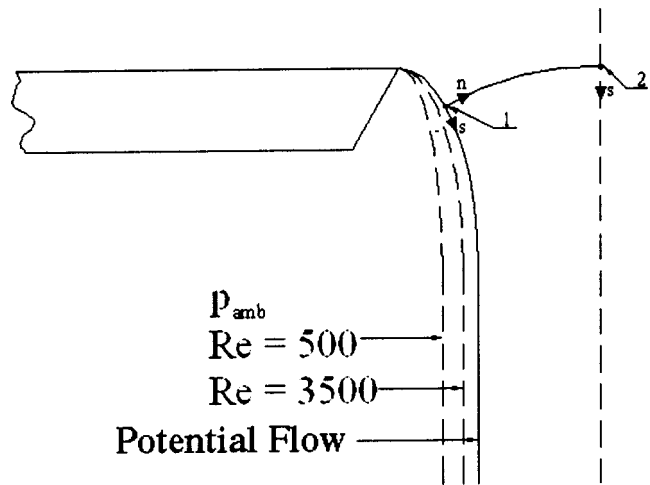


Fig. 5 Schematic representation of the influence of Re on the trajectory of the separating streamline. The curve 1–2 represents the path of integration normal to the streamline.

to the local streamlines and which extends from the atmosphere (1) to the jet centerline (2). This trajectory is shown schematically in Fig. 5. The centerline p_k distribution is given by

$$p_k(x,0) = p_{k-amb} + \int_1^2 \frac{\rho V^2}{R} dn \quad (11)$$

where p_{k-amb} is the ambient pressure in the receiver. (See, for example, Potter and Foss [12], for the kinetic pressure as well as the Euler n equation development.) It has been argued above that the radius of curvature of the separating streamline (near $x=0$, $y = \pm w/2$) increases with increasing value of Re . Hence, the integration path 1–2 shown in Fig. 5 will also change with Re . Apparently, this change occurs such that the nondimensional pressure distribution along the centerline remains independent of Re . In other words, an adjustment in the curvature of the streamlines in the vicinity of the exit plane of the jet is believed to be responsible for the quantitative agreement of the viscous and the potential flow $p_k(x,y=0)$ distributions. Note that in this description p_{k-amb} has been assumed to be constant along the curved path of the separating streamline. However, given the results of difference in the values of C_D for the two jets, and the fact that the asymptotic value of C_D is different from $C_D(t_N/w \approx 0)$, it is conjectured that p_k is smaller than the ambient value in the corner between the beveled surface of the nozzle plates and the separating streamlines. This will cause the jet to deflect outward from the centerline thus resulting in a larger value of C_D . The complete inference is, then, that a combination of the modified streamline trajectories and the reduced pressure near the separation point, are responsible for the increased C_D value. These effects would be difficult to experimentally assess. An accurate numerical simulation may be the most effective way to test this hypothesis.

Conclusions

The discharge coefficient, C_D , of a submerged two-dimensional slit-jet shows a strong Re dependence for $Re < 800$. For higher values of Re and for the nozzle design: $t_N/w = 0.5$, $\alpha_N = 60$ deg, C_D achieves an asymptotic value of 0.687, which is nominally 12% higher than the potential flow value: 0.611. (The measurement uncertainty is $\pm 1.5\%$ for $Re > 2000$ with a confidence interval of 95%). The experimental data also suggested an asymptotic value of $C_D = 0.720$ for $t_N/w = 1.0$ albeit the data are not sufficiently complete to fully test this inference. Hence, a geometric, as well as a Reynolds number, dependence is inferred for the slit-jet C_D values. The convergence of the C_D values for $Re < 1500$ suggests the limited influence of the geometric parameter:

t_N/w , for low Re values. Conversely, it is conjectured that a geometric parameter: the shape of the downstream portion of the nozzle, influences the entrainment path of the fluid for $Re > 1500$. This shape is inferred to alter the pressure field near the exit plane which, in turn, increases the discharge coefficient in response to these entrainment/pressure field effects.

Acknowledgments

This investigation was initially supported by the National Science Foundation through grant number MEA 8216946. Both authors acknowledge the subsequent support provided by the Michigan State University, E. Lansing, MI. The first author would also like to acknowledge the travel grant provided by the GIK Institute of Engineering Sciences & Technology, Topi, Pakistan, where he served as Visiting Associate Professor of Mechanical Engineering, during the preparation of this manuscript.

Nomenclature

A, B, C, D, E, F, G, I = elements of the experimental facility (see Fig. 1)
 A_j = area of slit-jet = $w \times B_N$
 B_N = breadth of nozzle
 C_D = discharge coefficient of the slit-jet (see Eqs. (1) and (3))
 g = acceleration due to gravity
 h = head of liquid column in the NH above the liquid level in the receiver G (see Fig. 1)
 h_I = head of immersion depth in the volume flow sensor B (see Fig. 1)
 h_G = head of liquid in the receiver G
 H = distance between the walls of the channel-like plenum (see Fig. 1)
 \mathbf{i} = unit vector in the streamwise direction
 n = outward direction normal to stream line (see Fig. 5)
 p_k = kinetic pressure (see Eq. (11))
 p_l = pressure in the inverted cup of the volume flow sensor B (see Fig. 1)
 p_0 = kinetic pressure at vena-contracta where $\bar{u} = U_0$ (see Eq. (11))
 R = radius of curvature of the separating streamline of the jet (see Eq. (11))

Re = Reynolds number based on w and $\langle U \rangle$
 t_N = thickness of nozzle plate (see Fig. 1)
 $\langle U \rangle$ = spatial/temporal average velocity of the jet at $x=0$ (see Eq. (2))
 U_0 = \bar{u} ($x \approx x_m, y=0$); $x_m \approx w$ for a viscous fluid, and $x_m \rightarrow \infty$ in the potential flow case
 \bar{u} = time mean of the longitudinal velocity $u(x, y, t)$
 u' = fluctuating component of $u(x, y, t)$
 V = magnitude of velocity
 V_r = velocity sensed by the cup of the volume flow sensor B (see Fig. 1)
 \mathbf{V} = time mean velocity vector
 w = slit width
 x, y, z = streamwise, lateral, transverse coordinates

Greek Symbols

α_N = bevel angle (see Fig. 1)
 β_0, β_1 = coefficients of linear regression (see Eq. (5))
 ν = kinematic viscosity
 ρ = density

References

- [1] Blevins, R. D., 1984, *Applied Fluid Dynamics Handbook*, Van Nostrand Reinhold, New York.
- [2] Birkhoff, G., and Zarantonello E. H., 1957, *Jets, Wake and Cavities*, Academic Press, New York.
- [3] Vallentine, H. R., 1959, *Applied Hydrodynamics*, 2nd Ed., Butterworths Scientific Publications, London.
- [4] Ali, S. K., 1991, "Instability Phenomena in a Two-Dimensional Slit-Jet Flow Field," Ph.D. dissertation, Michigan State University, East Lansing, MI.
- [5] Beavers, G. S., and Wilson, T. A., 1970, "Vortex Growth in Jets," *J. Fluid Mech.*, **44**, pp. 97–112.
- [6] Clark, J. A., and Kit, L., 1980, "Shear Layer Transition and the Sharp-Edged Orifice," *ASME J. Fluids Eng.*, **102**, pp. 219–225.
- [7] Foss, J. F., and Korschelt, D., 1983, "Instabilities in the Slit-Jet Flow Field," *J. Fluid Mech.*, **134**, pp. 79–86.
- [8] Ali, S. K., and Foss, J. F., 1995, "A Computer Controlled, Finite Duration 'Steady' Flow Facility," *Exp. Fluids*, **19**, pp. 250–254.
- [9] Adrian, Ronald J., 1983, "Laser Velocimetry," *Fluid Mechanics Measurements*, Richard J. Goldstein, ed., Taylor and Francis, Philadelphia.
- [10] Beck, J. V., and Arnold, K. J., 1977, *Parameter Estimation in Engineering and Science*, John Wiley and Sons, New York.
- [11] Idelchik, I. E., 1994, *Handbook of Hydraulic Resistance*, 3rd Ed., CRC Press, Boca Raton, FL.
- [12] Potter, M. C., and Foss, J. F., 1982, *Fluid Mechanics*, Great Lakes Press, Okemos, MI.

Anthony M. Falcone
Daniel Frankfurt P.C.
432 Park Avenue South,
New York, NY 10016

Joseph C. Cataldo
The Cooper Union for the Advancement of
Science and Art,
Department of Civil Engineering,
51 Astor Place,
New York, NY 10003

Entrainment Velocity in an Axisymmetric Turbulent Jet

Mean radial and turbulent radial velocity profiles were measured in a circular jet at up to 40 jet diameters downstream of the jet exit using an LDA. The mean radial velocity in the ambient reservoir (the entrainment velocity) is found to be inversely proportional to the radial distance from the jet centerline. The coefficient of proportionality, c , increases in the zone of flow establishment and reaches a constant after the transition zone. It is suggested that the traditional definition of entrainment velocity, which maintains direct proportionality to the local jet velocity by the entrainment coefficient, should be augmented by this inverse function. [DOI: 10.1115/1.1595674]

Introduction

Using the equation of continuity, one can show profiles of mean radial velocity in a turbulent jet to be “double S,” or antisymmetric curves. Examining one half of the jet from the centerline outward in a radial direction, the radial velocity is zero at the centerline, increases to some maximum directed away from the centerline and then passes through zero once again. This point shall be defined as the radial velocity inversion: The average position where turbulent jet spreading equals nonturbulent inflow towards the jet. After passing the inversion, the velocity changes sign and flow is now directed toward the jet centerline. The radial velocity continues to increase to some maximum and then decreases, asymptotically approaching zero as the radial distance approaches infinity. Mih [1] has shown that jet radial velocity equals zero when r/x equals 0 and 0.115 by assuming a Gaussian axial velocity distribution in axisymmetric flow and integrating the equation of continuity to yield

$$\frac{V}{U_c} = \frac{C_1}{\eta_M} \left[e^{-\eta_M^2} \left(\frac{1}{2} + \eta_M^2 \right) - \frac{1}{2} \right] \quad (1)$$

where V is the radial velocity, r is the radial distance, x is the axial distance, $\eta_M = r/C_2x$ and C_2 is 0.103 (an experimentally determined constant). The turbulent fluid has a radial component away from the centerline that flows no further than the line r/x equals 0.115 (the radial velocity inversion).

Many researchers do not measure the mean radial velocity component directly. Instead, they compute it by integrating mean axial velocity data and using the equation of continuity, [2,3]. This method functions only within the radial distance to which accurate axial velocity measurements are taken. In addition, most investigators do not measure axial velocity beyond the jet periphery because the axial velocity beyond the jet boundary is very small, difficult to measure accurately, and subject to measurement bias from recirculation within the region. While Fukushima et al. [4], Kassab et al. [5], and Sami et al. [6] report some directly measured radial velocity data beyond the inversion, Kimura et al. [7] and Liepmann and Gharib [8] are representative of radial velocity data taken at significant distances from the jet periphery.

Entrainment flows are generally inviscid flows directed towards the jet axis. Entrainment is the inclusion of fluid from outside the jet boundaries into the main turbulent stream. The consequence of entrainment is that mass flux increases with increasing distance from the jet exit, [9].

Sir Geoffrey Taylor first introduced the entrainment hypothesis, which maintains that the mean inflow velocity across a turbulent

interface is proportional to some characteristic velocity at the boundary of inflow, [10]. Assuming the inflow occurring at the boundary of the jet is some fraction, α , of the mean flow, one can write

$$V_e = \alpha U_c \quad (2)$$

and

$$\frac{dQ}{dx} = 2\pi b_w \alpha U_c \quad (3)$$

where V_e is the magnitude of the entrainment velocity, Q is the mass flux, b_w is the jet half-width, and α is the entrainment coefficient, [11]. It should be noted that U_c and b_w are defined by the type of mean axial velocity profile chosen (i.e., Gaussian, polynomial) and therefore α also depends on the profile chosen, [12]. Values for α range from 0.024 to 0.118. The most accepted value for α is 0.057.

Expressing the rate of entrainment in terms of the radial velocity by integrating the equation of continuity yields

$$\frac{dQ}{dx} = \lim_{r \rightarrow \infty} 2\pi r V. \quad (4)$$

The right side of Eq. (4) can be rearranged to show that the radial velocity is inversely proportional to the radial distance by some constant, c , as follows:

$$V = \frac{c}{r}. \quad (5)$$

The constant, c , with the units $m^2 s^{-1}$, is the rate at which the radial velocity falls to zero as radial distance increases. Combining Eq. (4) and Eq. (5) results in

$$\frac{dQ}{dx} = \lim_{r \rightarrow \infty} 2\pi r V = 2\pi c. \quad (6)$$

Using Eq. (3), the entrainment coefficient α can be related to c as follows:

$$\alpha = \frac{c}{b_w U_c}. \quad (7)$$

Using the mass flux equation, dimensional analysis can be used to show that

$$\frac{dQ}{dx} = C_3 \frac{Q_0}{D}. \quad (8)$$

This is commonly referred to as the jet dilution equation where Q_0 is the initial flow at the jet exit, and C_3 is a dilution constant typically determined by integrating the Gaussian approximation of axial velocity profiles. Typical values for C_3 range from 0.1 to

Contributed by the Fluids Engineering Division for publication in the JOURNAL OF FLUIDS ENGINEERING. Manuscript received by the Fluids Engineering Division Jan. 7, 2002; revised manuscript received Jan. 28, 2003. Associate Editor: M. V. Ötügen.

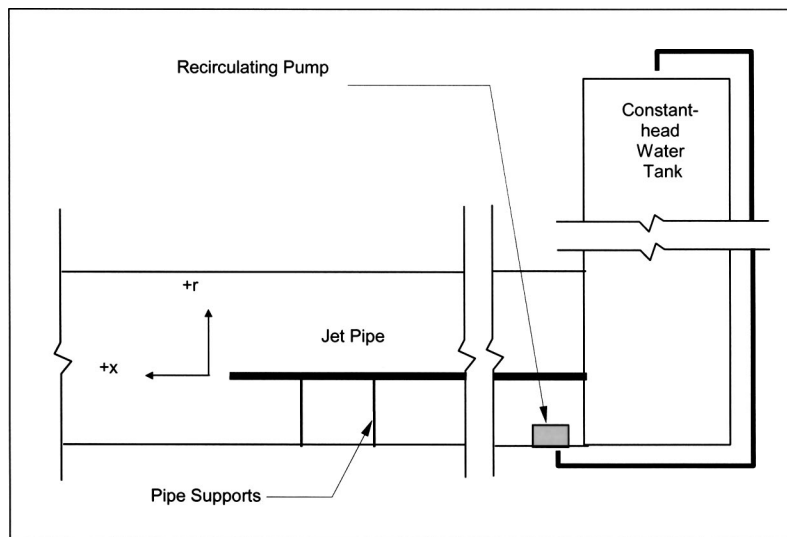


Fig. 1 Schematic of experimental apparatus

0.23 in the zone of flow establishment, and 0.185 to 0.34 in the zone of established flow. This equation links the mass flow at any axial distance to the initial flow.

It is generally accepted that jet exit conditions and Reynolds number affect the rate of entrainment. However, evidence on the degree and manner of these effects varies, [13–18]. Ricou and Spalding [19] show that entrainment decreases for Reynolds numbers less than 25,000, where it levels off. Hussein et al. [20] state that there is no reason to regard the entrainment rate of a jet as universal.

The lack of a comprehensive study of a jet's radial entrainment velocity has prompted the current investigation. The objective of this investigation is to obtain and analyze the radial velocity component in the ambient region surrounding a turbulent jet; establish a direct relationship between mean radial velocity, radial position, and mean axial velocities; and consequently, establish a relationship between mean radial velocity and jet entrainment.

Apparatus

A submerged axisymmetric nonbuoyant turbulent jet of water issues into a flume that acts as a nonstratified ambient reservoir. The flume is 21.3 meters long, 0.6 meters wide and 0.5 m deep with 1.5 m long glass-walled sections, and is filled to a height of 0.46 m (Fig. 1). One end of the flume holds a constant head tank fed by a pump from the flume, with an overflow spillway 2.16 m above the flume bottom. Water flows through a straight 9.44 meter long, 25.4 mm diameter copper pipe at the bottom of the constant head tank. The pipe diameter is reduced to 12.7 mm at a distance of two meters prior to the exit. The jet exit diameter is 12.7 mm, and exits at a height of 230 mm above the flume bottom.

Velocity is measured with a one-dimensional Dantec 55X modular optics LDA using a Dantec FVA covariance signal processor. The LDA is powered by a 20 mw HeNe laser and uses a 40 MHz frequency shift. Optical access is achieved via the glass walls that form the flume's sidewalls. Measurements were taken in backscatter mode using a 310 mm lens, and the data was residence-time weighed. The LDA is mounted on a computer-controlled traverse with three degrees of motion. A titanium dioxide and mica powder with a density of 2.9 gm/cm^3 and an average particle size of $54 \text{ }\mu\text{m}$ is used as velocimetry tracer particles. A particle frequency response analysis has determined that the average tracer particle follows flow frequencies up to 100 Hz—higher than what is expected beyond the jet periphery. A transparent coordinate grid is overlaid on the flume wall section in which the jet

exit is located. Flow visualization by the addition of methylene blue dye to the jet is photographed concurrent with the grid overlay to produce scaled photographs.

The estimate of uncertainty in the results from measurements made by the instrumentation is based on standard principles outlined in ASME [21] and Coleman and Steele [22]. In the present study, the number of samples was selected to ensure the uncertainty of the mean radial velocity was a maximum of 10% (0.001 m/s typical) based on two standard deviations. Each sample was separated by two integral time scales to ensure statistical independence, [23]. The integral time scale was found by integrating the area under the autocorrelation curve for the time series of the acquired data. Typical values of the integral time scale in this experiment are 0.4×10^{-3} sec in the jet and 18×10^{-3} sec beyond the jet periphery.

Kassab et al. [5] maintain that bias correction is not necessary to correct radial velocity results when the radial velocity component contains high velocity fluctuations relative to the mean transverse velocity, and a small magnitude compared to the total velocity vector. An analysis has been performed to compare typical mean radial velocity profiles via resident time-weighted, and un-weighted. The results agree with Kassab [5] in that profiles are perfectly coincident except within areas of turbulence. The results presented are calculated using the resident time-weighting technique, discussed in detail by Buchave et al. [24] and George [25].

Results

A series of 84 experiments is performed and radial velocity data is obtained over the range $0 < x/D < 40$. Each experiment consists of a centerline axial velocity measurement and radial velocity traverses. The average number of samples taken at each location is greater than 2000. Measurements within the jet are included for continuity.

The average exit velocity of the jet is 2.4 m/s and it can be considered a top-hat profile. The exit pipe diameter is 12.7 mm and the average Reynolds number is 27,000. Mean and turbulent axial velocity profiles for the same jet can be found in Rodko and Cataldo [26]. The potential core ends between 4 and 5 diameters downstream of the jet exit. The centerline decay rate, C_1 , corrected for confinement as per Capp [12], is 6.38. The half-width, b_w , is equal to $0.095x$ and forms an angle of 5.43 deg with the jet centerline. The half-width constant, C_2 , is equal to 0.114. The computed dilution constant, C_3 , is 0.332. Mean axial velocity

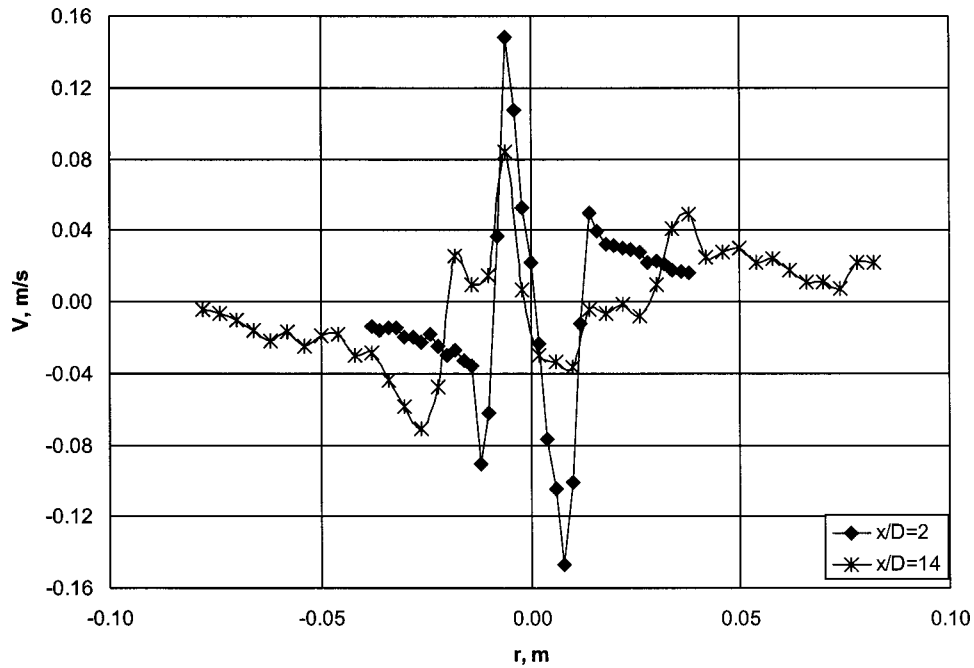


Fig. 2 Example of mean radial velocity profiles

similarity begins at 22 jet diameters and turbulent axial velocity similarity begins at 38 diameters. The present experimental apparatus conserves 98% of the jet's initial momentum at a distance of 20 diameters, and 91% at 40 diameters downstream. Within the range of this investigation, it is a reasonable model of a jet in an infinite environment, as per Hussein et al. [20].

The profiles shown in Fig. 2 are sample plots of mean radial velocity, V , versus the radial distance, r , from the jet centerline at a specific axial distance from the jet exit. These profiles follow the approximate "double S" shape. The location of the radial velocity inversion has been determined for 48 mean radial velocity pro-

files. For presentation, the absolute value of the inversion location has been plotted in Fig. 3. A straight line has been fit to the inversion data obtained from the LDA measured radial velocity:

$$\frac{r}{D} = 0.114 \frac{x}{D} + 0.462 \quad (9)$$

with a correlation coefficient, R^2 , of 0.813. The slope of 0.114 agrees with the computed value of 0.115 reported by Mih [1]. Using the value of 0.114 for C_2 from [26] and Eq. (1), the computed slope of the inversion line is 0.128. This is within 10% of

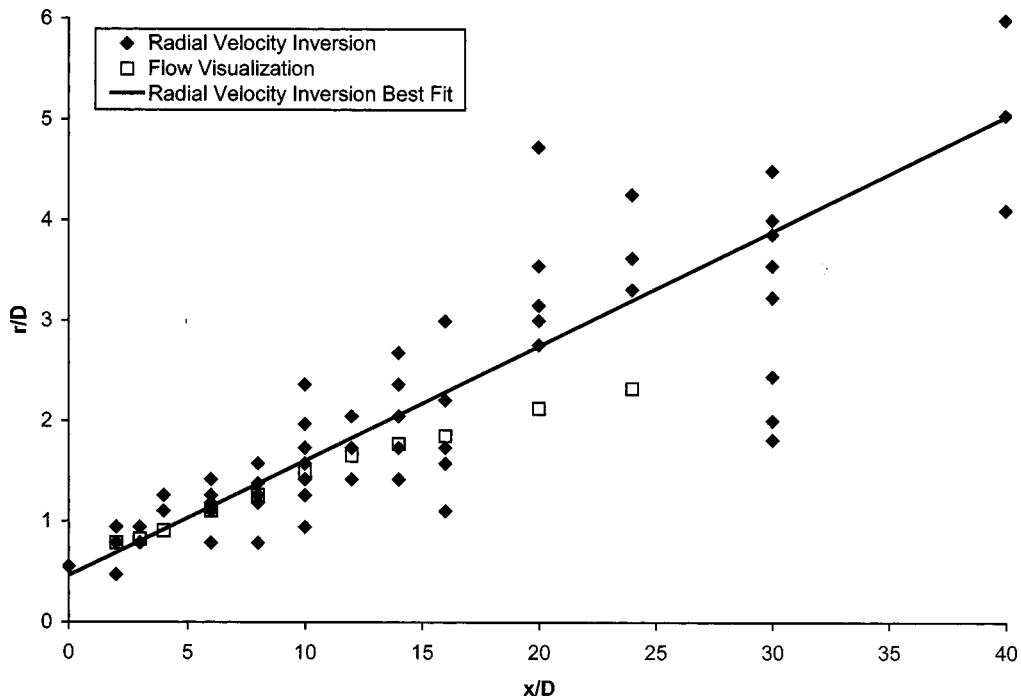


Fig. 3 Nondimensional mean radial velocity inversion

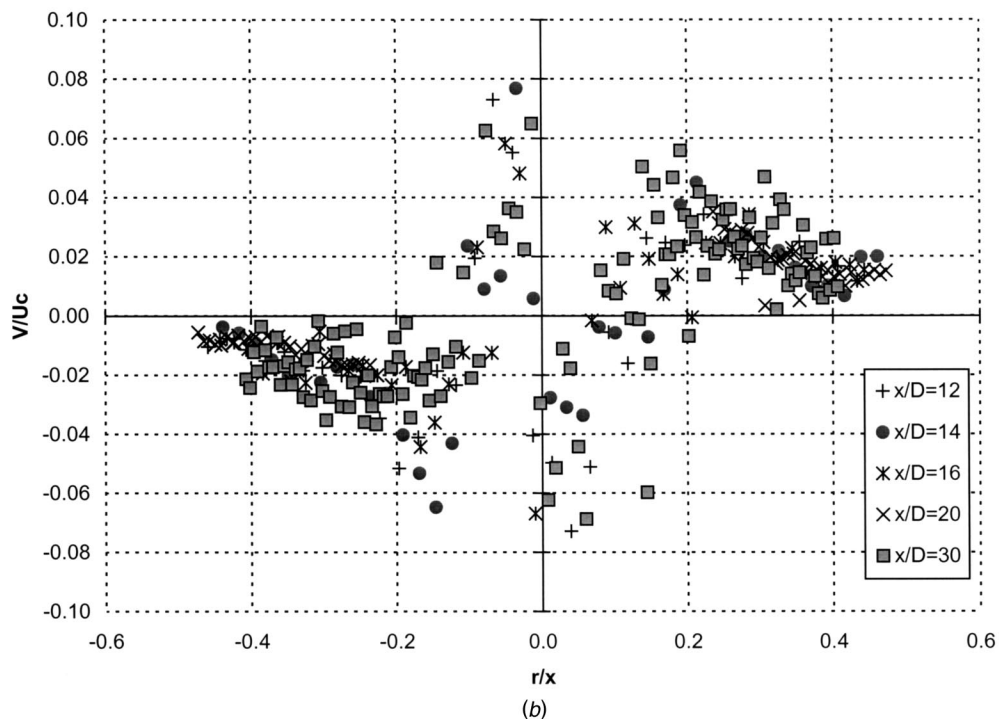
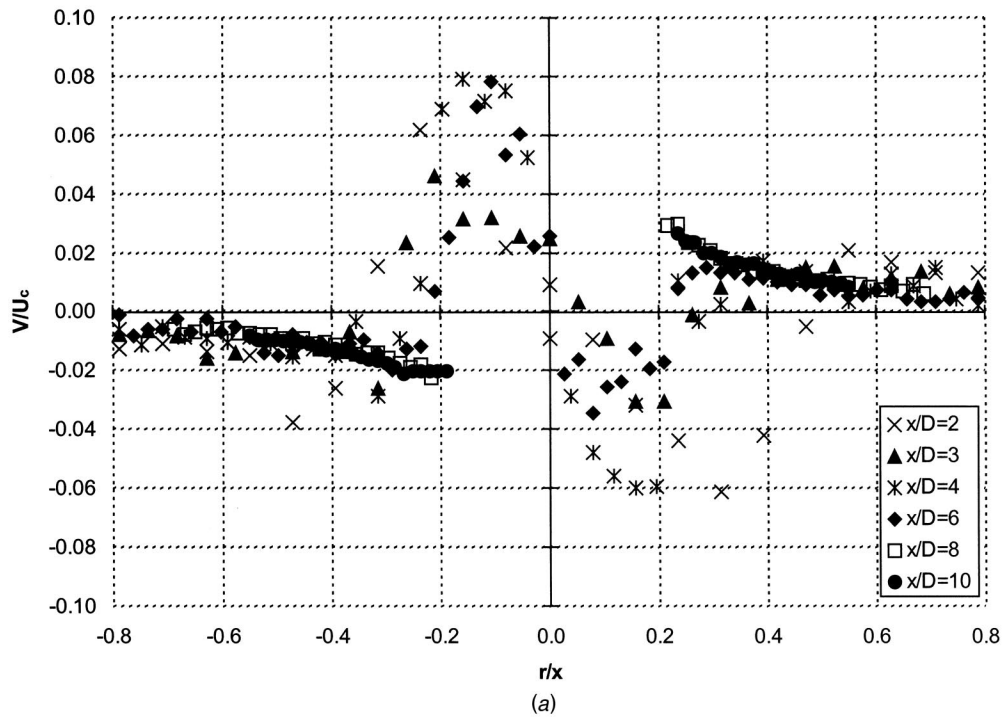


Fig. 4 (a) Normalized mean radial velocity profiles at distance < 12 jet diameters. (b) Normalized mean radial velocity profiles at distance ≥ 12 jet diameters.

the experimentally obtained value. The angle that the radial velocity inversion forms with the jet centerline is 6.50 deg (Fig. 3). This is greater than the jet half-width angle (5.43 deg) and implies that the jet is still undergoing radial expansion at the half-width. The width of the jet is also measured by scaled photographs of the dye flow visualization experiments (Fig. 3). The limit of radial dye spreading follows the velocity inversion data from the jet exit to 12 jet diameters. Its magnitude is smaller thereafter. There is no

reason given for this discrepancy. The limit of dye spreading was difficult to determine at distances greater than 25 diameters due to dilution.

The mean axial centerline velocity is used to normalize the mean radial velocity profiles at the axial distance where the profile is taken. Although there is a significant amount of scatter in the data, the radial velocity within the turbulent jet appears to become concurrent beyond 12 diameters (Figs. 4(a) and 4(b)).

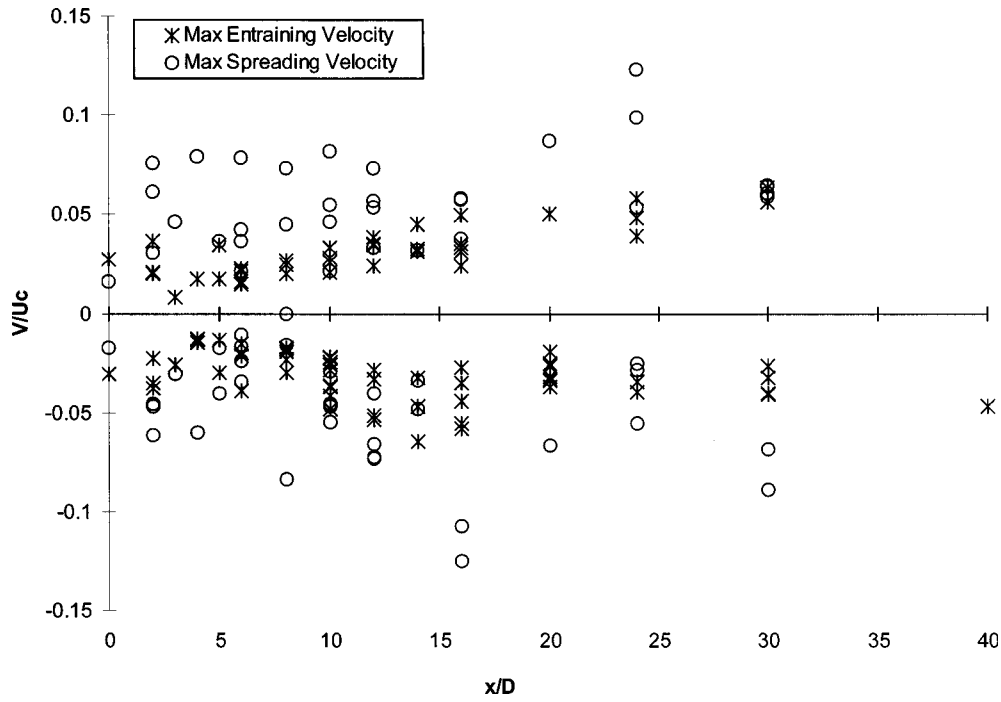


Fig. 5 Normalized maximum spreading and entraining velocity

The radial velocity at distances less than, and greater than the velocity inversion is defined as the spreading and entraining velocity, respectively. The normalized maximum entraining velocity (MEV) and normalized maximum spreading velocity (MSV) are plotted (Fig. 5). The MEV increases up to 20 jet diameters and appears to level off to a constant of 0.05 thereafter. This agrees with the accepted value for α of 0.057, the proportionality constant between V and U (Eq. (2)). The MSV is always greater in magnitude than the MEV. It increases similarly to the MEV and also appears to level off at 0.05 at an axial distance greater than 20 jet diameters.

The mean radial velocity beyond the jet periphery (the entrainment velocity) is curve fit using the inverse function, (Eq. (5)), for each profile. Figure 6 presents an example of the radial velocity data curve fit. The inverse function constant, c , has been determined for each profile. The average correlation coefficient is greater than 0.9 for axial distances less than 16 jet diameters, and greater than 0.7 for distances between 16 and 40 jet diameters, inclusive. The inverse function constant is normalized by the multiplying by D/Q_0 , and plotted (Fig. 7) along with the normalized c derived from several other researchers. The normalized c for axial distances less than 16 diameters is

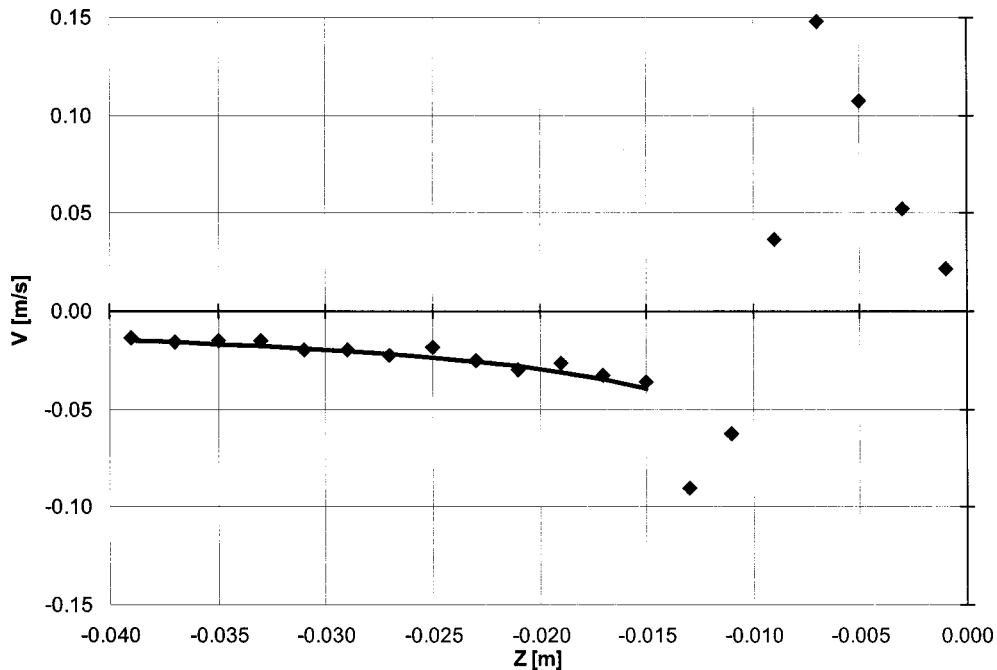


Fig. 6 Detail of inverse function curve fit for radial velocity at 1 jet diameters

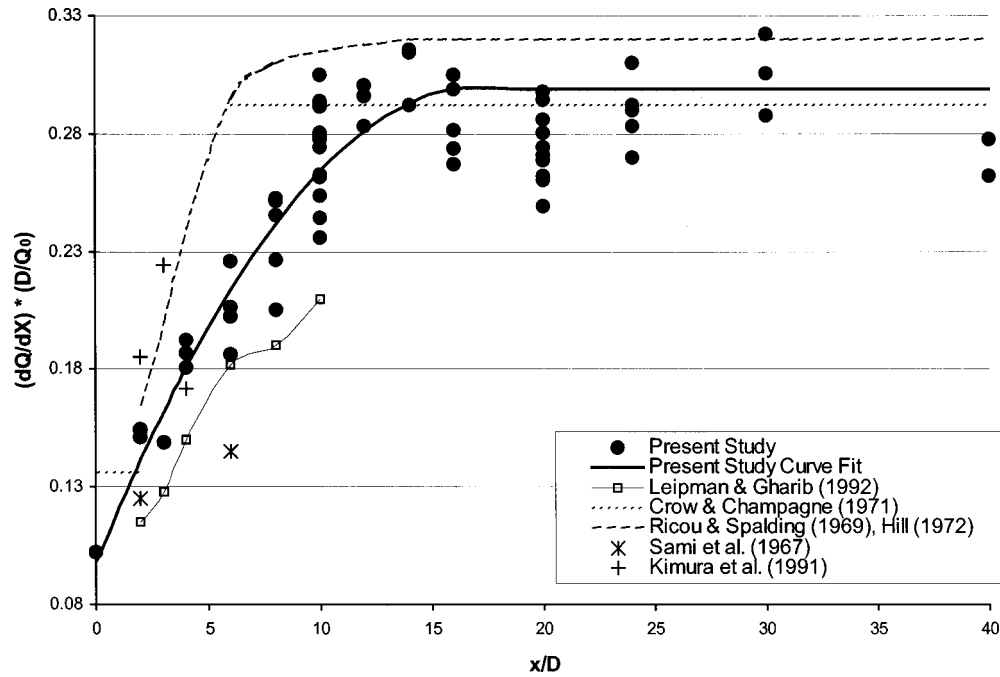


Fig. 7 Normalized plot of c versus axial distance

$$\frac{c}{DU_0} = -0.00009 \left(\frac{x}{D} \right)^2 + 0.003 \frac{x}{D} + 0.012 \quad (10)$$

and for values of greater than 16 diameters:

$$\frac{c}{DU_0} = 0.037 \quad (11)$$

with a correlation coefficient of 0.78 for each. Equation (6) and Eq. (8) are combined with Eq. (10) and Eq. (11) to obtain the dilution factor, C_3 from zero to 16 diameters:

$$C_3 = \frac{D2\pi c}{Q_0} = -0.0007 \left(\frac{x}{D} \right)^2 + 0.024 \frac{x}{D} + 0.096 \quad (12)$$

and a constant of

$$C_3 = 0.297 \quad (13)$$

for axial distances greater than 16 jet diameters. It is within 4% of Papanicolaou and List [27], 1.7% of Crow and Champagne [13], and 11% of Rodko and Cataldo [26], who use the same experimental apparatus and calculate C_3 by axial velocity profile integration.

Equation (7) is used with U_c , b_w , c , and the half-width data of Rodko and Cataldo [26] from the end of the potential core to the beginning of mean axial velocity similarity, to provide an equation for the entrainment coefficient, α :

$$\alpha = -0.0001 \left(\frac{x}{D} \right)^2 + 0.0064 \frac{x}{D} - 0.0006 \quad (14)$$

for less than 20 diameters, and

$$\alpha = 0.06 \quad (15)$$

for greater than 20 diameters. It is evident from Eq. (14) that α is not constant in the ZFE. Jet entrainment has a nonlinear behavior from zero to 16 jet diameters, which is in agreement with the range of values from Hill [15] and Fisher et al. [28]. The measurement of entrainment via mean radial velocity falls within the range of previous entrainment measurements that used more indirect methods, such as numerical integration of axial velocity pro-

files and axial pressure gradient data. Furthermore, the entrainment hypothesis (Eq. (2)) can be misleading: It implies a constant radial velocity at any radial distance, but it is actually a definition for a velocity scale. These authors suggest that it should be augmented with the inverse function definition.

The turbulent radial velocity, v' , is plotted against radial distance from the jet centerline. Turbulent radial velocity profiles exhibit the expected double peak for axial distances less than or equal to six jet diameters, which agrees with Boguslawski and Popiel [29]. The turbulent radial velocity profiles have been normalized by centerline velocity and plotted against r/x (Figs. 8(a) and 8(b)). The centerline values reach a maximum of 0.22 at 12 diameters, the beginning of turbulent radial velocity self-similarity. This maximum is within 4% of the values presented by Hussein et al. [20] and Rodi [30]. The location is less than other researchers, whose values range from 20 to greater than 150 jet diameters. These authors can find no justifiable reason for this deviation from theory.

Conclusions

Mean radial velocity profiles in an axisymmetric, turbulent jet have been measured with an LDA. The profiles are in the shape of “double S” curves. The position where the radial velocity changes sign, the radial velocity inversion, is plotted against axial distance. The slope of this line agrees with empirically computed values reported in previous work. Using characteristic jet constants, the slope of the inversion is analytically determined and falls within 10% of the experimental value. The angle that the radial velocity inversion forms with the jet centerline is 6.50 deg, which is greater than the jet half-width angle of 5.43 deg, implying that the jet is still spreading at the half-width. The radial velocity inversion is a more meaningful and definitive measure of jet width than the arbitrary half-width. The spreading distance of Methylene blue dye has also been used to measure the radial velocity inversion. When plotted against axial distance, it approximates the LDA-measured radial velocity inversion.

The maximum entraining velocity (MEV) is defined as the maximum mean radial velocity within the radial distance beyond

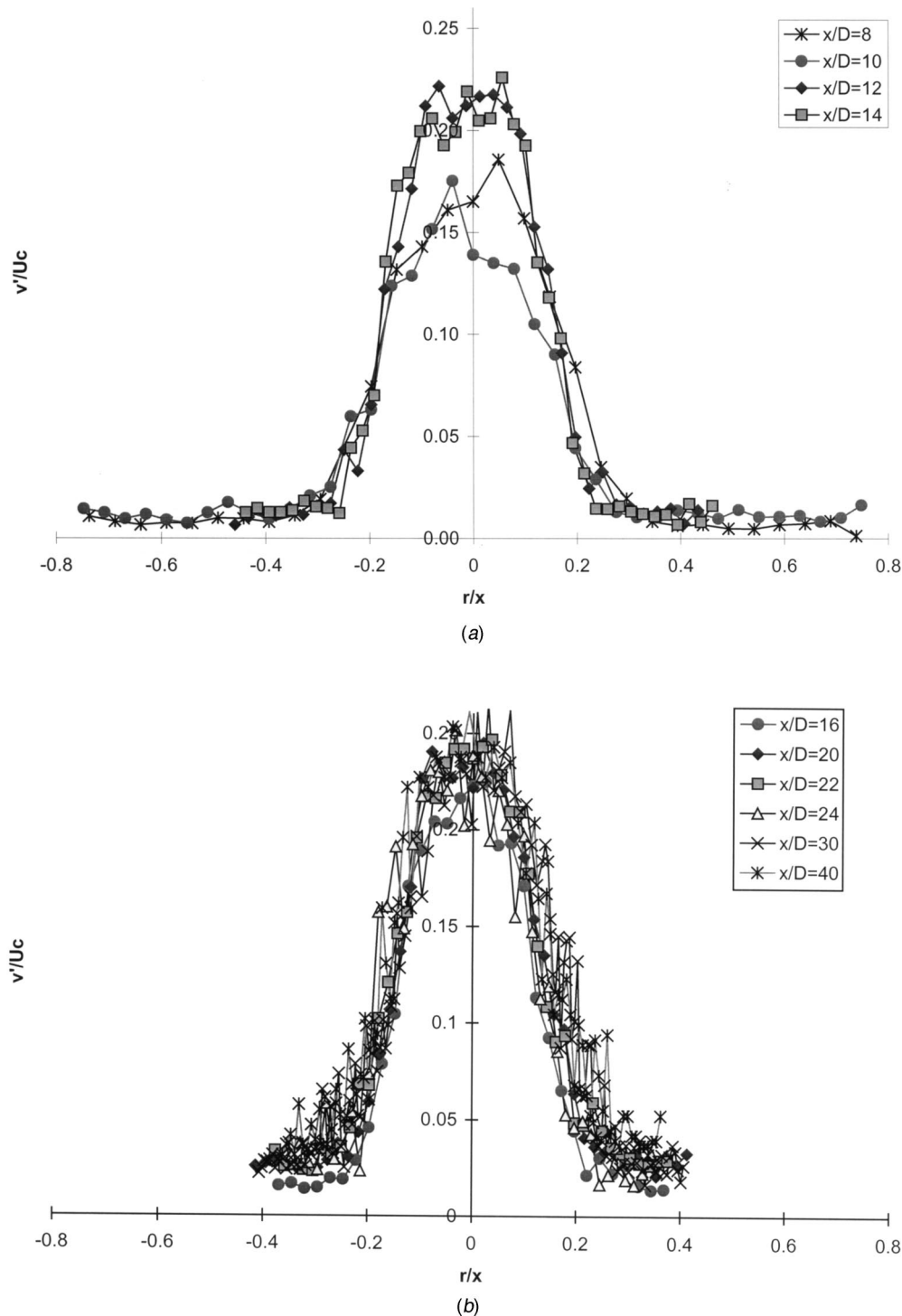


Fig. 8 (a) Turbulent radial velocity profiles (8 to 14 jet diameters). (b) Turbulent radial velocity sections (16 to 40 jet diameters).

the velocity inversion. The maximum spreading velocity (MSV) is defined as the maximum mean radial velocity within the turbulent jet. The MSV is always larger in magnitude than the MEV. Their normalized values appear to level off at a value of 0.05 at axial distances greater than 20 jet diameters.

The entrainment velocity profiles were curve fit using the inverse of the radial distance. The inverse function constant, c , of each profile was plotted against axial position. The normalized inverse function constant, cD/Q_0 , increases nonlinearly and reaches a constant of 0.037 at an axial distance of 16 jet diam-

eters. The jet dilution constant, C_3 , was computed directly from the inverse function constant, and found to be 0.297. This falls within the expected range of 0.185 to 0.34.

The inverse function constant was used to find the entrainment coefficient, α , which increases nonlinearly and reaches a constant of 0.06 at 16 jet diameters. The present value of α agrees with the value of 0.057 reported by most investigators. However, the entrainment constant is a misleading concept, in that there is no constant entrainment velocity that is directly proportional to the local axial velocity by a factor of α for all jet locations. The

entrainment velocity profile has been shown to be an inverse function of radial distance at any given axial location. Therefore, the concept of entrainment defined by α should be augmented with the inverse function definition.

References

- [1] Mih, W., 1989, "Equations for Axisymmetric and Two-Dimensional Turbulent Jets," *J. Hydraul. Eng.*, **115**(12), pp. 1715–1719.
- [2] Davies, P., Fisher, M., and Barratt, M., 1963, "The Characteristics of the Turbulence in the Mixing Region of a Round Jet," *J. Fluid Mech.*, **15**, pp. 337–367.
- [3] Wygnanski, I., and Fiedler, H., 1969, "Some Measurements in the Self-Preserving Jet," *J. Fluid Mech.*, **38**, pp. 577–612.
- [4] Fukushima, C., Aanen, L., and Westerweel, K., 2000, "Investigation of the Mixing Process in an Axisymmetric Turbulent Jet Using PIV and LIF," *10th Int. Symp. on Application of Laser Techniques to Fluid Mechanics, 19/0-13 July, Lisbon, Portugal*.
- [5] Kassab, S., Bakry, A., and Warda, H., 1996, "Laser Doppler Anemometry Measurements in an Axisymmetric Turbulent Jet," *Rev. Sci. Instrum.*, **67**(5), pp. 1842–1849.
- [6] Sami, S., Carmody, T., and Rouse, H., 1967, "Jet Diffusion in the Region of Flow Establishment," *J. Fluid Mech.*, **27**, pp. 231–252.
- [7] Kimura, M., Maeyama, M., Ono, K., and Saima, A., 1991, "Flow Structure in Near-Nozzle Region of Gas Jet," *Experimental Heat Transfer, Fluid Mechanics and Thermodynamics*, Elsevier, New York.
- [8] Liepmann, D., and Gharib, M., 1992, "The Role of Streamwise Vorticity in the Near-Field Entrainment of Round Jets," *J. Fluid Mech.*, **245**, pp. 643–668.
- [9] List, E., and Imberger, J., 1973, "Turbulent Entrainment in Buoyant Jets and Plumes," *J. Hydraul. Div., Am. Soc. Civ. Eng.*, **HY9**, pp. 1461–1474.
- [10] Morton, B. R., Taylor, G. I., and Turner, J. S., 1956, "Turbulent Gravitational Convection From Maintained and Instantaneous Sources," *Proc. R. Soc. London, Ser. A*, **A234**, pp. 1–23.
- [11] Turner, J., 1986, "Turbulent Entrainment: The Development of the Entrainment Assumption, and Its Application to Geophysical Flows," *J. Fluid Mech.*, **173**, pp. 431–471.
- [12] Capp, S., 1983, "Experimental Investigation of the Turbulent Axisymmetric Jet," Ph.D. thesis, State University of New York at Buffalo, Buffalo, NY.
- [13] Crow, S., and Champagne, F., 1971, "Orderly Structure of Jet Turbulence," *J. Fluid Mech.*, **48**, pp. 547–596.
- [14] Fondse, H., Leijdens, H., and Ooms, G., 1983, "On the Influence of the Exit Conditions on the Entrainment Rate in the Development Region of a Free, Round, Turbulent Jet," *Appl. Sci. Res.*, **40**, pp. 355–375.
- [15] Hill, B., 1972, "Measurements of Local Entrainment Rate in the Initial Region of Axisymmetric Turbulent Air Jets," *J. Fluid Mech.*, **51**, pp. 773–779.
- [16] Hussain, A., and Zaman, K., 1981, "The 'Preferred Mode' of the Axisymmetric Jet," *J. Fluid Mech.*, **110**, pp. 39–71.
- [17] Bayazitoglu, Y., and Peterson, J., 1992, "Measurements of Velocity and Turbulence in Vertical Axisymmetric Isothermal and Buoyant Jets," *ASME J. Heat Transfer*, **114**, pp. 135–142.
- [18] Trabold, T., Esen, E., and Obot, N., 1987, "Entrainment by Turbulent Jets Issuing From Sharp-Edge Inlet Round Nozzles," *Trans. ASME*, **109**, pp. 248–254.
- [19] Ricou, F., and Spalding, D., 1961, "Measurement of Entrainment by Axisymmetric Turbulent Jets," *J. Fluid Mech.*, **11**, pp. 21–32.
- [20] Hussein, H., Capp, S., and George, W., 1994, "Velocity Measurements in a High-Reynolds-Number, Momentum-Conserving, Axisymmetric, Turbulent Jet," *J. Fluid Mech.*, **258**, pp. 31–75.
- [21] ASME, 1998, "Test Uncertainty—Instruments and Apparatus—Supplement to ASME Performance Test Codes," ASME, New York, PTC-19.1-1998.
- [22] Coleman, H., and Steele, W., 1989, *Experimentation and Uncertainty Analysis for Engineers*, John Wiley and Sons, New York.
- [23] Bruun, H., 1995, *Hot-Wire Anemometry*, Oxford University Press, New York.
- [24] Buchave, P., George, W. K., and Lumley, J. L., 1979, "The Measurement of Turbulence With the Laser-Doppler Anemometer," *Annu. Rev. Fluid Mech.*, **11**, pp. 443–503.
- [25] George, W. K., 1988, "Quantitative Measurement With the Burst-Mode Laser-Doppler Anemometer," *Exp. Therm. Fluid Sci.*, **1**, pp. 29–40.
- [26] Rodko, A., and Cataldo, J., 1999, "Interaction of Surface Waves and a Jet," *International Journal of Fluid Mechanics Research*, **26**, Nos. 5 and 6.
- [27] Papanicolaou, P., and List, E., 1988, "Investigations of Round Vertical Turbulent Buoyant Jets," *J. Fluid Mech.*, **195**, pp. 341–391.
- [28] Fisher, H., List, E., Koh, R., Imberger, J., and Brooks, N., 1979, *Mixing in Inland and Coastal Waters*, Academic Press, San Diego, CA.
- [29] Boguslawski, L., and Popiel, C., 1979, "Flow Structure of the Free Round Turbulent Jet in the Initial Region," *J. Fluid Mech.*, **90**, pp. 531–539.
- [30] Rodi, W., 1975, "A Review of Experimental Data of Uniform Density Free Turbulent Boundary Layers," *Studies in Convection*, B. Launder ed., Academic Press, San Diego, CA.

Concentration Probe Measurements in a Mach 4 Nonreacting Hydrogen Jet

D. R. Buttsworth

Faculty of Engineering and Surveying,
University of Southern Queensland,
Toowoomba, QLD 4350, Australia

T. V. Jones

Department of Engineering Science,
University of Oxford,
Oxford OX1 3PJ, UK

A new probe technique is introduced for the measurement of concentration in binary gas flows. The new technique is demonstrated through application of the probe in a Mach 4 nonreacting jet of hydrogen injected into a nominally quiescent air environment. Previous concentration probe devices have mostly used hot wires or hot films within an aspirating probe tip. However, the new technique relies on Pitot pressure and stagnation point transient thin film heat flux probe measurements. The transient thin film heat flux probes are operated at a number of different temperatures and thereby provide stagnation temperature and heat transfer coefficient measurements with an uncertainty of around ± 5 K and $\pm 4\%$ respectively. When the heat transfer coefficient measurements are combined with the Pitot pressure measurements, it is demonstrated that the concentration of hydrogen within the mixing jet can be deduced. The estimated uncertainty of the reported concentration measurements is approximately $\pm 5\%$ on a mass fraction basis.

[DOI: 10.1115/1.1595671]

Introduction

Concentration measurements are needed in many environments where mixing and combustion occurs. Nonintrusive laser-based techniques such as laser-induced fluorescence are currently used in many laboratories to measure concentrations of species such as OH and NO. However, probe measurements can still make valuable contributions in many situations due to their low cost, and ease of installation and operation.

For concentration measurements in subsonic isothermal flows, various techniques based on hot wire anemometry have been demonstrated. For example, McQuaid and Wright [1,2] used exposed hot wire sensors for velocity and concentration measurements in subsonic jet flows. In general, at least two different overheat ratios are necessary if concentration measurements are to be obtained from exposed hot wire devices. However, if an aspirating probe is operated at choked conditions, then a single hot wire located within the probe is sufficient for concentration measurements provided the stagnation pressure and temperature do not vary. Brown and Rebollo [3] developed such a probe for subsonic mixing layer measurements. Shock tube calibration tests indicated a response time of around 0.2 ms for the Brown-Rebollo device, [3].

For concentration measurements in compressible flows, aspirating devices have also been used. Swithenbank [4] discussed a concentration probe which utilized pressure transducers to monitor the flow rate through a choked orifice which was located downstream of the aspirating probe tip. Ninnemann and Ng [5] used a hot wire upstream of a choked orifice with independent measurements of total pressure and temperature to measure concentration variations across a compressible shear layer. The maximum bandwidth for aspirating probes is limited to around 20 kHz because of the need to establish a quasi-steady choked flow within the probe, [6,7].

The current article introduces a new probe technique for concentration measurements in binary gas flows. The probe arrangement utilizes transient thin film heat flux gauge technology and represents a natural extension of the fast-response stagnation temperature probe technique that has been reported previously, [8]. When operated as either a stagnation temperature probe or a con-

centration probe, the device is robust and is well suited to compressible flow measurements. In the current work, the operating principles are first discussed and then the technique is demonstrated by describing stagnation temperature and concentration measurements in a nonreacting hydrogen free jet arrangement.

Measurement Technique

Transient Thin Film Probes. Platinum films were hand-painted onto the rounded end of fused quartz rods with a diameter of about 3 mm, as illustrated in Fig. 1. Three transient thin films were used in the present work. Low resistance gold leads were also painted onto the quartz and the active film length was less than 1 mm in each case.

The films were operated in a constant current mode so that the voltage drop across each film indicated the film resistance and thus its temperature. Each film was calibrated over its full range of operating temperatures and a quadratic temperature-resistance relationship was established for each film. The measurement technique (see Measurement of T_0 and h) requires heat flux measurements at different surface temperatures. To generate the different surface temperatures, an external preheating unit was positioned over film 1, as illustrated in Fig. 1. This preheating unit was swung away just prior to the probes traversing the jet.

Measurement of T_0 and h . When the stagnation enthalpy of the flow is relatively high, it is usual to express the convective heat transfer in terms of an enthalpy difference across the stagnation point boundary layer, [9]. However, because of the modest enthalpies encountered in the current application, the gases remain calorically perfect which means it is reasonable to express the stagnation point heat transfer as

$$q = h(T_0 - T_w). \quad (1)$$

Due to the low velocity at the edge of the stagnation point boundary layer, it is appropriate for the stagnation temperature to appear in the governing relationship, Eq. (1). Since the entire length of each film cannot be precisely at the stagnation point, the flow velocity at the boundary layer edge will actually be nonzero for the majority of the film length. However, for the present films which were within 20 deg of their respective stagnation points, the actual flow temperature at the edge of the boundary layer will be within about 0.5% of T_0 , even for $M_\infty \rightarrow \infty$, the hypersonic limit,

Contributed by the Fluids Engineering Division for publication in the JOURNAL OF FLUIDS ENGINEERING. Manuscript received by the Fluids Engineering Division July 5, 2001; revised manuscript received Mar. 10, 2003. Associate Editors: K. Zaman and J. Katz.

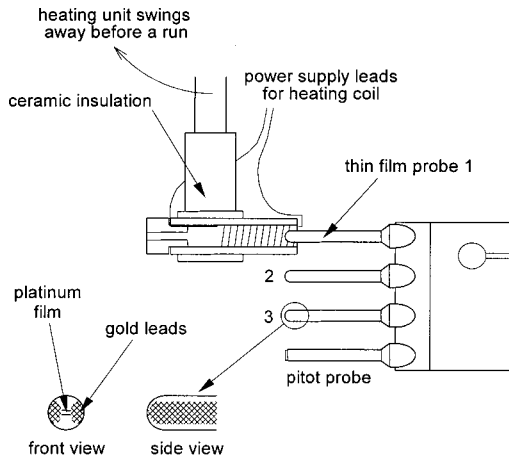


Fig. 1 Illustration of the probe arrangement

[10]. (The hypersonic limit produces the largest departure of the recovery temperature from T_0 for a given distance from the stagnation point.)

A single transient thin film heat flux probe will produce measurements of both q and T_w , so if two thin films are operated at different values of T_w , then both h and T_0 can be identified since h is virtually independent of T_w in the current experiments (see Measurement of Concentration). In the current work, three films were operated at a number of different temperatures so that RMS measurements of fluctuations could be obtained.

Measurement of Concentration. This section demonstrates how the concentration of a binary gas mixture can be identified from the transient thin film heat transfer coefficient measurements. Theoretical results, [9], suggest that the stagnation point heat transfer coefficient for a sphere at any Mach number can be correlated using

$$\text{Nu} = 0.763 \text{Pr}^{0.4} \text{Re}^{0.5} C^{0.1} \left(\frac{KD}{u_\infty} \right)^{0.5} \quad (2)$$

where

$$\text{Nu} = \frac{hD}{k_e} \quad (3)$$

$$\text{Pr} = \frac{c_p \mu_e}{k_e} \quad (4)$$

$$\text{Re} = \frac{\rho_e u_\infty D}{\mu_e} \quad (5)$$

$$K = \frac{du_e}{dx} \quad (6)$$

$$C = \frac{\rho_w \mu_w}{\rho_e \mu_e} \quad (7)$$

Pitot pressure measurements are routinely made in typical experiments, and the current work is no exception, so it is convenient to rearrange the heat transfer coefficient in terms of the Pitot pressure. Assuming measurements are made within a perfect gas, p_{pit} enters Eq. (2) through the Reynolds number (Eq. (5)) using

$$\rho_e = \frac{p_e}{RT_e} = \frac{p_{\text{pit}}}{RT_0} \quad (8)$$

The undisturbed freestream Mach number is

$$M_\infty = \frac{u_\infty}{(\gamma RT_\infty)^{0.5}} \quad (9)$$

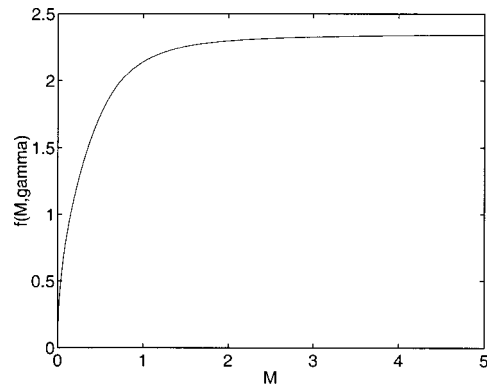


Fig. 2 Sensitivity of heat transfer coefficient to Mach number as indicated by $f(M_\infty, \gamma)$ for $\gamma=1.4$

and

$$R = \frac{\gamma - 1}{\gamma} c_p \quad (10)$$

Hence, it is possible to rearrange the heat transfer coefficient in Eq. (2) with the aid of Eqs. (8)–(10) as

$$h = 0.763 D^{-0.5} f(M_\infty, \gamma) f(\text{thermophysical properties}) p_{\text{pit}}^{0.5} \quad (11)$$

where

$$f(M_\infty, \gamma) = \gamma^{0.5} (\gamma - 1)^{-0.25} (M_\infty)^{0.5} \left(\frac{T_\infty}{T_0} \right)^{0.25} \left(\frac{KD}{u_\infty} \right)^{0.5} \quad (12)$$

and

$$f(\text{thermophysical properties}) = c_p^{0.15} k_e^{0.6} \mu_e^{-0.1} C^{0.1} T_0^{-0.25} \quad (13)$$

Equation (12) indicates that for subsonic flows, the heat transfer coefficient is a strong function of the Mach number but it rapidly becomes independent of the Mach number for supersonic flows as illustrated in Fig. 2 for a flow with $\gamma=1.4$. Equation (12) is therefore an important result because it indicates that in supersonic flows, it is not necessary to have a precise measurement of the Mach number in order to estimate the stagnation point heat transfer coefficient with reasonable accuracy. To obtain the result presented in Fig. 2, the temperature ratio T_∞/T_0 in Eq. (12) was evaluated using the usual isentropic relationship, and the velocity gradient term was determined using

$$\frac{KD}{u_\infty} \approx 3(1 - 0.252M_\infty^2 - 0.0175M_\infty^4) \quad \text{for } M_\infty < 0.8 \quad (15)$$

and

$$\frac{KD}{u_\infty} \approx \left(\frac{8\rho_\infty}{\rho_e} \right)^{0.5} \quad \text{for } M_\infty > 1.2 \quad (16)$$

with an interpolation between Eq. (15) and Eq. (16) for $0.8 < M_\infty < 1.2$. The stagnation point velocity gradient expressions given by Eq. (15) and Eq. (16) are approximate relationships suggested by White [9].

If the Pitot pressure is measured and the Mach number has been identified such that $f(M_\infty, \gamma)$ is known with sufficient precision, then $f(\text{thermophysical properties})$ can be identified from the heat transfer coefficient measurements (Eq. (11)) since the effective diameter of the probe is known or can be identified through a suitable calibration. The thermophysical properties of the flow are a function of the gas composition and Eq. (13) indicates that for gases with sufficiently dissimilar thermophysical properties, the measurement of convective heat transfer coefficient can be used to indicate the concentration of a binary gas mixture. Equation (13)

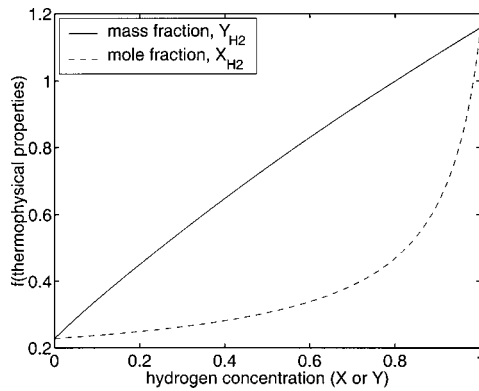


Fig. 3 Sensitivity of heat transfer coefficient to the concentration of the mixture as indicated by f (thermophysical properties) for a hydrogen-air mixture at $T_0=290$ K

is plotted in Fig. 3 as a function of the mole fraction and mass fraction of a hydrogen-air mixture with $T_0=290$ K and $T_w=290$ K. In Fig. 3, the viscosity and conductivity of the hydrogen-air mixture have been evaluated using the Wilke formula.

Experiment and Data Acquisition

Experiments were performed using the free jet arrangement illustrated in Fig. 4. The contoured Mach 4 injection nozzle had a throat diameter of 9.42 mm and was designed using the method of characteristics. The nozzle exit diameter was 29.5 mm and the lip thickness was 0.5 mm. The injection nozzle was located in the test section of the Oxford University Gun Tunnel. Either nitrogen or hydrogen was supplied to the Mach 4 nozzle from an unheated Ludwig tube. Prior to a run, the test section was evacuated to approximately 1.2 kPa, and the slug of gas in the Ludwig tube was isolated from the low pressure test section by a fast-acting valve.

A short time after opening the fast-acting valve, a pressure rise was indicated by the injection pressure transducer and the injection static pressure measured 3 mm upstream of the nozzle lip decreased during flow establishment and then increased back up to the steady injection value—see Fig. 5(a). The Ludwig tube filling pressure was chosen so that the steady injection static pressure was approximately the same as the initial test section pressure.

The thin film and Pitot pressure probes were initially located above the centerline of the jet and were driven across the jet at around 70 ms after the fast-acting valve was opened—Fig. 5(b). The traverse speed was approximately 1.7 m/s and the physical

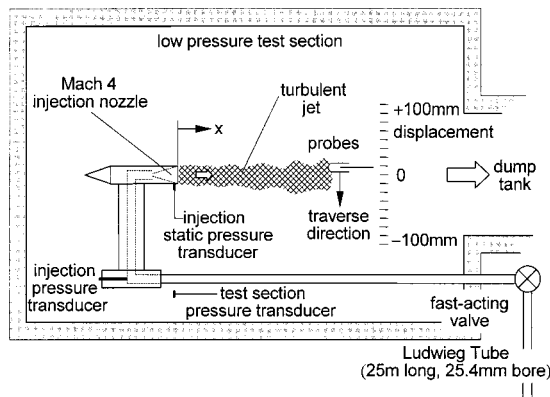


Fig. 4 Illustration of the Mach 4 free jet arrangement

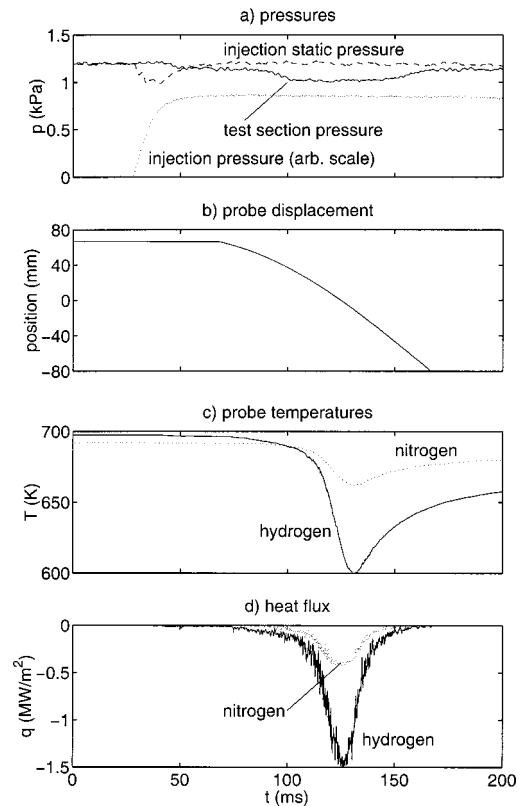


Fig. 5 Typical signals obtained during the experiments

separation of film 1 and the Pitot probe was 27 mm. Traverses were performed at 4 locations: $x=1, 100, 200,$ and 300 mm. The Pitot pressure probe utilized a commercial piezoresistive transducer with a perforated screen and was about 2.5 mm in diameter.

As previously mentioned, the measurement technique requires heat transfer measurements at different surface or film temperatures, and this was achieved in the current work using an external preheating unit as illustrated in Fig. 1. Although the preheating unit was positioned over film 1, the temperatures of films 2 and 3 also increased through radiative heat transfer from the unit. The temperature of film 1 was monitored during the preheating process, and when the required surface temperature was achieved, a run was manually initiated.

Prior to sampling, the amplified signal from the Pitot probe was low pass filtered with a cutoff frequency of about 60 kHz. Signals from all transducers were recorded at 8 kSamples/s and subsequently analyzed to yield the time averaged results. For the analysis of fluctuating results, signals from the thin film temperature probes were processed by electrical heat transfer analogue units, [11], and were then sampled at 500 kSamples/s. The bandwidth of the heat transfer analogue units extends to about 85 kHz.

The matching of injection static pressure and test section pressure remains somewhat uncertain because during a traverse of the jet, the test section pressure transducer registered a value lower than the initial test section pressure prior to flow establishment (Fig. 5(a)). During the traverse, the average test section pressure registered by the transducer was 1.05 kPa for the nitrogen jet and 1.08 kPa for the hydrogen jet. The difference between injection and test section pressures leads to the development of shock-expansion cells within the jet flow and some uncertainty in the static pressure within the jet for $x=100, 200,$ and 300 mm stations. The shock and expansion waves appear to have little influence on any of the probe measurements; no such waves were visible in schlieren flow visualization of the jet flows.

Table 1 Injection parameters

Parameter	Nitrogen Jet	Hydrogen Jet
M_∞	3.7 ± 0.1	3.8 ± 0.1
T_∞ (K)	78 ± 4	72 ± 4
p_∞ (kPa)	1.20 ± 0.04	0.81 ± 0.07
u_∞ (m/s)	664 ± 10	2450 ± 40
ρ_∞ ($\times 10^{-3}$ kg/m ³)	52 ± 3	2.7 ± 0.3

Estimates of the Mach 4 nozzle exit flow parameters are presented in Table 1. These values are based on measurements of the static pressure, Pitot pressure, and the flow total temperature as discussed in the next section. The uncertainties quoted in Table 1 are based on the estimated uncertainties and spatial variation of the measured quantities at $x=1$ mm. For the stations: $x=100$, 200, and 300 mm, the uncertainty in static pressure is $\pm 14\%$ for the nitrogen jet and $\pm 32\%$ for the hydrogen jet (substantially larger than quoted in Table 1) due to the mismatch of pressures discussed previously. These uncertainties in static pressure are substantial, but it is still possible to extract meaningful results from the measurements, as will be demonstrated in the remainder of this article.

Time-Averaged Results

Transient Heat Flux Analysis. The transient thin film heat flux probes provide a measurement of probe surface temperature that must be converted into a heat flux using an appropriate model for the transient heat conduction processes within the probe substrate. In the present work, the heat flux was identified from the surface temperature signals using a finite difference routine, [12], which accounts for the temperature-dependent thermal properties and the hemispherical geometry of the quartz substrates. It is important to properly account for the temperature-dependent thermal properties of the quartz because of the elevated surface temperatures encountered during the experiments and large probe surface temperature variations during jet traverses, particularly in the case of the hydrogen jet, Fig. 5(c). The hemispherical geometry can also be significant because the heat penetrates a significant distance relative to the probe radius during the 50 ms or so taken by the probe to traverse the jet, Fig. 5.

Typical examples of thin film temperature and corresponding heat flux measurements are illustrated in parts (c) and (d) of Fig. 5. The minimum heat flux (Fig. 5(d)) occurs earlier than the minimum probe surface temperature (Fig. 5(c)) because in its simplest form, the heat flux can be expressed as an integral involving the derivative of the surface temperature, [12].

The time-averaged components of the probe temperature and heat flux data were identified by digitally low-pass filtering the data such as that illustrated in Fig. 5(c) and (d). The cutoff frequency of the digital filter was varied with the traverse location: 1.0 kHz for $x=1$ mm, 0.5 kHz for $x=100$ mm, 0.2 kHz for $x=200$ mm, and 0.1 kHz for $x=300$ mm.

Stagnation Temperature and Heat Transfer Coefficients.

At each of the four locations downstream of injection ($x=1$, 100, 200, and 300 mm), a number of traverses—either, three or four—were performed at different initial probe temperatures. In principal, only two different probe temperatures are required for the identification of the flow total temperature and heat transfer coefficient (see Measurement of T_0 and h). However, as the spatial separation of the thin film probes was on the order of 10 mm, which is on the same order as the half-width of the jet, the fluctuations in heat flux at the different probes are poorly correlated so it is necessary to adopt an RMS analysis for the identification of fluctuations. While, the motivation for the use of multiple probe temperatures was principally the RMS fluctuation analysis, the analysis of the time-averaged results is also enhanced by the additional data at different probe temperatures. The same results

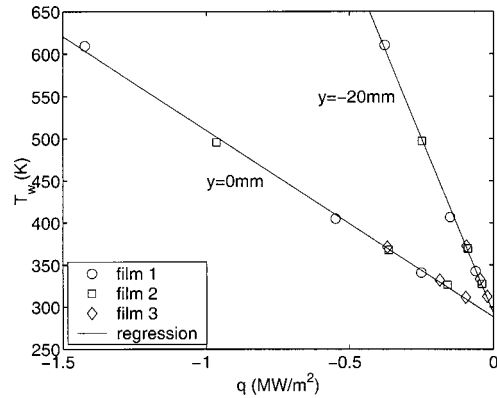


Fig. 6 Illustration of heat flux for various probe temperatures at two points across the hydrogen jet for $x=300$ mm

could have been obtained using a single probe traversing the jet a number of times. The use of multiple probes within the jet a number of times reduced the number of traverses that were required.

To identify the flow stagnation temperature and probe heat transfer coefficient distribution at each traverse location, the spatial variation of the probe temperature and heat flux data from each probe was referenced to the center line of the jet via the appropriate probe displacement measurement (e.g., Fig. 5(b)). A linear regression for the heat flux versus probe temperature data was performed at each position across the jet. Figure 6 illustrates the regression at two locations across the hydrogen jet at $x=300$ mm. The data presented in this figure were obtained from three traverses of the jet at the points in time when each film passed the locations $y=0$ and $y=-20$ mm. The film temperatures appear to be almost identical at these locations ($y=0$ and $y=-20$ mm) because the transient response of the films to the convective cooling resulted in relatively small differences in film temperature at the indicated locations (see Fig. 5 parts (b) and (c)). The intercept of the regression line and the vertical axis indicates the flow stagnation temperature (at that point within the jet) and the inverse of the slope of each regression line indicates the heat transfer coefficient of the probes (at that point within the jet).

The stagnation temperature and heat transfer coefficient results obtained in this manner are presented in Figs. 7 and 8. The bars illustrated on these figures indicate the magnitude of the 95% confidence intervals derived from the statistical analysis of the linear regression data (e.g., see Chatfield [13]). At the center of the nitrogen and hydrogen jets, the estimated uncertainty derived

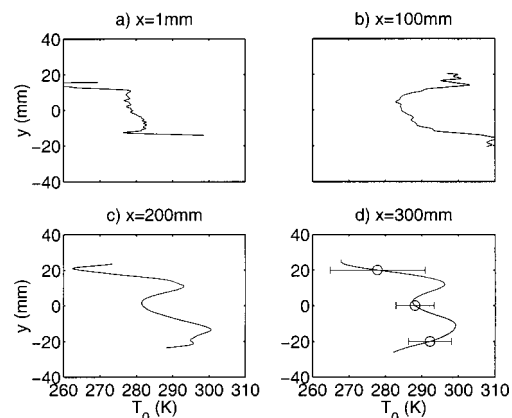


Fig. 7 Time-averaged stagnation temperature measurements in the hydrogen jet at 4 stations downstream of injection

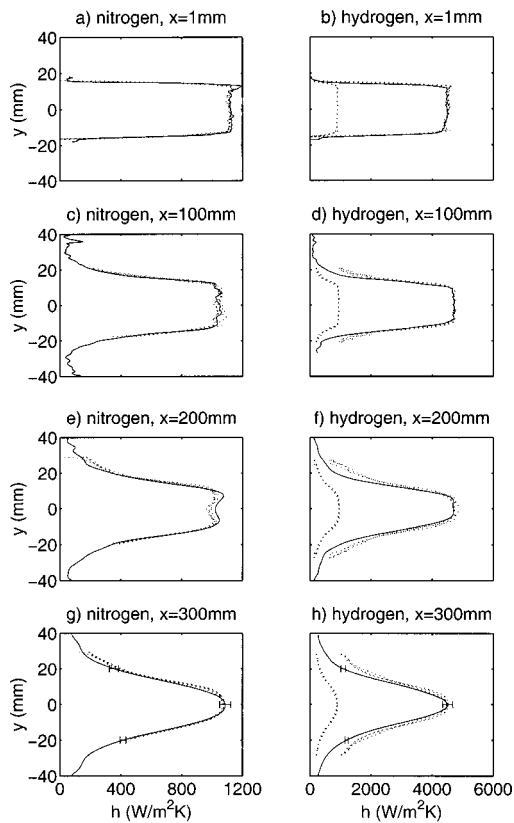


Fig. 8 Time-averaged heat transfer coefficient results at four stations downstream of injection. Solid lines: thin film probes; dots: Pitot probe predictions.

from this regression analysis was around ± 5 K for the stagnation temperature, and $\pm 3.5\%$ for the heat transfer coefficient. Generally, the relative measurement uncertainty in both stagnation temperature and probe heat transfer coefficient increases with distance from the jet center line because the magnitude of the heat flux approaches zero (Fig. 5). For example, see the bars reported in Fig. 7 and Fig. 8 at $x=300$ mm. The average uncertainties at $y = \pm 20$ mm are ± 10 K and $\pm 6\%$ in stagnation temperature and heat transfer coefficient, respectively.

The stagnation temperature measurements for the hydrogen jet, Fig. 7, indicate the existence of significant spatial variations on the order of ± 10 K. Similar results are obtained in the nitrogen jet, but the variations are less significant, [14]. Spatial variations in the stagnation temperature of jet flows have previously been observed in subsonic, [15], and Mach 2, [16], jet flows. Such effects have been described as “temperature separation” and can be explained in terms of either vortex or shock-vortex interaction processes, [15,16].

Concentration Measurements. Concentration can be identified from the heat transfer coefficient measurements provided the Pitot pressure is measured and Mach number is known to a reasonable precision, as indicated by Eq. (11). The distribution of flow properties identified from the Pitot probe (as with the data from the three heat transfer probes) are referenced to the jet center line with the aid of the probe displacement measurement for each traverse (e.g., Fig. 5(b)).

Pitot pressure measurements within the nitrogen jet were combined with static pressure measurements in order to identify the Mach number distribution within the jet flow. Static pressure was taken as equal to the value indicated by the injection static pressure transducer for the traverse at $x=1$ mm, however, for the remaining traverse stations ($x=100, 200,$ and 300 mm), the static

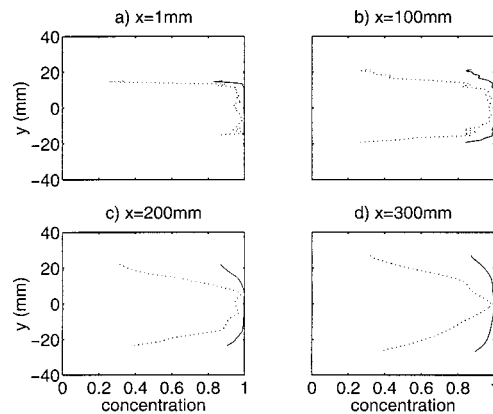


Fig. 9 Time-averaged hydrogen concentration profiles. Solid line: hydrogen mole fraction; dots: hydrogen mass fraction.

pressure within the jet was taken as the average value between the injection static pressure and the test section pressure values. The function described in Eq. (13) was then evaluated for the nitrogen using Sutherland’s law for the viscosity and conductivity, assuming the flow stagnation and probe temperatures were both 290 K.

The heat transfer coefficient (Eq. (11)) was then evaluated with the effective probe diameter D taken as 2.88 mm. The diameter of 2.88 mm was chosen so that the convective heat transfer coefficient predictions in the nitrogen jet at $x=1$ mm matched the thin film measurements, Fig. 8(a). The 3 mm diameter is only nominal and the stagnation point radius of curvature is generally less than 1.5 mm for these devices, [17]. Thus, the nitrogen jet at $x=1$ mm has been used to calibrate the probes—an effective diameter of 2.88 mm is physically reasonable.

At subsequent stations in the nitrogen jet (Fig. 8(c), (e), and (g)) predicted heat transfer coefficient distributions are in close agreement with the distributions identified from the thin film probes. Differences between the predictions and the measurements are apparent in the outer regions of the jet, for example, for $y > 20$ mm in Fig. 8(e) and Fig. 8(g). In these regions the Mach number is transonic or subsonic, and hence inaccuracies in the Mach number estimate (which arise due to uncertainties in the flow static pressure) will have a strong influence on the heat transfer coefficient prediction (Eq. (12), Fig. 2). Another obvious deviation between the measured and predicted results occurs at $x=200$ mm (Fig. 8(e)) towards the center of the jet. The magnitude of this deviation is on the same order as the estimated uncertainty in the thin film heat transfer coefficient measurements of around 3.5% near the center of the jet.

In the case of the hydrogen jet, Mach number distributions were identified from the pressure measurements as for the nitrogen jet. In Fig. 8, two heat transfer coefficient predictions based on the Pitot pressure measurements and Eq. (11) are presented. The higher of the two heat transfer coefficient predictions is for the case of pure hydrogen, and the lower result is for the case of air. Clearly, the thin film heat transfer coefficient measurements in the hydrogen jet generally fall between these two limits.

To identify the concentration of hydrogen at each position, the value of f (thermophysical properties) was effectively evaluated using Eq. (11) with the thin film value of h , the measured values of p_{pit} , the Mach number distribution estimated using the ratio of Pitot and static pressure, and $D=2.88$ mm (identified from the nitrogen jet experiments). Having obtained f (thermophysical properties), the concentration of hydrogen was identified from Eq. (13) which is principally a function of concentration as illustrated in Fig. 3. Results from the concentration analysis are presented in Fig. 9 at each station downstream of injection in terms of both mole fractions (the solid lines) and mass fractions (the dots).

On the jet center line, the results in Fig. 9 indicate that the

hydrogen concentration is around 0.998 in terms of mole fractions, or around 0.98 in terms of mass fraction. It is expected that the actual hydrogen concentration in the jet core was $X_{H_2} > 0.999$ or $Y_{H_2} > 0.99$ because high purity hydrogen was used and care was taken to evacuate and thoroughly flush out the Ludwig tube prior to final filling with the hydrogen. The fact that the concentration of hydrogen within the core was $Y_{H_2} \approx 0.98$ is indicative of the level of accuracy that can be anticipated with this technique, rather than a contaminated hydrogen stream.

The primary source of uncertainty in the measurement of concentration is the measurement of the thin film convective heat transfer coefficient of the probes and the estimation of $f(M_\infty, \gamma) \times p_{pit}^{0.5}$ using the Pitot and static data. The uncertainty in the thin film heat transfer coefficient measurements has been estimated as around $\pm 4\%$ in the jet core and uncertainty in $f(M_\infty, \gamma) \times p_{pit}^{0.5}$ predictions based on p_{pit} and p_∞ is estimated as around $\pm 3\%$. This leads to an uncertainty in the value of f (thermophysical properties) of around $\pm 5\%$ within the jet core. Given f (thermophysical properties) remains a reasonably linear function of hydrogen mass fraction, Fig. 3, the uncertainty in Y_{H_2} remains at around $\pm 5\%$ over the entire range of concentrations. However, as f (thermophysical properties) is a far more nonlinear function of hydrogen concentration when expressed on a mole basis (Fig. 3), the uncertainty in mole fraction varies between about $\pm 2\%$ for $X_{H_2} = 0.9$ up to about $\pm 25\%$ for $X_{H_2} = 0.4$, assuming the uncertainty in f (thermophysical properties) remains at $\pm 5\%$ over this range of concentrations.

Fluctuation Results

Transient Heat Flux Analysis. High bandwidth stagnation point heat flux results were identified from the analogue voltage signals using an appropriate analogue sensitivity which varied with the time-averaged probe temperature. This is a reasonable approach because at frequencies higher than about 1 kHz, the heat penetrates only a small distance relative to the probe radius, and the associated temperature fluctuations are not large enough to induce significant variable thermal property effects. Similar approaches have been used in previous studies with transient thin film probes, [14,17].

Fluctuations in the stagnation point heat flux were then identified by treating the sampled high bandwidth signals with the digital filters discussed previously (see Time-Averaged Results) in order to first identify a time-averaged result. This time-averaged result was then subtracted from the original high bandwidth results to obtain the fluctuating component.

Fluctuation Analysis. Resolving the total stagnation point heat flux into mean and fluctuating components,

$$q = \bar{q} + q', \quad (17)$$

and treating the heat transfer coefficient and temperatures in Eq. (1) in a similar manner, it is found that the fluctuations in the heat flux are related to the fluctuations in heat transfer coefficient and stagnation temperature according to

$$\frac{\overline{q'^2}}{\bar{h}^2} \approx \frac{\bar{h}'^2}{\bar{h}^2} (\bar{T}_0 - \bar{T}_w)^2 + 2 \frac{\bar{h}' T_0'}{\bar{h}} (\bar{T}_0 - \bar{T}_w) + \bar{T}_0'^2. \quad (18)$$

To achieve the result expressed in Eq. (18), it was necessary to neglect higher order terms and to recognize that the probe temperature fluctuations T_0' are less than 0.4% of q'/\bar{h} for the present conditions, and hence can be neglected.

If the heat flux probes are operated at a temperature very close to the flow stagnation temperature, then Eq. (18) indicates that the RMS stagnation temperature fluctuations can be directly identified from the fluctuations in heat flux and the time-averaged heat transfer coefficient measurements according to

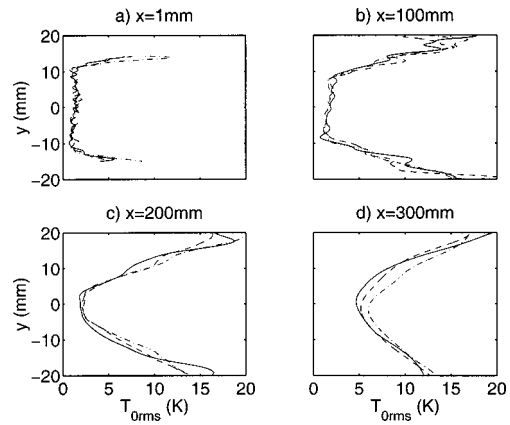


Fig. 10 Stagnation temperature fluctuations at four stations downstream of injection for three different values of $T_0 - T_w$

$$(\overline{T_0'^2})^{1/2} \approx \left(\frac{\overline{q'^2}}{\bar{h}^2} \right)^{1/2}. \quad (19)$$

If a number of different thin film probe operating temperatures are used, then each of the fluctuation terms on the right hand side of Eq. (18) can be identified from the measured fluctuations in the stagnation point heat flux and the measured time-averaged quantities. In supersonic flows, the fluctuations in the heat transfer coefficient will be primarily due to fluctuations in concentration and Pitot pressure, since the sensitivity to fluctuations in Mach number is low for supersonic flows, Eq. (12) or Fig. 2. However, the actual magnitude of the concentration fluctuations cannot be easily identified using the current approach because the term f' (thermophysical properties) $p_{pit}^{0.5}$ cannot be readily estimated.

If fluctuations in concentration are of interest in future applications, a better approach would be to reduce the spatial separation of the thin film probes and Pitot probe. A spatial separation of heated and unheated films of around 1 mm has already been demonstrated, [10]. Inclusion of a Pitot probe in close proximity to such a configuration would allow instantaneous concentration measurements to be made and by pass the treatment of fluctuations using mean-square quantities. However, for the time being, fluctuation measurements from the probe are restricted to stagnation temperature fluctuation results.

Results. Stagnation temperature fluctuations identified from the probe measurements according to Eq. (19) are presented in Fig. 10 for three different probe temperatures ranging from $\bar{T}_w = 315$ to 350 K. Taking the time-averaged flow stagnation temperature as around $\bar{T}_0 = 290$ K (a reasonable approximation for $x = 100, 200,$ and 300 mm, Fig. 7), the difference $(\bar{T}_0 - \bar{T}_w)$ for the data represented by the different lines in Fig. 10 typically varies between about -25 and -60 K. Given that the stagnation temperature results identified using Eq. (19) are very similar regardless of the actual probe temperatures within this range, it is concluded that results in Fig. 10 are a good representation of the actual stagnation temperature fluctuations.

The largest difference in RMS stagnation temperature fluctuations identified by using the different probe temperature occurs at $x = 300$ mm, Fig. 10. At this station, stagnation temperature fluctuations were also identified by curve fitting a quadratic function to the $(\bar{T}_0 - \bar{T}_w)$ versus $\overline{q'^2}/\bar{h}^2$ data for all of the probe temperatures up to $\bar{T}_w \approx 610$ K as suggested by Eq. (18). Results from this quadratic analysis are presented in Fig. 11 where a comparison is made with results obtained using the approximation given in Eq. (19). These results provide additional confirmation that the results in Fig. 10 are a valid representation of the actual stagnation temperature fluctuations.

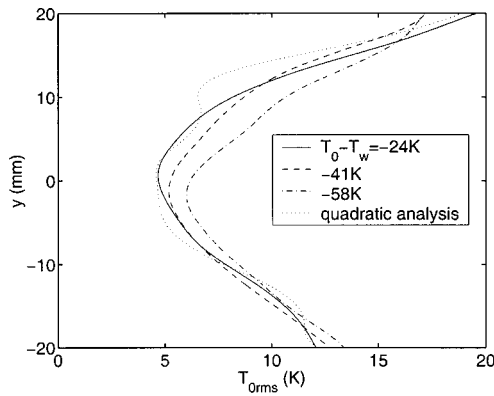


Fig. 11 Stagnation temperature fluctuations in the hydrogen jet at $x=300$ mm

Conclusions

The present work introduces a new concentration probe measurement technique for use in binary gas flows. The technique is based on the measurement of the convective heat transfer coefficient associated with nominally identical stagnation point transient thin film heat flux gauges. Pitot pressure measurements are used in conjunction with a heat transfer correlation and the heat transfer coefficient measurements to identify the concentration of the mixture. The stagnation point heat transfer correlation indicates that at supersonic speeds the convective heat transfer coefficient is virtually independent of the flow Mach number. Thus, it is not essential to have accurate measurements of static pressure provided the binary gas flow is supersonic.

As a demonstration of the new technique, the probe was operated in Mach 4 nitrogen and hydrogen free jets issuing into a low pressure air environment. The nitrogen jet results demonstrated that accurate predictions of the thin film probe heat transfer coefficient were made within the supersonic portion of the jet based on Pitot pressure measurements and estimates of the static pressure within the jet. When the probe was applied in the hydrogen jet, concentration measurements of around $Y_{H_2}=0.98$ were obtained within the jet core flow—a slightly lower hydrogen concentration than anticipated. However, this result is quite good considering that the uncertainty in mass fraction measurement is estimated as around $\pm 5\%$ for the technique in its present application. Hydrogen concentration measurements are presented for four stations downstream of the Mach 4 nozzle: $x=1, 100, 200,$ and 300 mm.

Stagnation temperature measurements have also been obtained using the probe. Although there was reasonable spatial uniformity of stagnation temperature across the hydrogen jet core flow at $x=1$ mm, significant peaks and troughs are apparent at the downstream stations. Similar spatial distributions of stagnation temperature have been observed previously in free jets flows at much lower Mach numbers and have been attributed to vortex-induced energy separation effects, [15,16]. RMS fluctuations in stagnation temperature have also been identified from the probe measurements. At the exit of the injection nozzle, RMS fluctuations of around 1 K are apparent, while at the last station ($x=300$ mm), RMS fluctuations of between about 5 K and 15 K occur within the central portion ($y < \pm 20$ mm) of the hydrogen jet flow.

The thin film probes are robust and have a frequency response that extends to around 100 kHz, and the measurement technique appears well suited to supersonic flow environments. However, two factors that may preclude the application of the present concentration probe arrangement in other supersonic mixing configurations are (1) the absence of a local static pressure measurement and (2) the operation of the external preheating unit. An additional cone or wedge pressure probe could be incorporated into the arrangement in cases where local static pressure measurements are

necessary. The external preheating unit could be replaced by an internal heating system in a hollow quartz probe, [17], or by exciting one film with a relatively high current pulse, [10]. The pulsed heating arrangement of [10] offers the additional advantage of higher spatial resolution, and if a pitot pressure transducer were incorporated into such a configuration, instantaneous measurements of concentration would also be possible.

Nomenclature

- c_p = specific heat
- C = Chapman-Rubensin parameter, defined in Eq. (7)
- D = probe diameter
- h = convective heat transfer coefficient
- k = conductivity
- K = stagnation point velocity gradient, defined in Eq. (6)
- M = Mach number
- n = exponent in power-law viscosity expression
- Nu = Nusselt number, defined in Eq. (3)
- p = pressure
- Pr = Prandtl number, defined in Eq. (4)
- q = surface heat flux
- R = specific gas constant
- Re = Reynolds number, defined in Eq. (5)
- T = temperature
- T_0 = stagnation temperature
- u = velocity
- x = distance from jet exit, or distance along probe surface from stagnation
- X = mole fraction
- y = distance from jet centerline
- Y = mass fraction
- γ = ratio of specific heats
- μ = viscosity
- ρ = density

Subscripts

- e = boundary layer edge
- pit = Pitot
- w = surface value
- ∞ = undisturbed freestream

References

- [1] McQuaid, J., and Wright, W., 1973, "The Response of a Hot-Wire Anemometer in Flows of Gas Mixtures," *Int. J. Heat Mass Transfer*, **16**, pp. 819–828.
- [2] McQuaid, J., and Wright, W., 1974, "Turbulence Measurements With Hot-Wire Anemometry in Non-Homogeneous Jets," *Int. J. Heat Mass Transfer*, **17**, pp. 341–349.
- [3] Brown, G. L., and Rebollo, M. R., 1972, "A Small, Fast-Response Probe to Measure Composition of a Binary Gas Mixture," *AIAA J.*, **10**, pp. 649–652.
- [4] Swithenbank, J., 1977, "Measurement in Combustion Processes," *Measurement of Unsteady Fluid Dynamic Phenomena*, B. E. Richards, ed., Hemisphere, Washington, DC, pp. 189–212.
- [5] Ninnemann, T. A., and Ng, W. F., 1992, "A Concentration Probe for the Study of Mixing in Supersonic Shear Flows," *Exp. Fluids*, **13**, pp. 98–104.
- [6] Ng, W. F., and Epstein, A. H., 1983, "High-Frequency Temperature and Pressure Probe for Unsteady Compressible Flows," *Rev. Sci. Instrum.*, **54**, pp. 1678–1683.
- [7] VanZante, D. E., Suder, K. L., Strazisar, A. J., and Okiishi, T. H., 1994, "An Improved Aspirating Probe for Total-Temperature and Total-Pressure Measurements in Compressor Flows," ASME Paper No. 94-GT-222.
- [8] Buttsworth, D. R., and Jones, T. V., 1998, "A Fast-Response Total Temperature Probe for Unsteady Compressible Flows," *ASME J. Eng. Gas Turbines Power*, **120**, pp. 694–702.
- [9] White, F. M., 1991, "Viscous Fluid Flow," 2nd Ed., McGraw-Hill, New York.
- [10] Buttsworth, D. R., and Jones, T. V., 1998, "A Fast-Response High Spatial Resolution Total Temperature Probe using a Pulsed Heating Technique," *ASME J. Turbomach.*, **120**, pp. 601–607.
- [11] Oldfield, M. L. G., Burd, H. J., and Doe, N. G., 1982, "Design of Wide-Bandwidth Analogue Circuits for Heat Transfer Instrumentation in Transient Wind Tunnels," *Proceedings 16th Symp. of International Center for Heat and Mass Transfer*, Hemisphere, Washington, DC, pp. 233–257.

- [12] Buttsworth, D. R., 2001, "A Finite Difference Routine for the Solution of Transient One Dimensional Heat Conduction Problems With Curvature and Varying Thermal Properties," Technical Report TR-2001-01, Faculty of Engineering and Surveying, University of Southern Queensland.
- [13] Chatfield, C., 1970, *Statistics for Technology*, Penguin, New York.
- [14] Buttsworth, D. R., and Jones, T. V., 2001, "Transient Temperature Probe Measurements in a Mach 4 Nitrogen Jet," *Exp. Fluids*, submitted for publication.
- [15] Fox, M. D., Kurosaka, M., Hedges, L., and Hirano, K., 1993, "The Influence of Vortical Structures on the Thermal Fields of Jets," *J. Fluid Mech.*, **255**, pp. 447–472 (and corrigendum, **261**, p. 376).
- [16] Fox, M. D., and Kurosaka, M., 1996, "Supersonic Cooling by Shock-Vortex Interaction," *J. Fluid Mech.*, **308**, pp. 363–379.
- [17] Buttsworth, D. R., Jones, T. V., and Chana, K. S., 1998, "Unsteady Total Temperature Measurements Downstream of a High Pressure Turbine," *ASME J. Turbomach.*, **120**, pp. 760–767.

G. Grégoire¹

Ph.D. Student

M. Favre-Marinet

Professor

Laboratory of Geophysical and Industrial Flows,
Grenoble University,
UJF-INPG-CNRS,
BP 53X,
38041 Grenoble Cedex 9, France

F. Julien Saint Amand

Research Scientist,
Center Technique du Papier,
BP 251,
38044 Grenoble Cedex 9, France

Modeling of Turbulent Fluid Flow Over a Rough Wall With or Without Suction

The turbulent flow close to a wall with two-dimensional roughness is computed with a two-layer zonal model. For an impermeable wall, the classical logarithmic law compares well with the numerical results if the location of the fictitious wall modeling the surface is considered at the top of the rough boundary. The model developed by Wilcox for smooth walls is modified to account for the surface roughness and gives satisfactory results, especially for the friction coefficient, for the case of boundary layer suction.
[DOI: 10.1115/1.1593705]

1 Introduction

Although numerical modeling of turbulent flows is continuously progressing, some questions remain open and need further investigation in many practical situations. Among them, the problem of modeling the flow over rough surface corresponds to a very common situation in industrial or geophysical applications and it has therefore received much attention from many researchers. A review of the different works on this subject can be found in Patel [1]. The simplest way of modeling high Reynolds number wall flows, and historically the oldest one, is to use a wall-function approach and to match the mean velocity profile to the logarithmic law near the wall. When a rough wall is considered, the velocity profile is well described by introducing a shift, called the roughness function and denoted ΔB , in the logarithmic law of the wall, [2,3]. Such a wall-function approach is desirable in many situations since it avoids detailed computations of the flow in the viscous sublayer and in the buffer layer and therefore saves large computation time. However, Patel [1] underlines “the uncertainty in the dependence of ΔB on the size and type of roughness and also in the effective location of the fictitious wall, from which the distance is measured.” Patel showed some inadequacy of the logarithmic law for modeling a turbulent flow over a wavy wall, which can be considered as a kind of rough surface and application of the wall-function approach is questionable for this type of surfaces.

Turbulent flows over porous walls with blowing or suction have been extensively investigated. A simple model was proposed by Stevenson [4] and in a modified version by Simpson et al. [5]. Wilcox [6] suggested modifying the von Karman’s constant and obtained results consistent with the experimental investigations of Andersen et al. [7]. However, these models did not specify the surface roughness and to our knowledge the problem of modeling a turbulent flow over a very rough wall with suction has not been considered yet.

The present study is concerned with turbulent flows over a wall with two-dimensional periodic roughness. This type of roughness is used in the paper and pulp industry and in industrial heat exchangers, for example. The purpose of this work is twofold, first to clarify the issue of the effective location of the wall for this

type of very rough impermeable surface and secondly to propose a modification of the suction or blowing laws when they are applied to such rough walls.

The flows were computed by using the Fluent™ CFD software with a two-layer zonal turbulence model, which is suitable for modeling the flow in the near-wall region. The law of the wall commonly used in the wall-function approach was compared to the results of the numerical computation.

2 Numerical Approach

2.1 Flow Conditions. The present study is motivated by optimization of the flow in pressure screens, which are used in the recycling paper industry to filter the paper pulp, [8]. In these devices, the pulp is forced to pass through very fine slots (width 0.1 mm), which are machined in the screen wall in order to retain the contaminants whereas the useful fibers are entrained by the flow across the slots. In order to avoid flocculation of fibers, a tangential motion parallel to the wall is imposed to the flow (for details, see [8]). This tangential velocity component is due to the entrainment of the fluid by two-dimensional foils moving in the pulp close to the wall (typical distance: 12 mm). In a reference frame fixed to the screen wall, the flow near the surface may be considered as a steady shear layer of uniform thickness perturbed periodically by the passage of the foils. Unsteady phenomena are localized during the passage of the foils and may be disregarded during the rest of the time in a first approach. As a result, the wall region is modeled in the present study as a layer of uniform thickness submitted to steady flow conditions.

The shape of the rough wall in the present work corresponds to that of industrial pressure screens. It consists of a periodic jagged profile (Fig. 1). The geometry considered and the flow are two-dimensional. The flow rate across the slots and the flow rate of the tangential motion are adjusted independently in the computation as well as in the industrial situation. The particular case of null flow rate across the slots corresponds to impermeable wall.

2.2 Computation Domain and Boundary Conditions. The wall profile is characterized by periodic steps of height k_s , equal to 1.2 mm and of wavelength L , equal to 3.2 mm (Fig. 1). Only three waves of the pattern are considered in the computation domain. The domain height H is kept constant for all the computa-

¹Presently, Engineer, Retec, Paris, France.

Contributed by the Fluids Engineering Division for publication in the JOURNAL OF FLUIDS ENGINEERING. Manuscript received by the Fluids Engineering Division November 21, 2000; revised manuscript received February 12, 2003. Associate Editor: E. W. Graf.

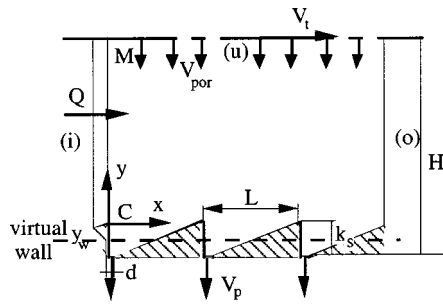


Fig. 1 Computation domain

tions, according to the assumptions discussed above. A more general case would correspond to the problem of developing boundary layers, but is not considered here.

The computed flow is assumed to be fully developed in the x -direction. It is therefore supposed to repeat periodically with the wavelength of the wall profile. Since the length of the computation domain is a multiple of the wavelength, periodic boundary conditions are assumed at the inlet and outlet sections (i) and (o) of the domain. In the case of impermeable wall, the flow rate Q per unit span across these sections is prescribed. In addition, a condition of symmetry is assumed on the upper boundary (u) of the domain, which is located at a distance H from the bottom of the troughs of the rough surface (Fig. 1).

When suction is applied through the wall, the velocity distribution in the slots is assumed to be uniform (suction velocity V_p). A uniform downward velocity V_{por} through the upper boundary is introduced in order to balance the outflow through the slots:

$$V_{por} = V_p d/L. \quad (1)$$

It is worth noting that the suction velocity V_{por} is constant along the upper boundary in keeping with the assumption that u is independent of x along the computation domain. Strictly speaking, the velocity field is periodic in x , but the influence of the jagged profile is limited to a narrow band near the surface (Section 3.1).

In the case of suction, it was no longer possible to set simultaneously a condition of symmetry and the above condition (Eq. (1)) on (u). A constant tangential velocity V_t was then assigned on (u) (details are given in Section 3.3).

2.3 Turbulence Model. The numerical computation employed the two-layer zonal model (denoted TLZM thereafter) first developed by Wolfstein [9] and later by Chen and Patel [10]. The present version is a combination of the k - ε RNG (renormalization group) model used far from the wall and a mixing length model used near the wall. The boundary between the two layers is defined by a turbulent Reynolds number, Re_{y_1} , based on the distance y_1 of a point (cell center in the numerical computation) to the nearest wall

$$Re_{y_1} = \rho k^{1/2} y_1 / \mu \quad (2)$$

where k is the turbulent kinetic energy.

For $Re_{y_1} < 200$, the one-equation model of Wolfstein is used. The turbulent viscosity is computed from

$$\mu_t = \rho C_\mu k^{1/2} l_\mu \quad (3)$$

$$l_\mu = c_1 y_1 (1 - \exp(-Re_{y_1}/A_\mu)).$$

The dissipation rate ε is modeled by introducing a second length scale l_ε

$$\varepsilon = k^{3/2}/l_\varepsilon. \quad (4)$$

$$l_\varepsilon = c_1 y_1 (1 - \exp(-Re_{y_1}/A_\varepsilon)).$$

The constants proposed by Chen and Patel [10] are

Table 1 Influence of the grid resolution on the velocity profile over the wall crest. Differences with the results of case 4 are given in %.

y/k_s	V/V_t (Case 4)	$\Delta V/V_t$ (Case 1)	$\Delta V/V_t$ (Case 2)	$\Delta V/V_t$ (Case 3)
0.005	0.255	-6.6	-4.4	-4.2
0.106	0.382	-1.9	0.2	0.5
0.537	0.571	-2.7	0.15	0.5
4.958	0.944	-0.9	0.05	0.2

$$c_1 = \kappa C_\mu^{-3/4}, \quad A_\mu = 70, \quad A_\varepsilon = 2c_1 \quad (5)$$

with $\kappa = 0.41$, $C_\mu = 0.09$

2.4 Numerical Scheme. We employed a hybrid mesh in order to optimize accuracy while insuring a reasonable time of computation. Rectangular cells were used near the wall in order to control most efficiently the distance to the wall and to have sufficient accuracy in the viscous sublayer. At least ten cells were placed in the near wall region ($Re_{y_1} < 200$). Triangular cells were used in the external flow ($Re_{y_1} > 200$) in order to minimize the cells number while keeping a low cells skewness when the size of the cells was increased. The whole mesh consisted of about 15,000 cells.

The equations were discretized by means of a second-order accurate finite volume method. As these equations are nonlinear, a SIMPLE (semi-implicit pressure linked equations) algorithm was used. This algorithm is based on a prediction-correction method, which allows the equations to be linearized. The drawback of this iterative method is the convergence slowness. It was checked in these calculations that the number of iterations is proportional to the number of cells. The computation started with uniform values of the various physical quantities. The software Fluent™ V6.0 was used on a PC HP Vectra Xu.

2.5 Numerical Accuracy. Tests were conducted for a typical case of flow with a moderate suction rate ($V_p = 3.5$ m/s, $V_t = 15$ m/s). The kinetic turbulent energy k and the rate of dissipation of the turbulent kinetic energy ε are the physical quantities, which converge with the slowest rate. The level of normalized residuals for k and ε reached 10^{-4} for both quantities after 2500 iterations, $5 \cdot 10^{-6}$ and 10^{-5} , respectively, after 10,000 iterations. Additionally, the flow rate near the wall was computed to follow the convergence of the calculations. It was defined in a cross section over a wall crest ($x=L$) by

$$q_w = \int_{y=0}^{y=0.5 \text{ mm}} u dy \quad (6)$$

The variation of q_w during 25,000 iterations showed that a minimum (-6% relative to the final value) was reached after 2500 iterations. The asymptotic value was approached with a good accuracy (+2%) after 10,000 iterations.

A first computation (case 1) was conducted with a grid of 15,700 cells, then the grid was refined in the region of high dissipation rate (downstream of the separation point at the wall crest). This case 2 used 18179 cells. Further refinement (case 3, 20,555 cells) was considered near the stagnation point, near the vortex center (Section 3.1) and in the region of high values of k . Finally, the grid of case 2 was otherwise refined (case 4, 19,118 cells) near the separation point and in the shear layer, which develops in the downstream direction behind this point. The influence of the resolution of the grid on the mean velocity profile over the wall crest was then investigated. Table 1 compares the computed values of the x -velocity with the results of case 4, which was considered as the more accurate solution, for several distances to the wall. According to Table 1, the mean velocity profile is computed with an accuracy better than 1% over most of the test section for cases 2 and 3. Errors can be estimated to 2–3% for

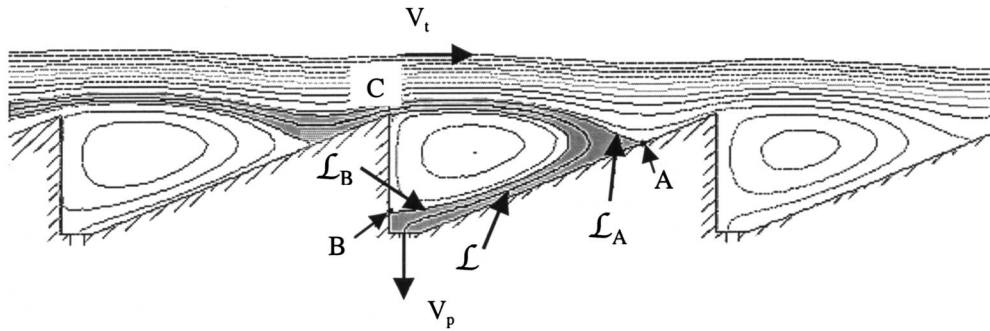


Fig. 2 Pattern of streamlines close to the screen basket. $V_p/V_t=1/3$.

case 1. The differences with the most refined case grow to 4–7% very near to the wall. The skin-friction coefficient is also slightly affected by the grid refinement (differences less than 1% between cases 2, 3 and 4, 7% between cases 1 and 4).

3 Results

3.1 Description of the Flow. A typical result showing the mean flow field is drawn in Fig. 2 for a moderate suction rate ($V_p/V_t=1/3$). The back-facing steps produce flow separation and create recirculation bubbles between two successive crests. Two particular streamlines may be considered for helping description of the flow. A streamline \mathcal{L}_A starting slightly upon a wall crest ends at a stagnation point A on the opposite side of the wall profile. On the other hand, a streamline \mathcal{L}_B starting at a wall crest C ends at a stagnation point B on the backside of the wall profile. \mathcal{L}_B is then the boundary of the recirculation bubble. \mathcal{L}_A and \mathcal{L}_B determine a streamtube corresponding to the flow through the slot. When the wall is impermeable, the flow features are essentially the same, except that only one particular streamline \mathcal{L}_A is to be considered. In this case, \mathcal{L}_A starts from C and it is the boundary of the recirculation bubble.

It is worth noting that the mean streamlines are only slightly perturbed by the wall even for small distances to the crests (Fig. 2).

3.2 Check of the Logarithmic Law for Impermeable Rough Wall. The purpose of the present section is to compare the mean velocity profile resulting from the preceding TLZM computations with the logarithmic law which is used in the wall-function approach for the case of impermeable wall ($V_p=0$). In this approach, the mean velocity profile is described in the fully rough regime, [3], by

$$u(Y)/u^* = 1/\kappa \ln(Y/k_s) + B \quad (7)$$

where u^* denotes the friction velocity equal to $\sqrt{\tau_w/\rho}$ (τ_w is the wall shear stress). $B=8.5$ for very rough walls, [3].

Y is the coordinate normal to the wall. In fluid mechanics textbooks, the origin of Y is not always clearly defined. In fact, the formulation of Eq. (7) implies that the wall is represented by a fictitious plane surface, which corresponds to the origin of Y . For very rough walls, it is crucial to clearly specify the effective location of this fictitious plane surface when using Eq. (7). The complementary issue of the present discussion concerns therefore the position of the fictitious wall which gives the best agreement of the logarithmic law with the mean velocity profile as given by the previous numerical computations. For sake of clarity, the results will be compared in a reference frame which origin is located at the top of the rough surface (point C of Fig. 1). y is the ordinate in this reference frame. If y_w denotes the location of the virtual surface introduced in the logarithmic law (Fig. 1), Y and y are related by

$$Y = y - y_w \quad (8)$$

The mean velocity profile is then given by

$$u(y)/u^* = 1/\kappa \ln((y - y_w)/k_s) + B \quad (9)$$

In order to compare the solutions associated to different positions of the virtual wall, u^* was adjusted for each value of y_w in Eq. (9) so as to give the prescribed mass flow rate Q through the cross section CM (Fig. 1) over a crest. The relation between Q and u^* was obtained by integrating the logarithmic law (Eq. (9)) from $y=0$ to $H - k_s$. The following relations are obtained:

$$u^* = \frac{Q}{D(H - k_s, y_w) - D(0, y_w) + B(H - k_s)} \quad (10)$$

with

$$D(y, y_w) = (y - y_w)(\ln((y - y_w)/k_s) - 1)/\kappa \quad (11)$$

$$V_t/u^* = 1/\kappa \ln[(H/k_s - 1 - y_w/k_s)] + B \quad (12)$$

In addition, the skin-friction coefficient was obtained from the above relations by

$$C_f = 2(u^*/V_t)^2 \quad (13)$$

The equivalent coefficient was computed with TLZM by integrating the total stress exerted on the wall profile contour C in the computational domain (1: curvilinear abscissa, element of length dl).

$$C_f = \frac{1}{\rho V_t^2/2} \frac{1}{3L} \left(\int_C p n_x dl + \int_C \tau_x dl \right) \quad (14)$$

where p is the pressure, n_x and τ_x are, respectively, the x -components of the normal unit vector and of the computed wall shear stress. C_f includes the pressure and friction effects for this nonhorizontal surface. This definition of an equivalent friction coefficient is the same as in Taylor et al. [11]. It is here nondimensionalized with the length $3L$ of the equivalent plane virtual wall.

The above calculations were performed for $k_s=1.2$ mm, $H=12$ mm, $Q=0.15$ m³/s/m which were of industrial interest. The Reynolds number based on external velocity and half-channel height is $V_t H/\nu=2.10^5$. It should be noted that the present geometry corresponds to a very rough wall ($k_s^+ \approx 1000$).

Table 2 and Fig. 3 show the results obtained for two extreme positions of the virtual wall, at the crests ($y_w=0$) and at the

Table 2 Influence of the position of the virtual wall on the friction velocity, axis-velocity, and friction coefficient

	u^* (m/s)	$V_t(H-k)/Q$	C_f^*100
$y_w = -k$	1.131	1.15	0.99
$y_w = 0$	1.219	1.21	1.04
Numerical computations	1.21	1.20	1.04

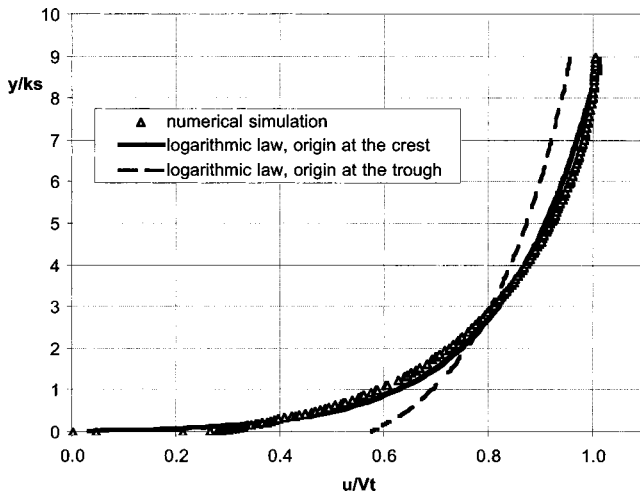


Fig. 3 Influence of the position of the virtual wall on the mean velocity profile at $x=0$

bottom of the troughs ($y_w = -k_s$) of the actual wall profile. The mean velocity profile computed over a crest by TLZM is also plotted in Fig. 3.

For this type of roughness, Fig. 3 clearly shows that the best agreement with the numerical results is obtained when the virtual wall is placed at the crests of the actual wall.

This conclusion is confirmed when computed velocity profiles are considered at three evenly distributed sections $L/3$ apart (Fig. 4). The velocity profiles almost collapse when the normalized distance to the wall, y/k_s , is higher than 0.4. Again the logarithmic law used with $y_w = 0$ (Eq. (9)) gives a good approximation of the velocity profiles. The actual mean velocity profile departs, however, significantly from the semi-logarithmic law for $y/k_s < 0.3$. Velocities are higher in this region because a mixing layer develops between the upper part of the flow and the recirculating vortex near the wall.

These results show that the details of the flow between the crests (separation, reattachment) as shown on Fig. 2, have little effect on the mean flow field at a sufficient distance ($\approx 0.4k_s$) to the wall. It is important to remark that the logarithmic plot of all the profiles uses the same mean friction velocity defined by Eq.

(13) and (14) and not the local value of the shear stress. This latter choice would have led to incoherent results since the shear stress is extremely variable on the wall and may even be equal to zero at the stagnation point A (Fig. 2).

For the case of an impermeable wall and for the present type of roughness (jagged wall profile), it may be concluded that the logarithmic law is a good approximation of the mean velocity profile over the whole rough surface. In this case, the location of the virtual wall modeling the rough surface must be taken at the top of the ridged wall.

3.3 Suction Effects. When suction is applied through the regularly spaced slots of the basket, the features of the flow are not very different from the impermeable case, as it was remarked in Section 3.1. In particular, the streamline pattern of the mean flow over the wall crests is not strongly affected by suction. Therefore, modeling suction effects over this rough wall may be tentatively undertaken by considering uniform suction through a fictitious plane porous wall. Considering the results of the impermeable case, it seems appropriate to locate this virtual wall at the crests of the wall.

The problem of suction through a smooth wall was studied by Stevenson [4] who proposed a mixing-length approach to model the flow. In this model, the mixing length is still supposed proportional to the distance to the wall whereas a source term due to suction is introduced in the momentum budget in the near-wall region. Integration in y of the x -momentum equation results in

$$\rho \kappa^2 y^2 \left| \frac{\partial u}{\partial y} \right| \left(\frac{du}{dy} \right) = \rho u^{*2} - \rho V_{\text{por}} u \quad (15)$$

where V_{por} is related to the suction velocity by Eq. (1).

Integrating Eq. (15) in y yields

$$2/V_{\text{por}}^+ ((1 + V_{\text{por}}^+ u^+)^{1/2} - 1) = 1/\kappa \ln(y^+) + C \quad (16)$$

where $V_{\text{por}}^+ = -V_{\text{por}}/u^*$.

The constant of integration C is obtained by matching Eq. (16) to the logarithmic law for smooth impermeable walls when V_{por}^+ tends to 0. This gives $C = B = 5.5$.

When a rough wall is considered and modeled by a virtual porous plane surface, the same method may be applied, but the right-hand side of Eq. (16) has to be matched with the logarithmic law corresponding to rough surfaces. In this case, we obtain

$$C = B - \Delta B = 5.5 - 1/\kappa \ln(1 + 0.3k_s^+) \quad (17)$$

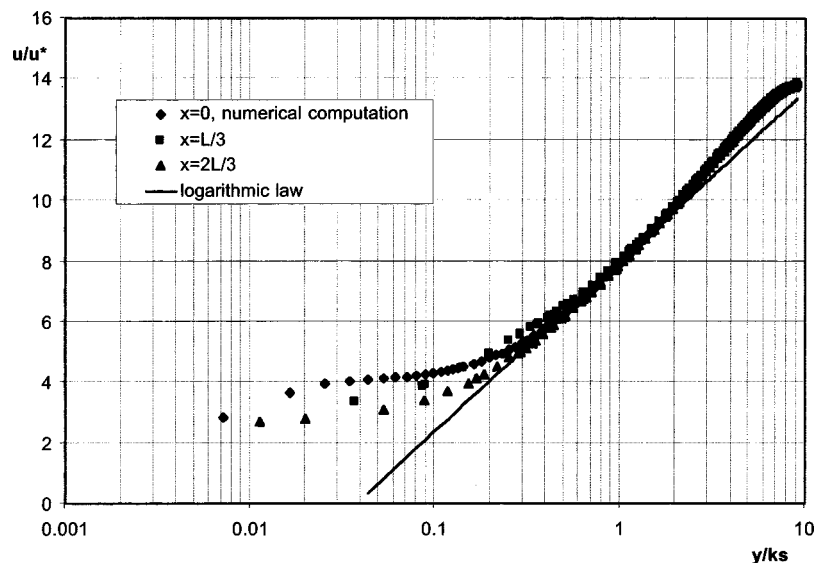


Fig. 4 Mean velocity profiles at different positions along the wall

where ΔB is the shift of the logarithmic law for a rough surface.

For the very high values of k_s^+ considered in the present study ($k_s^+ \approx 1000$), 1 is neglected in the logarithm in Eq. (17).

So finally, Stevenson's law modified for a rough surface is

$$u^+(y, k_s) = 1/\kappa \ln(y/k_s) + B - V_{por}^+ / 4(1/\kappa \ln(y/k_s) + B)^2. \quad (18)$$

We tried another approach by modifying Wilcox's formulation [6] for smooth surfaces with suction.

Starting from the experimental work of Andersen et al. [7], Wilcox obtained a good approximation of the velocity profiles by introducing the following variation of the von Karman's constant:

$$\kappa_w = \kappa / (1 + \Xi V_{por}^+) \quad (19)$$

with $\Xi = 3.11 + 0.61 \ln(y^+)$

For very rough impermeable surfaces, roughness effects lead to destruction of the viscous sublayer and the distance to the wall is then correctly scaled with the roughness height k_s instead of the viscous sublayer thickness ν/u^* . Assuming the same physical process for rough surfaces with suction, we propose to modify the law of Wilcox by replacing y^+ by y/k_s in Eq. (19). The mean velocity profile is then described by

$$u^+(y, k_s) = 1/\kappa \ln(y/k_s) + B - V_{por}^+ / \kappa (3.11 + 0.61 \ln(y/k_s)) \ln(y/k_s). \quad (20)$$

The similarity between the modified Stevenson's (Eq. (18)) and Wilcox's laws (Eq. (20)) is apparent.

Using one of these two laws, it is possible to calculate the friction velocity and the flow rate across the computation domain defined in Section 2.2 if the tangential velocity V_t is given.

When the modified Stevenson's law (Eq. (18)) is used, the following expression is obtained for the friction velocity:

$$u^*/V_t = 1/Z + Z/4V_{por}/V_t \quad (21)$$

with $Z = \lambda/\kappa + B$
 $\lambda = \ln(H/k_s - 1)$.

When the modified Wilcox's law (Eq. (20)) is considered, u^* is given by

$$u^*/V_t = (1 + 1/\kappa V_{por}/V_t (3.11 + 0.61\lambda)\lambda) / Z. \quad (22)$$

The flow rate is easily deduced from the above expressions of the friction velocity u^* by integrating, respectively, the Eq. (18) and (20) over the domain height, $H - k_s$.

As in the case of impermeable wall, the flow was also computed by using the two-layer zonal model. When suction is applied through the wall, it is necessary to compensate the suction flow rate in order to keep a constant streamwise flow rate and periodic conditions on (i) and (o) (Fig. 1). This implies the introduction of a normal velocity at the boundary (u) of the flow domain. However, as mentioned before, this condition is incompatible with the previous assumption of symmetry on the upper boundary. The solution used in this simulation is then to replace the condition of symmetry on (u), by a so-called VELOCITY INLET boundary condition. This condition implies the setting of two velocity components and the turbulence quantities on (u). In this case, it is still necessary to set the streamwise flow rate Q in order to complete the boundary conditions. In the present numerical procedure, Q was computed with the modified laws of Stevenson and Wilcox (Eq. (18) and (20)). Finally, the INLET turbulent quantities introduced are the turbulence length scale and intensity usually observed in a channel flow. The computation starts with a value of 5% for the turbulence intensity on (u). This quantity is adjusted slightly during the computation by using the result obtained far from the wall.

Figure 5 compares the friction velocity u^* obtained by the above computations with the results of the TLZM numerical simu-

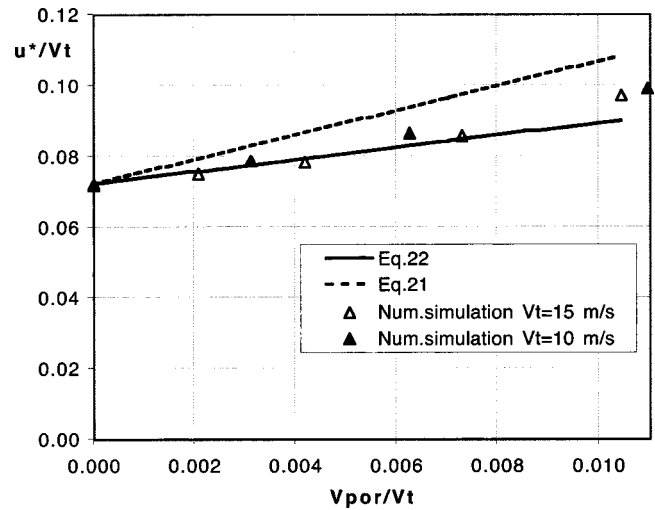


Fig. 5 Influence of suction on the friction velocity

lations for a range of suction ratios of industrial interest. u^* is given by Eqs. (13) and (14) and is normalized by the velocity V_t at the upper boundary. There is clearly an excellent agreement of TLZM results with the modified Wilcox's law (Eq. (22)) for low to moderate suction ratios. For the highest suction ratio considered in this study ($V_{por}/V_t > 0.01$), a more pronounced difference of 9% is observed between the two results. The prediction of the modified Stevenson's law overestimates the friction velocity.

It should be noted that roughness effects are stronger than suction effects for the present conditions. In fact, the nondimensionalized friction velocity was computed by using the Blasius law for a smooth wall in a channel of half-width H and center velocity V_t . Compared to this smooth wall value (≈ 0.04), the roughness effect gives a 80% increase in u^*/V_t . On the other hand, the highest suction ratio gives only a 23% increase in u^*/V_t in comparison to the rough impermeable case.

Figures 6 and 7 show mean velocity profiles over the crests computed by the different methods for two values of the suction ratio. For a moderate suction ratio ($V_{por}/V_t = 0.0073$), Fig. 6 indicates a good agreement of the TLZM results with the velocity profile given by the modified Stevenson's law (Eq. (18)). Equation (20) slightly overestimates the mean velocity. The shape of the mean velocity profile as given by TLZM is considerably modified for the highest suction ratio (Fig. 7, $V_{por}/V_t = 0.0104$). The stiffness of the velocity profile observed for $y/k_s > 3$ is accounted for by neither the modified Wilcox's law nor by the Stevenson's law. In this case, Eq. (20) (Wilcox's law) compares well with the numerical results for $y/k_s < 2$, but the corresponding velocity profile deviates significantly from the computed one in the outer part of the flow. Equation (18) does not give better agreement.

It should be remarked that the good agreement of TLZM with Eq. (18) observed in Fig. 6 deteriorates significantly when u is nondimensionalized by the friction velocity (Fig. 8). The differences in the velocity profiles reflect the discrepancy between u^* as given by the two methods.

4 Conclusions

In the present study, the flow near a ridged wall was computed by using a two-layer zonal model. The mean velocity profiles obtained by these two-dimensional computations are in very good agreement with the semi-logarithmic law for impermeable rough walls, provided the ordinate y used in this law is counted from a virtual wall located at the crests of the wall. Moreover, the friction coefficient is computed with a good approximation by using the logarithmic law throughout the flow. These results then justify the wall-function approach for this type of two-dimensional rough-

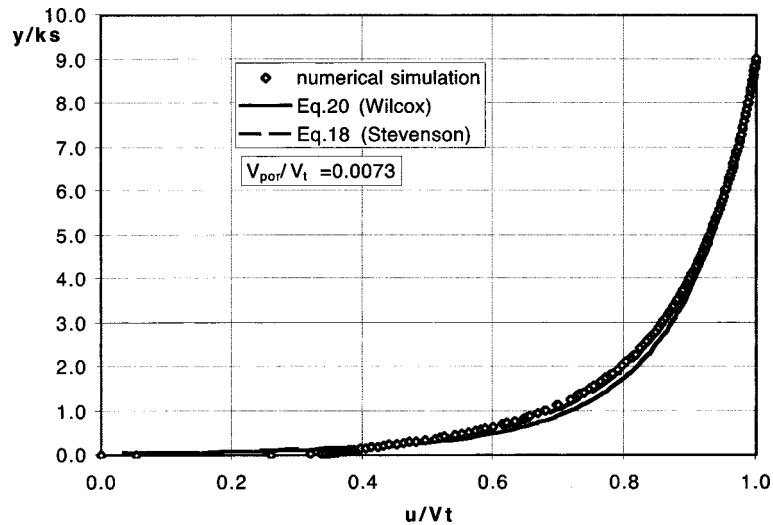


Fig. 6 Mean velocity profile at $x=0$ for a moderate suction ratio. $V_{por}/V_t=0.0073$.

ness. The shape of the wall gives rise to a sharp separation at the crests. Moreover the reattachment zone is much smaller than the separation region. This explains most likely why the best choice for the origin of the ordinate y is at the top of the rough surface ($y_w=0$). This result, which is useful for the paper and pulp industry, may also be relevant to transverse-rib roughness, which is used in tubes for enhanced heat transfer, [12]. In this case, the rib spacing will significantly affect the flow and the above conclusion should apply to small values of this parameter, which correspond to limited regions of reattachment, if any.

For three-dimensional roughness, as for Nikuradse's roughness, it is expected that the effects of separation will be weaker and consequently that the virtual origin will be located below the top of the surface ($-k_s < y_w < 0$).

The adaptation of the laws with suction from smooth to very rough walls seems also to be satisfactory if we assume that the numerical simulations are accurate. The adapted Wilcox's law gives the best results for the friction velocity and reasonable agreement for the mean velocity profiles. The proposed modification is very simple since it consists to replacing the viscous length scale by the roughness height in the modeling of the von Kar-

man's constant. Further confirmation of this model would require comparison of the present results with experiments.

The present work considered a layer of uniform thickness height, H to model the industrial problem of the flow in pressure screens. A more general case would correspond to developing turbulent boundary layers. However, longitudinal advection effects may be considered as small compared to friction effects as in Stevenson's analysis (Eq. (15)) in such flows. It is then thought that the present results would be only slightly affected by slow x -variations of H .

This method seems to be successful in the present case of two-dimensional roughness. It would be interesting to extend the conclusions of the present study in the following directions:

- further work could test the effect of the crest spacing on the position of the virtual wall.
- three-dimensional roughness could be considered, but it would require a significantly greater effort owing to the three-dimensional calculations, which would be necessary in this case.

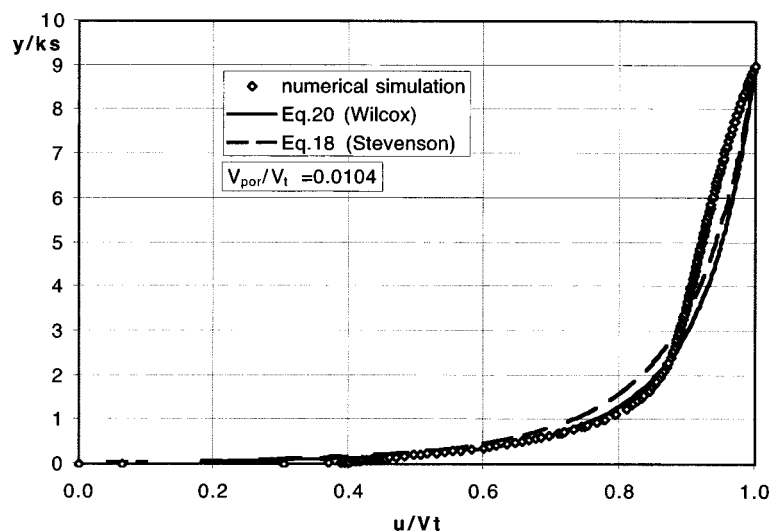


Fig. 7 Mean velocity profile at $x=0$ for a high suction ratio. $V_{por}/V_t=0.0104$.

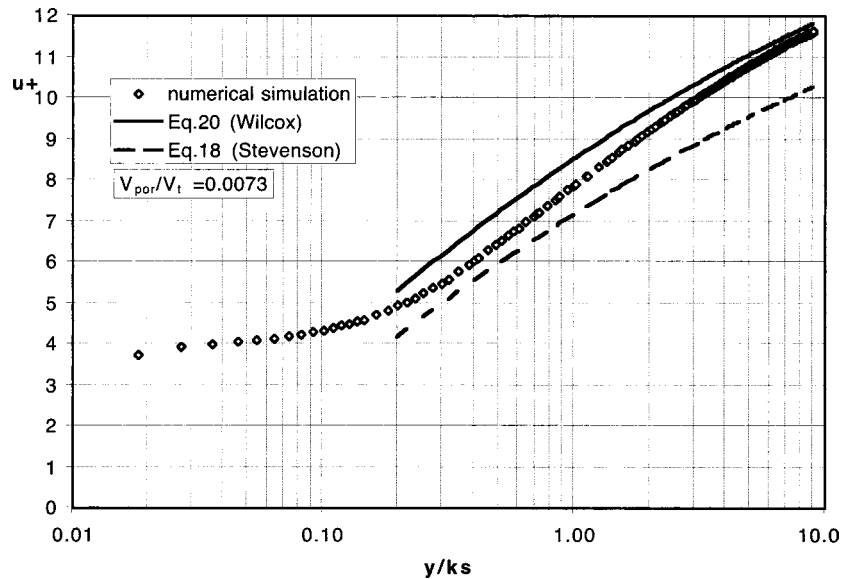


Fig. 8 Mean velocity profile at $x=0$ plotted with internal variables. $V_{por}/V_t = 0.0073$.

Acknowledgments

This research was supported by the company E.&M. LAMORT and by the French Ministry of Education, Research and Technology. Participation of Dariusz ASENDRYCH is gratefully acknowledged.

Nomenclature

- B = constant in the logarithmic law
- ΔB = roughness function
- C_f = skin-friction coefficient
- d = width of the slots
- H = height of the computation domain
- k = turbulent kinetic energy
- k_s = roughness height
- L = distance between two crests or two slots
- p = pressure
- Q = flow rate per unit length in the normal direction
- q_w = flow rate per unit length near the wall (Eq. (6))
- u = mean velocity
- u^* = friction velocity
- V_t = tangential velocity at the upper boundary of the computation domain
- V_p = suction velocity
- V_{por} = equivalent velocity for a uniformly porous wall
- x = abscissa counted from the wall crest
- y = ordinate counted from the wall crest
- y_w = ordinate of the virtual wall in the logarithmic wall
- y_1 = distance to the nearest wall
- Y = ordinate counted from the virtual wall
- ε = rate of dissipation of the turbulent kinetic energy

- κ = von Karman's constant
- ρ = fluid density
- τ_w = wall shear stress
- μ = dynamic viscosity
- ν = kinematic viscosity

References

- [1] Patel, V. C., 1998, "Perspective: Flow at High Reynolds Number and Over Rough Surfaces-Achilles Heel of CFD," *ASME J. Fluids Eng.*, **120**, pp. 434-444.
- [2] Clauser, F. H., 1956, "The Turbulent Boundary Layer," *Advances in Applied Mechanics*, **4**, Academic Press, New York.
- [3] White, F. M., 1991, *Viscous Fluid Flow*, McGraw-Hill, New York.
- [4] Stevenson, T. N., 1963, "A Law of the Wall for Turbulent Boundary Layers With Suction or Injection," Cranfield College, Aero. Report 166.
- [5] Simpson, R. L., Whitten, D. C., and Moffat, R. J., 1970, "An Experimental Study of the Turbulent Prandtl Number of Air With Injection or Suction," *Int. J. Heat Mass Transfer*, **13**, pp. 125-143.
- [6] Wilcox, D. C., 1993, "Turbulence Modeling for CFD," DCW Industries Inc., La Canada, CA.
- [7] Andersen, P. S., Kays, W. M., and Moffat, R. J., 1972, "The Turbulent Boundary Layer on a Porous Plate: An Experimental Study of the Fluid Mechanics for Adverse Free-Stream Pressure Gradients," Report No. HMT-15, Department of Mechanical Engineering, Stanford University, CA.
- [8] Marko, J. J., and LaRiviere, C. J., 1999, "The Use of Computational Fluid Dynamics (CFD) in Pressure Screen Design," *Tappi 99 Proceedings*, pp. 1477-1482.
- [9] Wolfstein, M., 1969, "The Velocity and Temperature Distribution of One-Dimensional Flow With Turbulence Augmentation and Pressure Gradient," *Int. J. Heat Mass Transfer*, **12**, pp. 301-318.
- [10] Chen, H. C., and Patel, V. C., 1988, "Near-Wall Turbulence Models for Complex Flows Including Separation," *AIAA J.*, **26**(6), pp. 641-648.
- [11] Taylor, R. P., Coleman, H. W., and Hodge, B. K., 1985, "Prediction of Turbulent Rough-Wall Skin Friction Using a Discrete Element Approach," *ASME J. Fluids Eng.*, **107**, pp. 251-257.
- [12] Webb, R. L., 1994, *Principles of Enhanced Heat Transfer*, John Wiley and Sons, New York.

Yuka Iga

Assistant Researcher,
Tohoku University,
2-1-1 Katahira,
Aoba-ku,
Sendai Miyagi 980-8577, Japan
e-mail: iga@ifs.tohoku.ac.jp

Motohiko Nohmi

Senior Researcher,
Ebara Research Co., Ltd.,
11-1, Haneda Asahi-cho,
Ohta-ku,
Tokyo 144-8510, Japan
e-mail: nohmi@ebara.co.jp

Akira Goto

Director,
Ebara Research Co., Ltd.
4-2-1, Honfujisawa,
Fujisawa 251-8502, Japan
e-mail: goto05296@erc.ebara.co.jp

Byeong Rog Shin

Associate Professor,
e-mail: shin@ifs.tohoku.ac.jp

Toshiaki Ikohagi

Professor,
e-mail: ikohagi@ifs.tohoku.ac.jp

Institute of Fluid Science,
Tohoku University,
2-1-1, Katahira,
Aoba-ku,
Sendai, Miyagi 980-8577, Japan

Numerical Study of Sheet Cavitation Breakoff Phenomenon on a Cascade Hydrofoil

Two-dimensional unsteady cavity flow through a cascade of hydrofoils is numerically calculated. Particular attention is focused on instability phenomena of a sheet cavity in the transient cavitation condition, and the mechanism of the breakoff phenomenon is examined. TVD-MacCormack's scheme employing a locally homogeneous model of compressible gas-liquid two-phase medium is applied to analyze the cavity flows. The present method permits us to treat the entire cavitating/noncavitating unsteady flowfield. By analyzing the numerical results in detail, it becomes clear that there are at least two mechanisms in the breakoff phenomenon of the sheet cavity: one is that re-entrant jets play a dominant role in such a breakoff phenomenon, and the other is that pressure waves propagating inside the cavity bring about another type of breakoff phenomenon accompanying with cavity surface waves. [DOI: 10.1115/1.1596239]

Introduction

Cavitation is usually observed in high-speed liquid flows around such obstacles as the impellers of fluid machinery. It is well known that cavity flow causes vibration, noise, damage, and a decline of efficiency in hydraulic systems. The improvement of the predictability of cavity flow is a common subject of study for designers of high-speed fluid machinery. In recent years, large-scale computations have become possible with the increased sophistication and speed of computers, and thus improvements in the prediction of cavity flow using numerical simulations is expected. However, because cavity flow includes complex and strong unsteady phenomena with phase changes, fluid transients, vortex shedding, and turbulence, equations to express cavity flow are expected to be very complex. Therefore, a mathematical modeling method is necessary for the numerical analysis of high-speed gas-liquid two-phase flow. Proposed mathematical models can be divided roughly into two categories, the single-phase and two-phase models (see Avva, Singhal, and Gibson [1]). The single-phase model (see, for example, Deshpande, Feng, and Merkle [2]) solves only the liquid phase outside the cavity, and hence is able

to describe clearly the liquid-vapor interface. On the other hand, the two-phase model treats the flowfield inside and outside the cavity as a mixture, and is better suited to unsteady analysis. A number of studies using this model have been published, for example, Kubota, Kato, and Yamaguti [3] have used this method taking bubble inception, growth, and destruction into account, and Reboud and Delannoy [4] have used it taking the barotropic relationship into account. The examination of the validity and applicability of these numerical methods is being steadily advanced.

In this study, a numerical method based on a "locally homogeneous model" of a compressible gas-liquid two-phase medium (see, for example, Shin and Ikohagi [5]), which belongs to the two-phase model, is applied to cavity flow through a cascade of static hydrofoils, the most fundamental element of turbomachinery (see, for example, Watanabe and Tsujimoto [6]). Particular attention is paid to the breakoff phenomenon (see, for example, Le, Franc and Michel [7] and Hofmann et al. [8]) of the sheet cavity in the transient cavitation condition and the mechanism of this phenomenon is examined for several cascade arrangements.

Numerical Method for Cavity Flow

Physical Modeling. The equation of state for the liquid phase can be expressed with the following equation proposed by

Contributed by the Fluids Engineering Division for publication in the JOURNAL OF FLUIDS ENGINEERING. Manuscript received by the Fluids Engineering Division Sept. 28, 2001; revised manuscript received Mar. 18, 2003. Associate Editor: S. Ceccio.

Gas-Liquid Two-Phase Media

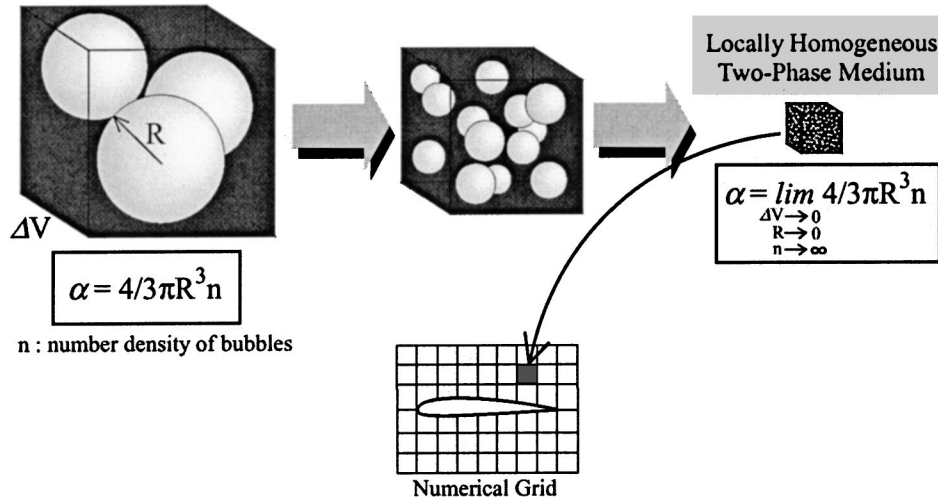


Fig. 1 Concept of the locally homogeneous model

Tammann [9]:

$$p_l + p_c = \rho_l K(T_l + T_0), \quad (1)$$

where p_l , ρ_l , and T_l are pressure, density, and temperature of the liquid (the subscript l representing the liquid phase), p_c and T_0 are the pressure and temperature constants of liquid, and K is the liquid constant. When the gas phase is assumed to be an ideal gas, the equation of state is

$$p_g = \rho_g R T_g, \quad (2)$$

where R is the gas constant and the subscript g represents the gas phase.

Generally, the void fraction (volume fraction of gas phase) α is expressed as follows, using bubble radius R and number density n :

$$\alpha = \frac{4}{3} \pi R^3 n. \quad (3)$$

In the locally homogeneous model of this study, the gas-liquid two-phase medium inside the cavity is treated as a locally homogeneous pseudo-single-phase medium. By supposing a limiting case of the control volume ΔV being infinitely small, R being infinitely small and n being infinitely large with the local α value being kept constant, a locally homogeneous medium can be obtained in an infinitely small volume element. The concept of this model is shown in Fig. 1. In practical calculations, by distributing the infinite number of infinitesimal bubbles in each computational cell having a different local void fraction, the gas-liquid mixture condition is specified macroscopically. Applying this model to the mixture condition inside the cavity, it is expected that unsteady and complex cavity flows can be simulated.

The mixture density ρ of a two-phase medium is expressed by combining linearly a gas phase density ρ_g and a liquid phase density ρ_l with the local void fraction α ,

$$\rho = (1 - \alpha)\rho_l + \alpha\rho_g. \quad (4)$$

Then, assuming the local equilibrium conditions, $p = p_l = p_g$ and $T = T_l = T_g$, the equation of state becomes, from Eqs. (1), (2), and (4),

$$\rho = (1 - \alpha) \frac{p + p_c}{K(T + T_0)} + \alpha \frac{p}{RT}. \quad (5)$$

Also, the following relation is obtained between the local void fraction α and the quality (mass fraction of the gas phase) Y :

$$\rho(1 - Y) = (1 - \alpha)\rho_l, \quad \rho Y = \alpha\rho_g. \quad (6)$$

Using Y from Eq. (6), the equation of state for a locally homogeneous compressible gas-liquid two-phase medium can be expressed as

$$\rho = \frac{p(p + p_c)}{K(1 - Y)p(T + T_0) + RY(p + p_c)T}. \quad (7)$$

Since the temperature change of the usual cavity flow is negligible, the speed of sound C under isothermal conditions is expressed as

$$C^2 = \frac{dp}{d\rho} = \frac{p(p + p_c)}{\rho} \times \frac{YR(p + p_c) + (1 - Y)Kp}{YR\{(p + p_c)^2 - Kp\} + Y(1 - Y)\rho KR p_c T_0 + Kp^2}. \quad (8)$$

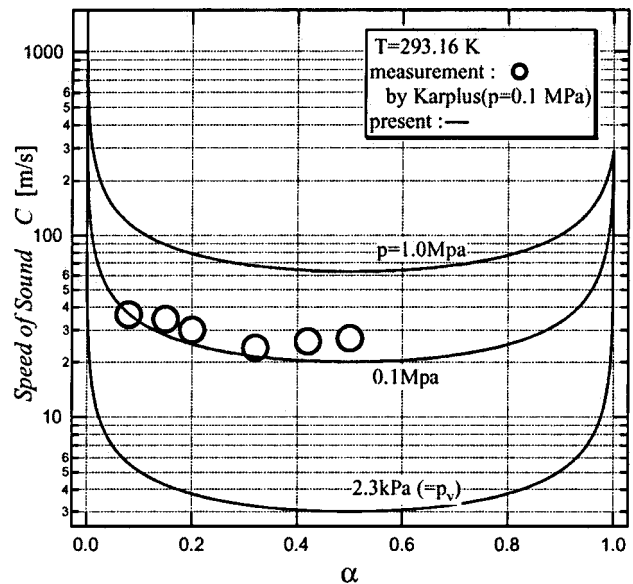


Fig. 2 Speed of sound under isothermal condition of $T = 293.16$ K

In Fig. 2, the relation between the speed of sound C to the void fraction α at 20°C is shown for different pressures. Also shown in Fig. 2 are experimental measurements of the speed of sound (see Karplus [10]) for a number of different void fractions. These measurements correspond well with the calculated values.

The viscosity coefficient μ , [11], is given by

$$\mu = (1 - \alpha)(1 + 2.5\alpha)\mu_l + \alpha\mu_g. \quad (9)$$

Fundamental Equations. The governing equations for the two-phase medium mentioned above are the two-dimensional compressible Navier-Stokes equations to which the mass conservation law of the gas phase is added:

$$\frac{\partial Q}{\partial t} + \frac{\partial(E - E_v)}{\partial \xi} + \frac{\partial(F - F_v)}{\partial \eta} = 0, \quad (10)$$

where the unknown variable vector \mathbf{Q} , the flux vectors \mathbf{E} and \mathbf{F} and the viscous terms \mathbf{E}_v and \mathbf{F}_v are

$$\begin{aligned} \mathbf{Q} &= \frac{1}{J} \begin{pmatrix} \rho \\ \rho u \\ \rho v \\ \rho Y \end{pmatrix}, \quad \mathbf{E} = \frac{1}{J} \begin{pmatrix} \rho U \\ \rho u U + \xi_x p \\ \rho v U + \xi_y p \\ \rho U Y \end{pmatrix}, \\ \mathbf{F} &= \frac{1}{J} \begin{pmatrix} \rho V \\ \rho u V + \eta_x p \\ \rho v V + \eta_y p \\ \rho V Y \end{pmatrix}, \\ \mathbf{E}_v &= \frac{1}{J} \begin{pmatrix} 0 \\ \xi_x \tau_{xx} + \xi_y \tau_{xy} \\ \xi_x \tau_{yx} + \xi_y \tau_{yy} \\ 0 \end{pmatrix}, \quad \mathbf{F}_v = \frac{1}{J} \begin{pmatrix} 0 \\ \eta_x \tau_{xx} + \eta_y \tau_{xy} \\ \eta_x \tau_{yx} + \eta_y \tau_{yy} \\ 0 \end{pmatrix}. \end{aligned} \quad (11)$$

In Eq. (11), u and v are the velocity components in Cartesian coordinates (x, y) , τ is viscous stress tensor, $J = \xi_x \eta_y - \eta_x \xi_y$ is the Jacobian, and U and V are contravariant velocity components in curvilinear coordinates (ξ, η) .

Numerical Method. In this study, unsteady cavity flows are simulated by solving the above governing Eq. (10) using the finite difference method. It is also necessary to simulate stably high-speed cavity flows with such discontinuities as a gas-liquid interface with a large density jump. Thus the TVD scheme is used to ensure monotonicity of the solution; specifically, the TVD-MacCormack scheme (Yee [12]), with second-order accuracy in time and space, is used. Furthermore, the time splitting method is used to improve the stability of the solution in multidimensional problems, such that two-dimensional problems can be reduced to one-dimensional problems. When the governing equations are made discrete by using the TVD-MacCormack scheme, time integration of the predictor-corrector step in both the ξ and η directions and TVD processing are done in order to modify the solution. Only the ξ direction is shown below because the η direction has the same form.

$$\text{Predictor step: } Q_i^{(1)} = Q_i^n - \frac{\Delta t}{\Delta \xi} ((E_i^n - E_{i-1}^n) - (E_{vi+1/2}^n - E_{vi-1/2}^n)), \quad (12)$$

$$\text{Corrector step: } Q_i^{(2)} = \frac{1}{2} (Q_i^n + Q_i^{(1)}) - \frac{1}{2} \frac{\Delta t}{\Delta \xi} ((E_{i+1}^{(1)} - E_i^{(1)}) - (E_{vi+1/2}^{(1)} - E_{vi-1/2}^{(1)})), \quad (13)$$

$$\text{TVD step: } Q_i^{n+1} = Q_i^{(2)} + (L_{i+1/2}^{-1})^{(2)} \Phi_{i+1/2}^{(2)} - (L_{i-1/2}^{-1})^{(2)} \Phi_{i-1/2}^{(2)}, \quad (14)$$

where the matrix of left eigenvectors $\partial E / \partial Q$ is represented by L , and the function for the TVD-MacCormack scheme, [12], is represented by Φ .

A stator condition of the constant angle of attack and a constant total pressure condition is applied to the inlet boundary, and the constant pressure condition are applied to the outlet boundary. Furthermore, a cyclic boundary condition between each cascade passage and a nonslip condition on the hydrofoil surface is imposed.

Results and Discussion

Validation of the Present Method (Comparison With Experimental Results). The present numerical method can be applied to the analysis of complex cavity flows because it can treat the whole flowfield at once. On the other hand, we can't help handling a so-called noncavitating flow approximately as a low Mach number flow because we use a compressible numerical scheme. Therefore, in both cavitating and noncavitating conditions, the applicability of the present method has been found by comparing the numerical results with experimental results.

Cavitating flow around a single hydrofoil and noncavitating flow around hydrofoils in a cascade were considered. The hydrofoil geometry used was ClarkY with a thickness ratio of 11.7% (see Knapp, Daily, and Hammit [13]), the performance data of which are available for comparison. The computational grid of the cascade hydrofoils with a pitch/chord ratio of $t/c = 0.9$ and a stagger angle of $\gamma = 30$ deg is shown in Fig. 3. This is an H-type grid system with a 220×71 mesh point and the cascade passage geometry can be composed cyclically. The length of the computational region is set to be a two-chord length from the inlet boundary to the leading edge and a five-chord length from the trailing edge to the outlet boundary. In the case of a single hydrofoil, an H-type grid having the same cyclicity was used, that is, a single hydrofoil condition is fulfilled approximately by setting a sufficiently large t/c , such as $t/c = 20$. In this case, the grid system has a 320×131 mesh point and the computational region is set to be a three-chord length from the inlet boundary to the leading edge and a five-chord length from the trailing edge to the outlet boundary.

First, the cavitating flow around a single hydrofoil ($t/c = 20$, $\gamma = 0$ deg) was simulated for various cavitation numbers σ and an angle of attack $\alpha_i = 5$ deg. The cavitation number σ is defined as

$$\sigma = \frac{P_\infty - P_v}{\frac{1}{2} \rho_\infty |\mathbf{U}_\infty|^2}, \quad (15)$$

with the reference pressure, density, and velocity evaluated on the outlet boundary. The inlet flow velocity is $U_{in} = 10$ m/s and the Reynolds number is $Re = 7.0 \times 10^5$. The time-averaged lift and drag coefficients C_L and C_D were calculated from numerical results, and comparison with experimental data at the same Reynolds number by Numachi, Tsunoda, and Chida [14] was made, as shown in Fig. 4. Generally, it is known that C_L decreases dramatically when σ becomes smaller than a certain critical value (the so-called cavitation breakdown). The numerical results can predict the qualitative trends of C_L and C_D against σ , although quantitative differences are seen. Our method tends to underestimate the value of C_L and overestimate the value C_D , and as a result, the present method tends to overestimate the cavity volume.

Next, noncavitating cascade flows for $U_{in} = 4.3$ m/s and $Re = 5.0 \times 10^5$ were calculated for angles of attack α_∞ based on the geometrical mean velocity of 1.4 deg, 4.3 deg, and 7.6 deg. The time-averaged lift and drag coefficients were calculated from the numerical results. A comparison with the values of the wind tunnel experiment of Kikuchi [15] is shown in Fig. 5. The numerical results show a qualitative tendency even though C_L and C_D values tend to be somewhat overestimated and underestimated, respectively, as in the case of the cavitating cascade above. The pressure distributions on a hydrofoil surface for these three values of α_∞ are shown in Fig. 6, along with the experimental measurements at α_∞ values near to those of the numerical results. The tendencies of the numerical results coincide well with those of the experimental

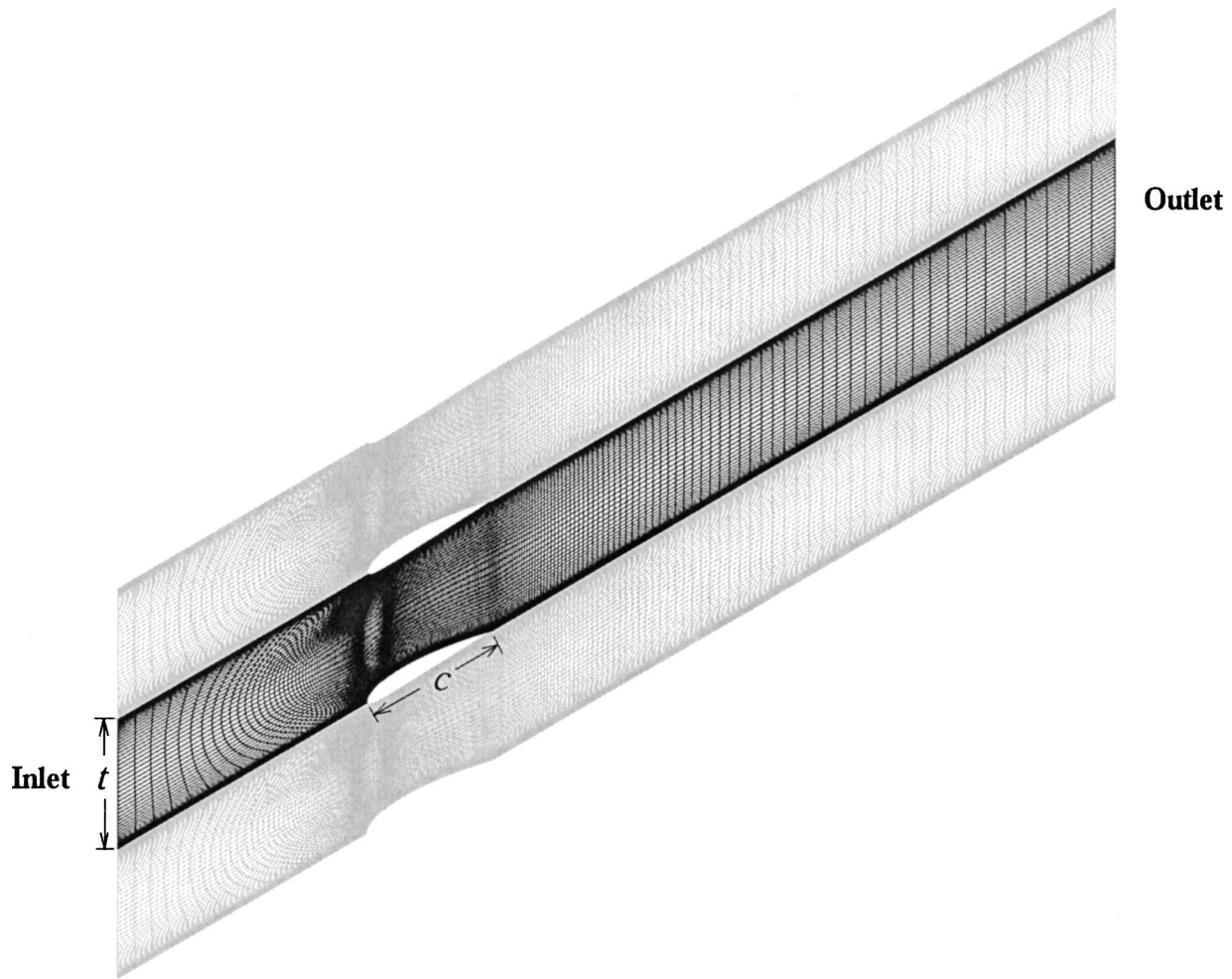


Fig. 3 Computational grid around cascade hydrofoils (Clark Y 11.7%, $t/c=0.9$, $\gamma=30$ deg)

data of the surface pressure distribution. However, because this method is a compressible numerical method, the computation of the noncavitation flowfield for Mach numbers less than 0.1 becomes unstable and numerical oscillation appears.

The comparison of the numerical results with the experimental data shows that the present numerical method is effective in evaluating the time-averaged characteristics of single and cascade hydrofoils for both noncavitation and cavitation conditions. However, discrepancies exist between the numerical and experimental data and hence further work is required to improve the quantitative accuracy.

Sheet Cavitation Breakoff Phenomenon. Numerical analysis of the aspect of cavity flow was carried out by examining the unsteady flow through a flat-plate cascade, which is closely related to that of the inducer. Particular attention was paid to the breakoff phenomenon of the sheet cavity in the transient cavitation condition where the unsteadiness becomes quite strong. In this section, the reference pressure, density, and velocity were evaluated on the inlet boundary to obtain σ .

First of all, the transient cavitating flow through the flat plate cascade ($t/c=0.9$, $\gamma=30$ deg) was analyzed for $\sigma/2\alpha_i=1.95$ and $\alpha_i=7$ deg, with a ratio of the maximum cavity length l_{\max} to the chord length of about $l_{\max}/c=0.28$. The time evolution of the void fraction, mass flux vectors, and pressure distributions on the suction side of the flat-plate cascade hydrofoil are shown in Fig. 7. Mass flux vectors are employed to distinguish between the separated flow and the re-entrant jet inside the cavity. Sheet cavitation formed from the leading edge on the suction surface (Frame 1 in

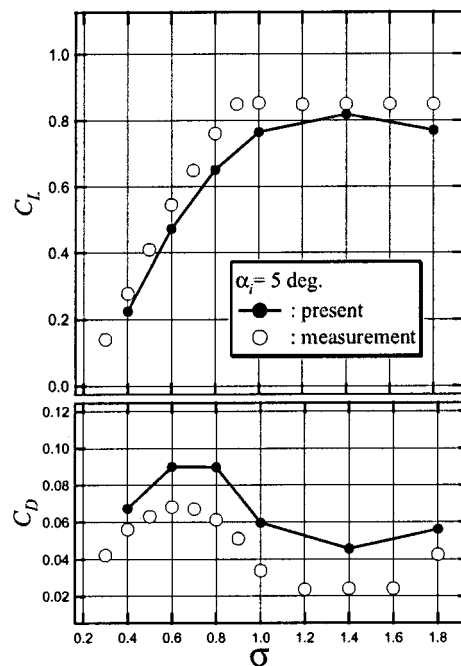


Fig. 4 Time-averaged lift and drag coefficients of a single hydrofoil at several cavitation numbers (Clark Y 11.7%)

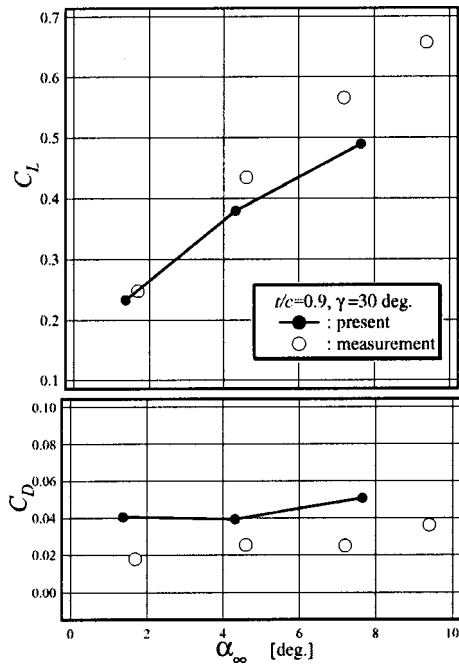


Fig. 5 Time-averaged lift and drag coefficients of a cascade of hydrofoils (Clark Y 11.7%, noncavitating state)

Fig. 7) develops toward the trailing edge (Frame 2). Then, a re-entrant jet forms due to the steep adverse pressure gradient near the cavity termination, and the re-entrant jet with a finite width moves toward the leading edge of the sheet cavity (Frames 3 and 4). In the vicinity of the leading edge, the jet impinges on the cavity surface layer, the thickness of which becomes smaller than the width of the jet. At this moment, a rapid pressure increase occurs around the impinging position near the leading edge of the cavity due to the water hammer effect, as explained later. Furthermore, a surface wave is also observed on the cavity surface near the leading edge (Frame 5). Subsequently, the sheet cavity begins to break off from the suction surface (Frame 6), and finally the cavity is detached from the suction surface and is shed in the downstream (Frame 7). At this time, another sheet cavitation has already begun to develop in a similar manner (Frame 8). Thus, a breakoff phenomenon due to re-entrant jet formation can be clearly simulated. The pressure jump on the suction surface near the impinging position ($x/c=0.01$, $y/c=0.001$) at the time of Frame 5 in Fig. 7 is about $\Delta C_p=0.42$. Generally, the water hammer pressure increase is $\Delta p_w=k\rho C|U|$, where $0.5 < k < 1$. Here, the water hammer pressure coefficient was evaluated to be $0.32 < \Delta C_{pw} < 0.64$ from the present numerical data; the value of ΔC_p given above is in this range. On the other hand, the stagnation pressure coefficient due to the re-entrant jet at same position was estimated to be $\Delta C_{ps}=0.21$, and does not correspond to the ΔC_p value. Therefore, the pressure jump is believed to be caused by the water hammer action of the re-entrant jet.

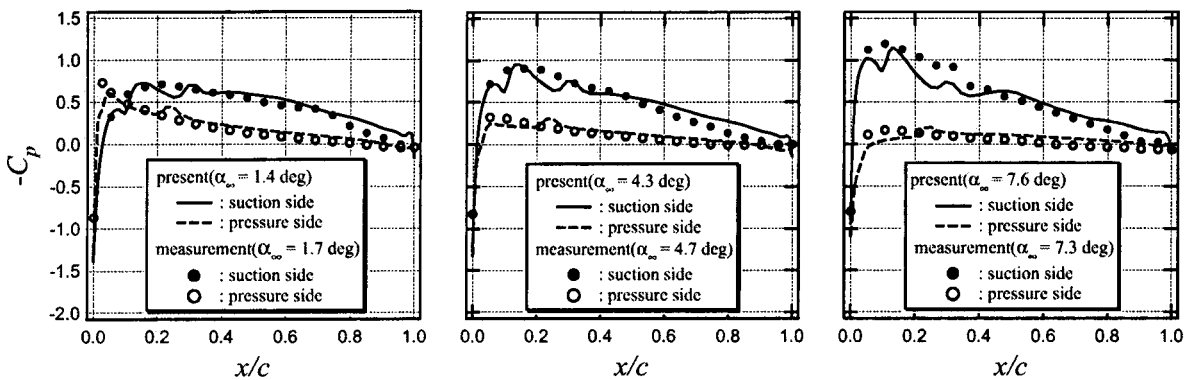


Fig. 6 Time-averaged pressure distribution of cascade hydrofoils (Clark Y 11.7%, noncavitating state)

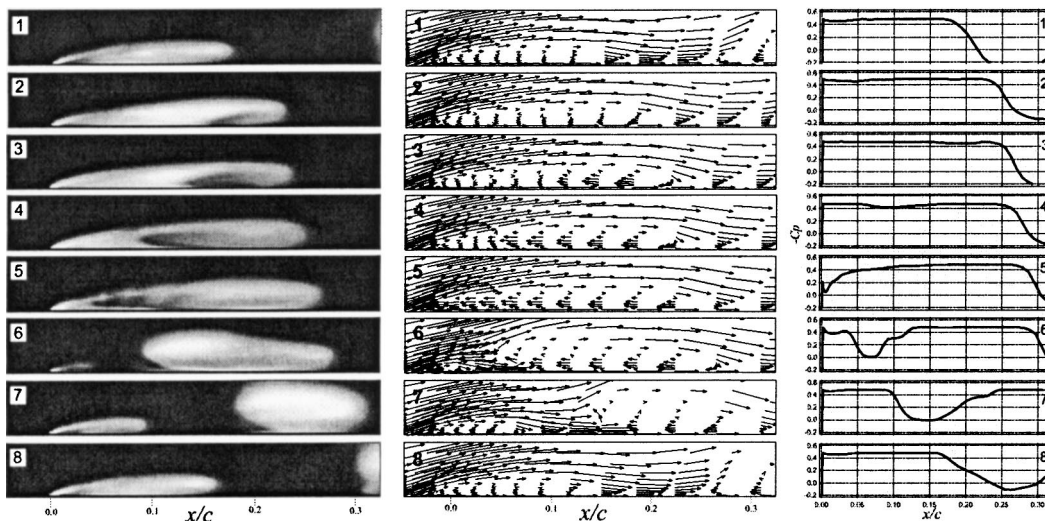


Fig. 7 Time evolutions of void fraction contours (left), mass flux vectors (center), and pressure distributions (right) around flat-plate cascade hydrofoils ($t/c=0.9$, $\gamma=30$ deg, $\sigma/2\alpha_1=1.95$, time interval=1.2 ms)

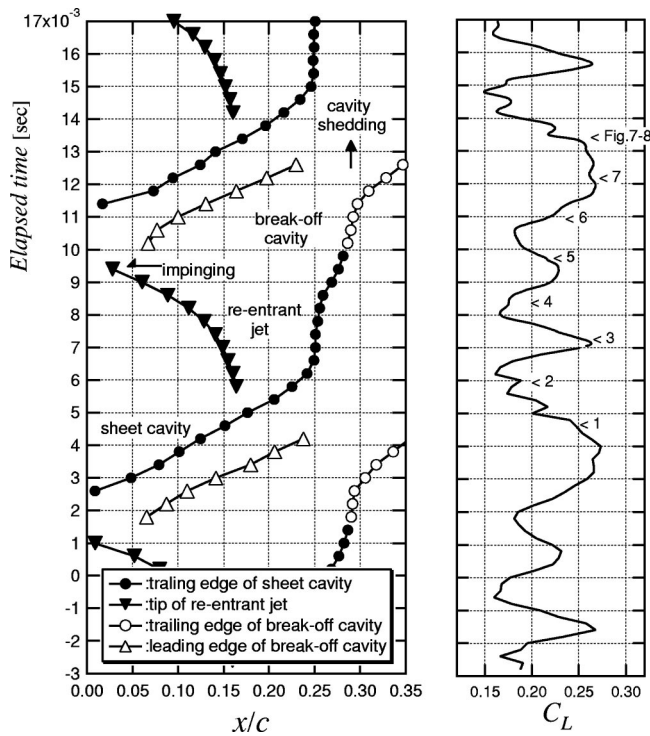


Fig. 8 Time evolutions of cavity lengths, re-entrant jet and lift coefficient ($t/c=0.9$, $\gamma=30$ deg, $\sigma/2\alpha_i=1.95$)

The time evolution of the cavity length, the tip position of the re-entrant jet and the lift coefficient are shown in Fig. 8. The lift fluctuates during the breakoff behavior, but roughly speaking the lift begins to increase gradually after the sheet cavity breaks off from the suction surface and decreases when the cavity is shed downstream. The velocity of the most accelerated re-entrant jet is 3.5 m/s. Since the average inlet velocity is 10.8 m/s, the re-entrant jet velocity is about 30% of the inlet velocity. The frequency of cavity shedding is $f=114$ Hz, so that the Strouhal number $(St)_c$ of cavity shedding based on chord length is about 0.75 and the Strouhal number $(St)_l$ based on maximum cavity length is 0.21. Furthermore, the power spectrum of the pressure in the center of the cascade throat in Fig. 9 has its peak at 110 Hz. It is believed, therefore, that the breakoff phenomenon is repeated regularly because of the evident peak. However, it should be noted that the breakoff phenomenon does not occur in the case of $\alpha_i=3$ deg and $1.29 < \sigma/2\alpha_i < 2.10$, for which a stable attached cavity was formed in the present simulation.

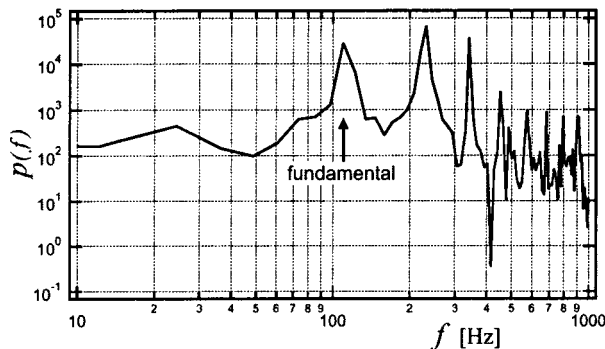


Fig. 9 Power spectrum of pressure at cascade throat center ($t/c=0.9$, $\gamma=30$ deg, $\sigma/2\alpha_i=1.95$)

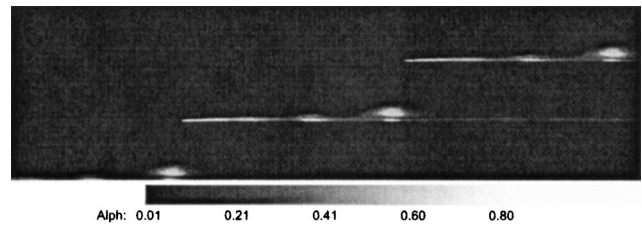


Fig. 10 Instantaneous void fraction contours around flat-plate cascade hydrofoils ($t/c=0.5$, $\gamma=75$ deg, $\sigma/2\alpha_i=1.27$)

Next, transient cavitating flow ($\sigma/2\alpha_i=1.27$ and $\alpha_i=3$ deg) through the flat-plate cascade ($t/c=0.5$, $\gamma=75$ deg), as shown in Fig. 10, was analyzed. In this cascade arrangement the stagger angle is larger, the pitch/chord ratio is smaller and the cascade interference becomes more intense than that of the previous cascade. In this case, the maximum cavity length is about $l_{max}/c=0.43$, and the trailing edge of the cavity is located in front of the cascade throat. The time evolution of the void fraction on the suction side of cascade hydrofoils is shown in Fig. 11. The breakoff phenomenon can be observed even in this case. However, no evident re-entrant jet occurs, unlike in the previous case. As shown in Fig. 12, pressure fluctuations can be seen on the hydrofoil surface inside the cavity at each time corresponding to each time interval of Fig. 11. By plotting these fluctuations carefully in Fig. 13, it is seen that pressure waves propagate inside the cavity, and that one of these waves causes part of the attached sheet cavity to break off (the breakoff wave). The local angle of attack α_{local} near the leading edge and local throat pressure p_l at the center of the cascade throat are also shown in this figure. When the breakoff cavity passes through the cascade throat, the throat width becomes narrow (see Fig. 10). Then, the liquid flow accelerates locally and the pressure in the cascade throat decreases. After the breakoff cavity is shed, the throat pressure recovers. Such pressure fluctuations cause a great variation in the local angle of attack of a neighboring hydrofoil. Furthermore, this rapid change of the local angle of attack causes cavity thickness fluctuations near the leading edge, and at the same time pressure waves are produced one after another from the leading edge of the cavity directed into the cavity. Finally, the cavity tends to break off due to the instability of the cavity surface associated with these pressure wave propagations. It is believed that the breakoff phenomenon is repeated by this mechanism in this case. At this time, the cavity shedding frequency is about $f=29.6$ Hz, so that $(St)_c$ is about 0.24 and $(St)_l$ is 0.11. In the power spectrum of the cascade throat pressure shown in Fig. 14, the power spectrum around 30 Hz is slightly high, although there is no evident peak. Hence, it is believed that this type of breakoff phenomenon is repeated somewhat irregularly.

Furthermore, the transient cavitating flow ($\sigma/2\alpha_i=0.23$ and $\alpha_i=5$ deg) in the same cascade arrangement was analyzed. In this case, the maximum cavity length is about $l_{max}/c=1.1$, and the trailing edge of the cavity is located in the rear of the cascade throat as shown in Fig. 15. This is similar to the previous case in that the evident re-entrant jet does not occur and pressure waves can be seen inside the cavity. Thus, the breakoff phenomenon seems to be caused by the same mechanisms as in the previous case. As shown in Frame 1 of Fig. 15, a small cavity occurs on the pressure side of the hydrofoil. This is because the passage distance of the cavity surface and the pressure side of the neighboring hydrofoil become narrow due to a large fluctuation of the cavity volume; the local pressure rapidly decreases and cavitates slightly. Even in this case, the breakoff phenomenon is repeated irregularly.

Strouhal numbers of cavity shedding are shown in Fig. 16, where the circles represent the case of a re-entrant jet dominant breakoff phenomenon ($t/c=0.9$, $\gamma=30$ deg) and the triangles rep-

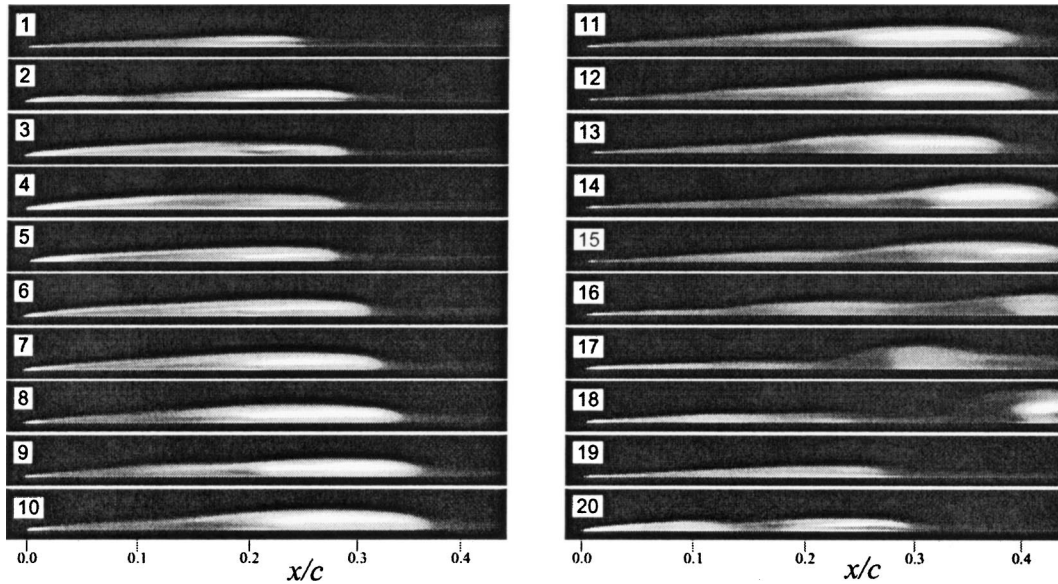


Fig. 11 Time evolution of void fraction contours around flat-plate cascade hydrofoils ($t/c=0.5$, $\gamma=75$ deg, $\sigma/2\alpha_i=1.27$, time interval=2.0 ms)

resent the case of a pressure wave dominant breakoff phenomenon ($t/c=0.5$, $\gamma=75$ deg). In the former case, $(St)_c$ based on the chord length increases as $\sigma/2\alpha_i$, while $(St)_l$ based on the maximum cavity length is almost constant at 0.2 and does not depend on $\sigma/2\alpha_i$ (see, for example, Le, Franc, and Michel [7]). On the other hand, in the latter case, both $(St)_c$ and $(St)_l$ values are scattered from 0.2 to 0.3 because of the somewhat irregular nature of the breakoff.

Conclusions

Comparing the numerical and experimental results of the time-averaged characteristics, it can be shown that the present numerical method based on a locally homogeneous model is effective

for the simulation of complex cavitating flows. However, the problem of improving the qualitative accuracy of the predictions remains for a later study.

Some trends of breakoff phenomena of sheet cavities on cascade hydrofoils were shown and discussed. The main results obtained can be summarized as follows:

1. It is clear that there are at least two mechanisms in the breakoff phenomenon of a sheet cavity. One is that the re-entrant jets play a dominant role in the breakoff phenomenon, and the other is that pressure waves propagating inside the cavity bring about another type of breakoff phenomenon accompanied by cavity surface waves.
2. In the case of the re-entrant jet dominant breakoff phenom-

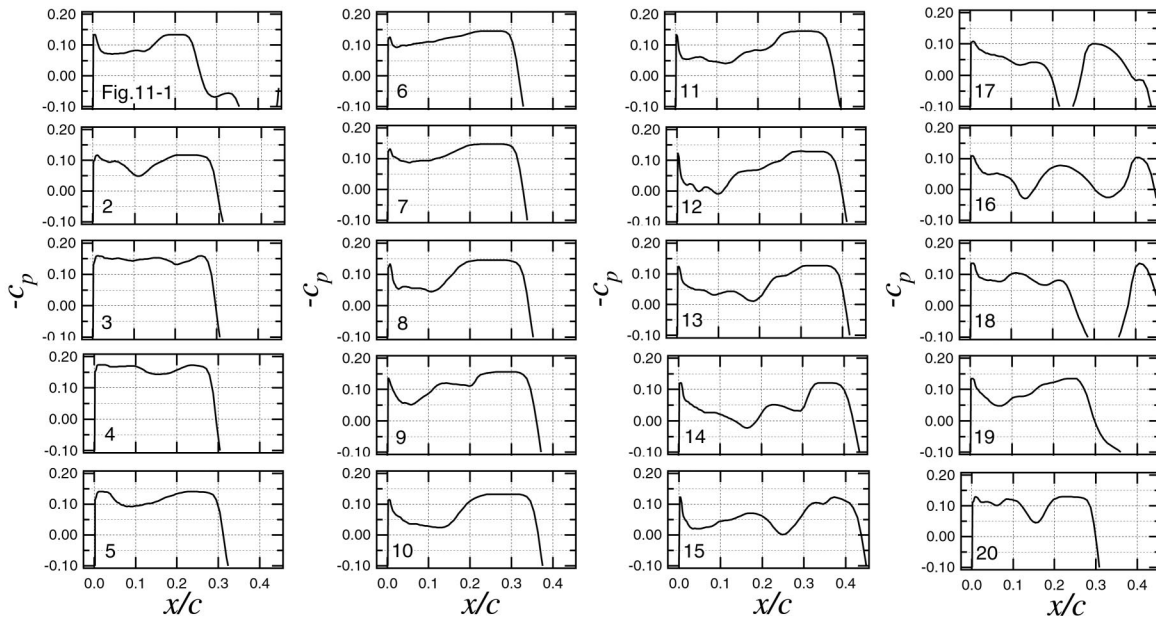


Fig. 12 Time evolution of pressure distribution on suction side of flat-plate cascade hydrofoils ($t/c=0.5$, $\gamma=75$ deg, $\sigma/2\alpha_i=1.27$, time interval=2.0 ms)

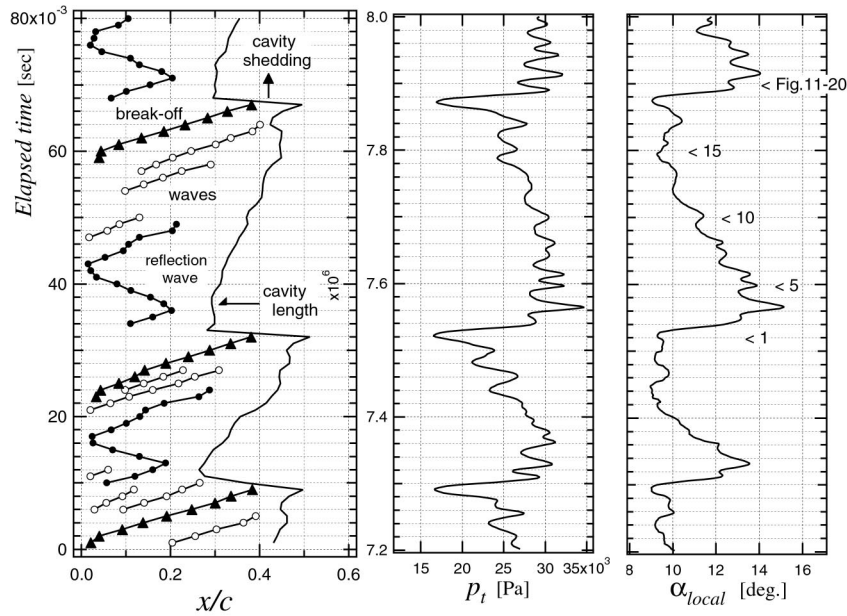


Fig. 13 Time evolutions of pressure waves inside cavity and cavity length ($t/c=0.5$, $\gamma=75$ deg, $\sigma/2\alpha_i=1.27$)

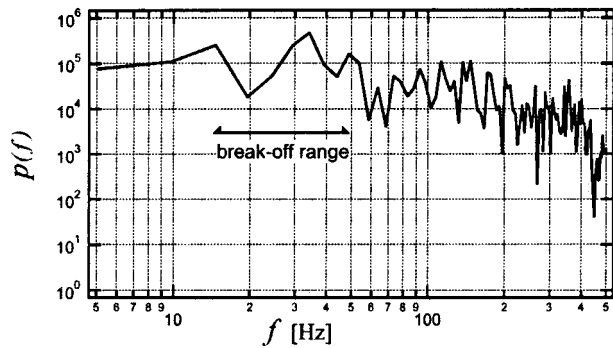


Fig. 14 Power spectrum of pressure at cascade throat center ($t/c=0.5$, $\gamma=75$ deg, $\sigma/2\alpha_i=1.27$)

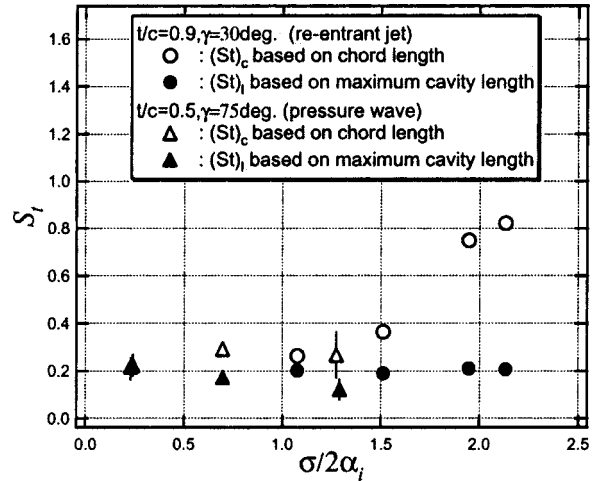


Fig. 16 Strouhal number of cavity shedding on flat-plate cascade hydrofoil

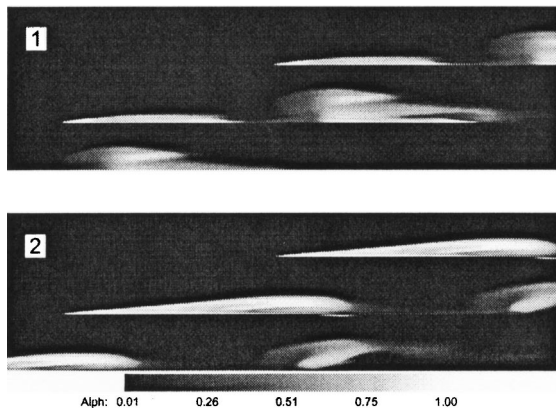


Fig. 15 Instantaneous void fraction contours around flat-plate cascade hydrofoils ($t/c=0.5$, $\gamma=75$ deg, $\sigma/2\alpha_i=0.23$)

enon, the impingement of the jet on the cavity surface layer is repeated regularly, and the pressure jump on the hydrofoil suction surface near the position of impingement is brought about by the water hammer action of the re-entrant jet. However, such a breakoff phenomenon does not occur in the case of a smaller angle of attack, in which a stable attached cavity is formed.

3. In the case of the pressure wave dominant breakoff phenomenon, a portion of the cavity tends to break off due to an instability of the cavity surface layer associated with pressure wave propagation. Pressure waves are produced by the fluctuation of the cavity thickness near the leading edge, which follows the time variation of the local angle of attack due to the throat area variation caused by the shedding of the breakoff cavity. This type of breakoff phenomenon is repeated somewhat irregularly.

4. Strouhal numbers of cavity shedding based on maximum cavity length remain constant at approximately 0.2, while Strouhal numbers based on the chord length increase depending on the cavitation number.

Acknowledgments

The numerical simulation was conducted using the super-computer, ORIGIN 2000, in the Institute of Fluid Science, Tohoku University.

Nomenclature

c	=	chord length
C	=	isothermal speed of sound
C_D	=	drag coefficient
C_L	=	lift coefficient
C_P	=	pressure coefficient
f	=	frequency
J	=	Jacobian = $\xi_x \eta_y - \eta_x \xi_y$
K	=	liquid constant
l_{\max}	=	maximum cavity length
p	=	pressure
p_c	=	pressure constant of liquid
p_v	=	vapor pressure
R	=	gas constant
Re	=	Reynolds number
$(St)_c$	=	Strouhal number of cavity shedding based on chord length = $fc/ \mathbf{U}_{\text{in}} $
$(St)_l$	=	Strouhal number of cavity shedding based on maximum cavity length = $fl_{\max}/ \mathbf{U}_{\text{in}} $
t	=	pitch
T	=	temperature
T_0	=	temperature constant of liquid
u, v	=	velocity components in Cartesian coordinates (x, y)
$ \mathbf{U} $	=	velocity = $\sqrt{u^2 + v^2}$
U, V	=	contravariant velocity components in curvilinear coordinates (ξ, η)
Y	=	quality (mass fraction of gas phase)
α	=	void fraction
α_i	=	angle of attack
α_{local}	=	local angle of attack near the leading edge
α_{∞}	=	angle of attack based on geometrical mean velocity
γ	=	stagger angle
μ	=	mixture viscosity coefficient
ρ	=	mixture density
σ	=	cavitation number

τ = viscous stress tensor

Subscripts

g	=	states of gas phase
in	=	inflow condition
l	=	states of liquid phase
t	=	cascade throat condition
∞	=	reference condition

References

- [1] Avva, Ram K., Singhal, Ashok K., and Gibson, Dennis H., 1995, "An Enthalpy Base Model of Cavitation," *Cavitation and Gas-Liquid Flow in Fluid Machinery Devices*, ASME, New York, FED-Vol. 226, pp. 63–70.
- [2] Deshpande, M., Feng, J., and Merkle, C. L., 1994, "Cavity Flow Predictions Based on the Euler Equations," *ASME J. Fluids Eng.*, **116**, pp. 36–44.
- [3] Kubota, A., Kato, H., and Yamaguti, H., 1992, "A New Modelling of Cavitating Flows: A Numerical Study of Unsteady Cavitation on a Hydrofoil Section," *J. Fluid Mech.*, **240**, pp. 59–96.
- [4] Reboud, J. L., and Delannoy, Y., 1994, "Two Phase Flow Modeling of Unsteady Cavitation," *Proc. 2nd Int. Symp. on Cavitation*, Tokyo, Japan, pp. 39–44.
- [5] Shin, B. R., and Ikohagi, T., 1999, "Numerical Analysis of Unsteady Cavity Flows Around a Hydrofoil," *ASME Paper No. 99-7215*.
- [6] Watanabe, S., Tsujimoto, Y., Franc, J. P., and Michel, J. M., 1998, "Linear Analyses of Cavitation Instabilities," *Proc. 3rd Int. Symp. on Cavitation*, Grenoble, France, pp. 347–352.
- [7] Le, Q., Franc, J. P., and Michel, J. M., 1993, "Partial Cavities: Global Behavior and Mean Pressure Distribution," *ASME J. Fluids Eng.*, **115**, pp. 243–248.
- [8] Hofmann, M., Lohrberg, H., Ludwig, G., Stoffel, B., Reboud, J.-L., and Fortes-Patella, R., 1999, "Numerical and Experimental Investigations on the Self-Oscillating Behavior of Cloud Cavitation," *ASME Paper Nos. 99-6755, 99-7259*.
- [9] Chen, H. T., and Colins, R., 1971, "Shock Wave Propagation Past an Ocean Surface," *J. Comput. Phys.*, **7**, pp. 89–101.
- [10] Karplus, H. B., 1958, "The Velocity of Sound in a Liquid Containing Gas Bubbles," *Armour Research Foundation of Illinois Institute of Technology*, Paper No. C00-248.
- [11] Beattie, D. R. H., and Whally, P. B., 1982, "A Simple Two-Phase Frictional Pressure Drop Calculation Method," *Int. J. Multiphase Flow*, **8**(1), pp. 83–87.
- [12] Yee, H. C., 1987, "Upwind and Symmetric Shock-Capturing Schemes," Paper No. NASA-TM 89464.
- [13] Knapp, T. R., Daily, W. J., and Hammit, G. F., 1970, *Cavitation*, McGraw-Hill, New York.
- [14] Numachi, F., Tsunoda, H., and Chida, I., 1949, "Cavitation Tests on Six Profiles for Blade Elements," *The Report of the Institute of High Speed Mechanics*, Tohoku Univ., **1**(1), pp. 1–16 (in Japanese).
- [15] Kikuchi, H., 1959, "Experimental Study on the Stall Characteristic of Wing Sections in Decelerating Cascade," *The Memoirs of the Institute of High Speed Mechanics*, Tohoku Univ., **14**(139), pp. 193–218 (in Japanese).

Influence of Roughness on the Two-Phase Flow Structure of Sheet Cavitation

B. Stutz¹

Université de Pau et des Pays de l'Adour,
Avenue de l'Université,
64000 Pau, France
e-mail: stutz@genserver.insa-lyon.fr

The purpose of this work is to describe the two-phase flow structure of sheet cavitation. The experimental study is performed in a cavitation tunnel equipped with a Venturi-type test section. Data treatments based on the analysis of transit time histograms and local time fraction histograms have been used. The rate of vapor production required to sustain the cavities is estimated. Wall pressure measurements and visualization techniques are also used to perform momentum balance. The influences of the roughness and the geometry of the divergent part located beneath the cavity on the internal two-phase flow are investigated. [DOI: 10.1115/1.1596240]

1 Introduction

The purpose of this work is to describe the two-phase flow structure of sheet cavitation. Cavitation is a sequence of vaporisation and condensation processes, related to the high acceleration of a liquid flow induced by the presence of a fixed or moving body. The knowledge of the two-phase structure of the flow is essential to estimate the interactions of the cavitation phenomenon with either the outer flow or the solid structures: The hydraulic unsteadiness as well as the erosion of the solid surfaces are related, respectively, to the entire volume of vapor and to the intensity of the phase transitions. The vaporisation process extracts heat from the surrounding fluid. It leads to temperature and vapor pressure reduction and thus limits the length of the cavity. This thermal effect depends on the rate of vapor production.

Experimental studies on sheet cavities are generally limited to the external liquid flow. The pressure and temperature at the wall, the external flow velocity, and the cavity shapes have been widely studied (Laberteaux et al. [1], Merle [2], and Le et al. [3]). The two-phase flow structure of attached cavities has been the subject of few measurements. Velocity measurements have been performed in natural and ventilated cavity conditions using a double hot wire velocimeter at a fixed point on a foil section (Kamono et al. [4]). Ceccio and Brennen [5] used silver epoxy electrodes flush-mounted on the surface of two-dimensional hydrofoil to detect individual bubble velocity. The thickness of the re-entrant jet has been measured using an ultrasonic method (Callenaere [6]).

A double optical probe device was developed to study the change in local variables such as void fraction, flow velocity, and bubble size within vapor or ventilated cavities (Stutz and Reboud [7]). It consists in two joined single probes fixed at a known distance from each other in the flow direction, the probes working independently. Each probe detects the phase surrounding its tip. Such a technique is based on the Snell-Descartes law. Infrared light is emitted inside each optical probe. Some part of this light is reflected back from the tip of the probe and measured. The intensity of the refracted light depends on the index of refraction of the medium surrounding the probe. The refractive indices of liquid and vapor are quite different and enable the phase detection. The tangential velocity of the fluid is estimated from the measured convection time of the liquid-gas interface moving from one probe tip to the other. A transit time found between the most

probable and the average time delay between the two stochastic signals is deduced using a cross-correlation technique (Serisawa et al. [8]). This method is accurate for steady bubbly flows. Bias may be introduced in measuring the mean value when the flows are unsteady (Galaup [9]). The widening of the cross-correlation peak is related to the velocity fluctuations, but it depends also on the bubble sizes, the void fraction, the fluctuations of the chord size between the two probes. Therefore it is not possible to estimate the velocity fluctuations using such a technique; thus the bias in measuring the mean value of the velocity cannot be rectified. Moreover the stability of the cavity shapes and the pressure measurements are rarely sufficient to allow conclusions concerning the stability of the internal two-phase flows (Stutz and Reboud [10]). New methods have been developed to estimate the time-averaged value and the standard deviation of the velocity, the time-averaged value and the standard deviation of the vapor phase within cavitating flows from double optical probe measurements. The methods consist in building histograms from which statistical values are calculated. They have been validated by studying periodic self-oscillating cavitating flows (Stutz and Reboud [11]). The purpose of this work is to apply such methods to sheet cavitation that look stable. The influence of the roughness and the geometry of the divergent part located beneath the cavity on the internal two-phase flow are investigated. The rate of vapor production required to sustain the cavities is estimated from the local measurements.

This work is an extension of previous work on the two phase flow structure of sheet cavitation, [10]. The data treatment techniques have been modified in order to reduce the bias induced by the velocity fluctuations, [11].

2 Measuring Techniques and Experimental Facility

Experimental Setup. The experiments were conducted in a closed loop at the Hydraulics and Mechanics School of the Institut National Polytechnique de Grenoble. The test section is 520 mm long, 44 mm wide, and 50 mm high at the inlet. A free-surface reservoir is used as a resorber. The total air content is kept near saturation during the experiments. The flow rate is set and controlled with an electro-magnetic flowmeter connected to the training pump through a microcomputer. The pressure is lowered until the desired cavitation number is reached. The upper and the side walls of the cross section are flat, whereas the height of the lower wall varies in order to form a convergent-divergent nozzle. The height of the throat section is 43.7 mm. In the present experiment

¹Currently at Center de Thermique de Lyon, UMR CNRS 5008, Institut National des Sciences Appliquées, 20 av. Albert Einstein, 69 621 Villeurbanne, France.

Contributed by the Fluids Engineering Division for publication in the JOURNAL OF FLUIDS ENGINEERING. Manuscript received by the Fluids Engineering Division March 14, 2002; revised manuscript received March 18, 2003. Associate Editor: S. Ceccio.

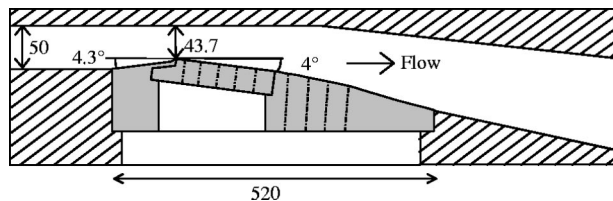


Fig. 1 Schematic diagram of the Venturi-type test section (dimensions are in mm)

the angle of the convergent part of the lower wall is 4.3 deg, and the angle of the divergent part is close to 4 deg (Fig. 1).

The turbulence level of the freestream flow was controlled by LDA and is about 1%. Taps are provided in the bottom of the convergent-divergent nozzle downstream from the throat. They can be equipped with Druck DPI 260 piezoresistive pressure transducers or with the double fiber optical probe, [10]. The experiments are performed with a mean cavity length of 80 mm, and a mean velocity at the throat of the test section of 12.4 m/s. The data acquisition system consists of a fast A/D data acquisition board Keithley DAS-1800 and a Pentium 180 microcomputer. The sampling rate is 130,000 samples per second and per channel.

Five different profiles including three straight profiles (a polished, a rough, and a striated one), and two convex profiles (a circle arc profile and a polynomial profile) have been studied in order to modify the geometry and the roughness beneath the cavity. The polynomial profile is a one-piece bottom. It has been the subject of previous study (Stutz and Reboud [7]) and is therefore considered as the reference profile. The pressure distribution along the reference profile is analogous to the one existing on the suction side of an inducer blade. The three straight profiles and the circle arc profile are interchangeable bases implanted on a second bottom (Figs. 1 and 2). The geometry and the roughness of the reference bottom and the second bottom upstream and downstream from the interchangeable bases are the same. The geometry and the roughness of the downstream part of the four interchangeable bases (located 80 mm downstream of the throat section) are the same.

Local Measurements With Double Optical Probe. The double optical probe consists of two 200 μm joined single-stretch glass probes placed inside a 0.8 mm stainless steel tube (Fig. 3). The distance between the tips is $2.02\text{ mm} \pm 0.02$. The ends of the fibers are stretched to provide 50 μm hemispherical tips. The double sensor probe is mounted inside a traversing mechanism fixed on the test section bottom. It can be moved perpendicularly to the lower wall of the test section with a micrometer screw gauge. The two sensor tips are aligned parallel to the axial flow direction. The position of the sensitive part of the probes is known with the following accuracy: 0.1 mm in height, 0.2 mm in horizontal direction and 5 deg in angle. The response time of the optoelectronic circuit is about 1 μs .

The local time fraction of the vapor phase $\beta(\mathbf{X}, T)$ is defined as the ratio of the gas phase residence time to the acquisition dura-

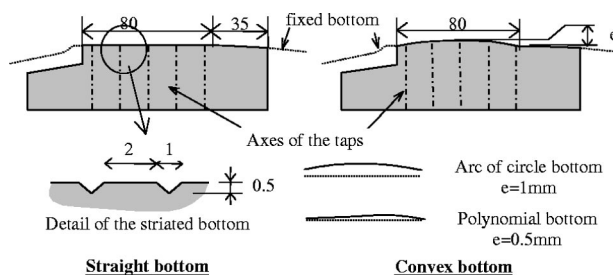


Fig. 2 Schematic diagram of the interchangeable bottom of the Venturi-type test section (dimensions are in mm)

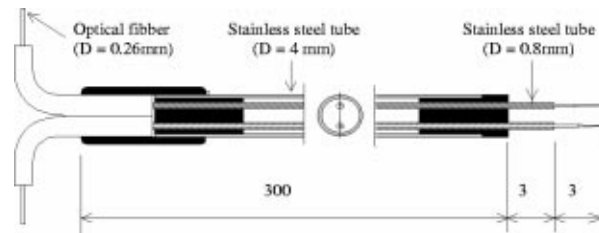


Fig. 3 Schematic diagram of the double optical probe (dimensions are in mm)

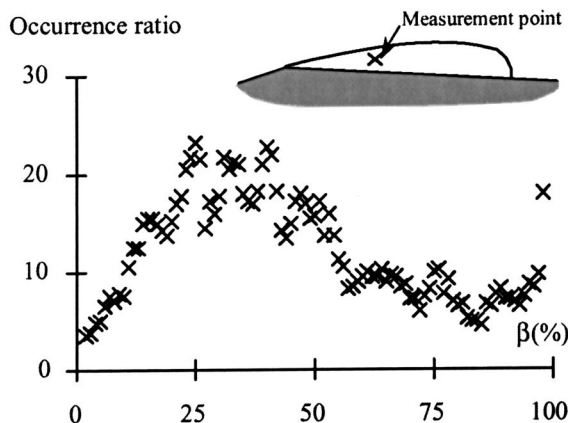
tion time T at geometrical point \mathbf{X} for short acquisition time (Eq. (1)). (T_{Gi} the residence time of the i th gas structure crossing the measurement point \mathbf{X}):

$$\beta(\mathbf{X}, T) = \frac{\sum T_{Gi}}{T} \quad (1)$$

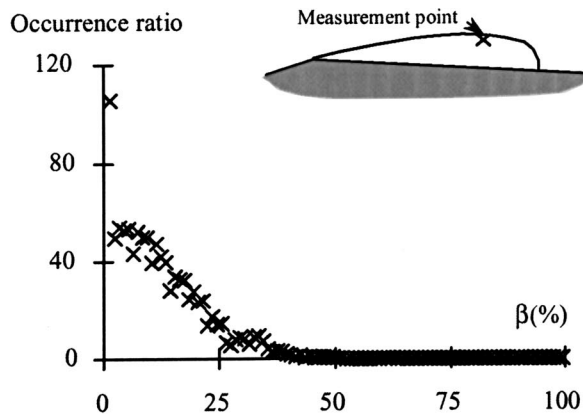
$\beta(\mathbf{X}, T)$ is determined by treating the signal from the upper probe and using a single threshold technique: this consists in determining the presence of gas when the signal is above a given trigger level. This statistical method is accurate whatever the flow conditions may be. The sampling frequency and the acquisition time must be large enough to have a significant statistical population. The optimal threshold level was determined by comparison with measurements performed using a gamma-ray attenuation device [7], and was set to 10% of the signal amplitude: This threshold is above the optoelectronic circuit noise level. The void fraction $\alpha(\mathbf{X})$ is defined as the ratio of the gas phase residence time to the acquisition duration time at geometrical point \mathbf{X} for long acquisition time and corresponds to the time average value of $\beta(\mathbf{X}, T)$. (This definition was previously used in Refs. [7] and [10]). The relative uncertainty concerning the void fraction is estimated at about 15% of the measured value. The results are extremely reproducible. The standard deviation of $\beta(\mathbf{X}, T)$ is representative of the two phase flow structure: Low fluctuation is representative of a steady bubbly flow. High fluctuation is representative of a fluctuating two-phase flow (slug flow for example). The difficulty consists in determining the optimum duration for the data blocks. Unsteady cloud cavitation are characterized by the shedding frequency f leading to a constant Strouhal number based on the cavity length L_{cav} and the velocity of the outer flow U : $St = fL_{\text{cav}}/U \approx 0.3$ (Stutz and Reboud [7], Lush and Skipp [12], and de Lange et al. [13]). The size of the data blocks is set to 1/5 of the shedding cycle period given by this relation. Figure 4 shows examples of the local time fraction histograms of the vapor phase (reference profile).

Local velocity histograms are computed from the transit time of bubbles successively detected by the two probe tips. Similar techniques were previously used by Serisawa et al. [8] and Revankar et Ishii [14]. The probe signals are first altered to a square-wave response by a trigger. The local velocity is then estimated by measuring the passage time of an interface on both upstream and downstream sensors. The range of transit times of successive bubbles from one probe to the other is estimated using the cross-correlation function on which a given trigger level is applied. The threshold level is set to 20% of the maximum of the function. Figure 5 shows examples of cross-correlation functions of the optical probe signals corresponding to the measurement points of Fig. 4.

The signature of a vapor structure impacting the upstream probe is compared with the signal recorded by the downstream probe in the range of the transit times previously estimated. Sequential signals detected by the two probes are assumed to belong to the same bubble impacting the two probes if the resident times of the gas phase at each measurement point are comparable. The velocity histogram is characteristic of the velocity of bubbles having impacted the two probes without having been deflected or



Measurement point located in the upstream part of the cavity (X=21mm ; Y=2,4mm) ; Void fraction $\alpha = 71\%$



Measurement point located near the interface of the cavity (X=56mm ; Y=6mm) Void fraction $\alpha = 5.4\%$

Fig. 4 Histograms of the local time fraction of the vapor phase β . X is the distance from the throat of the test section along the horizontal axis; Y is the distance from the throat of the test section along the vertical axis.

having been subject to a significant shape change. The uncertainty in determining of the transit time of vapor structures between the two probes depends on the flow velocity (Eq. (2)). The relative uncertainty is estimated at about 6% of the measured value for a flow velocity of 10 m/s.

$$\frac{\Delta V}{V} = \frac{\Delta d}{d} + \frac{\Delta t}{t} \approx \frac{\Delta d}{d} + \frac{V}{d \cdot f} \quad (2)$$

Miscounting is assumed to occur randomly with respect to time. A constant bias corresponding to this uniform background is therefore subtracted from the transit time histograms before calculating the time average and the standard deviation of the velocity. Figure 6 shows examples of velocity histograms corresponding to the measurement points of Figs. 4 and 5.

The sheet cavities are made with moving vapor structures. The transfers of heat and mass between the liquid and the vapor phase depend on the interfacial area, and thus on the shape and the size of the vapor structures. The chord length $l_c(\mathbf{X})$ of the vapor structure crossing at a geometrical point \mathbf{X} is defined as the product of the resident time $T_G(\mathbf{X})$ by the velocity $V_G(\mathbf{X})$ of the vapor phase crossing at that point: $l_c(\mathbf{X}) = T_G(\mathbf{X}) \cdot V_G(\mathbf{X})$ (Fig. 7). The mean chord length $\bar{l}_c(\mathbf{X})$ of the bubbles detected by the probes is cal-

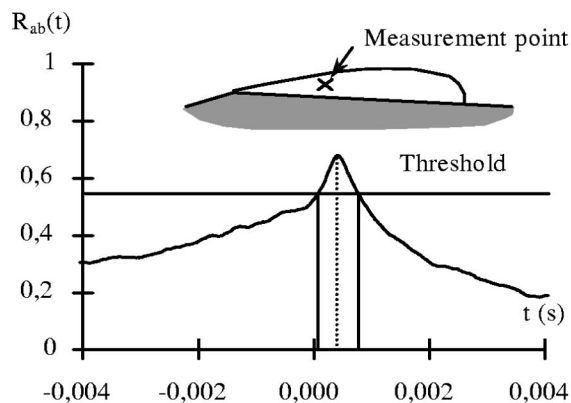
culated from the void fraction $\alpha(\mathbf{X})$, the number $n_b(\mathbf{X})$ of bubbles impacting the upstream probe during the acquisition duration T and the average of the absolute value of the velocity $\overline{|V(\mathbf{X})|}$ (Eq. (3)).

$$\bar{l}_c(\mathbf{X}) = \frac{\alpha(\mathbf{X})T}{n_b(\mathbf{X})} \overline{|V(\mathbf{X})|} \quad (3)$$

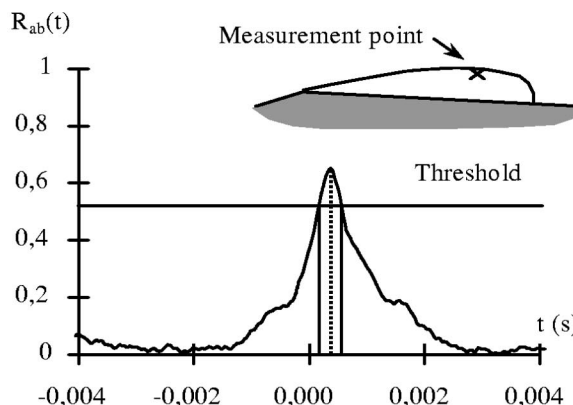
The determination of the size of the vapor structures from the distribution of the chord length requires important hypotheses on the shape of the structures, the probability of piercing, the velocity of each structure, [15]. Therefore it can not be calculated in the present experiment.

3 Experimental Results

Outer Flow. A photograph of sheet cavitation is shown in Fig. 8 (the Venturi test section is equipped with the reference base). Mean cavity shapes are provided by image processing. The horizontal and vertical scales are determined using a reflecting tip introduced through the Venturi bottom at a known position and its height is being controlled. The roughness and the geometry of the divergent part located beneath the cavity do not appear to influ-

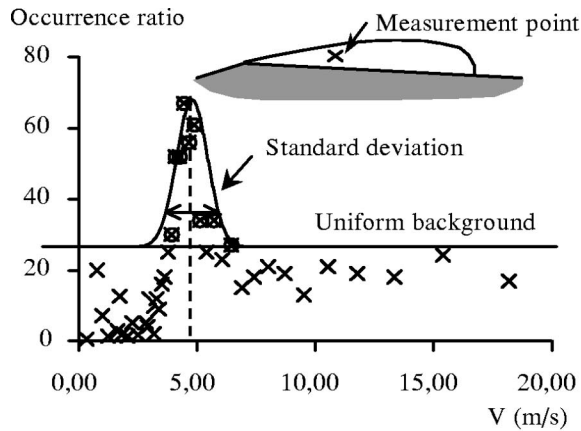


Measurement point located in the upstream part of the cavity (X=21mm ; Y=2,4mm)

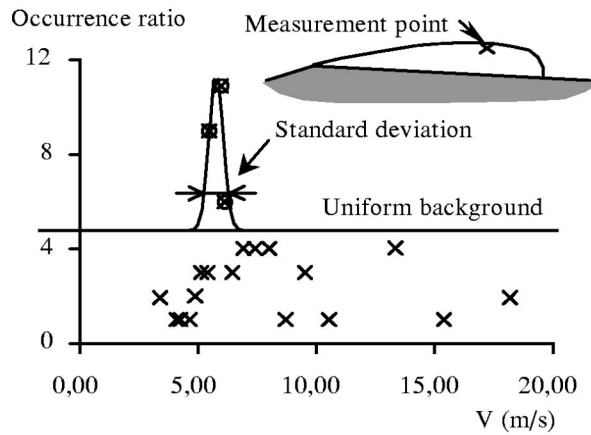


Measurement point located near the interface of the cavity (X=56mm ; Y=6mm)

Fig. 5 Example of cross-correlation function $R_{ab}(t)$ of the optical probe signals



Measurement point located in the upstream part of the cavity ($X=21\text{mm}$; $Y=2,4\text{mm}$)



Measurement point located near the interface of the cavity ($X=56\text{mm}$; $Y=6\text{mm}$)

Fig. 6 Examples of velocity histograms

ence the mean cavity shapes or the observations of the cavitating flows even using a stroboscopic light. The three-quarters upstream parts of the cavities are quite stable whereas the downstream quarter fluctuates and sheds horseshoe vortices in the main flow.

The cavitation number is expressed as (Eq. (4))

$$\sigma_{\text{ref}} = \frac{P_{\text{ref}} - P_{\text{vap}}}{0.5\rho V_{\text{ref}}^2} \quad (4)$$

ρ , P_{vap} , P_{ref} , V_{ref} are, respectively, the water density, the vapor pressure, the pressure, and the mean velocity in the reference section S_{ref} ($S_{\text{ref}}=44\text{ mm}\times 45\text{ mm}$). Figure 9 shows the distribution of the cavitation number as a function of the cavity length. The maximum mean cavity length before choking is about 120 mm. It occurs at $\sigma_s=0.295\pm 0.005$. The roughness of the base has no significant influence on the relation between the cavity length and the cavitation number. The thickness added to the base does not

modify the length of the cavity when it is located beneath the cavitating flows. If it is longer than the cavitating flows, the added base thickness reduces the cavity length.

Pressure fluctuations are measured along the wall of the test section. Measurement taps are connected with 50 mm long rigid tubes to Druck DPI 260 piezoresistive pressure transducers. No characteristic frequency corresponding to cloud shedding can be observed in the power spectrum of the pressure signals (the frequency response of the measurement taps equipped with the pressure transducers is about 1 kHz).

Two-Phase Flow Within the Cavity. Figures 10, 11, and 12 show the distribution of local time fraction of the vapor phase, the time-averaged tangential velocity, and mean chord length within the cavity. The cavity length fluctuation is about 15%. The cavitation number based on the mean velocity and the pressure P_{ref} in the upstream section is $\sigma=0.307$. Three acquisitions of 3s have been performed for each measurement point in order to verify the reproducibility of the results. The tangential velocity measured at the interface of the cavity is constant on the upstream 70% part of the cavity where it reaches a value close to the throat velocity

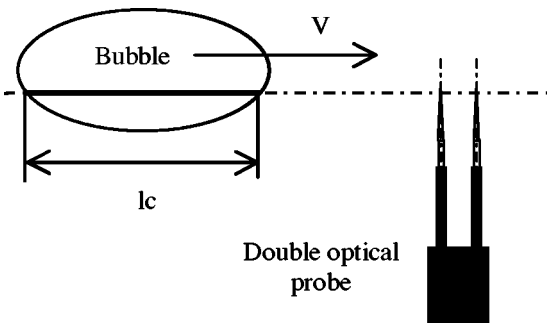


Fig. 7 Chord length l_c of vapor structure



Fig. 8 Photograph of sheet cavitation

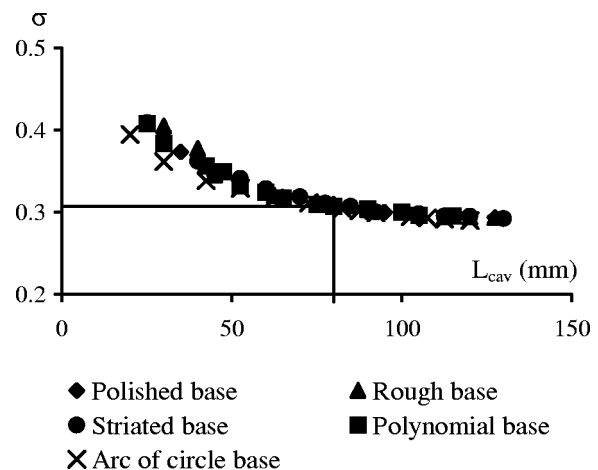


Fig. 9 Influence of the geometry and the roughness of the base on the relation between the cavity length L_{cav} and the cavitation number $\sigma = (P_{\text{ref}} - P_{\text{vap}}) / (0.5\rho V_{\text{ref}}^2)$. (Cavity length of 80 mm corresponds to cavitation number $\sigma_{\text{ref}}=0.31$).

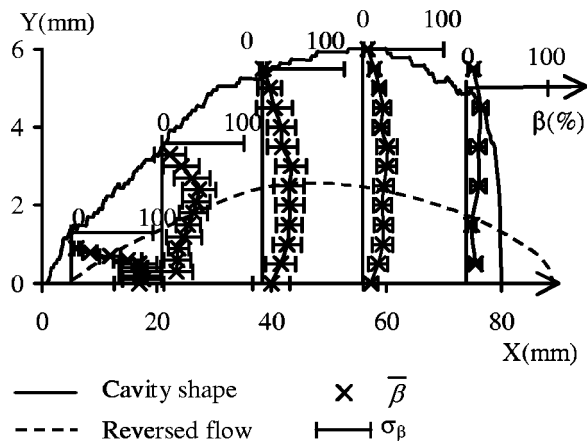


Fig. 10 Time average and standard deviation of the local time fraction of the vapor phase β within the cavity. Cavity length $L_{cav}=80$ mm; velocity in the upstream section $V_{ref}=12$ m/s. The test section is equipped with the reference profile.

($P \sim P_{vap}$). It decreases in the downstream part of the cavity where the vapor condenses. The measurements at the interface of the cavity are in good agreement with the one obtained with LDA (Stutz and Reboud [10]). (Void fraction is smaller than 2% there and the LDA signal isn't much affected by the presence of bubbles.) A reversed two-phase flow occurs along the solid surface. It extends 10 mm downstream of the throat whereas it is

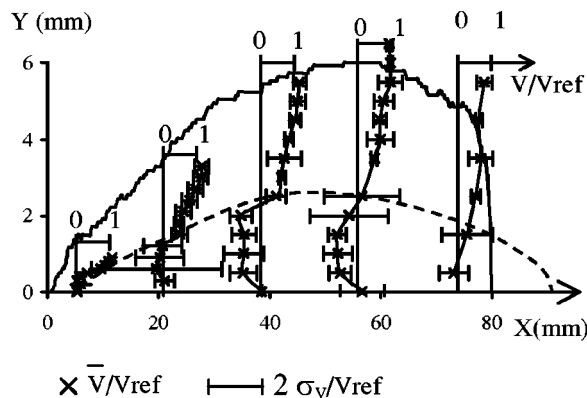


Fig. 11 Time average and standard deviation of the velocity. Cavity length $L_{cav}=80$ mm; velocity in the upstream section $V_{ref}=12$ m/s. The test section is equipped with the reference profile.

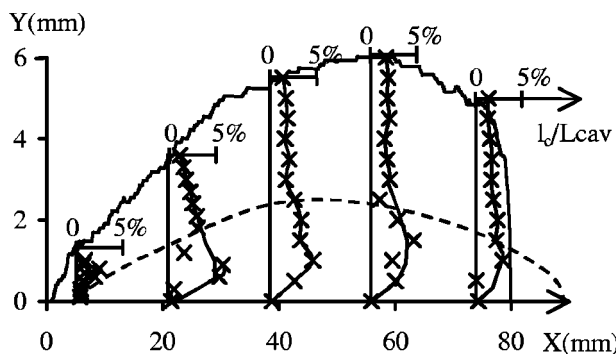


Fig. 12 Time-averaged chord lengths l_c of vapor structures within the cavity. Cavity length $L_{cav}=80$ mm; velocity in the upstream section $V_{ref}=12$ m/s. The test section is equipped with the reference profile.

limited to about 15 mm downstream of the cavity. Under noncavitating conditions, no reversed flow is observed. The velocity calculated with the cross-correlation function on the entire signal approximately equals the mean velocity estimated using transit time histograms except for the positions characterized by large fluctuations (in the closing part of the cavity) or alternate flows (near the interface between the main and the reversed two-phase flow).

The maximum void fraction varies regularly from 80% at the upstream end of the cavity to 10% in the downstream part. It is generally maximum at mid-height of the cavity. No discontinuity appears on the vertical distribution of void fraction between the main and the reversed flow. Chord length is minimum near the interface and in the upstream part of the cavity and becomes maximum near the bottom of the cavity. Coalescence processes may occur within the cavity (the bubble sizes growth whereas void fraction remains constant or decreases).

Figures 10 and 11 show the distribution of the standard deviation of the local time fraction β and of the velocity within the cavity. Velocity in the main two-phase flow is quite stable. Velocity fluctuations occur in the closure part of the cavity and in the reversed two-phase flow, but no pulsing re-entrant jet has been observed beneath the cavity. The two-phase flow structure of the cavity looks like a flat vortex with length fluctuations. No significant fluctuation of β characteristic of significant vapor fraction fluctuation can be pointed out.

Figure 13 shows the distribution of the void fraction and mean velocity within cavities having different bottom geometry and roughness. A cavity shape has been provided by image processing using a CCD video camera and a laser light sheet with the reference bottom profile. Its shape has been plotted on each diagram of Fig. 13. Void fraction distribution agree well with this shape whatever the bottom may be: the interface of the cavity always corresponds to a void fraction of about 2%. It confirms the fact that the roughness and the thickness of the bottom located beneath the cavity does not influence the shape of the cavity. No significant differences between the cavitating two-phase flows appear in the case of a striate, a rough or a polished bottom. The presence of stria is not sufficient to affect the reversed two-phase flows. Investigations where performed by Kawanami et al., [16] to control cloud cavitation by introducing obstacles on the suction side of a cavitating foil. Only the insertion of obstacles with significant height may stop the re-entrant jet. In case of steady cavitation and Venturi-type test sections, the roughness of the bottom beneath the cavity does not influence the cavitating two phase flow: No significant difference appears on the distribution of the time average or the root mean square of the local measurements.

The depth of the bottom does not influence the depth of the reversed flow (the same depth is observed for a flat or a convex bottom). Therefore the distance between the cavity interface and the reversed flow decreases when the bottom beneath the cavity is thicker. Instabilities may occur with a thicker bottom if the reversed flow reaches the interface of the cavity.

The volume flow rate of vapor is estimated at each measuring position, assuming two-dimensional flow and neglecting side wall effects, by using the expression $Q_{vap} = \int_0^h (V(y) \alpha(y)) b dy$ where b and h are the width and the height of the two-dimensional cavity in the cross section of the measurement axis. Results normalized as $Cq = Q_{vap} / (V_{ref} b L_{cav})$ are shown in Fig. 14. The maximum vapor flow rate is measured at $X/L_{cav} = 0.25$. The vapor flow rate distributions between the different profiles reach a value close to $Cq = 2 \cdot 10^{-3}$ in the rear part of the cavities. Differences appear with results obtained previously, [10]. They are attributed to the velocity measurement method: In the present case, velocity is computed from transit time histograms, when it was computed using a cross-correlation function in the past. The cross-correlation technique induces significant bias in measuring the time-average velocity when there are large velocity fluctuations as in the case of reversed two-phase flow.

The difference of temperature between the liquid and the vapor

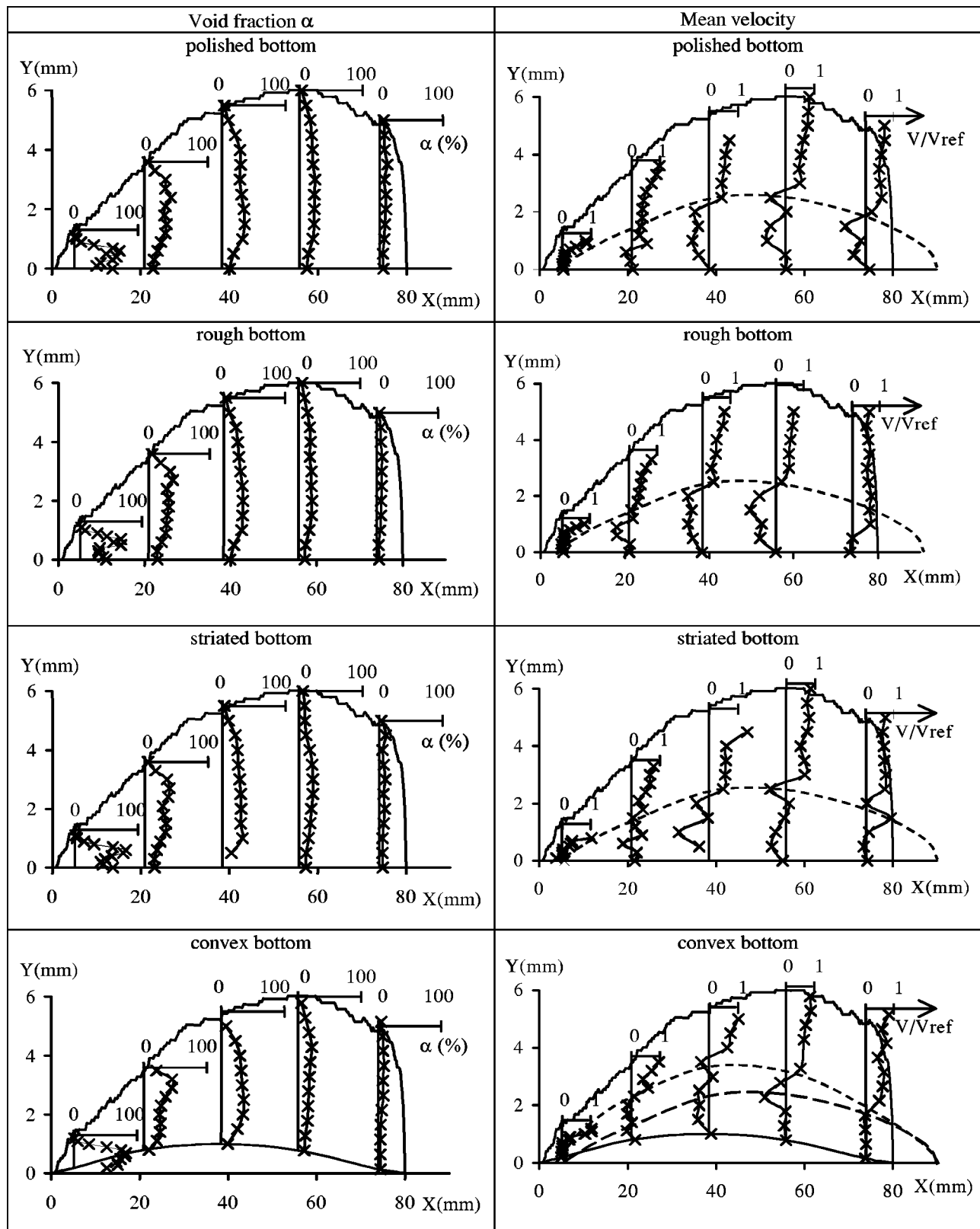


Fig. 13 Influence of the geometry and the roughness of the bottom on the spatial distribution of void fraction α and of time-average velocity within the cavity (cavity length $L_{cav}=80$ mm; velocity in the reference section $V_{ref}=12$ m/s)

constitutes the thermal effect. It is particularly significant in cryogenic liquids such as those used in the turbo-pumps of a space launcher. Vapor production extracts heat from the surrounding fluid and induces temperature decrease. Conversely vapor conden-

sation gives heat to the surrounding fluid and induces temperature increase. Vaporization processes occur during the entry of the liquid in the cavitating area near the interface of the cavity and within the reversed flow. The presence of liquid-vapor interfaces

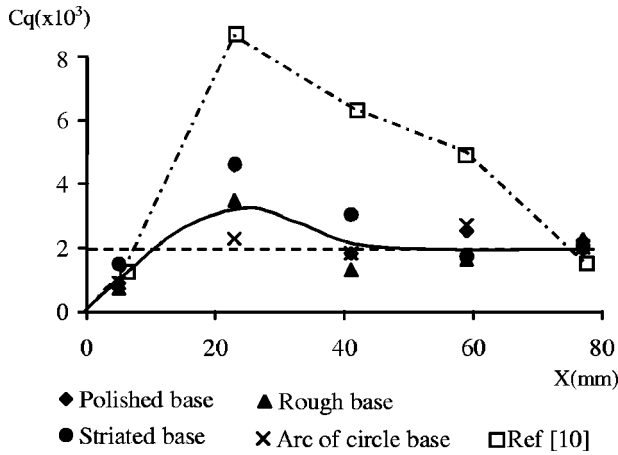


Fig. 14 Influence of the geometry and the roughness of the base on the distribution of the volume flow rate within the cavities. Cavity length $L_{cav}=80$ mm; velocity in the reference section $V_{ref}=12$ m/s. Cq is the volume flow rate coefficient ($\times 10^3$).

prevents metastable states. The vapor production required to sustain a cavity is usually estimated by assuming that it is equal to the noncondensable gas flow rate necessary to sustain a ventilated cavity of identical geometry and is compared to the vapor flow extracted from the cavity. Fruman et al. [17] determine that the flow coefficient Cq was constant and independent of the geometry of the tested body with a value close to 5.2×10^{-3} . This value is about twice that the vapor flow rate convected downstream calculated using the local measurements in the rear part of the cavity.

Mass and momentum balances may be determined using the experimental data. The cavity is divided into five parts limited by a boundary located outside of the cavitating flows, by the Venturi faces and by the measurement sections (Fig. 15). The continuity and momentum balances are performed with the following assumptions: The internal flow is taken to be two-dimensional; the pressure is kept constant in the direction normal to the profile (there is no transverse pressure gradient due to the small cavity thickness); the ratio of the density between the vapor and liquid phases means that the contribution of the mass and momentum influxes of vapor can be neglected in the integral balances; the velocity shift between the liquid and vapor phases is neglected since vaporization and condensation take place spontaneously, and buoyancy forces are negligible in comparison with inertial forces. The mass influx from the outer flow is deduced from the mass balance (Eq. (5)).

$$\rho_L \cdot Q_{ext} = b \int_C^D (1 - \alpha) \cdot \rho_L \cdot V \cdot dy - b \int_A^B (1 - \alpha) \cdot \rho_L \cdot V \cdot dy \quad (5)$$

The momentum influx from the outer flow is deduced from the mass balance (Eq. (6)).

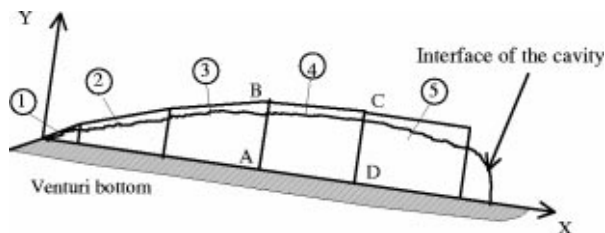


Fig. 15 Partitioning of the cavity

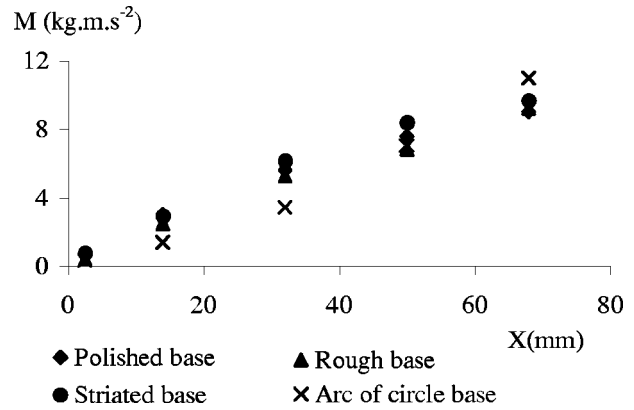


Fig. 16 Influence of the geometry and the roughness of the base on the distribution of the momentum flux M within the cavities. Mean cavity length $L_{cav}=80$ mm; velocity in the reference section $V_{ref}=12$ m/s.

$$b \int_B^C (1 - \alpha) \cdot \rho_L \cdot |V| \cdot V \cdot dy \approx \rho_L \cdot Q_{ext} \cdot V_{ext} \quad (6)$$

The pressure distribution within the cavity is deduced from pressure measurements. The shearing stress C_{xy} at the boundary BC is neglected (the boundary position is determined where the velocity gradient is zero). The skin-friction drag F_p on the lower wall of the test section is estimated by momentum balance (Eq. (7)).

$$F_p = b \int_A^B (1 - \alpha) \cdot \rho_L \cdot |V| \cdot V \cdot dy - b \int_C^D (1 - \alpha) \cdot \rho_L \cdot |V| \cdot V \cdot dy + \rho_L \cdot Q_{ext} \cdot V_{ext} - P_{AB} \cdot AB + P_{CD} \cdot CD - P_{BC} \cdot (h_C - h_B) \quad (7)$$

Figure 16 shows the momentum flux within the cavities. The results are quite similar for the polished, the rough, and the striated bases. The lower momentum flux in the upstream part of the cavity for the circle arc base is due to the thickening of the geometry.

The skin friction drag is quite negligible in the upstream three-quarters of the cavity (Fig. 17). Its negative values in the middle part of the cavity are due to the reversed flow in that area. Mean velocity is oriented in the main flow direction in the upstream and downstream parts of the cavity. The roughness of the bases located beneath the cavities has no significant influence on the skin

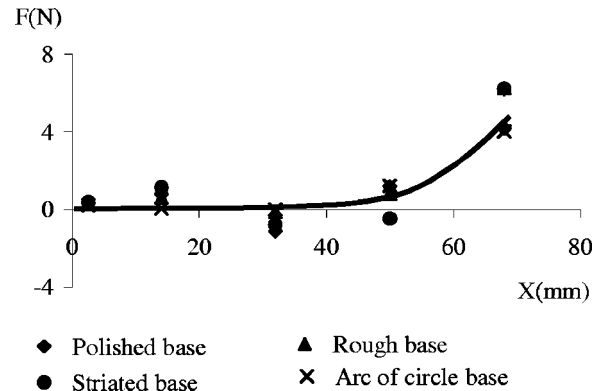


Fig. 17 Influence of the geometry and the roughness of the base on the distribution of the skin friction drag F within the cavities. Cavity length $L_{cav}=80$ mm; velocity in the reference section $V_{ref}=12$ m/s.

friction drag. The presence of a great quantity of bubbles seems to act as a “ball bearing” on the flow which reduces effects of roughness.

Conclusion

The two-phase flow structure of steady attached cavities developing on the wall of a Venturi-type test section has been investigated using a double optical probe. Data treatments based on the analysis of transit time histograms and local time fraction histograms have been used. The cavitating two-phase flow looks like a steady vortex whose length fluctuates about $\pm 15\%$. The upstream part of the cavity is mainly filled with vapor. A reversed two-phase flow occurs along the solid surface. Fluctuations of the velocity and the time fraction of the vapor phase occur in the reversed two-phase flow, but no pulsating re-entrant jet has been observed. No significant vapor fraction fluctuation has been measured within the cavity. The shape of the cavities, the distribution of void fraction and time-average velocity are not significantly influenced by the roughness of the bottom located beneath the cavity. The depth of the bottom does not influence the depth of the reversed flow. Instabilities may occur with thicker bottom if the reversed flow reaches the interface of the cavity. The roughness of the bases located beneath the cavities has no significant influences on the skin friction drag. The presence of a great quantity of bubbles reduces the roughness effects.

Acknowledgments

This work was performed under contract from the French space agency (Center National d' Etudes Spatiales): The authors wish to express their gratitude for this support.

Nomenclature

B	= width of the test section (m)
Cq	= volume flow rate coefficient
f	= frequency (Hz)
F	= skin friction drag (N)
h	= height of the test section (m)
l_c	= chord length (m)
L_{cav}	= cavity length (m)
M	= momentum
P	= pressure (Pa)
Q	= volume flow rate (m^3/s)
Rab	= cross-correlation function
S	= section (m^2)
St	= Strouhal number
T	= time lag (s)
T_{Gi}	= resident time of the i th gas particle at M (s)
V	= velocity ($m \cdot s^{-1}$)
X	= measurement point

X	= distance from the throat of the test section (m)
Y	= distance from the Venturi bottom (m)
α	= void fraction measured at M
β	= volume fraction of the vapor phase
ρ	= density ($kg \cdot m^{-3}$)
σ_{ref}	= cavitation number

Subscripts

ext	= external liquid flow
l	= liquid
ref	= reference section
vap	= vapor

References

- [1] Laberteaux, K. R., and Ceccio, S. L., 1998, “Flow in the Closure Region of Closed Partial Attached Cavitation,” *Proceedings of the Third International Symposium on Cavitation*, J. M. Michel and H. Kato, eds., Grenoble, France, **1**, pp. 197–202.
- [2] Merle, L., 1994, “Etude Experimentale et modèle Physique d'un écoulement Cavitant Avec Effect Thermodynamique,” Doctoral thesis, Institut National Polytechnique de Grenoble.
- [3] Le, Q., Franc, J. P., and Michel, J. M., 1993, “Partial Cavities: Global Behavior and Mean Pressure Distribution,” *ASME J. Fluids Eng.*, **115**, pp. 243–248.
- [4] Kamono, H., Kato, H., Yamaguchi, H., and Miyanaga, M., 1993, “Simulation of Cavity Flow by Ventilated Cavitation on a Foil Section,” *ASME, New York*, ASME-FED-153, pp. 183–189.
- [5] Ceccio, S. L., and Brennen, C. E., 1991, “Observations of the Dynamics and Acoustics of Travelling Bubble Cavitation,” *J. Fluid Mech.*, **233**, pp. 633–660.
- [6] Callenaere, M., 1999, “Etude des poches de Cavitation Partielle en écoulement Interne,” Doctoral thesis, Institut National Polytechnique de Grenoble.
- [7] Stutz, B., and Reboud, J. L., 1997, “Experiment on Unsteady Cavitation,” *Exp. Fluids*, **22**, pp. 191–198.
- [8] Serisawa, A., Kataoka, I., Michivik, M., and Park, S. H., 1975, “Turbulence Structure of Air-Water Bubbly Flow—Measuring Techniques,” *Int. J. Multiphase Flow*, **2**, pp. 221–233.
- [9] Galaup, J. P., 1975, “Contribution à l'Etude des Méthodes de Mesure des Ecoulements Diphasiques,” Doctoral thesis, Institut National Polytechnique de Grenoble.
- [10] Stutz, B., and Reboud, J. L., 1997, “Two Phase Flow Structure of Sheet Cavitation,” *Phys. Fluids*, **9**, pp. 3678–3686.
- [11] Stutz, B., and Reboud, J. L., 2000, “Measurements Within Unsteady Cavitation,” *Exp. Fluids*, **29**, pp. 545–552.
- [12] Lush, P. A., and Skipp, S. R., 1986, “High Speed Cine Observations of Cavitating Flow in a Duct,” *Int. J. Heat Fluid Flow*, **7**, pp. 283–290.
- [13] de Lange, D. F., de Bruin, G. J., and van Wijngaarden L., 1994, “On the Mechanism of Cloud Cavitation—Experiment and Modelling,” *Proceedings of the Second International Symposium on Cavitation*, H. Kato, ed., Tokyo, Japan, pp. 45–49.
- [14] Revankar, S. T., and Ishii, M., 1992, “Local Interfacial Area Measurement in Bubbly Flow,” *Int. J. Heat Mass Transfer*, **35**, pp. 913–925.
- [15] Van der Well, R., 1985, “Void Fraction, Bubble Velocity and Bubble Size in Two-Phase Flow,” *Int. J. Multiphase Flow*, **11**, pp. 317–345.
- [16] Kawanami, Y., Kato, H., Yamaguchi, H., Tayaga, Y., and Tanimura, M., 1997, “Mechanism and Control of Cloud Cavitation,” *ASME J. Fluids Eng.*, **119**, pp. 788–794.
- [17] Fruman, D., Reboud, J. L., and Stutz, B., 1999, “Estimation of Thermal Effects in Cavitation of Thermosensible Liquids,” *Int. J. Mass Transfer*, **42**, pp. 3195–3204.

An Evaluation of a Two-Fluid Eulerian-Liquid Eulerian-Gas Model for Diesel Sprays

Venkatraman Iyer¹
Graduate Research Assistant

John Abraham²
Professor
e-mail: jabraham@ecn.purdue.edu

Maurice J. Zucrow Laboratories,
School of Mechanical Engineering,
Purdue University,
West Lafayette, IN 47907-2014

A two fluid Eulerian-liquid Eulerian-gas (ELEG) model for diesel sprays is developed. It is employed to carry out computations for diesel sprays under a wide range of ambient and injection conditions. Computed and measured results are compared to assess the accuracy of the model in the far field, i.e., at axial distances greater than 300 orifice diameters, and in the near field, i.e., at axial distances less than 100 orifice diameters. In the far field, the comparisons are of drop mean velocities and drop fluctuation velocities and in the near field they are of entrainment velocities and entrainment constants. Adequate agreement is obtained quantitatively, within 30 percent, and qualitatively as parameters are changed. Unlike in traditional Lagrangian-drop Eulerian-fluid (LDEF) approaches that are employed for diesel spray computations, adequate resolution can be employed in the near field to achieve numerical grid independence when the two-fluid model is employed. A major source of uncertainty in the near field is in the modeling of liquid jet breakup and atomization. [DOI: 10.1115/1.1593708]

Introduction

The numerical modeling of diesel sprays is a challenging problem because of the wide range of spatial and temporal scales associated with the physics of the sprays. An approach that is widely employed is the Lagrangian-drop Eulerian-fluid (LDEF) approach originally proposed by Duckowicz [1] and implemented for spray computations by O'Rourke and Bracco [2]. In the LDEF approach, the droplets which are formed through the atomization process of the liquid jet are tracked in a Lagrangian frame of reference through Monte-Carlo methods whereas the gas phase is described in an Eulerian frame of reference. Momentum, mass, and energy equations are solved for each drop and collisions and secondary breakup are modeled. The LDEF approach is, in principle, valid only for dilute sprays when the local gas void fraction is greater than 99 percent. This criterion is not satisfied in the region close to the injector orifice in the case of diesel sprays, i.e., within about 50 orifice diameters, where the presence of an intact liquid core and the dense spray regime results in relatively small gas void fractions. Hence, relatively large computational grid sizes are employed near the orifice to enforce the criterion. It has been shown that these grids are inadequate to resolve the flowfield in the near-nozzle region. This may give rise to unphysical results, [3–6]. Hence, alternate approaches have to be pursued.

In this work, we present an evaluation of a two-fluid Eulerian-liquid Eulerian-gas (ELEG) model, that we have developed for sprays, by comparing measured and computed mean drop velocities, drop fluctuation velocities, and entrainment characteristics. The numerical limitations highlighted above are minimized with the ELEG approach. Prior applications of the model, with a locally homogeneous flow assumption, have focused on computing liquid penetrations [7,8]. The detailed derivations of the two-fluid modeling equations are given in several references [9–12]. In the following section, the model is briefly discussed. In the section that follows, details of the measurements will be given. The computational conditions will then be discussed. Results and discussions follow. The paper closes with summary and conclusions.

¹Current address: GE Global Research Center, Niskayana, NY 12309.

²To whom correspondence should be addressed.

Contributed by the Fluids Engineering Division for publication in the JOURNAL OF FLUIDS ENGINEERING. Manuscript received by the Fluids Engineering Division October 16, 2001; revised manuscript received January 22, 2003. Associate Editor: E. W. Graf.

The Eulerian-Liquid Eulerian-Gas (ELEG) Two-Fluid Model

The essential idea of ELEG modeling of sprays is to solve continuum Eulerian equations for the liquid and gas phases. The formulation involves averaging the local and instantaneous equations for each phase. Eulerian ensemble averaging is used where the independent variables are the spatial coordinate, \mathbf{X} , and time, t . Comprehensive reviews of the subject are given by several authors, [9–11]. Reference [12] gives the detailed derivation of the specific equations employed in this work.

The ensemble-averaged conservation of mass equation for phase k is written as

$$\frac{\partial \alpha_k \rho_k}{\partial t} + \nabla \cdot (\alpha_k \rho_k \mathbf{U}_k) = \Gamma_k \quad (1)$$

where α_k is the volume fraction of phase k , ρ_k is the density of phase k , and \mathbf{U}_k its velocity. Γ_k is a source term due to phase change.

The ensemble-averaged momentum equation for phase k is written as

$$\frac{\partial \alpha_k \rho_k \mathbf{U}_k}{\partial t} + \nabla \cdot (\alpha_k \rho_k \mathbf{U}_k \mathbf{U}_k) = -\alpha_k \nabla P_k + \nabla \cdot \alpha_k (\underline{\underline{\tau}}_k + \underline{\underline{\tau}}_k^d) + \Gamma_k \mathbf{U}_{k,i} + (P_{k,i} - P_k) \nabla \alpha_k + \mathbf{M}_k^d \quad (2)$$

\mathbf{M}_k^d represents the transfer of momentum from one phase to the other due to forces at the interface. It includes the forces of drag, virtual mass, Saffman lift, Basset and Magnus forces [11]. P_k is the average pressure of phase k and $P_{k,i}$ is the average interfacial pressure. $\mathbf{U}_{k,i}$ is the average interfacial velocity. In this work we have considered only the drag force. The virtual mass force is brought about by transient effects when the drop is accelerated through the carrier fluid. This effect is important only if the density of the carrier fluid is greater than the density of the particle such as in bubbly flows. For diesel sprays the droplet density is about 30 times more than the gas density so the virtual mass effect is not significant. The Basset force accounts for the delay in the boundary layer development as the relative velocity changes with time. This effect may be important near the orifice where the droplets are accelerating the surrounding gas, but evaluation of this force is computationally very intensive because it involves integration over all previous times. Moreover this force is an un-

steady one and not relevant for steady sprays. It may affect the transient evolution and may be an interesting study for future research. The Saffman lift and Magnus forces depend on drop spin. The drop spin in diesel sprays is not known with any degree of certainty.

When the drag force alone is considered, the ensemble-averaged expression for the momentum transfer term is

$$\mathbf{M}_g^d = C_f \{ \alpha_l \alpha_g (\mathbf{U}_l - \mathbf{U}_g) - (\alpha_l \eta_l + \alpha_g \eta_g) \nabla \alpha_g \} \quad (2a)$$

where the coefficient, C_f , is given by

$$C_f = \frac{3\rho_g |U_r| C_D}{d_p}$$

$$C_D = \frac{24}{\text{Re}_d} (1 + 0.15 \text{Re}_d^{0.687})$$

η_l and η_g are the turbulent diffusivities of the liquid and the gas, respectively. U_r is the relative velocity between the two phases. d_p is the drop diameter. We have assumed $\eta_l = \eta_g$. The turbulent diffusion of the drop may differ from the turbulent diffusion of the gas when the relative velocity between the drop and the gas is comparable to the turbulent kinetic energy of the gas, [13,14]. For diesel spray with drop diameters of the order of 20 microns, the ratio of the drop response time to the characteristic gas flow time, i.e., the Stokes number, is very small so the drop essentially follow the gas flow field. The relative velocity is small in this case. The drop sizes are smaller than the Kolmogorov length scales that are of the order of 100 microns for the flows considered here. So the drops remain within the turbulent eddies and are transported by them. So the liquid turbulent diffusivities are not expected to be very different from the gas diffusivities. η_g is obtained from the k - ε turbulence model. This correlation for C_d is valid for $1 < \text{Re}_d < 1000$. This condition on Re_d is satisfied in the spray except near the injector orifice. The sum of the momentum transfer in the gas and the liquid is zero. So $\mathbf{M}_g^d + \mathbf{M}_l^d = 0$.

Following Ref. [9], the ensemble-averaged energy equation is written as

$$\frac{\partial \alpha_k \rho_k E_k}{\partial t} + \nabla \cdot (\alpha_k \rho_k E_k \mathbf{U}_k) = -\nabla \cdot (\alpha_k \rho_k \mathbf{U}_k P_k) - \nabla \cdot (\mathbf{q}_k + \mathbf{q}_k^t) + \nabla \cdot \{ \alpha_k (\underline{\tau}_k + \underline{\tau}_k^t) \cdot \mathbf{U}_k \} + Q_k \quad (3)$$

where E_k , \mathbf{q}_k , and Q_k are the specific energy (internal + kinetic) of phase k , is the molecular heat flux of phase k , and the interfacial energy transfer to phase k , respectively.

In the case of multicomponent flows, where both the phases can consist of different components moving with the phase velocity, conservation equations are needed to solve for the mass fractions of all the components/species within each phase. The ensemble-averaged equation for conservation of species j within phase k can be formulated analogous to single phase species conservation equations, [15]. The equation is written as

$$\frac{\partial \alpha_k \rho_k Y_{k,j}}{\partial t} + \nabla \cdot (\alpha_k \rho_k \mathbf{U}_k Y_{k,j}) = \nabla \cdot (\alpha_k \eta_{k,j} \nabla Y_{k,j}) + \Gamma_{k,j} \quad (4)$$

where $Y_{k,j}$ is the mass fraction of species j in phase k and $\eta_{k,j}$ is the diffusivity of species j in phase k . In an ensemble-averaged formulation of the equation for diesel sprays, only the turbulent diffusivity is important in which case the diffusivities of all the species within a phase can be considered equal.

The k - ε model is employed to represent turbulence. The k - ε model is reasonable for modeling gas-phase turbulence in shear layers as encountered in jets and mixing layers. Turbulence in diesel sprays is primarily produced in the shear layer of the jet, so this model is widely employed for sprays. The k - ε model solves for the turbulent kinetic energy, k_g , of the gas-phase and the dissipation rate of the gas-phase turbulent kinetic energy, ε_g , with the transport equations given below.

$$\frac{\partial \alpha_g \rho_g k_g}{\partial t} + \nabla \cdot (\alpha_g \rho_g k_g \mathbf{U}_g) = \nabla \cdot \left(\frac{\alpha_g \rho_g \nu_g'}{\text{Pr}_k} \nabla k_g \right) + \alpha_g (G - \rho_g \varepsilon_g) + S_k \quad (5)$$

$$\frac{\partial \alpha_g \rho_g \varepsilon_g}{\partial t} + \nabla \cdot (\alpha_g \rho_g \varepsilon_g \mathbf{U}_g) = \nabla \cdot \left(\frac{\alpha_g \rho_g \nu_g'}{\text{Pr}_\varepsilon} \nabla \varepsilon_g \right) + \alpha_g \frac{\varepsilon_g}{k_g} (C_1 G - C_2 \rho_g \varepsilon_g) + S_\varepsilon \quad (6)$$

The production term, G , is related to the mean velocity field of the gas-phase by the relation: $G = \underline{\tau}_g' : \nabla \mathbf{U}_g$. Also, $\nu_g' = C_\mu k_g^2 / \varepsilon_g$. Standard model constants are employed for C_1 , C_2 , C_μ , Pr_k , and Pr_ε , [16,17]. S_k and S_ε are terms that represent turbulence modulation. In our work, the contributions of these terms are neglected. The effect of drops in a dilute spray is to induce an extra dissipation of turbulent kinetic energy in the gas due to the acceleration/deceleration of the drops. This is important only if the drops are large enough that their response time to changes in the gas flow is large. For diesel sprays where the drop diameters are of the order of 20 microns, this effect may not be significant. The effect of drops may be significant in the near injector region where the spray is dense. However, there are no good models to account for back effect of drops in a dense spray.

We have discussed, in prior publications, [7,8], two models for vaporization of the liquid phase. The first model, which we refer to as the equilibrium vaporization model, is developed for a locally homogeneous flow (LHF) where the entire mixture of liquid and gas is assumed to behave as a single fluid, i.e., the spray is treated as a single-phase multicomponent flow with the liquid fuel, vapor fuel, and the ambient air as the individual components, [8]. State relationships are employed to determine the fraction of liquid vapor and air for a given set of thermodynamic conditions. Phase equilibrium between liquid and vapor is assumed. In the second model, that we refer to as the nonequilibrium vaporization model, the conservation of mass equation, Eq. (1), is solved for each phase. The vaporization source term Γ_k is obtained by assuming a D^2 -law for droplet vaporization in each computational cell. Reference [7] may be consulted for a complete description.

An equation for the surface area concentration has been derived and employed in the work to capture the variation in drop sizes due to vaporization, break-up and coalescence. According to Ishii [9], the interface is convected with the interface velocity. In the case of dispersed two-phase flows, the interface velocity is approximately equal to the dispersed phase velocity. So we formulate a transport equation for the surface area concentration on the assumption that it is convected with the mass-averaged liquid-phase velocity, \mathbf{U}_l :

$$\frac{\partial L_s}{\partial t} + \nabla \cdot (\mathbf{U}_l L_s) = \phi_v + \phi_b + \phi_c \quad (7)$$

where L_s is the surface area concentration. ϕ_v , ϕ_b , and ϕ_c are the source terms due to vaporization, atomization, and drop breakup and coalescence, respectively.

To model atomization, we employ the blob-atomization model of Reitz [18] in which liquid blobs are injected with a radius equal to the orifice radius and the Kelvin-Helmholtz instability then leads to the breakup of the blobs. The breakup model postulates that a parent blob of radius, r_p , breaks to form new stable droplets of radii r_c where $r_c = B_0 \Lambda$, where Λ represents the wavelength of the fastest growing wave. The constant B_0 is given a value of 0.61 as suggested by Reitz [18] and Beale and Reitz [19]. The breakup occurs in a characteristic time that is inversely proportional to the growth rate of the fastest growing wave, Ω . According to Reitz [18], the breakup time τ_b is given by

$$\tau_b = \frac{3.726 B_1 r_p}{\Omega \Lambda} \quad (8)$$

where the constant B_1 has been given values ranging from 10 to 60 in comparisons of computed and measured results, [18,19]. For practical purposes the constant B_1 is considered as a model constant that should be calibrated for a given set of conditions. The rate of decrease of the drop radius is given by the following empirical relation:

$$\frac{dr_p}{dt} = -\frac{r_p - r_c}{\tau_b} \text{ for } r_c < r_p, \quad \text{or } = 0 \text{ for } r_c \geq r_p. \quad (9)$$

In the two-fluid model, the breakup model is implemented by deriving an expression for the rate of increase of the surface area concentration due to the breakup of the drops. This is done as follows. The surface area concentration is related to the local Sauter mean radius of the drop by $L_s = 3\alpha_l/r_p$. The differentiation of this expression with respect to time, keeping the volume fraction of the liquid constant during the breakup process and substitution of Eq. (9) for the rate of breakup yields the following expression:

$$\phi_b = L_s \frac{1 - r_c/r_p}{\tau_b}. \quad (10)$$

During the implementation of the blob model, the value of the orifice radius, a , is initially set equal to the local Sauter mean radius of the droplets, r_p , at the injector orifice.

We have developed a methodology to model the outcome of collisions between drops within the context of ELEG modeling. Collisions between drops can change the surface area concentration and subsequently the interface transport rates of mass, momentum, and energy. Collisions can be important in the dense spray regime since the frequency of collisions is proportional to the number density of the drops. According to the kinetic theory for granular flow, [2,20], the frequency of collisions between two classes of drops, denoted by a and b , is given by

$$\nu_{ab} = (N/V)_a(N/V)_b \pi(r_a + r_b)^2 |U_{ab}| \quad (11)$$

where $(N/V)_a$ and $(N/V)_b$ are the number density of droplets, r_a and r_b are the radii of the droplets in classes a and b , respectively, and $|U_{ab}|$ is the relative velocity between the two drop classes. In the two-fluid model, we solve for the local Sauter mean radius of the drops, r_p , and we assume the classes a and b to be identical, each having drops of radius r_p . We then obtain the mean collisional frequency density, ν_{coll} as

$$\nu_{\text{coll}} = (N/V)^2 \pi 4 r_p^2 |U'| \quad (12)$$

where we have approximated the relative velocity between the droplets with the average fluctuating velocity of the droplets, $|U'|$. The outcome of a collision is determined by the probability of coalescence, η_c , once a collision has occurred. The probability, η_c , is obtained from the physical criterion that the colliding drops separate if the rotational energy of the coalesced drop pair exceeds the surface energy required to reform the original drops from the coalesced pair. The expression for η_c as given by O'Rourke [21] is

$$\eta_c = \min(2.4g(\xi)/We_{c,l}, 1) \quad (13)$$

where ξ is the drop size ratio r_b/r_a which is equal to 1 in our model. $g(1) = 1.3$. $We_{c,l}$ is the collisional Weber number given by $We_{c,l} = \rho_l U'^2 r_p / \sigma_l$, where σ_l is the surface tension coefficient. Each coalescence event decreases the local number of droplets by 1. So the rate of decrease due to coalescence can be expressed as

$$d(N/V)/dt = -\eta_c \nu_{\text{coll}}. \quad (14)$$

The rate of decrease of surface area concentration due to coalescence is obtained from Eq. (14) by relating the surface area concentration to the number density. Eliminating the drop diameter, the following relation may be obtained for the surface area concentration [12]:

$$L_s^{3/2} = 3 \sqrt{4\pi\alpha_l(N/V)^{1/2}}. \quad (15)$$

Differentiating Eq. (15) keeping the volume fraction of the liquid constant during coalescence, the following expression may be obtained for the rate of change of surface area concentration due to coalescence.

$$\phi_c = (dL_s/dt)_{\text{coalescence}} = -\eta_c L_s^2 |U'|/12. \quad (16)$$

In deriving Eq. (16), the rate expression given by Eq. (14) is used along with the expression for the collisional frequency given by Eq. (12). The value of the average fluctuation in the drop velocity is assumed to be proportional to the RMS of the liquid velocity fluctuations, $U_{\text{rms}} = \sqrt{2k_l/3}$, where k_l is the turbulent kinetic energy of the liquid phase. A constant of proportionality is introduced to allow for the uncertainties in the droplet velocity distributions. Thus we obtain

$$|U'| = C_{\text{coll}} \sqrt{2k_l/3}. \quad (17)$$

The ratio of the liquid turbulence to gas turbulence in a spray depends on the density ratio and the response time of the drop. In this work, we have assumed the liquid turbulence to be equal to the gas turbulence which is generally true except very close to the orifice, [12]. The constant C_{coll} is treated as a model constant in this work that can be changed to study the effect of collisions and coalescence on the spray behavior. We have employed values for C_{coll} so that the effect of collisions are relatively small. Iyer [12] presents a detailed evaluation of the effects of collisions.

The equations given above for the ELEG model are supplemented by equations for thermal and caloric equations of state.

A finite volume numerical method based on staggered grid and donor-cell convective fluxes is employed to solve the equations above. The method follows the semi-implicit formulation of Patankar and Spalding [22], Liles and Reed [23], and Magi [24]. In this method, the pressure, the momenta, and the energy are used as primary dependent variables. A Poisson-type equation is formulated for the pressure by manipulating the continuity and the momentum equations with the constraint of the equation of state. This scheme is well suited to low Mach number flows because of the weak linkage between the pressure and the density, [22,24]. Staggered grid is employed for the vector quantities with respect to the scalar quantities. The staggering avoids decoupling of the pressure and velocity fields, [25]. The pressure based numerical scheme employed in this work is accurate for Mach numbers less than 0.3. It can be used for higher Mach numbers except that it cannot capture the propagation of shock waves. The Mach numbers for the flows used in this work may be high, very close to the orifice, but they decrease rapidly as the jet expands and diffuses out. The Mach numbers are within the range of applicability of the numerical scheme beyond about 10–20 orifice diameters downstream of the orifice.

Measurement Details

In this work, comparisons of computed and measured results will be presented for two sets of measurements. One set of measurements focuses on the far field of sprays (i.e., $x/d > 300$) whereas the second set focuses on entrainment characteristics in the near field (i.e., $x/d < 100$) where x is the axial distance and d is the orifice diameter.

Measurements of axial and radial drop velocities in steady sprays were made by Wu et al. [26]. The fuel, n-hexane, was injected into quiescent nitrogen at room temperature but at high pressures such that the ratio of the gas density to the injected liquid density is similar to that in a diesel engine cylinder at top dead center, i.e., at the end of compression. The conditions in the measurements are shown in Table 1. The spray was injected into a constant volume chamber of 19 cm internal diameter and length of 90 cm. For more details on the measurement technique and the laser-Doppler velocimetry (LDV) optics employed, the reader is referred to the experimental paper, [26]. The data was taken in a time window between 0.5–1.0 s after start of injection (ASI). The authors of the experimental paper state that steady state is reached

Table 1 Conditions for velocity measurements in diesel sprays, [26]. Fuel: n-hexane, $\rho_l=665 \text{ kg/m}^3$, $\mu_l=3.2 \times 10^{-4} \text{ N}\cdot\text{s/m}^2$, $\sigma_l=1.84 \times 10^{-2} \text{ N/m}$, $d=127 \text{ microns}$

Case	P (MPa)	ρ_a (kg/m^3)	U_{inj} (m/s)
A	4.24	48.68	127
B	1.48	17.024	127
C	4.24	48.68	194

well before 1.0 s due to the high velocity and small sizes of the drops. The characteristic time for steady state as reported by Wu et al. [26] is about 0.03 s. Statistics of the mean axial velocity and the mean fluctuations in the axial drop velocities were obtained from the instantaneous LDV measurements. The estimated error in the mean axial velocity was reported to be less than 2 percent and the error in the fluctuation amplitude was reported to be less than 3 percent. The statistics of the radial component of the drop velocities were not reported due to a large error. The measurements of the mean and fluctuating axial velocities were reported at axial stations of $x/d=300, 400, 500, 600,$ and 800 downstream of the orifice.

We will also present comparisons of computed and measured entrainment velocities and constants in sprays. The measurements are those of Cossali et al. [27] and Andriani et al. [28]. They studied air entrainment in a transient diesel spray using LDV to measure gas velocities. Their focus was to study the effect of gas density and temperature. The spray was injected into a confined quiescent environment and the entrainment flow rate was evaluated by measuring the air velocity component normal to a cylindrical geometric surface surrounding the spray. The injection conditions in the measurements are summarized in Table 2. The closed cylindrical chamber had an internal diameter of 206 mm, with injection along the axis of the cylinder. The duration of injection was measured using laser beam obscuration and was measured as 3.3 ms. The average mass of fuel injected was obtained as 0.0306 g per injection. Cossali et al. [27] estimated the injected mass flow rate as a function of time from the total mass injected, the injection duration, and the measured injection pressure history. Figure 1 shows the estimated injected mass flow rate as a function of time during the period of injection. The average injection velocity obtained from the total mass injected and the injection duration is 230 m/s as given in Table 2.

The injection conditions are kept constant for all the measured cases. Five different measured ambient conditions were considered in the work of Cossali et al. [27] and are given in Table 3. Each case given in Table 3 has a different combination of ambient temperature and density. The ambient temperatures were varied from 298 K to 473 K and the ambient densities were varied from 1.17 kg/m^3 to 7.02 kg/m^3 . The objective of choosing the conditions given in Table 3 is to study the independent effects of ambient temperature and ambient density on the entrainment characteristics. For example, Cases 1, 3, and 4 have the same ambient temperature of 298 K but different ambient densities. Cases 4 and 5 have the same ambient density but different ambient temperatures. The maximum uncertainties in the measured temperatures as stated by Cossali et al. [27] are $\pm 5 \text{ K}$ and the uncertainties in the density are $\pm 1.5 \text{ kg/m}^3$.

Table 2 Injection conditions for entrainment measurements, [27,28]

Orifice diameter, d	0.25 mm
Injected mass	0.306 g
Injection duration	3.3 ms
Density of injected fuel ρ_l	820 kg/m^3
Average injection velocity U_{inj}	230 m/s

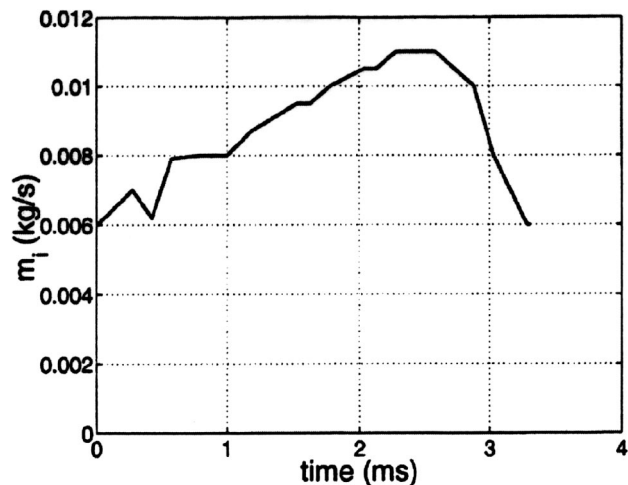


Fig. 1 Injected mass flow rate versus time. Measurements of Cossali et al. [27].

Computational Conditions

The comparisons with the measurements of Wu et al. [26] are performed in an axisymmetric chamber of length 20 cm and diameter 10 cm. The farthest axial location in the measurements was $x/d=800$ which corresponds to an axial distance of about 10 cm. From our prior work, we know that keeping the length of the domain at 20 cm is sufficient to ensure that the far downstream boundary conditions do not affect the computed values up to a downstream axial distance of 10 cm. The diameter of the computational chamber was kept to be 10 cm, though the diameter of the chamber in the measurements was 19 cm. However, it was found that the radial spread of the spray was less than 2.5 cm even at the farthest downstream location for which comparisons were made. Also, from prior work, a diameter of 10 cm has been shown to be sufficient to minimize the effect of the side walls on the spray, [7]. The computational grid is shown in Fig. 2. The axial grid resolution is uniform with $\Delta x=0.1 \text{ cm}$. There is a stretching of the grid in the radial direction with two cells in the orifice radius. The radial grid size is 0.003 cm at the centerline and is stretched to a maximum of about 0.3 cm beyond a radius of about 3 cm from the centerline. The total number of grid cells in the radial direction is 56.

The conditions in the computations are identical to the measured conditions that are shown in Table 1. The properties of n-hexane are used for the liquid fuel and nitrogen is used as the ambient. The initial ambient temperature is 300 K. The equilibrium vaporization model is employed because vaporization is not significant in these sprays. The blob atomization model is employed with the constant $B_1=20$. Computations were also performed with $B_1=10$, but the computed liquid velocity and the turbulent kinetic energy values did not show a noticeable change for axial locations greater than 300 orifice diameters. Compari-

Table 3 Ambient conditions for entrainment measurements, [27,28]

Case	Temperature (K)	Density kg/m^3
1	298	7.02
2	413	5.06
3	298	1.17
4	298	5.06
5	473	5.06

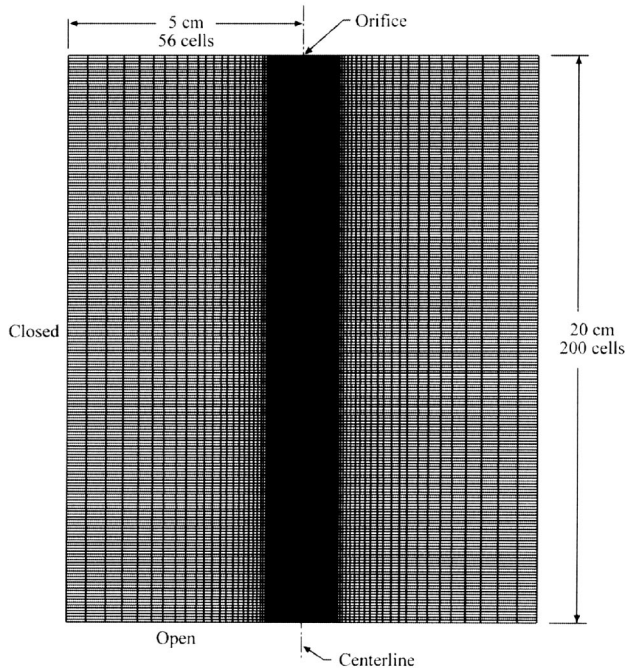


Fig. 2 Computational grid. Parameters indicated are for comparisons with measurements of Wu et al. [26].

sions are made of the mean liquid axial velocity profiles and the turbulent kinetic energy profiles. The turbulent kinetic energy is related to the amplitude of the fluctuating velocity that is measured.

In the case of the comparisons with the measurements of Cosali et al. [27], computations are performed in a closed axisymmetric chamber with a chamber radius of 10.3 cm as was the case in the measurements. The chamber length was taken as 24 cm. This length was sufficient to avoid spray impingement on the far wall during the injection period. The structure of the computational grid is similar to the one shown in Fig. 2. The number of cells in the radial direction is 86 with four cells inside the orifice radius that gives a minimum grid size of 3.125×10^{-3} cm inside the orifice. The grid in the radial direction is stretched as shown in Fig. 2 to a maximum radial size of 0.4 cm beyond a radius of 4 cm from the centerline. This grid will be referred to as the lower resolution grid. A finer grid referred to as the higher resolution grid is also employed. The higher resolution grid has eight cells in the orifice radius and a total of 130 cells in the radial direction. Both the resolutions have a uniform axial grid size of 0.1 cm.

The orifice diameter, the total mass injected and the injection duration in the computations are identical to those in the measurements. A constant injection velocity equal to the average injection velocity of 230 m/s as given in Table 2 is used in several of the computations. A computation is also performed with the injection rate as shown in Fig. 1. The ambient conditions corresponding to the five cases given in Table 3 are used in the computations. Tetradecane is used as the injected fuel to represent diesel fuel. The density of the fuel is taken as 820 kg/m^3 as given in the measurements. The surface tension and viscosity of the liquid required in the core breakup model are $1.4 \times 10^{-2} \text{ N/m}$ and $3.5 \times 10^{-5} \text{ N}\cdot\text{s/m}^2$, respectively, values typical for tetradecane at room temperature. Vaporization is predicted using the equilibrium vaporization model.

Results and Discussions

Results in the Far Field (i.e., $x/d > 300$). We now compare the computed steady axial liquid velocities with the measurements

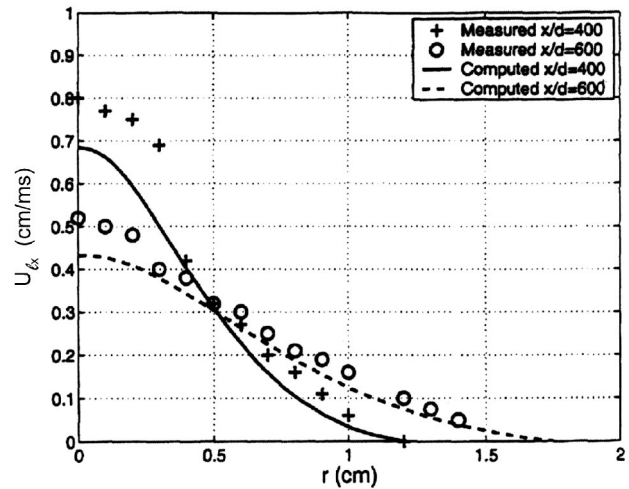


Fig. 3 Axial velocity versus radial distance: comparisons with measurements: Case A

of Wu et al. [26]. Figure 3 shows the computed and measured steady axial liquid velocity as a function of the radial distance from the centerline at axial locations of $x/d=400$ and 600 for Case A. The computed and the measured velocities are maximum at the centerline and decrease with increase in the radial distance. The computations appear to underpredict the axial velocities near the centerline by about 20 percent at both the axial locations. Beyond a radial distance of 0.5 cm the computed and measured values agree within 10 percent. The computed and measured radial spread of the axial velocity profile appear to show reasonable agreement at both the axial locations. Figure 4 shows the computed and measured steady axial liquid velocity as a function of the radial distance for Case B. In Case B, the ambient density is lower than that in Case A, the other conditions remaining the same. Figure 4 shows that the axial liquid velocities near the centerline ($r=0$) are greater than those for Case A at the same axial locations in both measurements and computations. This is expected since the spray penetrates more when the ambient density is lower and so the centerline liquid velocities are greater at the same axial location. The computed axial liquid velocities for Case B are higher than the measured values by about 20–30 percent near the centerline. The agreement between the computed and the measured values are better beyond a radius of 0.5 cm.

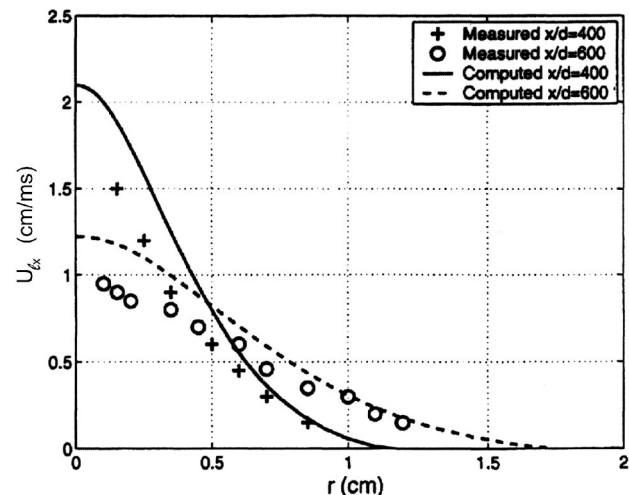


Fig. 4 Axial liquid velocity versus radial distance: comparisons with measurements: Case B

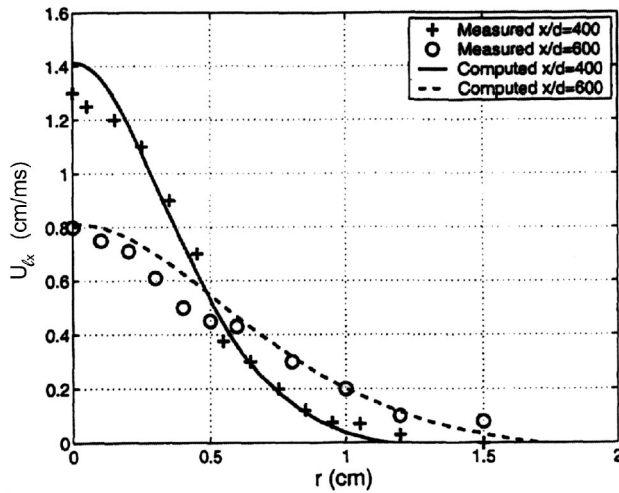


Fig. 5 Axial liquid velocity versus radial distance: comparisons with measurements: Case C

Figure 5 shows the computed and measured steady axial liquid velocity as a function of radial distance for Case C. The injection velocity in Case C is greater than in Case A. So the axial liquid velocities near the centerline are greater for Case C as compared to Case A as shown in Fig. 5. The agreement between the computed and the measured values is within 15 percent for Case C for both the axial locations ($x/d=400$ and 600) considered.

Overall, there is reasonable agreement between the computed and the measured velocity profiles for the three cases considered. The maximum discrepancies are of the order of 20–30 percent that can be attributed to a combination of uncertainties in the measurements and the interface transport models, especially the momentum transfer model that is the most relevant for the non-vaporizing sprays considered in this study. Indeed the higher injection velocity case, Case C, shows the closest agreement between the computed and the measured velocities since the momentum transfer rates are faster at higher velocities and so the flow field is close to that in a homogenous flow where the degree of uncertainty is less. This is significant as the injection velocities in diesel sprays which are of the order of 200–400 m/s are closer to the conditions in Case C than in Cases A and B. So the comparisons presented in this section imply that the model shows better agreement with measurements when conditions are closer to those in diesel engines.

We now compare the computed steady turbulent kinetic energy of the liquid with the measurements of Wu et al. [26]. It should be noted that the assumption is made that the turbulent kinetic energy of the liquid is same as that of the gas as equations for the mixture turbulence are solved. The measurements were made of the RMS of the liquid axial velocity fluctuations, $\sqrt{U_x'^2}$. We assume isotropic turbulence and relate the measured RMS of the fluctuations to the turbulent kinetic energy of the liquid. The turbulent kinetic energy is then related to the RMS of the fluctuations by

$$k_l = \frac{3U_x'^2}{2} \quad (18)$$

The k_l so obtained from Eq. (18) is then treated as the measured liquid turbulent kinetic energy that is compared with the computed values. Figure 6 shows the computed and measured turbulent kinetic energy of the liquid as a function of the radial distance from the centerline for Case A for axial locations of $x/d=400$ and 600 . For each axial location, the turbulent kinetic energy is normalized by the square of the centerline liquid axial velocity, $U_{\xi 0}^2$, at that location and is plotted against the radial distance normalized by the half-width of the jet, $r/r_{1/2}$, at that axial location. The half-

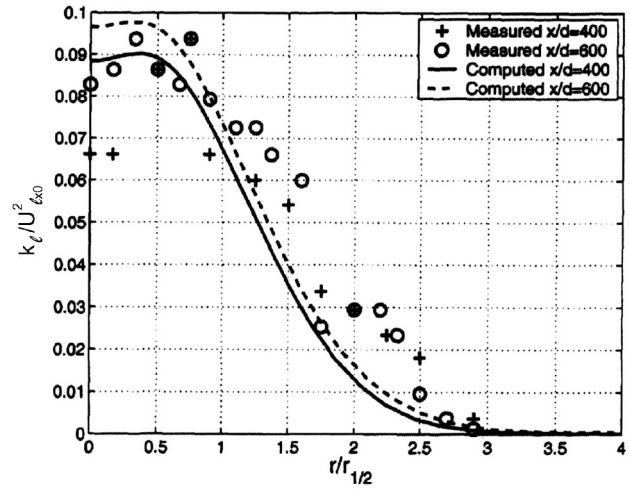


Fig. 6 Turbulent kinetic energy versus radial distance: comparisons with measurements: Case A

width at an axial location is defined as the radial distance from the centerline where the liquid velocity decreases to half its centerline value at the axial location. Figure 6 shows that the computed normalized turbulent kinetic energy reaches a maximum at a radial distance of about 0.5 half-widths from the centerline for both the axial locations. The measurements show a similar trend. This is because turbulence is generated in the region of large velocity gradients that are located radially away from the centerline. The computed values of the normalized turbulent kinetic energies at the two axial locations are within 15–20 percent of each other. This implies that the kinetic energy profiles are approximately self-similar. There is more scatter in the measured data near the centerline. The computed profiles agree quantitatively within 20 percent with the measured data beyond $r/r_{1/2}=1$. Nearer to the centerline ($r < r_{1/2}$) the computed values overpredict the measured data by about 40 percent at $x/d=400$ and by about 20 percent at $x/d=600$ indicating that the measured values reach a self-similar state at a greater axial distance. For radial distances beyond the half-width, the computed values appear to underpredict the measured data by about 20–30 percent.

Figures 7 and 8 show the normalized turbulent kinetic energy profiles for Cases B and C respectively at the axial locations of $x/d=400$ and 600 . There is an overall agreement in trend for both

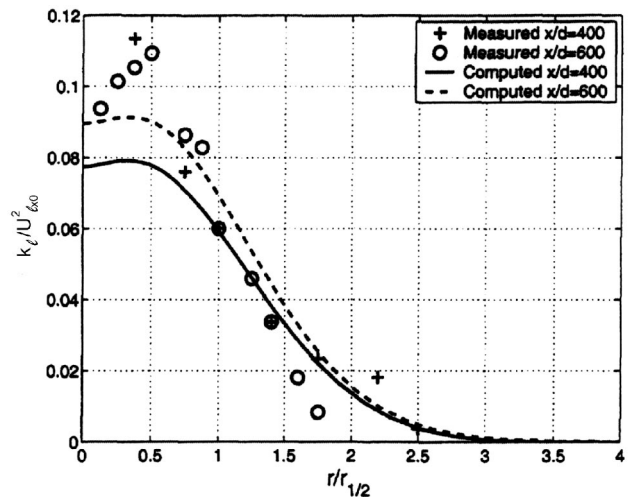


Fig. 7 Turbulent kinetic energy versus radial distance: comparisons with measurements: Case B

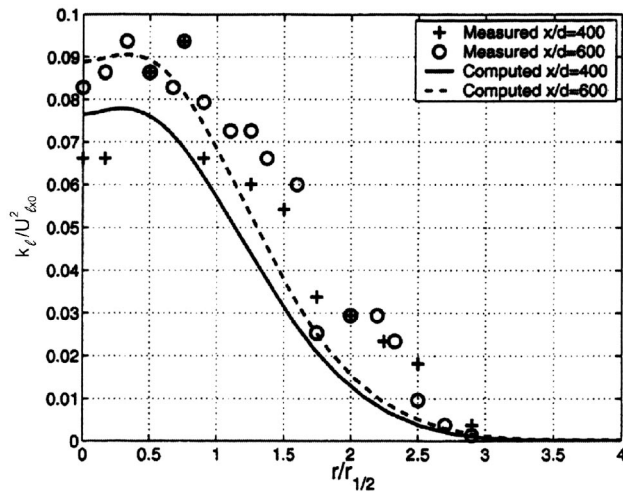


Fig. 8 Turbulent kinetic energy versus radial distance: comparisons with measurements: Case C

these cases as in Case A. The profiles are close to self-similar for both the cases because the values at the two axial locations do not differ by more than 20 percent. The differences in the computed values at the two axial locations are more near the centerline as is the case with the measurements. Overall there is reasonable agreement in trends between the computed and measured turbulent kinetic energy profiles for the three cases considered. The discrepancies in quantitative values can be attributed to the uncertainties in the measured data, to the assumption of isotropy in estimating the measured turbulent kinetic energy and to the assumption that the computed turbulent kinetic energy of the liquid is equal to that of the gas.

Results in the Near Field (i.e., $x/d < 100$)

Comparisons of Computed and Measured Entrainment Velocity. Details of the measurements of Cossali et al. [27] and Andriani et al. [28] have been given earlier. They measured the radial velocity of the gas at a radius of 10 mm from the centerline and defined that as the entrainment velocity, V_e . The radius of 10 mm was chosen as a compromise between the difficulties in measuring velocities too close to the centerline and the large relative errors in the radial velocities with increasing radial distance from the centerline. The entrainment velocity, V_e , can be expressed as

$$V_e = -V_{g,r}(x, r_s, t) \quad (19)$$

where the radius of the control surface, r_s , is 10 mm. $V_{g,r}(x, r_s, t)$ is the radial gas velocity at a surface located at radius r_s , at axial location x , and time t . The negative sign is used because entrainment velocity is considered positive if the gas velocity is directed radially inwards, i.e., towards the centerline of the spray. The computed entrainment velocity is defined in an identical manner.

Figure 9 shows the computed and measured entrainment velocity as a function of time for Case 1. The entrainment velocity is shown for three different axial locations $x = 22.5$ mm, $x = 32.5$ mm, and $x = 57.5$ mm. $B_1 = 10$ is employed in the atomization model. The figure shows that for the three axial locations the computed and the measured entrainment velocities start decreasing to negative values after an initial period of zero entrainment velocity. The decrease is associated with the passage of the head vortex of the jet where the gas tends to be pushed radially outwards by the incoming liquid jet. The velocity reaches a maximum negative value for all the axial locations shown and then starts increasing. The entrainment velocity then becomes positive, which implies that the head vortex has passed the axial location considered and the jet is now entraining the ambient gas at that

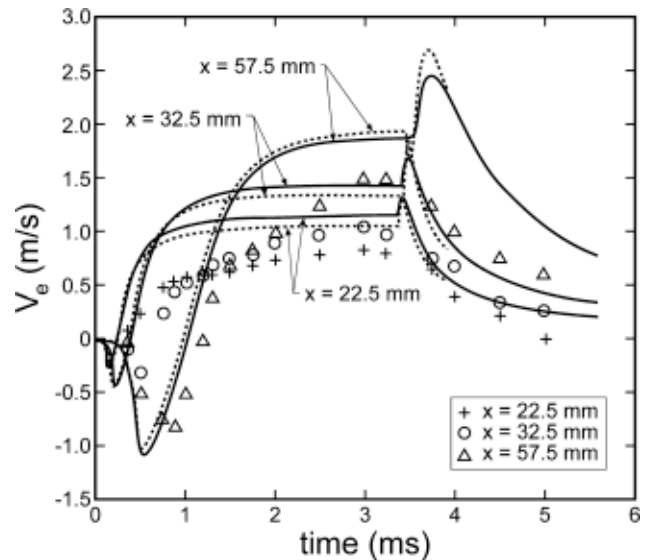


Fig. 9 Entrainment velocity versus time: computed ($B_1 = 10$) and measured: Case 1: +, \circ , Δ measured; — computed, lower resolution; --- computed, higher resolution

location. It appears from Fig. 9 that the computed maximum negative entrainment velocity increases with increase in axial location for the axial locations considered. This implies that the strength of the head vortex as measured by the velocity with which the gas is pushed out, increases as the vortex travels downstream from the orifice. A similar implication is made by other researchers, [28,29], that the size of the head vortex increases because of the quasi-steady jet that feeds it. Once the jet starts entraining, the velocity increases with time and reaches a steady value before the end of injection at 3.3 ms as shown by the computations in Fig. 9. The computed steady entrainment velocity increases with increase in axial location. The measurements and computed results show the same trend. The computed steady entrainment velocities appear to be greater than the measured values, with the computations overpredicting the steady entrainment velocity by about 30 percent at $x = 57.5$ mm. Figure 9 also shows the computed entrainment velocities as a function of time for the three axial locations when the higher grid resolution is employed. The computed velocities are almost identical for the two resolutions at $x = 57.5$ mm. The higher resolution appears to predict a lower steady entrainment velocity for $x = 22.5$ and $x = 32.5$ mm. However, the differences in the computed velocities are not more than 10–15 percent.

The quantitative discrepancies between the computed and the measured entrainment velocities shown in Fig. 9 may be attributed to the uncertainties in the computational models used for atomization and interface transport. One particular model where uncertainties are expected is the core breakup model. We now explore the sensitivity of the entrainment velocity to the model constant B_1 . Figure 10 shows the computed and measured entrainment velocities as a function of time for Case 1 at the three different axial locations with $B_1 = 20$. The variation of the computed V_e with time appears similar to that shown in Fig. 9 but agrees more closely with the measurements. The steady velocities at $x = 57.5$ mm and $x = 32.5$ mm appear to agree with the measurements within 15 percent and the steady velocity at $x = 22.5$ mm appears to agree within 20–25 percent. Subsequent results will be presented with $B_1 = 20$. The computed and the measured entrainment velocities shown in Figs. 9 and 10 decrease after the end of injection as expected. The computations show a sudden rise in velocities after the end of injection before the velocity decreases. This may be an unsteady effect due to the sudden stop of injection after a constant injection rate. To investigate this possibility we

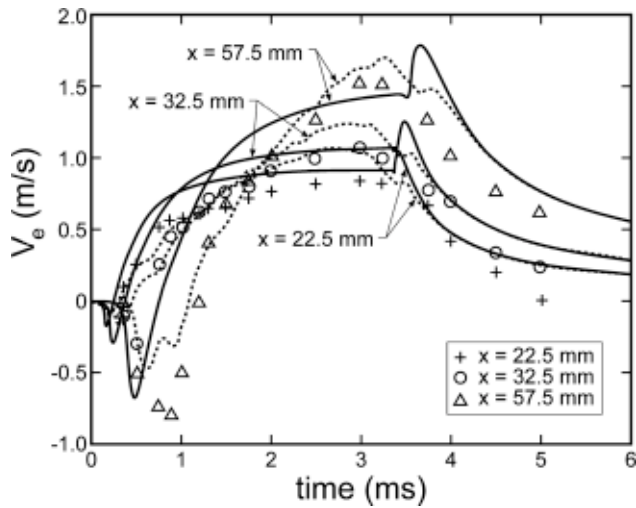


Fig. 10 Entrainment velocity versus time: computed with measured injection rate profile for Case 1: +, O, Δ measured; — computed with uniform rejection rate; --- computed with measured injection rate

performed a computation where we employ the injection rate profile as estimated by Cossali et al., in their measurements and shown in Fig. 1. This injection profile has a gradual decrease in the injection mass flow rate towards the end of injection. Figure 10 also shows the computed and measured entrainment velocity as a function of time for Case 1 when the computations are performed with the measured injection rate profile. The computed velocities do not show the sudden rise at the end of injection and the decay of the entrainment velocity is in reasonable agreement with the measurements.

Comparison of Computed and Measured Entrainment Constant

The entrainment constant, K_e , is a nondimensional entrainment rate and is defined at a given location, x , as

$$K_e = \frac{d\dot{m}_e(x)}{dx} \frac{d}{\dot{m}_i} \left(\frac{\rho_l}{\rho_a} \right)^{1/2} \quad (20)$$

where \dot{m}_e is the total mass flow rate of the entrained gas across the cross section of the jet at axial location, x . d is the orifice diameter. \dot{m}_i is the injected mass flow rate. ρ_l and ρ_a are the injected and ambient densities, respectively. $d\dot{m}_e(x)/dx$ may be written as $2\pi r \rho_a V_e$, [30]. Notice that the entrainment constant as defined by Eq. (20) is relevant only in the steady portion of the jet. In the measurements, [27], Eq. (27) with the substitution for $d\dot{m}_e(x)/dx$ was used to calculate entrainment constant because the entrainment velocity was the only data measured. However, in the computations, it is convenient to employ Eq. (20) directly since the entire velocity field is computed. For this purpose, the mass flow rate across the jet cross section at an axial location, x , is defined as the total positive mass flow rate at s , integrated radially across the domain. Thus,

$$\dot{m}_e(x) = \int_{r=0}^{r=R_c} 2\pi r \alpha_g \rho_g [[V_x(r), 0]] dr \quad (21)$$

where R_c is the chamber radius, V_x is the axial velocity, and the operation $[[a, b]]$ represents the maximum of a and b .

Computations are performed to evaluate the effect of ambient density on the entrainment constant in sprays. The ambient conditions corresponding to Cases 1, 3, and 4 are chosen for this purpose. All these cases have the same ambient temperature of 298 K but different ambient densities. Figure 11 shows the computed and measured entrainment constant as a function of the axial distance from the orifice for Cases 1, 3, and 4. The computed

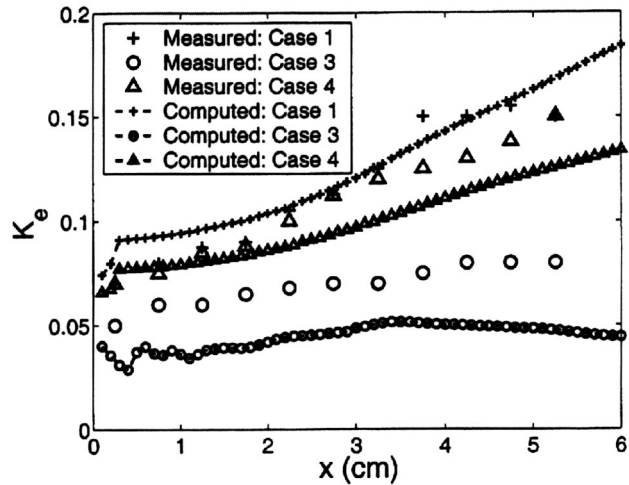


Fig. 11 Entrainment versus axial distance: computed and measured: effect of ambient density

values are averaged in the time interval between 2 and 3 ms after start of injection, i.e., once steady values are reached. The figure shows that the measured entrainment constant decreases with decrease in ambient density at all the axial locations shown. The computed entrainment constant shows a similar trend. Decrease in ambient density increases the drop sizes and the breakup length. So the transfer of momentum from the liquid to the gas is slower as the ambient density is decreased. So it is expected that the entrainment constant in the near field decreases with decreasing ambient density. The quantitative agreement between the measurements and the computations is good for Case 1. However, for Cases 3 and 4, the computations appear to underpredict the entrainment constant by more than 40 percent at all the axial locations shown. This may be due to uncertainties in our knowledge of atomization and break up processes in diesel sprays and it requires more theoretical and experimental investigations.

It should be noted that the measurements of Cossali et al. [27] are for ambient densities that are lower than those in diesel engines near top dead center. Also, the measurements are for non-vaporizing sprays. It would be of interest to investigate the behavior of the entrainment constant for vaporizing diesel sprays for different ambient densities. There are no reported measurements of entrainment constant in vaporizing diesel sprays to our best knowledge. So we can only look at the computed entrainment constant under these conditions. Figure 12 shows the computed entrainment constant as a function of the axial distance from the orifice for five ambient densities range from 3.3–60 kg/m³. The five cases correspond to the spray penetration measurements performed at the Sandia National Laboratories, [31]. The conditions are shown in Table 4. The ambient temperature is 1000 K and the injection pressure is 136 MPa. Figure 12 shows that the entrainment constant increases with axial distance in the near field for all the cases. However, for ambient densities greater than 14.8 kg/m³, K_e reaches a steady value of about 0.32 within 1.5–2.0 cm, i.e., about 15 effective diameters downstream of the orifice. The value of 0.32 is approximately the value of the entrainment constant in steady gas jets as shown in prior works, [29,32,33]. For lower ambient densities the steady value is reached at a further downstream location and the value of K_e in the near field is lower. Thus it appears from Fig. 12 that under typical diesel conditions, ($\rho_a = 14.8\text{--}30 \text{ kg/m}^3$), the entrainment constant reaches a steady value of about 0.32 for all densities within several diameters from the orifice. A steady entrainment constant was not obtained in the measurements of Cossali et al. [27], because of the low ambient densities and also because of the fact that the measurements were confined to the near field.

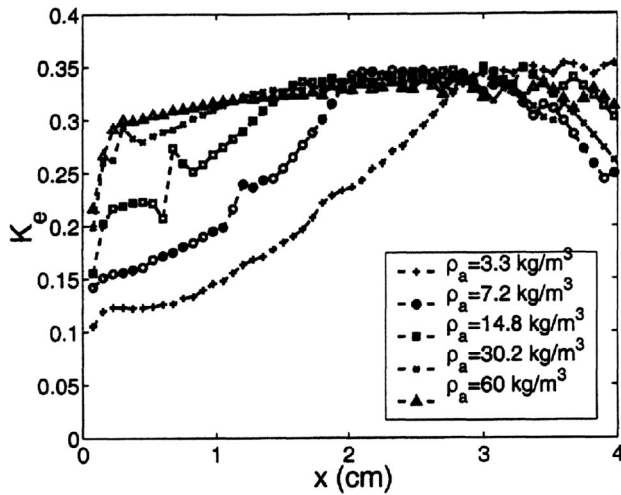


Fig. 12 Computed entrainment constant versus axial distance for vaporizing sprays: effect of ambient density

Figure 13 shows the computed and measured entrainment constant as a function of the axial distance from the orifice for Cases 4 and 5 of Cossali et al. [27] shown in Table 3. Both these cases have the same ambient density of 5.6 kg/m^3 but Case 4 has an ambient temperature of 298 K whereas Case 5 has an ambient temperature of 473 K. The figure shows that the measured entrainment constant for Case 5 is greater than that for Case 4 by as large as a factor of 2 at the axial location of 4 cm from the orifice. The computations also predict an increase in the entrainment constant when the ambient temperature is increased from 298 K in Case 4 to 473 K in Case 5 but by about 30 percent, which is not as large as in the measurements. Cossali et al. [27], have mentioned that a possible explanation for the increase in the entrainment constant is

Table 4 Experimental conditions for vaporizing sprays, [31]

Case	ρ_a (kg/m ³)	T_a (K)	ρ_l (kg/m ³)	P_l (MPa)	d mm
A	3.3	988	706	137	0.257
B	6.85	1010	705	139	0.257
C	13.9	1001	703	142	0.257
D	28.1	1000	703	147	0.257
E	58.4	1002	699	121	0.257

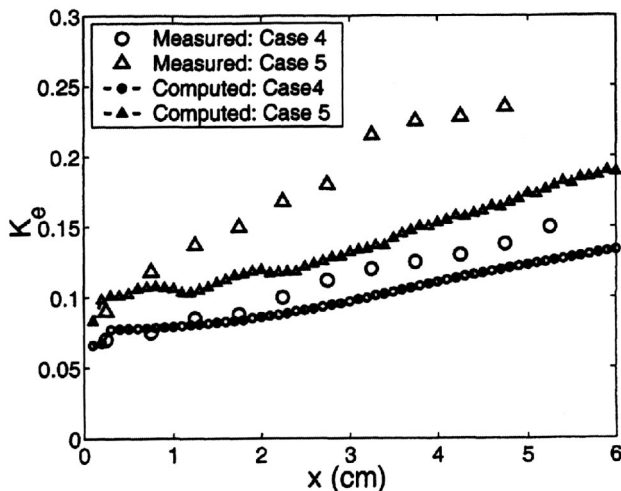


Fig. 13 Entrainment constant versus axial distance: computed and measured: effect of ambient temperature

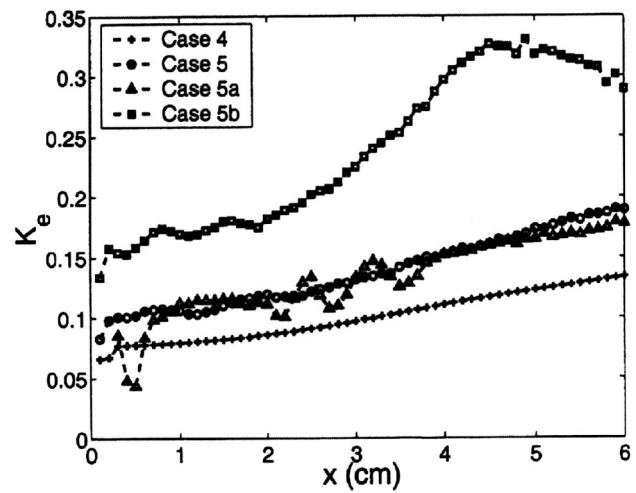


Fig. 14 Computed entrainment constant versus axial distance: effect of drag and vaporization

that the increase in the gas temperature increases the laminar viscosity of the gas and enhances momentum transfer by drag forces. The increase in the laminar viscosity is about 30 percent when the temperature is increased from 298 K to 473 K. There is also another possible explanation: The liquid may vaporize at the higher temperature, which may increase the efficiency of liquid-gas momentum transfer due to the transfer of the momentum carried by the evaporating mass. This fact has also been mentioned by Cossali et al. [27]. To test the two possible explanations mentioned above, we performed two more computations that we denote by Case 5a and Case 5b. Case 5a is a computation for the same ambient conditions as Case 5 but the laminar viscosity in Case 5a is set equal to that at 298 K corresponding to that of Case 4. This exercise removes the dependence of the viscosity on the temperature and helps us to test whether increase in viscosity is the reason for the increase in the value of entrainment constant. In Case 5b, octane is used as the injected fuel, the other injection and ambient conditions remaining identical to those in Case 5. We employ octane to assess the effect of vaporization. Octane being more volatile than tetradecane should show an increase in entrainment constant if vaporization is the cause for the increase in entrainment constant.

Figure 14 shows the computed entrainment constant as a function of axial distance from the orifice for Cases 4, 5, 5a, and 5b. The figure shows that the entrainment constant for Case 5a is similar to that for Case 5 excluding some minor fluctuations. If increase in viscosity were the reason for the increase in entrainment constant, then Case 5a should have predicted entrainment constant values that are closer to Case 4. As that is not the case according to Fig. 14, the effect of viscosity in increasing the momentum transfer due to drag is probably not significant for the conditions considered. However, there appears to be an effect of vaporization on the entrainment constant because Case 5b with octane as the injected fuel predicts a significant increase in the entrainment constant compared to Case 5. In fact, the behavior of the entrainment constant for Case 5b is similar to that in vaporizing diesel sprays as shown in Fig. 12 in that K_e approaches a steady value in the range of 0.3–0.33. Thus it appears that the increase in the entrainment constant with increase in the ambient temperature is most likely due to the vaporization of the fuel. It is possible that the diesel fuel used in the measurements might have had some volatile components that vaporizes at 473 K. So the measured sensitivity of K_e to temperature is more than those predicted by computations with tetradecane as the injected fuel. There can also be a possible effect of the temperature on the atomization process for which no quantitative models exist, [27].

Summary and Conclusions

A two-fluid Eulerian-liquid Eulerian-gas model for diesel sprays is employed to compute drop mean axial velocity and drop velocity fluctuations in the far field of a spray, i.e., at axial distances that are greater than 300 orifice diameters, and entrainment characteristics in the near field, i.e., at axial distances that are less than 100 orifice diameters, of a spray. The results are compared with measurements. The drop mean axial velocity values agree within 20 percent. In the case of drop velocity fluctuations, the agreement is within 40 percent at all radial distances. It is shown that the agreement between computed and measured values improves at chamber conditions closer to those in diesel engines. In the near field, the trends in entrainment velocity and entrainment constant are reproduced with adequate accuracy. Quantitative agreement is achieved within 30 percent. However, the quantitative results are sensitive to the choice of constants in the atomization model. Hence, there is a need to improve the understanding of the physics of atomization. Most importantly, unlike in traditional LDEF approaches, adequate numerical resolution can be employed in the near field with the ELEG model. This makes it possible to study the physics without the difficulties associated with numerical errors.

Acknowledgments

The authors thank the Cummins Engine Company, the Detroit Diesel Company, and the Purdue Research Foundation for their support of this work. Useful discussions with Prof. Vinicio Magi are gratefully acknowledged.

Nomenclature

d	= orifice diameter
d_p	= droplet diameter
E_k	= ensemble-averaged specific energy (internal+ kinetic) of phase k
K_e	= entrainment constant
k_k	= turbulent kinetic energy of phase k
L_s	= surface area concentration
M_k^d	= averaged interfacial force density for phase k
P_k	= average pressure of phase k
$P_{k,i}$	= averaged interface pressure on phase, k side
Q_k	= interfacial energy transfer to phase k
$\mathbf{q}_k, \mathbf{q}_k^t$	= molecular and turbulent heat flux of phase k , respectively
r_p	= radius of droplet
Re	= Reynolds number
\mathbf{U}_k	= Favre-averaged velocity of phase k
x	= axial distance in a jet
α_k	= volume fraction of phase k
ε_k	= dissipation of turbulent kinetic energy of phase k
η_k	= gas-phase diffusivity of phase k
Γ_k	= phase-change source term for phase k
ν_k^t	= turbulent viscosity of phase k
ρ_k	= averaged density of phase k
$\underline{\underline{\tau}}_k, \underline{\underline{\tau}}_k^t$	= molecular and turbulent stress tensor of phase k , respectively

Subscripts

a	= ambient fluid
g	= gas
i	= interface
j	= component j
k	= phase k
l	= liquid

References

- [1] Dukowicz, J. K., 1980, "A Particle-Fluid-Numerical Model for Liquid Sprays," *J. Comput. Phys.*, **35**(2), pp. 229–253.

- [2] O'Rourke, P. J., and Bracco, F. V., 1980, "Modeling of Drop Interactions in Thick Sprays and Comparison with Experiments," *The Institution of Mechanical Engineers, Publication 1980-9*, pp. 101–116.
- [3] Abraham, J., 1997, "What is Adequate Resolution in the Numerical Computations of Transient Jets?" *Transactions of the SAE*, **106**(3), pp. 141–155.
- [4] Iyer, V. A., and Abraham, J., 1997, "Penetration and Dispersion of Transient Gas Jets and Sprays," *Combust. Sci. Technol.*, **130**, pp. 315–335.
- [5] Aneja, R., and Abraham, J., 1998, "How Far Does the Liquid Penetrate in a Diesel Engine: Computed Results vs. Measurements?" *Combust. Sci. Technol.*, **138**, pp. 233–255.
- [6] Subramaniam, S., and O'Rourke, P. J., 1998, "Numerical Convergence of the KIVA-3 Code for Sprays and Its Implications for Modeling," Los Alamos Laboratory Report UR-98-5465, Los Alamos, NM.
- [7] Iyer, V. A., Abraham, J., and Magi, V., 2001, "Exploring Injected Droplet Size Effects on Steady Liquid Penetration in Diesel Spray With a Two-Fluid Model," *Int. J. Heat Mass Transfer*, **45**, pp. 519–531.
- [8] Iyer, V. A., Post, S. L., and Abraham, J., 2000, "Is the Liquid Penetration in Diesel Sprays Mixing Controlled?" *Proceedings of the Combustion Institute*, **28**, pp. 1111–1118.
- [9] Ishii, M., 1975, *Thermo-Fluid Dynamic Theory of Two-Phase Flows*, Eyrolles, Paris.
- [10] Drew, D. A., 1983, "Mathematical Modeling of Two-Phase Flow," *Annu. Rev. Fluid Mech.*, **15**, pp. 261–291.
- [11] Crowe, C., Sommerfeld, M., and Tsuji, Y., 1998, *Multiphase Flows With Droplets and Particles*, CRC Press, Boca Raton, FL.
- [12] Iyer, V. A., 2001, "Modeling of Diesel Sprays Using an Eulerian-Liquid Eulerian-Gas Two-Fluid Model," Ph.D. dissertation, Purdue University, West Lafayette, IN.
- [13] Csanady, G. T., 1963, "Turbulent Diffusion of Heavy Particles in the Atmosphere," *J. Atmos. Sci.*, **105**, pp. 329–334.
- [14] Issa, R. I., and Oliveira, P. J., 1996, "Validation of Two-Fluid Mixing in Shear-Free Mixing Layer," *Proceedings of the Fluids Engineering Division Summer Meeting*, ASME, New York, **1**, pp. 113–120.
- [15] Chan, S. H., and Abou-Ellail, M. M. M., 1994, "A Two-Fluid Model for Reacting Turbulent Two-Phase Flows," *ASME J. Heat Transfer*, **116**, pp. 427–435.
- [16] Launder, B. E., and Spalding, D. B., 1974, "The Numerical Computation of Turbulent Flows," *Comput. Methods Appl. Mech. Eng.*, **3**, pp. 269–289.
- [17] Abraham, J., and Magi, V., 1998, "Computations of Jets-RNG vs. Standard $k-\varepsilon$ Model," *SAE Trans.*, **106**(3), pp. 1442–1452.
- [18] Reitz, R. D., 1987, "Modeling Atomization Processes in High Pressure Vaporizing Sprays," *Atomization and Spray Technology*, **3**, pp. 309–337.
- [19] Beale, J. C., and Reitz, R. D., 1999, "Modeling Spray Atomization With the Kelvin-Helmholtz/Rayleigh-Taylor Hybrid Model," *Atomization Sprays*, **9**, pp. 623–650.
- [20] Gidaspow, D., 1984, *Multiphase Flow and Fluidization: Continuum and Kinetic Theory Descriptions*, McGraw-Hill, New York.
- [21] O'Rourke, P. J., 1981, "Collective Drop Effects on Vaporizing Liquid Sprays," Ph.D. dissertation, Department of Mechanical and Aerospace Engineering, Princeton University, Princeton, NJ.
- [22] Patankar, S. V., and Spalding, D. B., 1972, "A Calculation Procedure for Heat, Mass and Momentum Transfer in Three-Dimensional Parabolic Flows," *Int. J. Heat Mass Transfer*, **15**, pp. 1787–1806.
- [23] Liles, D. R., and Reed, W. H., 1978, "A Semi-Implicit Method for Two-Phase Fluid Dynamics," *J. Comput. Phys.*, **26**, pp. 390–407.
- [24] Magi, V., 1987, "REC-87: A New 3-D Code for Flows, Sprays and Combustion in Reciprocating and Rotary Engines," Mechanical and Aerospace Engineering Report 1793, Princeton University, Princeton, NJ.
- [25] Patankar, S. V., 1980, *Numerical Heat Transfer and Fluid Flow*, Hemisphere, Washington DC.
- [26] Wu, K. J., Santavicca, A., Bracco, F. V., and Coghe, A., 1984, "LDV Measurements of Drop Velocity in Diesel-Type Sprays," *AIAA J.*, **22**(9), pp. 1263–1270.
- [27] Cossali, G. E., Berlaano, A., Coghe, A., and Brunello, G., 1996, "Effect of Gas Density and Temperature on Air Entrainment in a Transient Diesel Spray," *SAE Paper 960862*.
- [28] Andriani, R., Coghe, A., and Cossali, G., 1996, "Near-Field Entrainment in Unsteady Gas Jets and Diesel Sprays: A Comparative Study," *Proceedings of the Combustion Institute*, The Combustion Institute, Pittsburgh, PA, **26**, pp. 2549–2556.
- [29] Witze, P. O., 1980, "The Impulsively Started Incompressible Turbulent Jet," Sandia Laboratories Energy Report SAND80-8617, Sandia National Laboratories, Livermore, CA.
- [30] Post, S. L., Iyer, V. A., and Abraham, J., 2000, "A Study of Near-Field Entrainment in Gas Jets and Sprays Under Diesel Conditions," *ASME J. Fluids Eng.*, **122**, pp. 385–395.
- [31] Naber, J. D., and Siebers, D. L., 1996, "Effects of Gas Density and Vaporization on Penetration and Dispersion of Diesel Sprays," *SAE Paper 960034*.
- [32] Abraham, J., 1996, "Entrainment Characteristics of Transient Gas Jets," *Numer. Heat Transfer*, **30**, pp. 347–364.
- [33] Ricou, F., and Spalding, D., 1961, "Measurements of Entrainment by Axisymmetrical Turbulent Jets," *ASME J. Fluids Eng.*, **11**, pp. 21–32.

Effect of Reynolds Number and Surface Roughness on the Efficiency of Centrifugal Pumps

J. F. Gülich

Sulzer Pumps,
Winterthur and Ecole Polytechnique,
Lausanne, Switzerland

A procedure has been developed to predict the effects of roughness and Reynolds number on the change in efficiency from a model or baseline to a prototype pump ("efficiency scaling"). The analysis of individual losses takes into account different roughnesses of impeller, diffuser/volute, impeller side disks, and casing walls in the impeller side rooms. The method also allows to predict the effect of roughness and Reynolds number on the hydraulic efficiency. The calculations are based on physical models but the weighting of impeller versus diffuser/volute roughness and the fraction of scalable losses within impeller and diffuser/volute are determined empirically from the analysis of tests with industrial pumps. The fraction of scalable impeller/diffuser/volute losses is found to decrease with growing specific speed. Roughness effects in the diffuser/volute are stronger than in the impeller, but the dominance of the stator over the rotor decreases with increasing specific speed. The procedure includes all flow regimes from laminar to turbulent and from hydraulically smooth to fully rough. It is validated by tests with viscosities between 0.2 to 3000 cSt and Reynolds numbers between 1500 and 10^8 . The hydraulic losses depend on the patterns of roughness, near-wall turbulence, and the actual velocity distribution in the hydraulic passages. These effects—which are as yet not amenable to analysis—limit the accuracy of any efficiency prediction procedure for decelerated flows. [DOI: 10.1115/1.1593711]

1 Introduction

As with the flow in a pipe or over a flat plate, energy losses in turbomachinery depend on Reynolds number Re and relative surface roughness ε/d . The efficiency η of a centrifugal pump is thus affected by these parameters in various ways; it depends on size, speed, viscosity and roughness. "Efficiency scaling" predicts the efficiencies of *geometric similar pumps* as a function of Reynolds number and roughness. Important practical applications of said dependency are:

1. "efficiency scaling," i.e., the estimation of the efficiency $\eta_a = f(Re_a, \varepsilon_a/d_a)$ of a prototype from the measured efficiency $\eta_M = f(Re_M, \varepsilon_M/d_M)$ of a model or baseline pump.
2. estimation of the efficiency expected in the plant at higher speed and/or different viscosity from a works test with cold water at lower speed. A typical application would be a boiler feed pump tested for example at 1500 rpm with water of 20°C running in the power station at 6000 rpm with water of 180°C.
3. estimation of pump performance with highly viscous liquids, e.g., oil with 3000 cSt, from performance curves established from cold water tests.
4. assessment of efficiency gain expected from a roughness reduction versus extra costs involved in surface finish improvement.
5. impact of roughness of impeller versus volute or diffuser on efficiency; i.e., answering the question, where efforts to improve surface finish are best spent. This effect is expected to depend on the type and the specific speed n_q of the pump.

While items 1 and 2 have been dealt with traditionally by formulas for "efficiency scaling," [1–10], pump performance with highly viscous fluids (item 3) is estimated from empirical corre-

lations, [11], or loss analysis, [12,13]. Due to the complexity of turbulent flows over rough surfaces items 4 and 5 are less well documented.

The energy losses in a pump consist essentially of head losses in the hydraulic passages of impeller and casing, volumetric and disk friction, as well as mechanical losses.

The objectives of the present contribution are thus:

- to present a unified procedure for estimating the impact of speed, size, viscosity and roughness on efficiency in order to handle applications as listed above under items 1 to 5;
- to provide also a method for scaling the *hydraulic* efficiency as function of Reynolds number and roughness; this topic is scarcely documented in a generic way.
- to cover the entire range from hydraulically rough (turbulent) flows to laminar flows as well as the transition between turbulent and laminar flow for technically rough surfaces;
- to include the effect of specific speed on loss distribution in said procedure; and
- to predict efficiency if the various pump components have different surface roughness.

2 Previous Work on Efficiency Scaling

Due to the important technical and economic impact of Reynolds and roughness effects on efficiency a large number of publications have been devoted to this topic. A detailed review of these efforts is beyond the scope of this contribution, but a short overview of past work is given below in order to review the various approaches taken and their limitations. Osterwalder and Hippe [1–4] present detailed reviews of work done till the end of the early 1980s and the limits of application as well as problems of various approaches to efficiency scaling. In [2] and [4] 15 formulas of varying complexity for efficiency scaling are listed and discussed. Scaling of the *inner* efficiency $\eta_i = \eta / \eta_m$ is physically more meaningful than scaling the *overall* efficiency.

Various methods are available to efficiency scaling, [5]:

Contributed by the Fluids Engineering Division for publication in the JOURNAL OF FLUIDS ENGINEERING. Manuscript received by the Fluids Engineering Division July 23, 2002; revised manuscript received February 4, 2003. Associate Editors: Tsujimoto.

- analytical "efficiency scaling" formulas of various complexity based on drag coefficients of pipes or flat plates assuming either hydraulically smooth or rough surfaces.
- empirical formulas or graphs based on statistics of efficiency as function of specific speed and design flow rate, which intend to capture the effect of size and speed.
- by a detailed analysis of all energy losses in the model ("baseline") and the prototype the dependence of the individual losses on Reynolds and roughness is calculated and the prototype efficiency determined.
- numerical flow calculations of model and prototype.

2.1 Efficiency Scaling for Hydraulically Smooth Surfaces.

Earlier attempts considered the effect of the Reynolds number and recognized that only a fraction V of the energy losses are Re dependent:

$$\frac{1 - \eta_{i,a}}{1 - \eta_{i,M}} = V + (1 - V) \left(\frac{\text{Re}_M}{\text{Re}_a} \right)^m \quad (1)$$

Equation (1) considers the inner efficiency $\eta_i = P_u/P_i = \eta/\eta_m$. For turbulent, hydraulically smooth flow $m=0.2$ and $V=0.5$ were proposed. The main weakness of Eq. (1) is that the exponent m depends on the Reynolds number and roughness as pointed out by various authors (e.g., [1–5]): In the fully rough flow region the exponent would become $m=0$; in the general case m depends on Reynolds and roughness and can vary between zero and 1.0 with laminar flow. Wiesner [6] quotes 15 authors which have used Eq. (1) to correlate their test data; these authors found $V=0$ to 0.57 and $m=0.1$ to 0.5 depending on their individual test data.

2.2 Efficiency Scaling for Hydraulically Smooth and Rough Surfaces. A more general approach is to use the ratio of friction factors $\lambda_R = f(\text{Re}, \varepsilon/d)$ rather than the Reynolds number for efficiency scaling, [1–5]. This leads to formulas of the type given for compressors by Strub et al. [7]:

$$\frac{1 - \eta_{i,a}}{1 - \eta_{i,M}} = \frac{V + (1 - V) \frac{\lambda_{R,a}}{\lambda_{R,\infty,a}}}{V + (1 - V) \frac{\lambda_{R,M}}{\lambda_{R,\infty,M}}} \quad (2)$$

$$\lambda_R = \frac{1}{\left(1.74 - 2 \log \left[\frac{2\varepsilon_{\text{CLA}}}{b_2} + \frac{18.7}{\text{Re} \sqrt{\lambda_R}} \right] \right)^2}$$

In Eq. (2) was set $V=0.3$ and pipe friction data $\lambda_R = f(\text{Re}, \varepsilon/d)$ were taken; for explicit formula see [5]. λ_R is determined for $\text{Re}_{b_2} = u_2 b_2 / \nu$ and the CLA (center line average) or AA (arithmetic average) roughness ε_{CLA} . $\lambda_{R,\infty}$ is the friction factor for fully rough flow at the relative roughness considered, calculated from Eq. (2) for $\text{Re} = \infty$.

Casey's approach for compressors [8] can be written in terms used for pumps as

$$\Delta \eta = \frac{2C \eta_h}{\psi} (\lambda_{R,a} - \lambda_{R,M}) \quad \text{with } C = 5.0 \text{ for } b_2^* = b_2/d_2 > 0.06 \text{ and } C = \frac{15.5}{1 + 35b_2^*} \text{ for } b_2^* < 0.06. \quad (3)$$

In Eq. (3) C accounts indirectly for the influence of specific speed; C was determined empirically from tests with centrifugal compressors. Casey uses Re_{b_2} defined as above but determines the friction factors for an equivalent sand roughness $\varepsilon = 2\varepsilon_{\text{CLA}}$. Diffuser and impeller roughness were averaged; disk friction roughness effects are not considered separately.

3 Efficiency Scaling by Loss Analysis

In this approach hydraulic, disk friction and volumetric losses are scaled individually as function of the relevant Reynolds numbers and roughness of hydraulic passages, impeller side disks, and close running clearances. While volumetric and disk friction losses are extensively documented, little consistent and generic data is available on the influence of Reynolds and roughness on the hydraulic efficiency.

Based on sample calculations Osterwalder and Hippe have developed graphs for efficiency scaling in an attempt to avoid lengthy calculations, [2,4]. Guiton and Canvelis [9] as well as Ida [10] have developed efficiency scaling formulas which attempt to capture the effect of individual losses in a simplified way. The loss analysis method has been used to correlate and predict the performance of centrifugal pumps operating with highly viscous fluids; it is described in detail in [5] and [12]; comparisons between prediction and test data are given in [12]. Numerous other publications rely on a loss analysis for assessing and modelling pump performance, e.g., [2–4] and [13–17].

3.1 Derivation of the Efficiency Scaling Factor. The power P absorbed at the coupling of a centrifugal pump (operating without partload recirculation) is given by the useful power $P_u = \rho g H_{\text{tot}} Q$ and all energy losses:

$$P = \frac{\rho g H_{z_{st}} Q}{\eta_{\text{vol}} \eta_h} + P_{RR} + P_m \quad \eta = \frac{P_u}{P} = \frac{\rho g H_{z_{st}} Q}{P} \quad (4)$$

The first term represents the work done by the impellers. Leakage flows around the impeller and over the axial thrust balancing device are taken into account by the volumetric efficiency η_{vol} . The term P_{RR} represents the sum of disk friction losses on all rotating parts of the rotor, which are wetted by the fluid; P_{RR} includes impeller side disks and axial thrust balancing devices (if any). The term P_m represents all mechanical losses of shaft seals and bearings. Per Eq. (4) the efficiency can be written as

$$\eta = \frac{\eta_{\text{vol}} \eta_h}{1 + \eta_{\text{vol}} \eta_h \left(\frac{P_{RR}}{P_u} + \frac{P_m}{P_u} \right)} \quad (5)$$

The quantities η_{vol} , η_h , and P_{RR} depend on Reynolds and roughness, while the P_m/P_u may be considered constant in the present context. The deviation from the scaling laws of flow and head i.e., the relation between prototype and scaled model may be expressed by multipliers per Eq. (6):

$$f_Q = \frac{\varphi_a}{\varphi_M} \quad f_H = \frac{\psi_a}{\psi_M} \quad f_\eta = \frac{\eta_a}{\eta_M} \quad f_{\eta_h} = \frac{\eta_{h,a}}{\eta_{h,M}} \quad f_{\eta_{\text{vol}}} = \frac{\eta_{\text{vol},a}}{\eta_{\text{vol},M}}$$

$$f_{\eta_m} = \frac{\eta_{m,a}}{\eta_{m,M}} \quad (6)$$

The factors f_Q and f_H are traditionally applied for highly viscous fluids; they capture the effect of the losses on flow rate and head at the best efficiency point, for details see [12].

The disk friction for the prototype is $P_{RR,a} = k_{RR,a} \rho_a \omega^3 r_2^5 f_{\text{geo}}$ and for the model $P_{RR,M} = k_{RR,M} \rho_M \omega^3 r_2^5 f_{\text{geo}}$. The useful power of the prototype is $P_{u,a} = \rho_a g H_a Q_a$ and for the model $P_{u,M} = \rho_M g H_M Q_M$. With f_Q and f_H from Eq. (6) it follows $P_{u,a} = P_{u,M} f_H f_Q \rho_a / \rho_M$. Using these expressions we get

$$\left(\frac{P_{RR}}{P_u} \right)_a = \left(\frac{P_{RR}}{P_u} \right)_M \frac{k_{RR,a}}{k_{RR,M} f_H f_Q} \quad (7)$$

Writing Eq. (5) for prototype and model we can establish the ratio η_a / η_M . Inserting Eqs. (6), (7) in the obtained expression the efficiency scaling factor f_η is derived:

$$f_{\eta} \equiv \frac{\eta_a}{\eta_M} = \frac{f_{\eta h} f_{\eta \text{vol}} \left[1 + \left\{ \left(\frac{P_{RR}}{P_u} \right)_M + \left(\frac{P_m}{P_u} \right)_M \right\} \eta_{\text{vol},M} \eta_{h,M} \right]}{1 + \left\{ \left(\frac{P_{RR}}{P_u} \right)_M \frac{k_{RR,a}}{k_{RR,M}} + \left(\frac{P_m}{P_u} \right)_M \frac{\rho_M f_{\eta m}}{\rho_a} \right\} - \frac{f_{\eta h} f_{\eta \text{vol}}}{f_H f_Q} \eta_{\text{vol},M} \eta_{h,M}} \quad (8)$$

Equation (8) is exact if all losses are included as described above. For any given pump this equation can be evaluated by using appropriate correlations to estimate leakage, disk friction, and head losses in hydraulic passages, [5]. Often some simplifications are justified. In the present contribution it has been assumed: (1) $f_{\eta \text{vol}}=1.0$ for lack of details of labyrinths (this assumption is fulfilled exactly for evaluating roughness effects); (2) $f_{\eta m}=1.0$ since effect is small and difficult to determine; $\rho_a=\rho_M$ (exact in the present investigation); (3) $f_H=f_{\eta h}$ as discussed below; (4) $f_Q=f_H$ which means that the flow at maximum efficiency moves on the volute or diffuser characteristic as demonstrated by test data analyzed in [12]. f_Q and f_H are significant only for high viscosities, but their inclusion yields a consistent method for calculating Reynolds and roughness effects for turbulent as well as laminar flows.

Introducing these assumptions into Eq. (8) yields Eq. (T20) in Table 1, which lists all equations used for evaluating the test data and needed for efficiency scaling predictions.

The assumption $f_H=f_{\eta h}$ needs further comments because $f_{\eta h}$ cannot be determined directly from tests with moderate viscosities for the following reasons: (1) When the Reynolds number changes, the leakage flows through the labyrinths change and this gives a slight shift in the Q - H curve, since the actual flow through the impeller $Q_{La}=Q/\eta_{\text{vol}}$ is modified. (2) The impeller side disks act like a friction pump: In the boundary layers the circumferential velocity is close to u_2 and the boundary layers throwoff hub and shroud thus add some moment of momentum to the main stream leaving the impeller. The effect grows with decreasing specific speed. (3) Even a roughness increase of the impeller passages has been observed repeatedly to result in a small increase in head; in such cases the roughness apparently had an effect on the slip factor through an increase of the absolute velocity in the boundary layers and an impact on secondary flow. With a double-entry impeller $n_q=10$ Varley [18] measured $f_H=1.1$ when increasing the roughness from $\varepsilon=0.025$ to 0.87 mm (while the efficiency factor dropped to $f_{\eta}=0.84$). With $n_q=7$ from the test data used in this study the head increased over the entire Q - H curve by 2.0 m (1.1%) when the impeller channel roughness was increased from $\varepsilon_{\text{CLA}}=1.6$ to 20 μm . Even tests with $n_q=135$ showed also a slight increase in head when the impeller channels were roughened. Such effects were present also in the tests described in [19] where the head increased when the viscosity was increased from 1 to 45 cSt; only above 100 cSt additional head losses due to viscosity overcame the effects of reduced leakage flow and side disk pumping).

The effects of side disk pumping, shift in leakage flow, and change in slip factor cannot be separated from the effect of hydraulic losses; it is therefore not possible to determine $f_{\eta h}=(\text{Re}, \varepsilon)$ from any differences in head measured between model and prototype, when $\text{Re}_a/\text{Re}_M < 100$.

3.2 Equivalent Sand Roughness and Friction Coefficients.

Friction coefficients are taken from flat-plate data per Eq. (T16) rather than pipe correlations, since flow in the hydraulic channels of a pump are considered by most authors as not fully developed. Since only ratios of friction factors are used in the relevant equations, the same Reynolds number $\text{Re}=\omega r^2/\nu$ is used for hydraulic and disk friction losses.

The roughness of the pump components tested has been determined by "Rugotest" which gives the CLA (center line average) roughness ε_{CLA} . In order to calculate the friction factors from Eq.

(T16) the equivalent sand roughness ε must be used. The relation between maximum roughness depth ε_{max} , average roughness ε_{CLA} , and sand roughness ε are given by Eq. (9):

$$\varepsilon = \frac{\varepsilon_{\text{max}}}{c_{eq}} \quad \text{or with} \quad \varepsilon_{\text{max}} = 6\varepsilon_{\text{CLA}} \quad \varepsilon = \frac{6\varepsilon_{\text{CLA}}}{c_{eq}} \quad (9)$$

The roughness equivalence factor c_{eq} depends on the structure of the roughness; Grein provides the following values, [20]: Roughness pattern perpendicular to flow direction: $c_{eq}=2.6$; roughness pattern parallel to flow direction: $c_{eq}=5$.

For technical surfaces (machined, ground, or cast) there is no relative minimum in the function $c_f=f(\text{Re})$ in the transition between laminar and turbulent flow. Therefore the calculation switches from Eq. (T16) to (T17) where $c_{f,\text{laminar}} > c_{f,\text{turbulent}}$.

3.3 Disk Friction, Volumetric and Mechanical Losses.

Disk friction losses are evaluated with disk friction coefficients from Eq. (T9) which has been discussed and validated in [21]. This equation covers the whole range from laminar to turbulent flow and agrees well with the four correlations given in [22] and data from [23] as correlated by [24]. When impeller side disk and casing wall have different roughness ($\varepsilon_{\text{impeller}} \neq \varepsilon_{\text{casing}}$) the core flow in the impeller side room is affected: with $\varepsilon_{\text{impeller}} > \varepsilon_{\text{casing}}$ the core flow is accelerated (k_o increases) and when $\varepsilon_{\text{impeller}} < \varepsilon_{\text{casing}}$ the core flow is slowed down (k_o decreases). The advantage of using Eq. (T9) is thus to include these effects. Four multipliers in Eq. (T9) allow to take into account: (a) thermal effects when handling highly viscous fluids (f_{therm} from Eq. (T11) for details see [12]); (b) pump-out vanes, if any, per f_{RS} from Eq. (T10) or more accurately by correlations given in [5]; (c) the influence of leakage through the impeller side room on disk friction per f_L as estimated from an empirical correlation Eq. (T12) from [5]; and (d) the roughness of the impeller side disk by factor f_R as calculated from Eq. (T7). The factor f_R is derived from flat plate friction coefficients described by Eq. (T16). At any given Reynolds-number f_R is the ratio of the friction on a rough plate to that on a smooth plate $f_R=c_f(\varepsilon>0)/c_f(\varepsilon=0)$. This formulation is able to cover fully rough flow conditions as well as the transition from smooth to rough surfaces (if the roughness term becomes small in relation to the Reynolds term in Eq. (T7) f_R tends to 1.0). Equations (T7) and (T9) agree reasonably well with test data in [25] and [26] as shown in [21].

When the impeller side disks and/or casing walls are machined and roughness grooves are thus in tangential direction the equivalence factor for flow parallel to roughness pattern must be applied ($c_{eq}=5$). Geis [27] found virtually no increase in disk friction when increasing the roughness from a polished to a machined surface with $\varepsilon_{\text{max}}=120$ μm . For cast surfaces $c_{eq}=2.6$ would be used. The ratio of disk friction losses P_{RR} to the useful power P_u is given by Eq. (T13).

Volumetric losses through the close running clearances between rotor and stator can be calculated from various literature sources, albeit with considerable uncertainty, [5]. Focussing on the effect of roughness, in the present study they were estimated from Eq. (T3) in most cases.

The volumetric efficiency is defined by Eq. (T4). In case of multi-stage pumps the interstage leakage Q_{s3} is multiplied by the ratio $\Delta H_{s3}(z_{st}-1)/(H_{st}z_{st})$ to account for the fact that the head

Table 1 Procedure of efficiency scaling


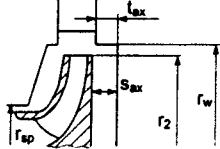
		Eq.
Quantities given for "model," baseline or water	$n_M, Q_{opt,M}, H_{opt,M}, d_{2,M}, \eta_M, \nu_M$, roughness ϵ_M of the different components	
Quantities given for "prototype" or viscous fluid	$n_a, Q_{opt,a}, d_{2,a}, \nu_a$, roughness ϵ_a of the different components	
Specific speed	$\omega_s = \omega \frac{\sqrt{Q_{opt}}/f_q}{(gH_{opt})^{0.75}} = \frac{n_q}{52.9}$ $n_q = n \frac{\sqrt{Q_{opt}}/f_q}{H_{opt}^{0.75}}$	ω_s is dimensionless; n_q is with rpm, m ³ /s, m (T1)
Reynolds number	$Re = \frac{u_2 r_2}{\nu} = \frac{\omega r_2^2}{\nu}$	Re is used for hydraulic channels and disk friction (T2)
Estimation of leakage flow, if no details of labyrinths are available	$\frac{Q_{sp}}{Q_{opt}} = \frac{4.1}{n^{1.6}} = \frac{7.16 \times 10^{-3}}{\omega_s^{1.6}}$	Can be used for Q_{sp} and Q_E as first approximation (T3)
Volumetric efficiency $\Delta H_{s3}/H_{st} = 0.4$ is a good estimation	$\eta_{vol} = \frac{Q}{Q + Q_{sp} + Q_E + Q_{s3} \frac{\Delta H_{s3}(z_{st} - 1)}{H_{st} z_{st}}}$	 (T4)
Equivalent (sand) roughness $c_{eq} = 2.6$	$\epsilon = \frac{\epsilon_{max}}{c_{eq}} = \frac{6\epsilon_{CLA}}{c_{eq}}$ $\epsilon_{max} = 6\epsilon_{CLA}$	Used in friction factor correlation Eqs. (T16) and (T7) (T5)
Average roughness for hydraulic channels	$\epsilon_{av,h} = (1 - a_\epsilon)\epsilon_{La} + a_\epsilon\epsilon_{Le}$	$a_\epsilon = 0.98 - 0.0012n_q/f_q$ (T6)
Roughness effect on disk friction	$f_R = \left\{ \frac{\log \frac{12.5}{Re}}{\log \left(0.2 \frac{\epsilon}{R_2} + \frac{12.5}{Re} \right)} \right\}^{2.15}$	Calculated with equivalent sand roughness $\epsilon_{impeller}$ and ϵ_{casing} (T7)
Rotation of fluid with zero leakage ($Q_{sp} = 0$). Open side rooms $r_w = r_2$; $t_{ax} = 0$.	$k_o = \frac{c_u}{\omega r} = \frac{1}{1 + \left(\frac{r_w}{r_2}\right)^2 \sqrt{\left(\frac{r_w}{r_2} + 5 \frac{t_{ax}}{r_2}\right) \frac{f_{R,casing}}{f_{R,imp}}}}$	 (T8)
Disk friction coefficient k_{RR} per side: $P_{RR} = k_{RR} \rho \omega^3 r_2^5 f_{geo}$	$k_{RR} = \left[\frac{\pi}{2 Re s_{ax}^*} + \frac{0.0625}{Re^{0.2}} (1 - k_o)^{1.75} f_{R,imp} f_{LRS} \right] f_{them}$	$s_{ax}^* = \frac{s_{ax}}{r_2}$ (T9)
Effect of pumpout vanes	$f_{RS} = 0.63 + 0.6 d_{RS}/d_2$ $d_{RS} = \text{o.d. of pumpout vanes}$	$f_{RS} = 1.0$ if no pumpout vanes (T10)
Thermal effect on disk friction (empirical)	$f_{them} = \exp \left\{ -2 \times 10^{-5} \left(\frac{\nu}{\nu_{Ref}} \right)^{1.34} \right\}$ $\nu_{Ref} = 10^{-6} \text{ m}^2/\text{s}$	from [12] (T11)
Influence of leakage, valid for $r_{sp}/r_2 > 0.3$	$f_L = \exp \left\{ -\frac{300 Q_{sp}}{\pi r_2^3 \omega} \left(\frac{r_2}{r_{sp}} - 1 \right) \right\}$	Direction of leakage: *radially inwards: Q_{sp} positive; *radially outwards: Q_{sp} negative (T12)
Disk friction loss P_{RR}/P_u is independent from z_{st}	$\left(\frac{P_{RR}}{P_u} \right)_M = \frac{8\sqrt{2} k_{RR,M} f_{geo}}{\omega_s^2 \psi_{opt}^{2.5} f_q} = \frac{31680 k_{RR,M} f_{geo}}{n_q^2 \psi_{opt}^{2.5} f_q}$	$f_{geo} \approx 1.22$ for typical radial impellers (T13)
Mechanical losses	$\frac{P_m}{P_u} = \frac{0.0045}{\eta} \left(\frac{Q_{Ref}}{Q} \right)^{0.4} \left(\frac{n_{Ref}}{n} \right)^{0.3}$	$Q_{Ref} = 1 \text{ m}^3/\text{s}$ $n_{Ref} = 1500 \text{ rpm}$ (T14)
Hydraulic efficiency	$\eta_h = \frac{\eta}{\eta_{vol} \left[1 - \eta \left(\frac{\sum P_{RR}}{P_u} \right)_M \frac{k_{RR,a}}{k_{RR,M}} + \frac{P_m}{P_u} \right]}$	calculated from measured overall efficiency and loss analysis for model and prototype (T15)
Friction coefficient for turbulent flow for $Re > Re_{crit}$	$c_f = \frac{0.136}{\left[-\log \left(0.2 \frac{\epsilon}{r_2} + \frac{12.5}{Re} \right) \right]^{2.15}}$ $Re_{crit} = \frac{3 \times 10^6}{1 + 10^4 Tu^{1.7}}$	c_f is calculated with ϵ_{av} from Eq. (T6). Tu = turbulence level; valid for $Tu < 0.1$ [36] (T16)
Friction coefficient for laminar flow for $Re < Re_{crit}$ [36]	$c_f = c_{f,lam} = \frac{2.65}{Re^{0.875}} - \frac{2}{8 Re + 0.016/Re} + \frac{1.328}{\sqrt{Re}}$	$0.01 < Re < Re_{krit}$ Transition Re_{krit} depends on roughness and turbulence (T17)

Table 1 (Continued)

			Eq.
Fraction of losses dependent on roughness and Reynolds number	$\frac{\zeta_{R,M}}{\psi_{BEP}} = \left\{ \frac{1}{\eta_{h,M}} - 1 \right\} (a_1 - b_1 n_q \sqrt{f_q})$	$a_1 = 0.635$ $b_1 = 0.0016$	(T18)
Correction factor for hydraulic efficiency	$f_{\eta_{h,BEP}} = 1 - \frac{\zeta_{R,M}}{\psi_{BEP}} \left(\frac{c_{f,a}}{c_{f,M}} - 1 \right)$	$c_{f,a}$ and $c_{f,M}$ from Eq. (T16)	(T19)
Correction factor for efficiency with: $f_{\eta_{vol}} = 1.0$ $f_{\eta_m} = 1.0$; $\rho_a = \rho_M$ $f_Q = f_H = f_{\eta_h}$	$f_{\eta} = \frac{\eta_a}{\eta_M} = \frac{f_{\eta_h} \left[1 + \left\{ \left(\frac{P_{RR}}{P_u} \right)_M + \left(\frac{P_m}{P_u} \right)_M \right\} \eta_{vol,M} \eta_{h,M} \right]}{1 + \left\{ \left(\frac{P_{RR}}{P_u} \right)_M \frac{k_{RR,a}}{k_{RR,M}} + \left(\frac{P_m}{P_u} \right)_M \right\} \frac{\eta_{vol,M} \eta_{h,M}}{f_{\eta_h}}}$	if $\eta_{vol,a} \neq \eta_{vol,M}$ use Eq. (8) from text	(T20)
Predicted efficiency	$\eta_a = f_{\eta} \eta_M$ f_{η} from Eq. (T20)		(T21)
Predicted hydraulic efficiency	$\eta_{ha} = f_{\eta_h} \eta_{hM}$ f_{η_h} from Eq. (T19)	Note: $f_Q = f_H = f_{\eta_h}$ for highly viscous fluids	(T22)

The above efficiency scaling procedure is to be followed for the best efficiency point. The factor f_{η} is then applied to the entire curve $\eta_a(Q_a) = f_{\eta} \eta_M(Q_M)$.

ΔH_{s3} dissipated in this seal is a fraction only of the head per stage H_{st} and that only $z_{st} - 1$ stages are affected by this loss. Usually $\Delta H_{s3} / H_{st} = 0.4$ is a good estimation.

Mechanical losses were estimated from Eq. (T14), [5]; this equation should be used with caution when considering very small process pumps where the mechanical seal can absorb a considerable portion of the power at the coupling.

3.4 Hydraulic Losses. The hydraulic losses in inlet, impeller and volute/diffuser are made up by scalable (“friction”) losses $\zeta_R = f(\text{Re}, \varepsilon)$, which depend on Reynolds-number and surface roughness, and by losses created by exchange of momentum ζ_M whenever the velocity distribution is non-uniform. Such non-uniformities (for short “mixing losses”) are caused by the work transfer from the blades, deceleration of the fluid, incidence or even local flow separation. Mixing losses usually are considered as independent from the Reynolds-number.

According to basic centrifugal pump theory the theoretical head coefficient ψ_{th} is the sum of the coefficients of useful head ψ and hydraulic losses, e.g., [5]. Usually it is assumed that the theoretical head is independent of Reynolds-number and roughness. For model and prototype it is thus:

$$\psi_{th} = \psi_M + \zeta_{R,M} + \zeta_{M,M} = \psi_a + \zeta_{R,a} + \zeta_{M,a} \quad (10)$$

By definition ζ_M stands for that part of the losses which are independent of Reynolds-number and roughness; this means that $\zeta_{M,M} = \zeta_{M,a}$ cancel in Eq. (10). The friction losses are proportional to the friction factors $c_{f,a}$ of the prototype and $c_{f,M}$ of the model. Equation (10) can thus be re-written in terms of the multiplier f_{η_h} :

$$f_{\eta_h} = \frac{\eta_{h,a}}{\eta_{h,M}} = 1 - \frac{\zeta_{R,M}}{\psi_M} \left(\frac{\zeta_{R,a}}{\zeta_{R,M}} - 1 \right) = 1 - \frac{\zeta_{R,M}}{\psi_M} \left(\frac{c_{f,a}}{c_{f,M}} - 1 \right) \quad (11)$$

The change in hydraulic efficiency due to variations in Reynolds-number and/or roughness can thus be calculated from the friction factors $c_{f,a}$ and $c_{f,M}$ and the ratio of friction losses to the head $\zeta_{R,M} / \psi_M$ of the model. This ratio depends on the geometrical features, the specific speed, the surface roughness and (weakly) on the Reynolds-number. It may be estimated for any specific pump geometry from simplified loss models such as presented in [5,13,16,17]; but in the present contribution it was determined empirically from Eq. (12). The reasons for this choice are discussed in Section 6.

$$\frac{\zeta_{R,M}}{\psi_{BEP}} = \left\{ \frac{1}{\eta_{h,M}} - 1 \right\} (a_1 - b_1 n_q \sqrt{f_q}) \quad (12)$$

In Eq. (12) the hydraulic efficiency of the model $\eta_{h,M}$ is calculated in the usual way from the overall efficiency and the secondary losses, Eq. (T15). $\Sigma \zeta / \psi = (1/\eta_h - 1)$ is the sum of all hydraulic losses, while the fraction of friction losses is defined by the empirical coefficients a_1 and b_1 derived from the test data, since there is no sound theoretical way to determine that part of the hydraulic losses which depends on Re and roughness.

The friction coefficients are evaluated from Eqs. (T16 and T17) using Re as defined by Eq. (T2). In order to avoid any discontinuity in the function $c_f = f(\text{Re})$ always the larger value of $c_{f,turb}$ and $c_{f,lam}$ was used. When impeller and diffuser or volute have different roughness, a weighted average of the roughness has been used as defined in Eq. (T6); the weighting factors are determined experimentally as described below.

4 Analysis of Test Data

4.1 Roughness Test Data. A total of 19 pumps has been evaluated (18 were industrial pumps, one pump from [28]). From these pumps 32 pairs of tests were available where the roughness of impeller channels, impeller side disks, diffuser or volute and/or casing side room walls have been changed. In most of the tests the roughness of only one of the above components has been modified at a time in order to determine the roughness influence of individual surfaces. The roughness was modified by sand blasting, grinding or by applying a coating (in [28] by gluing sand grains). During 2×2 tests the Reynolds number has been varied by speed and/or water temperature. The test data cover the following range of parameters: $n_q = 7$ to 135; $D_2 = 180$ to 405 mm; $n = 1200$ to 7000 rpm; $u_2 = \omega r_2 = 22$ to 113 m/s; $T = 20$ to 160°C; $\text{Re} = 2.5 \times 10^6$ to 9.1×10^7 ; average roughness $\varepsilon_{CLA} = 0.4$ to 75 μm and equivalent sand roughness $\varepsilon = 1$ to 130 μm .

4.2 Procedure for Test Data Evaluation. Using the formulas in Table 1 and with the assumptions described above, all test data have been analyzed. For each of the 32 test pairs the data file contains a “model” or “baseline” test (subscript M) with one roughness, speed and viscosity and a “prototype” test (subscript a) with one or more of these parameters different. For each pair of tests the ratios of measured overall and hydraulic efficiencies can be determined:

$$f_{\eta,\text{test}} = \frac{\eta_{a,\text{test}}}{\eta_M} \quad f_{\eta_h,\text{test}} = \frac{\eta_{ha,\text{test}}}{\eta_{hM}} \quad (13)$$

The predicted efficiency multiplier $f_{\eta,\text{pred}}$ was calculated from Eq. (T20), while Eq. (T19) yields $f_{\eta_h,\text{pred}}$. The efficiency ratios E_R of prediction to test

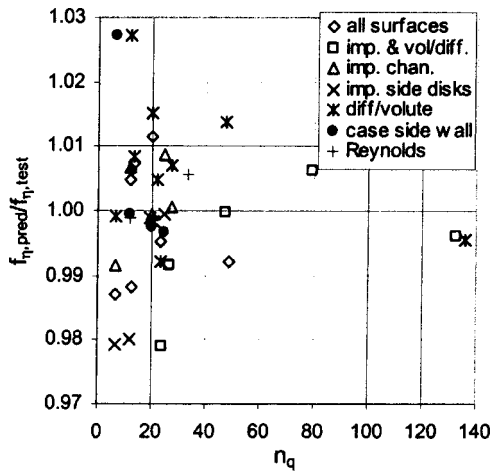


Fig. 1 Multipliers for overall efficiency versus specific speed

$$E_{R,\eta} = \frac{f_{\eta,\text{pred}}}{f_{\eta,\text{test}}} \quad E_{R,\eta_h} = \frac{f_{\eta_h,\text{pred}}}{f_{\eta_h,\text{test}}} \quad (14)$$

are used to assess the accuracy of the prediction (when these ratios are 1.0 prediction is equal to test).

The roughness weighting factor a_e of Eq. (T6) and the empirical coefficients a_1 and b_1 in Eq. (T18) have been optimized to achieve an average of the efficiency correction factors $\Sigma E_{R,\eta}/N_t = 1.0$ and $\Sigma E_{R,\eta_h}/N_t = 1.0$ and to minimize the standard deviation (N_t = number of tests).

4.3 Results. The ratios of predicted to measured efficiency scaling factors defined by Eq. (14) are plotted in Figs. 1 and 2 against the specific speed, while Figs. 3 and 4 compare measured versus predicted change in efficiency. The labels used for the various data points in these graphs define which parameters had been modified; (“all surfaces” means that roughness of impeller, volute/diffuser, impeller side disks and side room casing were modified. The results show:

- most of the predicted efficiency differences $\Delta\eta$ lie between $\pm 1\%$ (band defined by dotted lines in Figs. 3 and 4). This accuracy may be deemed acceptable when large efficiency differences are involved (e.g., a drastic improvement in surface roughness for a

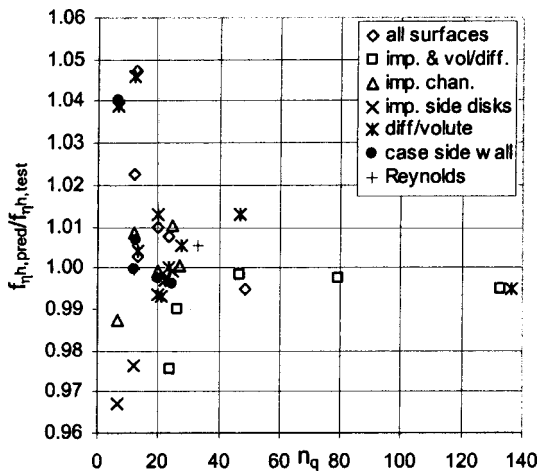


Fig. 2 Multipliers for hydraulic efficiency versus specific speed

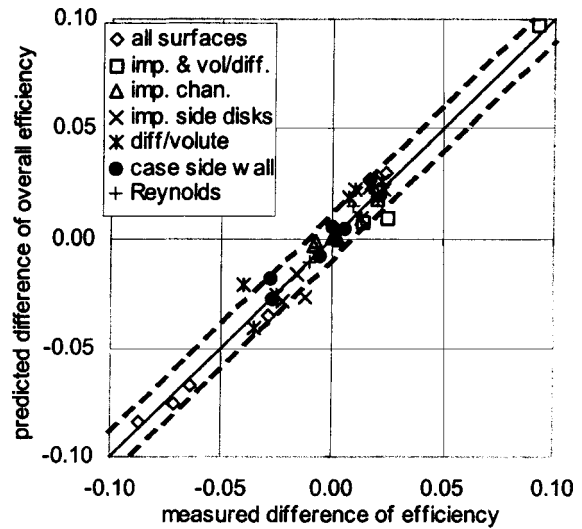


Fig. 3 Difference between predicted and measured overall efficiency

pump of moderate size) but it is not really sufficient to predict a small improvement. Still, at present it may provide the best estimate.

- standard deviation for $E_{R,\eta}$ is $\pm 1.0\%$ and for E_{R,η_h} it is $\pm 1.5\%$.
- within the scatter all combinations of roughness modifications are equally well represented by the calculation. This includes those cases where only the casing wall in the impeller side rooms were modified (corroborating the choice of Eqs. (T7 to T9).
- scatter increases for low specific speed pumps because of the uncertainty of predicting disk friction and volumetric losses which gather importance as n_q is reduced.
- for the same reason the scatter of hydraulic efficiency prediction is larger than for overall efficiency prediction, since η_h is calculated from Eq. (T15) and depends thus strongly on P_{RR} and η_{vol} for low n_q .
- by a more rigorous analysis of volumetric losses and their impact on disk friction the accuracy with low n_q could possibly be improved.

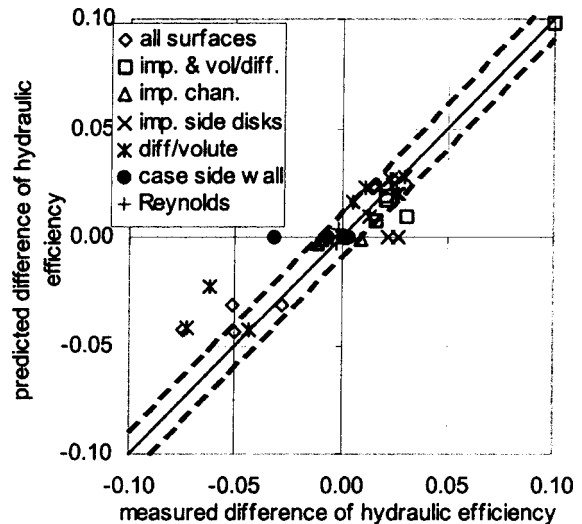


Fig. 4 Difference between predicted and measured hydraulic efficiency

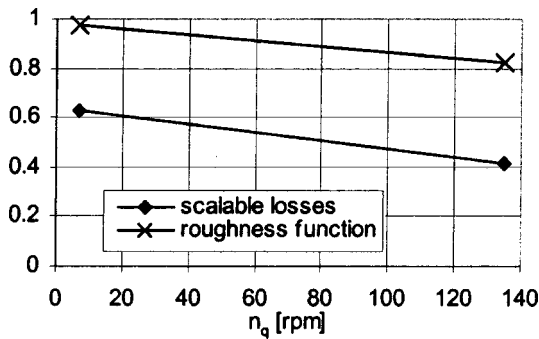


Fig. 5 Fraction of scalable losses in hydraulic passages and roughness function

- varying the roughness equivalence factor c_{eq} or the ratio $\varepsilon_{\max}/\varepsilon_a$ demonstrated that the values defined above with Eq. (9) were about optimum, i.e., resulted in the smallest standard deviation.

- the roughness weighting factor in Eq. (T6) decreases with increasing specific speed, Fig. 5, which may be expected intuitively. The resulting dependence $a_e = 0.98 - 0.0012 n_q \sqrt{f_q}$ demonstrates the preponderance of the diffuser or volute losses over roughness effects in the impeller. For low n_q pumps this finding is no surprise; but even at $n_q = 150$ we find $a_e = 0.82$ which suggests that at high specific speeds diffuser roughness is still important, even though the contribution of the diffuser to the head rise provided by the pump declines as n_q grows. Although more test data would be welcome to corroborate this finding, it is physically plausible, since the deceleration in the diffuser or volute is much more sensitive to changes in the boundary layer flow (e.g., by roughness effects) than the impeller where boundary layers are subject to strong centrifugal forces. It should be noted, however, that a_e is a factor only to determine a suitable average of roughness effects in impeller and diffuser/volute; the weighting factor does not imply that the absolute losses in the impeller are of little concern with high n_q pumps: When absolute losses in the impeller are high (which is expected at high n_q) surface quality of the impeller remains important.

- the fraction of scalable hydraulic losses as defined by Eq. (T18) was found to decrease with the specific speed, Fig. 5, confirming the expectation that friction losses are most important for low n_q applications.

5 Highly Viscous Fluids

As mentioned above the loss analysis method, [12], as applied to pumps operating with highly viscous fluids has been refined in the present contribution. It was therefore of interest to check whether the new procedure could be used also for high viscosities. Following the logic in Section 4.2 and [12] the test data reported in [12,13,15,19,29,30] have been analyzed (using equations of Table 1) with one modification: The mechanical losses of small process pumps can be appreciably higher than estimated from Eq. (T14); also the absence of detailed design data makes a calculation of the hydraulic efficiency from Eq. (15) uncertain; for these reasons the hydraulic efficiency has been estimated from $\eta_h = 0.5(1 + \eta)$ if overall efficiency with water performance was reported below $\eta = 0.5$. Thus unrealistically high theoretical heads, which would follow from very low hydraulic efficiencies, were avoided. The predicted and measured correction factors for overall efficiency and head have been plotted in Figs. 6 and 7 against a modified Reynolds number (Re_{mod}) defined in Eq. (15), which accounts for the influence of specific speed and single versus double-entry impellers.

$$Re_{\text{mod}} = Re \omega_s^{1.5} f_q^{0.75} \quad (15)$$

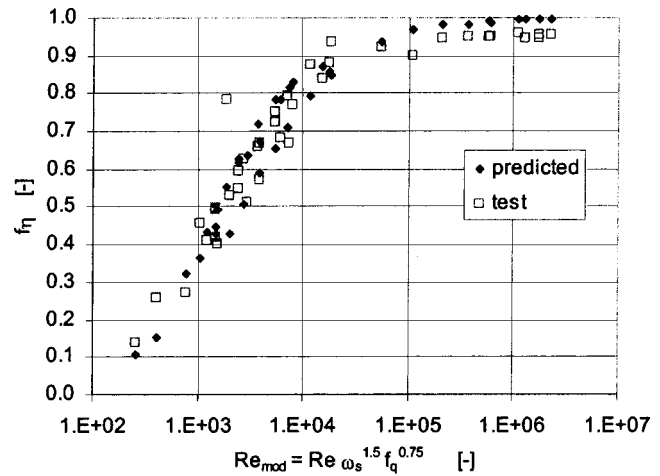


Fig. 6 Predicted versus measured overall efficiencies for highly viscous flows

The use of Re_{mod} reduces the data spread in plots like Figs. 6 or 7 and allows thus to compare tests with different pumps, but has, of course, no impact on the prediction. Since test data from different pumps were plotted in Figs. 6 and 7, not all of the data spread is due to any difference between prediction and test. The actual accuracy of the prediction in terms of standard deviation is about $\pm 15\%$. Overall the efficiency impairment is hence fairly well predicted in a wide range: $250 < Re_{\text{mod}} < 10^7$ or $1500 < Re < 10^8$. Effects of pump size, type, and specific speed are accounted for in a first approximation. Some of the scatter is due to the fact that roughness and axial side room clearances had to be assumed as typical for industrial process pumps, since no design details of the pumps analyzed have been available. Another source of uncertainty are thermal effects: high wall shear stresses with fluids above 1000 cSt lead to a local increase in fluid temperature and an associated reduction in local viscosity and friction factor, [12,14]. Applying the empirical factor f_{therm} from [12] slightly improves the prediction, but a detailed analysis is beyond the scope of this contribution. Any factor f_{therm} would also depend on the rate of heat removal from the boundary layer (hence Nusselt and Prandtl numbers, pump design details). The widely used statistical procedure for viscous performance prediction of [11] or the loss analysis procedure used in [13] witness to the difficulty of precise performance prediction with highly viscous fluids.

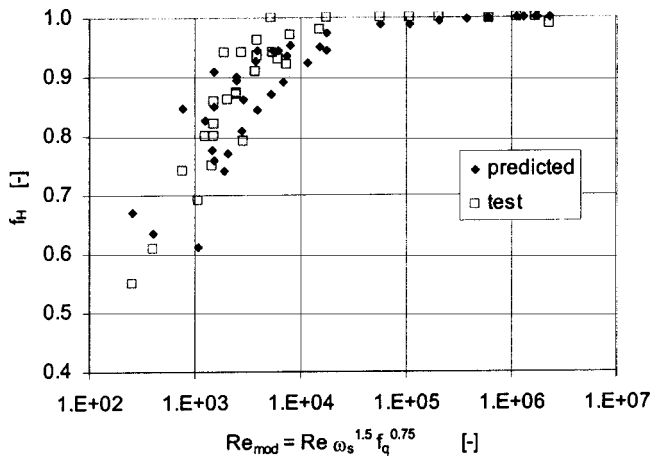


Fig. 7 Predicted versus measured hydraulic efficiencies for highly viscous flows

When applying the procedure given in Table 1 to predict performance with high viscosities (say above 100 cSt) it should be noted that the best efficiency point moves on the diffuser/volute characteristic to lower flow as the losses increase ($f_Q = f_H < 1$); the complete procedure to estimate viscous performance curves is described in [12].

6 Discussion of Results

The large number of publications on efficiency scaling testifies to the fact that this is essentially an unsolvable problem: One attempts to predict accurately a small difference between two comparatively large figures. Such attempts are inherently subject to considerable uncertainties which are discussed below.

Testing uncertainties: Quite often the true efficiency difference is in the range of 0.5 to 2%. If the prototype is scaled from a model test to larger dimensions and/or speed, the testing is usually done in different installations, e.g., a model test is compared to a works test (or even plant test) with the prototype. The absolute measuring errors of both tests stands clearly limit the efficiency difference due to scaling, which can be determined with confidence, since the measured efficiency difference can be in the range of $\Delta \eta_{\text{measured}} = \Delta \eta_{\text{true}} \pm (\delta_a + \delta_M)$ if $\Delta \eta_{\text{true}}$ is the true (unknown) scale effect and δ_a , δ_M are the measuring tolerances of prototype and model. In industrial pump testing $\delta_a = \delta_M = \pm 0.5\%$ may be a good estimate; efficiency measurement in plants may have tolerances of about $\pm 1\%$ but often above.

In the present investigation (with one exception) any given pump performance has been measured with different roughness (or speed) in the same test loop; hence only the reproducibility of the readings has affected the test data. The reproducibility is estimated to about 0.2 to 0.3% at maximum.

When scaling the efficiency from cold to hot conditions the thermal expansion of the impeller (d_2 and b_2) has an impact on the head and power, [31].

Statistical relevance: The method in Table 1 uses five empirical parameters: Eqs. (T6) and (T18) and c_{eq} . Changing the optimized parameters in various ways gives correlations of similar accuracy (albeit with slightly increased standard deviation). More test data would be needed to improve the statistical relevance of the empirical coefficients.

Roughness effects may be considered as most critical with respect to scaling accuracy, because they are difficult to quantify for a number of reasons:

1. The roughness has been determined by comparing the hydraulic component to a surface quality standard (“rugotest”) as used in the industry. Such measurements are to some degree subject to individual judgement. Changing the roughness by a few μm has an impact on the predicted efficiency. More sophisticated roughness measurements may not really improve the situation because of reasons discussed below.

2. Often the roughness of pump components is not uniform throughout the surface according to the accessibility for cleaning, grinding, or coating.

3. The actual structure of both surface roughness and turbulence near the wall determine the influence of the roughness on the losses. Height, pitch, and density of roughness elements as well as their direction with respect to the flow have an important impact on the losses. The interaction between roughness elements and turbulence depends in particular on the density of the roughness elements on the surface, this is demonstrated by Fig. 8 where the equivalence factor is plotted against the ratio of roughness pitch to height (data from [26] and [32]). Equivalence factors reported in the literature for technical surfaces can therefore assume any value between 0.5 to 5; refer also to [1–4,26,28,33,34]. Figure 8 allows to estimate the equivalence factor for a given (measured) roughness.

4. The interaction between roughness and turbulence may be illustrated by two extremes: (a) Tests with small grooves parallel

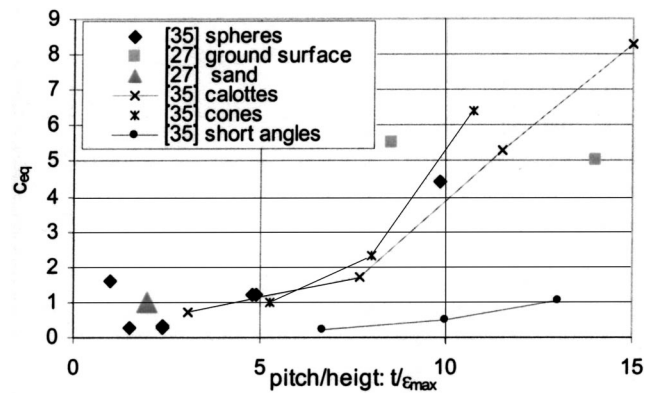


Fig. 8 Roughness equivalence factor as function of roughness pitch to height

to the flow direction reduced disk friction losses by up to 10%, [35]. Such grooves must be dimensioned in accordance with the turbulence scale near the wall (Reynolds number). (b) A strong increase in losses can be caused on the other hand by a ripple type roughness perpendicular to the flow direction. Such ripples are generated by the flow itself: wall near turbulence creates/erodes a pattern of deposits with a regular wavy structure (as sand ripples formed by wind or water) creating excessive pressure drop as observed sometimes in boiler tubes or pipelines with deposits.

5. While in pipe flow (or other flows with $dp/dx < 0$) the losses increase with increasing wall shear stress, losses in decelerated flow ($dp/dx > 0$) grow with decreasing shear stress: at flow separation ($\tau_w = 0$) there are high (mixing) losses with zero wall stress (theoretically zero “friction” loss). To put it in another way: a diffuser with rough walls has lower “friction” losses than a diffuser with smooth walls, but higher overall (mixing) losses, because the roughness leads to less uniform velocity profiles. The effect of any given roughness on the losses therefore depends on the velocity profiles and near-wall turbulence within the hydraulic passages. The nonuniformity of the velocity distributions in the hydraulic channels is expected to increase with the specific speed. The portion of Reynolds-dependent losses on the head, $\zeta_{R,M}/\psi_M$, is determined by this effect, which cannot be calculated by simple loss models such as given in [5,13,16,17]. It is for this reason that $\zeta_{R,M}/\psi_M$ has been determined by a correlation derived from the test data, Eq. (12), rather than from theoretical calculations. Also CFD calculations appear to be unable to model losses correctly, since often the wall shear stress is imposed by a wall function for smooth or rough flow conditions.

6. The physical concept of “friction” versus “form” or “mixing” losses makes sense for fully attached versus fully separated flows. The notion appears less meaningful in decelerated flows or flows with strongly nonuniform velocity profiles.

For very low Reynolds numbers $f_{\eta h}$ from Eq. (T19) can become zero or negative. Physically this would make no sense; for viscosities above 1000 cSt and low Reynolds numbers thermal effects may become appreciable. The friction factors to be used in Eq. (T19) must then be evaluated with some local viscosity.

Disk friction and volumetric losses as calculated from the correlation in Table 1 or other sources are subject to considerable uncertainty. Again roughness effects are one of the causes; this is true also for leakage losses (it is not correct to consider the machined surfaces of labyrinth as smooth, since the relative roughness is always high because of the small absolute clearances). Leakage flow and disk friction interact; this interaction depends on the velocity distribution at the impeller outlet (disk friction decreases with growing leakage flow and circumferential velocity at the impeller exit), [21]. These effects and associated uncertainties are important with low specific speed pumps but lose influ-

ence with increasing n_q . The uncertainty of efficiency scaling with high n_q thus is mainly influenced by the roughness of the hydraulic passages and its interaction with local velocity distributions.

7 Conclusions and Recommendations

- Table 1 provides a step-by-step procedure for the prediction of roughness and Reynolds effects on overall efficiency and hydraulic efficiency; this includes laminar flow when pumping highly viscous fluids.

- The procedure for efficiency scaling is based on physical models which are valid for laminar and turbulent, smooth or fully rough flows and the transition between any of these regimes. For viscosities above 1000 to 2000 cSt the local heating of the fluid and its influence on the viscosity in the boundary layer becomes important, but no easy methods are available to calculate this effect.

- The lower the hydraulic efficiency the higher is the gain from surface improvement.

- The higher the Reynolds number the more is to be gained from surface improvement.

- At a given Reynolds number the *relative* roughness ε/r_2 is relevant. Surface improvement with small pumps brings therefore a higher efficiency gain than with large pumps.

- When changing the roughness or the Reynolds number the effect on the Q - H curve is confounded with three other influences: (1) the Q - H curve is shifted slightly to smaller flow when the Reynolds number increases due to an increased leakage; (2) the roughness of the impeller channels may modify the flow pattern within the impeller due to a change in boundary layer thickness and secondary flow, having a slight impact on slip factor and theoretical head; (3) the pumping action of the impeller side disks is influenced by their roughness.

- The hydraulic losses depend on the actual roughness geometry, near-wall turbulence and the local velocity distributions in the hydraulic passages. Roughness and turbulence are statistical phenomena; the same may be said almost of velocity distributions in impellers and diffusers—within present knowledge. These effects are not yet amenable to analysis; they inherently limit the accuracy of any efficiency prediction procedure for decelerated flows. More test data can improve the statistical relevance but scarcely remove the scatter.

- When estimating the performance of highly viscous fluids the present method should not be extrapolated to $Re_{mod} < 250$ or $\nu > 3000$ cSt, because local heating of the fluid in the boundary layer is not accounted for.

Nomenclature

b_2 = impeller exit width
 c_{eq} = roughness equivalence factor, Eq. (9)
 c_f = friction coefficient of a flat plate, Eqs. (T16), (T17)
 d_2 = impeller outer diameter
 $f, f_\eta, f_{\eta h}$ = (efficiency) multipliers, Eq. (6)
 f_q = impeller eyes per impeller: single-entry $f_q = 1$; double-entry $f_q = 2$
 g = acceleration due to gravity (rounded: $g = 9,81$ m/s²)
 H = head *per stage*
 $k_o = c_u / (\omega r)$ = fluid rotation factor for impeller side room, Eq. (T8)
 k_{RR} = disk friction factor, Eq. (T9)
 n = rotational speed (rpm)
 n_q = specific speed (rpm, m³/s, m), Eq. (T1)
 P = power at coupling, Eq. (4)
 P_i = inner power: $P_i = P - P_m$
 P_m = mechanical power losses, Eq. (T14)
 P_{RR} = disk friction power loss, Eq. (T9)

P_u = useful power transferred to fluid $P_u = \rho g H_{tot} Q$
 Q = useful volumetric flow rate (in discharge branch)
 Q_E = flow rate through axial thrust balancing device
 Q_{sp} = leakage flow rate through impeller neck ring, Eq. (T3)
 Q_{s3} = leakage flow rate through interstage seal
 Re = Reynolds number, Eq. (T2)
 r_2 = impeller outer radius
 s_{ax} = width of axial gap between impeller and casing
 V = fraction of nonscalable losses (independent from Re and ε), Eq. (1)
 z_{st} = number of stages
 ε = equivalent sand roughness, Eq. (9)
 ε_{CLA} = average depth of roughness (CLA, AA), Eq. (9)
 ε_{max} = maximum depth of roughness, Eq. (9)
 η_{vol} = volumetric efficiency, Eq. (T4)
 η = overall efficiency (at coupling), Eq. (4)
 η_i = inner efficiency: $\eta_i = \eta / \eta_m$
 η_h = hydraulic efficiency: $\eta_h = H / H_{th}$
 η_m = mechanical efficiency: $\eta_m = 1 - P_m / P$
 ζ_R = hydraulic friction losses (i.e., scalable losses in impeller, volute, diffuser)
 ζ_M = mixing (nonscalable) losses
 λ_R = friction coefficient for pipes and channels, Eq. (2)
 ν = kinematic viscosity
 ρ = density
 φ = flow coefficient: $\varphi = Q / (2 \pi b_2 \omega r_2^2)$
 ψ = head coefficient: $\psi = 2 g H / (\omega r_2)^2$
 ψ_{th} = theoretical head coefficient (Euler head)
 ω = angular rotor velocity
 ω_s = universal (dimensionless) specific speed, Eq. (T1)

Subscripts, Superscripts, and Abbreviations

a = prototype, changed roughness or viscosity
 M = model or baseline or water performance
 pred = predicted from loss analysis method per Table 1
 opt or
 BEP = operation at maximum efficiency (BEP)
 imp = impeller side disk (hub or shroud)
 Ref = reference value
 sp = gap, leakage flow
 test = derived from experiment

References

- [1] Osterwalder, J., 1978, "Efficiency Scale-Up for Hydraulic Turbo-Machines With due Consideration of Surface Roughness," *J. Hydraul. Res.*, **16**(1), pp. 55–76.
- [2] Osterwalder, J., and Hippe, L., 1981, *Betrachtungen zur Aufwertung bei Serienpumpen*, VDI-Berichte (424), pp. 1–17.
- [3] Osterwalder, J., and Hippe, L., 1984, "Guidelines for Efficiency Scaling Process of Hydraulic Turbo-Machines With Different Technical Roughnesses of Flow Passages," *J. Hydraul. Res.*, **22**(2), pp. 77–102.
- [4] Hippe, L., 1984, "Wirkungsgradaufwertung bei Radialpumpen unter Berücksichtigung des Rauheitseinflusses," Diss. TH Darmstadt.
- [5] Güllich, J. F., 1999, *Kreiselpumpen—Ein Handbuch für Entwicklung, Anlagenplanung und Betrieb*, Springer, Berlin.
- [6] Wiesner, F. J., 1979, "A New Appraisal of Reynolds Number Effects on Centrifugal Compressor Performance," *ASME J. Eng. Gas Turbines Power*, **101**, pp. 384–396.
- [7] Strub, R. A., et al., 1987, "Influence of the Reynolds Number on the Performance of Centrifugal Compressors," *ASME J. Turbomach.*, **109**, pp. 541–544.
- [8] Casey, M. V., 1985, "The Effect of Reynolds Number on the Efficiency of Centrifugal Compressor Stages," *ASME J. Eng. Gas Turbines Power*, **107**, pp. 541–548.
- [9] Guiton, P., and Canavelis, R., 1970, "Contribution à l'étude de l'effet d'échelle sur le rendement des pompes," IAHR Symp. Stockholm, Paper D2.
- [10] Ida, T., 1979, "Analysis of Scale Effects on Centrifugal Pumps," *Science Reports of Research Inst. for Engng Kanagawa University, Japan* (2), pp. 21–43.

- [11] Hydraulic Institute, *Standards for Centrifugal, Rotary & Reciprocating Pumps*, 1983, 14th Ed., Hydraulic Institute, Cleveland, OH.
- [12] Gülich, J. F., 1999, "Pumping Highly Viscous Fluids With Centrifugal Pumps," *World Pumps*, **395**(6).
- [13] Hamkins, C. P., et al., 1987, "Prediction of Viscosity Effects in Centrifugal Pumps by Consideration of Individual Losses," *ImechE*, **C112/87**, pp. 207–217.
- [14] Stoffel, B., et al., 1978, "Untersuchungen von Einzelverlusten in Kreiselpumpen bei viskosen Flüssigkeiten," Pumpentagung Karlsruhe, K10.
- [15] Hergt, P., et al., 1981, "Verlustanalyse an einer Kreiselpumpe auf der Basis von Messungen bei hoher Viskosität des Fördermediums," VDI Ber 424.
- [16] Neumann, B., 1991, *The Interaction Between Geometry and Performance of a Centrifugal Pump*, MEP, London.
- [17] Lauer, J., and Stoffel, B., 1997, "Theoretische Untersuchungen zum maximal erreichbaren Wirkungsgrad von Kreiselpumpen," *Industriepumpen + Kompressoren*, **3**(4), pp. 222–228.
- [18] Varley, F. A., 1961, "Effects of Impeller Design and Surface Roughness on the Performance of Centrifugal Pumps," *Proc. Inst. Mech. Eng.*, **175**(21), pp. 955–969.
- [19] Li, Wen Guang, 2000, "The "Sudden-Rising Head" Effect in Centrifugal Oil Pumps," *World Pumps*, **409**, pp. 34–36.
- [20] Grein, H., 1975, "Einige Bemerkungen über die Oberflächenrauheit der benetzten Komponenten hydraulischer Großmaschinen," *Escher Wyss Mitteilungen* (1), pp. 34–40.
- [21] Gülich, J. F., 2002, "Disk Friction Losses of Closed Turbo Machinery Impellers," submitted to *Forsch Ing Wes (Engineering Research)*, **68**.
- [22] Dailey, J. W., and Nece, R. E., 1960, "Chamber Dimension Effects on Frictional Resistance of Enclosed Rotating Disks," *ASME J. Basic Eng.*, **82**, pp. 217–232.
- [23] Pantell, K., 1949, "Versuche über Scheibenreibung," *Forsch Ingenieurwes*, **16**(50), pp. 97–108.
- [24] Linneken, H., 1957, "Der Radreibungsverlust, insbesondere bei Turbomaschinen," *AEG Mitt*, **47**(1/2), pp. 49–55.
- [25] Nece, R. E., and Daily, J. W., 1960, "Roughness Effects on Frictional Resistance of Enclosed Rotating Disks," *ASME J. Basic Eng.*, **82**, pp. 553–562.
- [26] Fukuda, H., 1964, "The Effect of Surface Roughness on the Performance of a Francis Turbine," *Bull. JSME*, **7**(26), pp. 346–356.
- [27] Geis, H., 1985, "Experimentelle Untersuchungen der Radseitenverluste von Hochdruck-Wasserturbinen radialer Bauart," Diss. TH Darmstadt.
- [28] Münch, A., 1999, "Untersuchungen zum Wirkungsgradpotential von Kreiselpumpen," Diss. TU Darmstadt.
- [29] Saxena, S. V., et al., 1996, "Ermittlung von Korrekturfaktoren für Hochleistungs-Pipeline-Kreiselpumpen beim Fördern von Mineralölen mit erhöhter Viskosität," Pumpentagung Karlsruhe, Paper C7-3.
- [30] Mollenkopf, G., 1976, "Einfluß der Zähigkeit des Fördermediums auf das Betriebsverhalten von Kreiselpumpen unterschiedlicher spezifischer Schnel-läufigkeit," Pumpentagung Karlsruhe, K10.
- [31] Gülich, J. F., et al., 1991, "Rotor Dynamic and Thermal Deformation Tests of High-Speed Boiler Feedpumps," EPRI Report GS-7405, July.
- [32] Schlichting, H., 1982, *Grenzschicht-Theorie*, 8. Aufl, Braun, Karlsruhe.
- [33] Childs, P. R. N., and Noronha, M. B., 1999, "The Impact of Machining Techniques on Centrifugal Compressor Impeller Performance," *ASME J. Turbomach.*, **121**, pp. 637–643.
- [34] Nichtawitz, A., 1996, "Further Development of Step-Up Formula Considering Surface Roughness," *18th IAHR Symp*, pp. 343–351.
- [35] Brodersen, S., 1993, "Reduzierung der Scheibenreibung bei Strömungsmaschinen," *Forsch Ingenieurwes*, **59**, pp. 184–186.
- [36] Churchill, S. W., 1988, *Viscous Flows. The Practical Use of Theory*, Butterworth Ser Chem Engng, London.

A Criterion to Define Cross-Flow Fan Design Parameters

A. Lazzaretto

Department of Mechanical Engineering,
University of Padova,
Via Venezia, 1,
35131 Padova, Italy

The paper presents an original criterion to parameterize systematically a cross-flow fan configuration according to the most significant variables defining the geometry and then affecting performance and efficiency. This choice of parameters has proved to be effective in a systematic series of experimental tests aimed at investigating directions for design improvement. [DOI: 10.1115/1.1593709]

Introduction

Theoretical and experimental studies appearing in the literature, [1–19], do not set definite criteria about cross-flow fan design. These mainly depend on the complexity of the flow field within the impeller, always featuring an eccentric vortex (Fig. 1) the shape and position of which is directly influenced by the impeller and casing geometry, and affects fan performance and efficiency. To define cross-flow fan geometry in a general way, many variables are required, having more or less influence on different characteristics of fan performance (i.e., pressure coefficients, efficiency, flow rates).

A criterion for selecting the geometrical variables that define in a general sense the geometry of the impeller and shape and position of the casing walls is presented here starting with a short review of theoretical and experimental work by others on the influence of geometrical design parameters on cross-flow fan performance. The approach mainly focuses on casing geometry and is based on the simple idea that the area around the impeller is to be divided into sectors either “covered” by the casing walls or free to form the suction and delivery zones. The geometry of rear and vortex walls are defined to include all the positions that supply good fan performance using the minimum number of independent variables. Experimental tests showing the effectiveness of the presented geometry parameterization are shown in [20].

Cross-Flow Fan Design in the Literature

Impellers. A simplified, one-dimensional, theoretical model of the double passage through the blade cascade was proposed by Eck [9]. He argued that the only case in which shock-free operation is possible occurs when the internal blade angle (β_1 in Fig. 2) equals 90 deg. β_1 can be lowered to 75 deg if the effects of a finite number of blades is considered. On the other hand, only the external blade angle (β_2) is important in determining the overall energy transfer, [9]. The lower the external blade angle, the higher the fan performance in terms of total pressure coefficient in spite of largely negative reactions. Ikegami and Murata [4] and Yamafuji [12,13] developed detailed analytical flow models in which shockless flow inside the impeller is obtained for $\beta_1 = 90$ deg and the total pressure coefficient depends on the only cotangent of β_2 .

Some authors in the literature, [3,6], consider the effect of impeller design on cross-flow fan performance only secondary, without providing clear evidence neither theoretical nor experimental. Some others, [18,19], propose a range of blade angles they consider as optimal. Most of the researchers, [6,17,21–23], realize that the best performance is obtained in defined ranges based on previous experience, and choose impeller blade angles within those ranges.

Casing Shapes. Several experimental investigations [6,8,9,14,15,21] have been conducted in the literature on the effects of casing shape on performance, but a general design method is still not available. Eck's research led to a high efficiency and low noise patented casing configuration, [10]. The rear wall profile is made up of two circular arcs and results in a small radial width, the clearance between the nearest of the two circular arcs and the impeller being constant. The vortex wall is thick and has a decreasing clearance in the direction of rotation. It also shows a diffusing section immediately before discharge.

The basic casing shape in Preszler and Lajos's [8] test fan features a wider rear wall having a single circular arc profile and a vortex wall similar to Eck's (thick wall, decreasing clearance, diffusing section). The angle of the diffusing section, vortex wall clearance size, and suction to discharge arc ratio were varied one at a time. Characteristic curves of head and flow coefficients were given but information on some of the geometric parameters, the test method, and experimental rig were omitted, as observed by Clayton [11].

Porter and Markland [6] simplified Eck's vortex wall using a straight thin wall with a simple radius close to the impeller. This modification led to a marked increase in pressure and flow rate but lower efficiency. Then, they introduced a log-spiral rear wall to have a stronger vortex, placed at the internal periphery of the impeller at all flow conditions, that moves towards the rear wall as the flow is reduced. A stable characteristic curve was obtained, maximum flow rate being increased by 60% and static pressure more than doubled. Total pressure was also higher than Eck's and fairly constant, but peak efficiency was somewhat lower owing to the fact that the impeller and blades pass through the closed vortex for all flows.

The need of standardization was stressed in a comprehensive review by Clayton [11], for an even comparison of performance characteristics obtained using different test rigs.

The design parameters chosen by Murata and Nishihara [14,15] in a systematic investigation of fan performance were not independent from each other. The rear wall profile is a single circular arc of variable width. The vortex wall consists of a simple flat plate, which can be positioned at different heights and distances with respect to the impeller. The experimental tests showed that lower clearances and lower heights of the vortex wall result in higher total pressure coefficients at intermediate flow rates. These two parameters, however, should be set together, since their mutual influence on the maximum attainable total pressure coefficient is strong. The length of the rear wall arc also has a great influence upon both total pressure and efficiency; however, this influence is mixed because of the interactions with the two other design parameters.

Allen [16] demonstrated that the aerodynamic performance mainly depends on five primary parameters of the casing, and established limits within which rotor and casing geometry should remain to obtain an optimal fan design. However, results were

Contributed by the Fluids Engineering Division for publication in the JOURNAL OF FLUIDS ENGINEERING. Manuscript received by the Fluids Engineering Division January 14, 2002, revised manuscript received January 31, 2003. Associate Editor: Y. Tsujimoto.

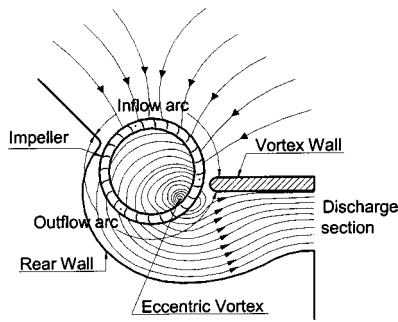


Fig. 1 A cross-flow fan configuration

presented for one parameter at a time without supplying values of the other parameters and thus can be used with some difficulty in the overall cross-flow-fan design.

Martegani et al. [21] performed several tests on a 100 mm rotor by varying one geometric parameter of the casing at a time. A new criterion for the parameterization of the casing geometry and results of tests based on this criterion on a 152.4 mm rotor were then presented by Lazzaretto et al. [22]. An extension and generalization of that work is presented here.

Definition of Design Parameters

Parameters of the Impellers. Cross flow fan impeller blades are usually simple forward-curved thin blades having a circular arc profile. This shape is preferred to aerodynamic profiles because of the double passage of the flow through the blade cascade. The following quantities are required to define univocally the geometry of the impeller (Fig. 2): length to external diameter ratio (L/D_2), internal to external diameter ratio (D_1/D_2), number of blades (Z), and internal and external blade angles (β_1/β_2).

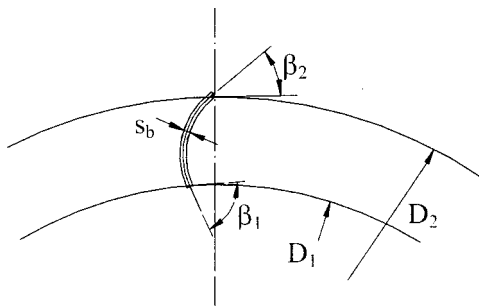


Fig. 2 Impeller geometry

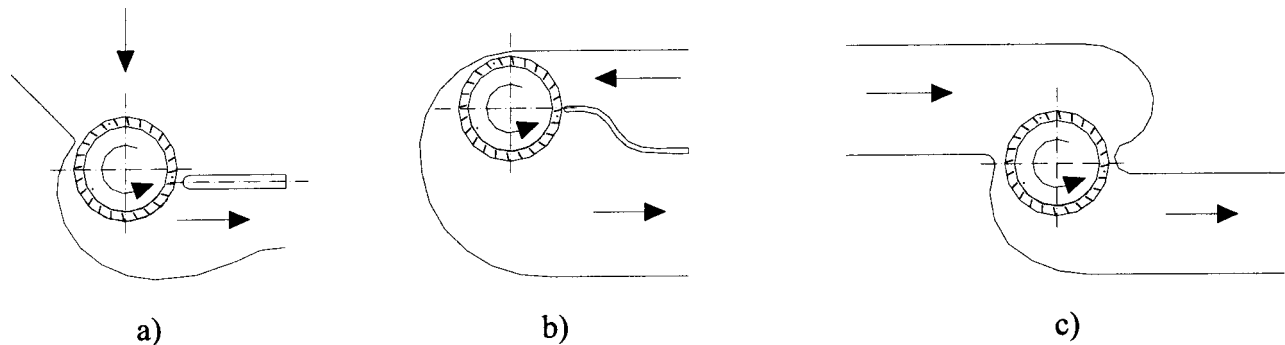


Fig. 3 Various cross-flow fan configurations characterized by different angles between inlet and outlet flows: (a) 90 deg, (b) 180 deg, (c) 0 deg

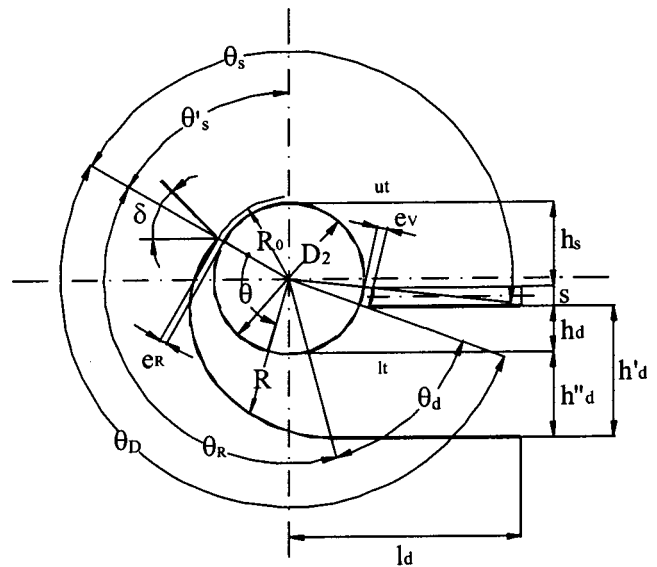


Fig. 4 Geometric variables of the casing walls

Blade thickness is not included in the list, since it is often imposed by structural or technological constraints. The set of parameters defining the shape of the impeller is therefore

$$\tau_1 = \{L/D_2, D_1/D_2, Z, \beta_1, \beta_2\}. \quad (1)$$

Parameters of the Casing. The directions of inflow and outflow streams can be very different in cross-flow fans depending on the application being considered. Accordingly, the casing assumes different shapes, as shown in Fig. 3.

The question arises of how the two casing walls fill the space around the impeller. The arc occupied by the rear wall around the impeller (Fig. 1) mainly depends on the directions of inlet and outlet flows. On the other hand, the vortex wall has often a simple shape, like the flat one, with different angles with respect to the outflow direction. Depending on its thickness, the vortex wall covers different arcs around the impeller, too. Besides the two walls the space around the impeller is occupied by the inflow and outflow zones, the extension of which depends on the dimensions of the two walls. It is the right combination of shape and dimension of each part that leads to the best velocity and pressure distribution along suction and discharge zones and, accordingly, to the highest throughflow and energy transfer. Thus, it is crucial to analyze all the ways in which the two casing walls fill the space around the impeller circumferentially and radially. Since these ways are theoretically infinite, the problem is to find a set of polar variables that defines good performance casing shapes. Only the

Table 1 Ranges of variation for the main impeller geometrical parameters according to various authors in the literature (Reynolds number refers to blade chord and impeller tip speed)

Authors	β_1 [deg]	β_2 [deg]	D_2 [mm]	D_1/D_2	L/D_2	Z	N (rpm)	Re
Laakso [1]	-	-	560	0.84	1.27	-	565	49500
Tramosch [2]	90	≈15	60	0.79	2.1	24	1800–3600	2400–4800
Ilberg, Sadeh [3]	90	45	230	0.74	0.26	44	1000–2600	24,000–62,000
Porter, Markland [6]	70–90	25–45	152	0.70–0.80	1.5	24	2000–2250	16,000–18,000
Preszler, Lajos [8]	90–97	22–30	-	0.80–0.86	0.94–1.0	36	-	-
Yamafuji [12], [13]	≈90	15–45	157–160	0.63–0.91	0.66–0.71	18–35	1200	4700
Murata, Nishihara [14], [15]	90	25	120–240	0.80–0.83	1.17–2.33	30	600–1200	5100
Allen [16]	90	25–35	95–195	0.72–0.76	2.05–3.37	24–36	-	-
Tuckey et al. [17]	90	26	625	0.78	1.6	24	400	60000
Tanaka, Murata [18], [19]	90	25	75–200	0.85	1	36	400–2500	1700–15,000
Lazzarotto et al. [23]	70	38	86–199	0.81	1.5	24	120–2000	1000–20,000

fan type in Fig. 3(a) is considered here, the most common in industrial applications. Separate studies are needed for the other two types in Figs. 3(b) and 3(c).

Rear Wall. The rear wall is artificially subdivided here into two parts to analyze separately the effects on performance. The first part “envelopes” the impeller and defines the rear wall angle θ_R (Fig. 4), the second links the first part with the discharge section. Although the whole rear wall is indeed a channeler, this subdivision aims at verifying whether only the first part or both parts have influence on vortex position and strength, and indirectly on the energy transfer, as suggested in [6,11]. In the past, the second part was often shaped as a diffuser to increase static pressure. However, this solution is not so effective because of strongly nonuniform velocity distribution in the discharge zone. Actually, diffusion depends on the radial width of the first part of the rear wall, which may act as a volute, [17]. Natural diffusion effects are also due to the vortex location and generally take place between the vortex wall and the second part of the rear wall.

To vary the radial width using a single parameter, a log-spiral profile is considered here, as already suggested in [6]:

$$R = R_0 e^{\theta/\theta^*} = R_2 \left(1 + \frac{e_R}{R_2} \right) e^{\theta/\theta^*} \quad (2)$$

where θ^* is the parameter that defines the radial width. The starting point of the rear wall is located at the angle θ'_s measured from the vertical axis of the impeller (Fig. 4). At this point, the radial clearance between rear wall and impeller is e_R . The log spiral arc profile covers the angle θ_R , and it is followed by the duct connecting the fan to the discharge section, having a rectilinear shape, as in Fig. 4, or other curved shapes. The total discharge angle (θ_D) is the sum of the rear wall angle θ_R and the angle of the discharge duct θ_d (or the equivalent height h'_d). In conclusion, the set of parameters defining position and shape of the rear wall is

$$\tau_R = \{ \theta'_s, \theta_R, \theta^*, e_R/D_2, \delta \}. \quad (3)$$

Vortex Wall. The analysis is limited here to flat and horizontal vortex walls, the effects of other shapes being considered as minor, [6,11,16]. Porter and Markland [6] first proposed the use of a flat and constant section vortex wall with rounded shape close to the impeller. They stated that this wall acts mainly as a divider to separate the inflow from the discharge and to locate the vortex center under free blowing conditions. Tuckey et al. [17] and Allen [16] also suggested a simple, flat wall to obtain the best design. Several tests conducted by the author and co-workers with thin walls having a curved leading edge, both upwards or downwards, showed that the position of the end itself mainly acts on performances. Very similar performances can then be obtained using flat walls having the leading edge in the same position.

To define the shape and the position of a flat vortex wall of constant section, the following parameters are chosen here (Fig. 4): wall thickness (s); radial clearance between vortex wall and impeller (e_V); vortex wall height (h_d).

Parameters s and h_d are not strictly consistent with the suggestion of using polar variables. However, they are more practical when considering straight horizontal walls, even though they define the position of the vortex wall only within the upper and lower horizontal tangents to the impeller (ut and lt in Fig. 4). On the other hand, in most of the cross flow fans having the configuration of Fig. 3(a), the position of the vortex wall is included in this range. Preliminary investigations performed by the present author and co-workers confirmed that unacceptable performance is obtained outside this range. For other configurations, as in Figs. 3(b) and 3(c), the polar variables could be more suitable.

According to these choices, the set of nondimensional parameters defining the shape of the vortex wall is

$$\tau_V = \{ s/D_2, e_V/D_2, h_d/D_2 \}. \quad (4)$$

The sets of parameters in Eqs. (3) and (4) completely define the position and shape of the two casing walls under all the hypotheses considered here. Accordingly, the angular dimensions of the inflow and outflow zones are also defined, i.e., the inlet flow angle (θ_s), the total discharge angle (θ_D) and the angle of the discharge duct, θ_d . Moreover, for a given outflow duct, the height of the discharge section h'_d (and, consequently h''_d) is also defined (see Fig. 4).

Planning a Systematic Investigation of Fan Performance and Efficiency

Ranges of Variations for Impeller Design Parameters. The values of the variables included in the set τ_I (see Eq. (1)) adopted in experimental works in the literature are presented in Table 1. Note that most of the analyses were performed using small diameter impellers in a range of operation of low Reynolds numbers in which the cross-flow fan is more competitive than other types, [11]. From Table 1 we observe that

- the impeller length to diameter ratio should, in general, not be lower than 1 to avoid strong border effects.
- many authors, [6,11], showed that the influence of diameter ratio is small in the range $0.7 \leq D_1/D_2 \leq 0.85$.
- the number of blades in the experiments is usually 24. Japanese researchers more commonly used a higher number ($30 < Z < 36$). This design choice is a secondary issue resulting from a compromise between structural characteristics, friction losses and flow deflection due to cascade effect, [17].
- blade angles can be chosen in the ranges $20 \text{ deg} \leq \beta_2 \leq 45 \text{ deg}$ and $70 \text{ deg} \leq \beta_1 \leq 130 \text{ deg}$, according to experimental works in the literature, [6,14–16,21–23]. β_1 is generally set at 90 deg (shock-free entry in the second blade passage according to [9]). Preszler and Lajos [8] found that maximum pressure coefficient and efficiency decrease abruptly for external blade angles lower than 20 deg. Angles at the limits of the above ranges did not lead to good performance in any of the mentioned works, and can generally be avoided.

Ranges of Variations for Casing Design Parameters

Rear Wall. The highest performances were obtained in the literature using θ_R in the range 120–155 deg, [3,6,9,14,15,21]. Other authors, [8,16], do not supply exact information about this parameter.

Various experiments conducted by the present author and co-workers demonstrated that optimal performances are achieved for $50 \text{ deg} \leq \theta'_s \leq 70 \text{ deg}$. Allen [16] also gave similar indications. Other authors in the literature adopt values in this range even if they do not present specific analyses under variations of this parameter.

Most authors in the literature, [6,9,16], use values of δ included in the range 20–50 deg.

Little is known on experimental tests under variation of e_R/D_2 . Various ranges were suggested in [6,14,15]. Consensus exists on $2 \leq e_R/D_2 \leq 10\%$ to get optimal design, [16,17].

According to author's and co-workers' experiments, high performances are obtained using $359 \text{ deg} \leq \theta^* \leq 139 \text{ deg}$. A wider range was tested, [6], where, however, for $\theta^* = 126 \text{ deg}$ (i.e., a big radial width) a lower pressure coefficient and efficiency were obtained than for a smaller radial width ($\theta^* = 191 \text{ deg}$). Other authors presented single arc, [14,15], or double arc, [10], profiles that can be approximated by values of θ^* in the suggested range.

A separate discussion is to be made to account for the influence on fan performances of the discharge duct, which does not appear explicitly in the list of variables defining the rear wall shape. Diffusing ducts are not considered here because their effectiveness is penalized by largely nonuniform discharge flow. As shown in [8], any diffuser angle increases fan static pressure, but decreases total pressure, flow rate, and total efficiency. A diffuser would be moderately beneficial only with small discharge sections. When wider rear walls are considered, two shapes can be suggested:

- a discharge duct with sinusoidal shape, linking the end of the log-spiral profile with the discharge section. Using this duct, the height of the discharge section (h'_d) remains the same for every rear wall for a fixed position of the vortex wall (note that $h'_d = h_d + h''_d$).
- a rectilinear discharge duct. In this case the height of the discharge section for a fixed position of the vortex wall varies according to the rear wall width.

Vortex Wall. Tests conducted by the present author and co-workers using thin and flat vortex walls of constant section and rounded end (on the impeller side) showed that optimal fan performances are obtained when the value of the radial clearance between impeller and vortex wall is in the range $0.02 < e_V/D_2 < 0.1$. In this range fan performances are not very sensitive to variations of e_V . Similar indications were already given in [6,17].

When the thickness of the vortex wall increases, author's and co-workers' experiments demonstrated the advantage of using wider clearance and decreasing values of radial clearance in the direction of rotation to obtain high performances, as already shown by Eck [10]. The only contrary indication is found in [3], where an increasing radial clearance in the direction of rotation was adopted.

When the casing is built using rear walls having $359 \text{ deg} \leq \theta^* \leq 139 \text{ deg}$ and thin flat vortex wall, preliminary tests and indications from the literature, [6,14,15], demonstrated that satisfactory performances are obtained only if the vortex wall height varies in the range $0.05 < h_d/D_2 < 0.58$. Variations in vortex wall thickness

and height imply different dimensions of the suction and/or of the discharge zones. Thus, both directions of thickness modifications should be considered in order to take into account the corresponding variations of suction and/or discharge arcs. No indication can be found in the literature about this point, which is crucial to determine optimum fan performance and efficiency.

Conclusions

A criterion to parameterize in a general way cross-flow fan configurations is presented in this work. An application to the most common case in which flow direction is changed by 90 deg is shown. The criterion can be used in systematic tests to find paths towards design improvements and/or cut branches that lead to unfavorable solutions.

References

- [1] Laakso, H., 1957, "Querstromventilatoren mit Druckkennwerten $\psi > 4$," *Heizung-Luftung-Haustechnik* **8** (12).
- [2] Trampusch, H., 1964, "Cross-Flow Fan," ASME Paper No. 64-WA/FE-25.
- [3] Ilberg, H., and Sadeh, W. Z., 1965–1966, "Flow Theory and Performance of Tangential Fans," *Proc. Inst. Mech. Eng.*, **180**, Part 1, (19).
- [4] Ikegami, H., and Murata, S. A., 1966, "Study of Cross Flow Fan. I. A Theoretical Analysis," *Technol. Rep. Osaka Univ.*, **16**, pp. 557–578.
- [5] Porter, A. M., 1969, "A Study of the Tangential Fan," Ph.D. thesis, Queen's University, Belfast.
- [6] Porter, A. M., and Markland, E., 1970, "A Study of the Cross Flow Fan," *J. Mech. Eng. Sci.*, **12**(6).
- [7] Bush, E. H., 1972, "Crossflow Fans—History and Recent Developments," *Conference on Fan Technology and Practice*, Apr. 18–19, London.
- [8] Preszler, L., and Lajos, T., 1972, "Experiments for the Development of the Tangential Flow Fan," *Proc. of the 4th Conference on Fluid Machinery, Akademiai Kiado, Budapest*, pp. 1071–1082.
- [9] Eck, B., 1973, *Fans*, Pergamon Press, New York.
- [10] Eck, B., U.S. Patent 2 942 773.
- [11] Clayton, B. R., 1975, "A Review and Appraisal of Crossflow Fans," *Building Services Engineer*, **42**, pp. 230–247.
- [12] Yamafuji, K., 1975, "Studies on the Flow of Cross-Flow Impellers—1st Report, Experimental Study," *Bull. JSME*, **18**(123).
- [13] Yamafuji, K., 1975, "Studies on the Flow of Cross-Flow Impellers—2nd Report, Analytical Study," *Bull. JSME*, **18**(126).
- [14] Murata, S., and Nishihara, K., 1976, "An Experimental Study of Cross Flow—1st Report, Effects of Housing Geometry on the Fan Performance," *Bull. JSME*, **19**(129).
- [15] Murata, S., and Nishihara, K., 1976, "An Experimental Study of Cross Flow—2nd Report, Movements of Eccentric Vortex inside Impeller," *Bull. JSME*, **19**(129).
- [16] Allen, D. J., 1982, "The Effect of Rotor and Casing Design on Cross-Flow Fan Performance," "International Conference on Fan Design and Applications," Sept. 7–9, Guilford, England, Paper No. J1.
- [17] Tuckey, P. R., Holgate, M. J., and Clayton, B. R., 1982, "Performance and Aerodynamics of a Cross Flow Fan," International Conference on Fan Design and Applications, Sept. 7–9, Guilford, England, Paper No. J3.
- [18] Tanaka, S., and Murata, S., 1994, "Scale Effect in Cross-Flow Fans (Effects of Fan Dimension on Performance Curves)," *Bull. JSME*, series B **37**(4).
- [19] Tanaka, S., and Murata, S., 1995, "Scale Effect in Cross-Flow Fans (Effects of Fan Dimension on Flow Details and the Universal Representation on Performances)," *Bull. JSME*, series B **38**(3).
- [20] Lazzaretto, A., Toffolo, A., and Martegani, A. D., 2003, "A Systematic Experimental Approach to Cross-Flow Fan Design," *ASME J. Fluids Eng.*, **125**, pp. 684–693.
- [21] Martegani, A. D., Macor, A., and Lazzaretto, A. 1995, "Ricerca e Sperimentazione sui Ventilatori a Flusso Trasversale. Part I: Considerazioni Teoriche e Linee di Sviluppo," Part II: Sperimentazione di un Modello L'Installatore Tecnico, year 10, (3) and (4), CIDA ed., Mar.–Apr. 1996 (in Italian).
- [22] Lazzaretto A., Macor A., Martegani A. D., and Martina, V., 1997, "Ricerca della Configurazione Ottimizzata della Cassa di un Ventilatore a Flusso Trasversale," *Proceedings of 52th Congresso Nazionale ATI*, Sept. 22–26, Cernobio, SGEditoriali Padova, Italy, pp. 919–937 (in Italian).
- [23] Lazzaretto, L., Lazzaretto, A., Macor, A., and Martegani, A. D., 2001, "On Cross-Flow Fan Similarity: Effects of Casing Shape," *ASME J. Fluids Eng.*, **123**, pp. 1–9.

A. Lazzaretto
 A. Toffolo
 A. D. Martegani

Department of Mechanical Engineering,
 University of Padova,
 Via Venezia, 1,
 35131 Padova, Italy

A Systematic Experimental Approach to Cross-Flow Fan Design

A systematic investigation of cross-flow fan performances is presented according to an original criterion for the parameterization of fan geometry. Test facility and procedures are set up following ISO standards. The aim is to find which are the parameters most affecting fan performances and the effects of their design choice. Indications are found to design fans according to the desired objectives, such as maximum total pressure, total efficiency, and flow rate. [DOI: 10.1115/1.1593710]

Introduction

General design criteria are difficult to draw from the experimental investigations on cross-flow fan performance performed in the literature, [1–10], owing to the high number of variables that are required to define fan geometry. In spite of the many and often systematic tests conducted in the design variable space, some studies do not select independent variables to define fan geometry, while others present the effect of a parameter on performance without specifying whether or how the remaining parameters are varied. Above all, there is a lack of test procedure standardization, which may well account for some doubtful results obtained in the past.

To overcome these difficulties, an original criterion for the parameterization of fan geometry and guidelines to set up a systematic test program are given in [11]. According to these results, three test programs are proposed and performed here, the first two varying casing shape and the third mainly devoted to determining the combined effects of different casing and impeller configurations. All tests are performed at fixed rotational speed using an ISO standardized test rig.

Test Facility and Procedures

A very important point with aerodynamic tests, as various authors pointed out, [12,13], is that no standard method was used in many experiments in the past. The inconsistency of testing methods and procedures may well account for the apparently superior performances reported.

A fan test facility with chamber on the delivery (Fig. 1) was built following the UNI 10531, [14], standard on industrial fan test methods and acceptance conditions (equivalent to ISO 5801, [15]). After the chamber, the air passes through a venturi nozzle, a honeycomb straightener duct, and an auxiliary fan to overcome pressure losses.

Static pressure measurements were performed using three water micromanometers having a 1/100 mm precision, one being of differential type for flow rate measurement. The direct current motor includes a tachimetric dynamo for measuring rotational speed. Torque was measured using a load cell arranged in the stator part of the electrical motor. The power absorbed by mechanical devices and winding was evaluated using a bladeless runner having the same disks and moment of inertia as the actual ones.

In each test, the curves of total pressure coefficient and total efficiency versus flow coefficient were obtained according to the following definitions:

$$\psi_t = \frac{P_t}{0.5\rho u_2^2}; \quad \phi = \frac{q}{u_2 D_2 L}; \quad \eta_t = \frac{P_t q}{P}. \quad (1)$$

Experimental data were measured from fully closed conditions (null flow rate) to fully open conditions (null static pressure at fan discharge). All tests were performed at 1000 rpm and with 152.4 mm impellers.

Description of the Test Programs

The parameterization of cross-flow fan geometry defined in [11] led to three sets of variables (Figs. 2 and 3) that describe impeller, rear wall and vortex wall, respectively:

$$\begin{aligned} \tau_I &= \{L/D_2, D_1/D_2, Z, \beta_1, \beta_2\}; \\ \tau_R &= \{\theta_s, \theta_R, \theta^*, e_R/D_2, \delta\}; \quad \tau_V = \{s/D_2, e_V/D_2, h_d/D_2\} \end{aligned} \quad (2)$$

The number of variables included in these sets would clearly result in too many cases to be handled if all the combinations of values included in the chosen ranges were to be tested. It is therefore necessary to reduce the number of tests by organizing a selected number of subprograms to be systematically investigated. On the other hand, this reduction should not cause any loss of generality in the analysis of the results. Three subprograms are proposed here according to the indications given. In the first one, the shape of casings featuring a thin vortex wall is varied and matched with a single impeller geometry. In the second program, casing shapes featuring different thick vortex walls are matched to the same impeller. Finally, in the third program, different impellers are matched with a selected number of casing configurations.

To further reduce the number of tests, the variables having more separable or lighter effects are isolated and their values fixed within the ranges discussed in [11]. According to the indications discussed there, the values of the rear wall variables θ_R , θ'_s , e_R/D_2 and δ are fixed to $\theta_R=135$ deg, $\theta'_s=60$ deg, $e_R/D_2=0.04$ and $\delta=45$ deg, and the values of the impeller variables $L/D_2, Z$ and D_1/D_2 are fixed to $L/D_2=1.5$, $Z=24$ and $D_1/D_2=0.81$. The three sets of parameters associated with rear wall, vortex wall and impeller geometry are therefore reduced to the following:

$$\tau'_R = \{\theta^*\}; \quad \tau'_V = \{s/D_2, e_V/D_2, h_d/D_2\}; \quad \tau'_I = \{\beta_1, \beta_2\} \quad (3)$$

Program 1: Tests Under Variation of Casing Shape (Thin Vortex Wall). In this program the variables θ^* , e_V/D_2 , and h_d/D_2 are varied, and the resulting casing configurations are all matched with the same impeller, having $\beta_1=70$ deg and $\beta_2=38$ deg. This impeller, first proposed in [4], was already used to prove the validity of similarity laws in Lazzaretto et al. [16].

Contributed by the Fluids Engineering Division for publication in the JOURNAL OF FLUIDS ENGINEERING. Manuscript received by the Fluids Engineering Division January 14, 2002; revised manuscript received January 31, 2003. Associate Editor: Y. Tsujimoto.

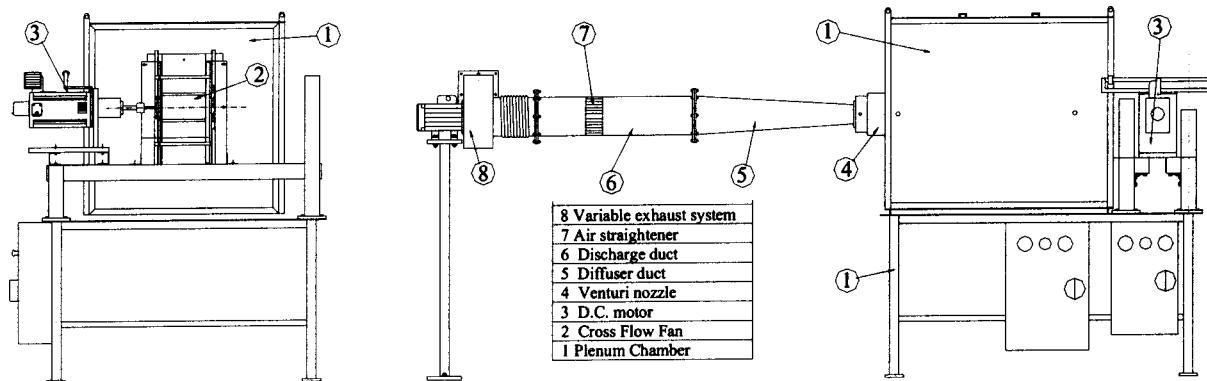


Fig. 1 Schematic of the test facility

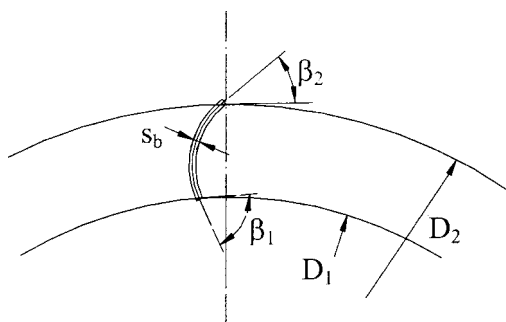


Fig. 2 Impeller geometry

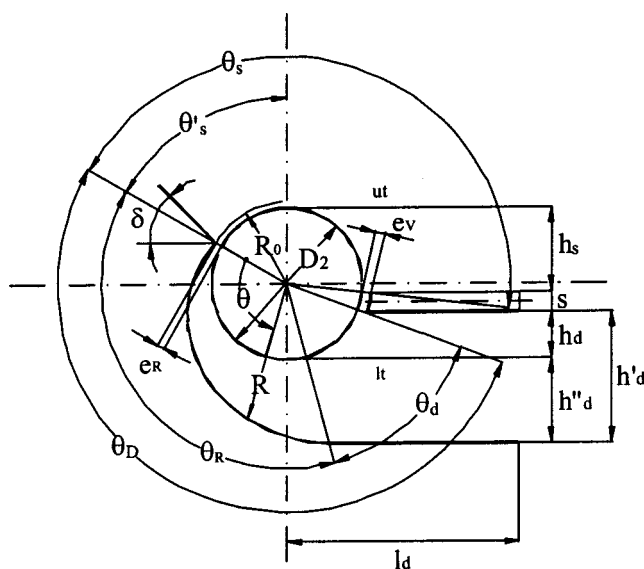


Fig. 3 Geometric variables of the casing walls

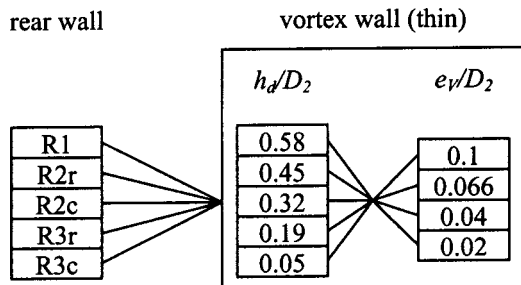


Fig. 4 Test program 1: "tree" of tests

Three values of θ^* are considered in the range 359 deg–139 deg, resulting in the following rear walls:

- R1: a small width rear wall ($\theta^* = 359$ deg), similar to that patented by Eck [17];
- R2: an intermediate width rear wall ($\theta^* = 191$ deg), which supplied the highest values of pressure coefficient in a wide range of flow rates in [4];
- R3: a large width rear wall ($\theta^* = 139$ deg).

The rear walls R2 and R3 are named R2c and R3c if the duct linking the end of the log spiral profile with the discharge section has a curved sinusoidal shape or R2r and R3r if the duct is rectangular (Fig. 3).

The series of casings shapes to be tested are derived from the so defined five rear walls, by adding a *thin vortex wall* of constant thickness ($s/D_2 = 0.13$) and rounded leading edge at different radial clearances and heights. All the combinations of four values of the radial clearance e_v/D_2 (0.02, 0.04, 0.066, and 0.1) and five vortex wall heights h_d/D_2 (0.05, 0.19, 0.32, 0.45, and 0.58) are considered. The test "tree" of the program under variation of casing shape featuring thin vortex walls is shown in Fig. 4 (100 tests in total).

Program 2: Tests Under Variation of Casing Shape (Thick Vortex Wall). In this program the variables θ^* , s/D_2 and h_d/D_2 are varied and the resulting casing configurations are all matched with the same impeller, having $\beta_1 = 70$ deg and $\beta_2 = 38$ deg, already used in test program 1.

The same values of θ^* (359 deg, 191 deg, and 139 deg) are considered, defining the same five rear walls (R1, R2r, R2c, R3r, and R2c). The casing shape is now completed by adding a thick modu-

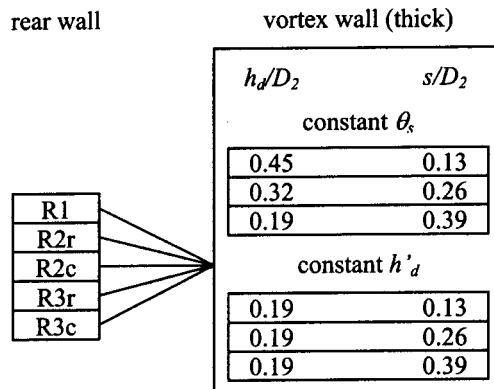


Fig. 5 Test program 2: "tree" of tests

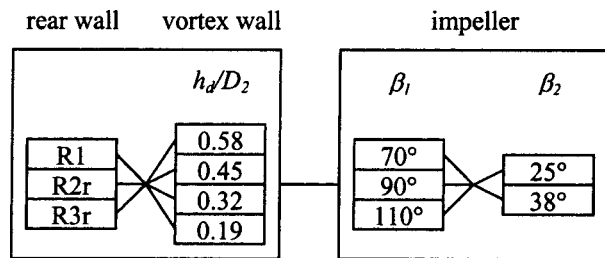


Fig. 6 Test program 3: "tree" of tests

lar vortex wall of variable thickness ($s/D_2=0.13, 0.26,$ and 0.39) composed of modules having $s/D_2=0.13$ each. Two subseries of casings are considered:

- In the first series, one module was placed at $h_d/D_2=0.45$, and the second and third modules were then added on its lower surface to increase the vortex wall thickness while leaving unchanged the length of the inflow arc θ_s . Accordingly, the height of the discharge section is decreased ($h_d/D_2=0.32$ and 0.19) as the wall thickness is increased.
- In the second series, the first module was placed at $h_d/D_2=0.19$, the other two modules being added afterwards on its upper surface to keep constant the height of the discharge section h'_d .

The modules were arranged so that the radial clearance (e_v/D_2) between vortex wall and impeller decreases in the rotating direction of the impeller, according to a log spiral law, from $e_v/D_2=0.066$ to $e_v/D_2=0.15$

The test "tree" of the program under variation of casing shape featuring thick vortex walls is shown in Fig. 5 (30 tests in total).

Program 3 Tests Under Variation of Impeller Geometry.

In this program the variables θ^* , h_d/D_2 , β_1 , and β_2 are varied. The combinations of two external angles β_2 (25 deg and 38 deg) and three internal angles β_1 (70 deg, 90 deg, and 110 deg) are considered. The resulting six impellers are named by a five-digit number, the first two digits representing the external blade angle and the last three representing the internal blade angle.

A subset of casing shapes featuring a thin vortex wall ($s/D_2=0.13$) is selected on the basis of the results of the first two test programs. The radial clearance e_v/D_2 is kept constant at 0.066. Three rear walls (R1, R2r, and R3r) and four vortex wall heights ($h_d/D_2=0.19, 0.32, 0.45,$ and 0.58) are matched with each of the six impellers.

The test "tree" of the program under variation of impeller geometry is shown in Fig. 6 (72 tests in total).

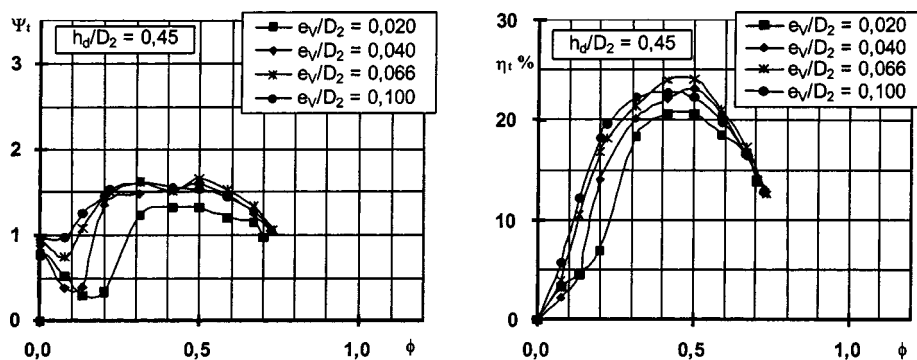


Fig. 7 Total pressure coefficient and total efficiency obtained using a small radial width rear wall ($\theta^*=359$ deg) and a thin vortex wall ($s/D_2=0.13$) having $h_d/D_2=0.45$, under variation of the radial clearance (e_v/D_2) between vortex wall and impeller

Experimental Results

Variation of Casing Shape (Thin Vortex Wall)—Program 1.

The results of the experimental tests using thin vortex walls of constant thickness are presented in this section. All the tests proved that the radial clearance has little effect on performance for any value of the other parameters, as shown, for instance, in Fig. 7 using the rear wall R1 and $h_d/D_2=0.45$. In general, the highest performance has been obtained using radial clearance values in the middle of the range considered here. For this reason, only the results for $e_v/D_2=0.066$ are presented in the following.

For each rear wall, the values of ψ_t versus ϕ under a variation of h_d/D_2 (for $e_v/D_2=0.066$) are presented in Fig. 8. The maximum values of η_t are shown in Table 1. To facilitate the comprehension of the results, the effect of each variable on fan performances is analyzed separately.

Rear Wall Radial Width θ^* . The radial width of the rear wall has a remarkable effect on pressure-flow characteristics (ψ_t - ϕ curves). For a fixed position of the vortex wall, a small radial width generally leads to unstable curves (i.e., static pressure does not increase monotonically as flow is throttled), and a large radial width leads to stable curves. Thus, the radial width can be used to "control" the slope of these curves, and an intermediate width, combined with the appropriate position of the vortex wall, allows almost constant values of ψ_t to be obtained over the range of flow rates. The intermediate rear wall supplies the highest values of ψ_t , and, at $h_d/D_2=0.32$ (see Table 1), also the highest values of total efficiency.

Vortex Wall Height h_d/D_2 . For each rear wall considered, increased values of the vortex wall height (h_d/D_2) lead to more stable curves. Therefore, smaller radial width rear walls, which are intrinsically less stable, would preferably be combined with vortex walls having higher values of h_d/D_2 to improve stability. Lower values of h_d/D_2 are preferable for larger radial width rear walls, which are intrinsically more stable, to get higher values of ψ_t . This is in agreement with the results of Porter and Markland [4], indicating maximum fan total pressure when the vortex is free to move along the inner impeller periphery under throttling. In other words, there exists an optimal distance h'_d between the two casing walls to get the maximum total pressure coefficient. The influence of the vortex wall height (h_d/D_2) on total efficiency also shows that an optimal distance h'_d exists, which is generally different from the former. For a small radial width rear wall, lower values of h_d/D_2 lead to lower efficiencies. For a larger radial width rear wall, a maximum is apparent and is obtained for decreasing values of h_d/D_2 .

Discharge Duct. Higher values of ϕ are generally obtained using the rectilinear discharge ducts (R2r, R3r) instead of the

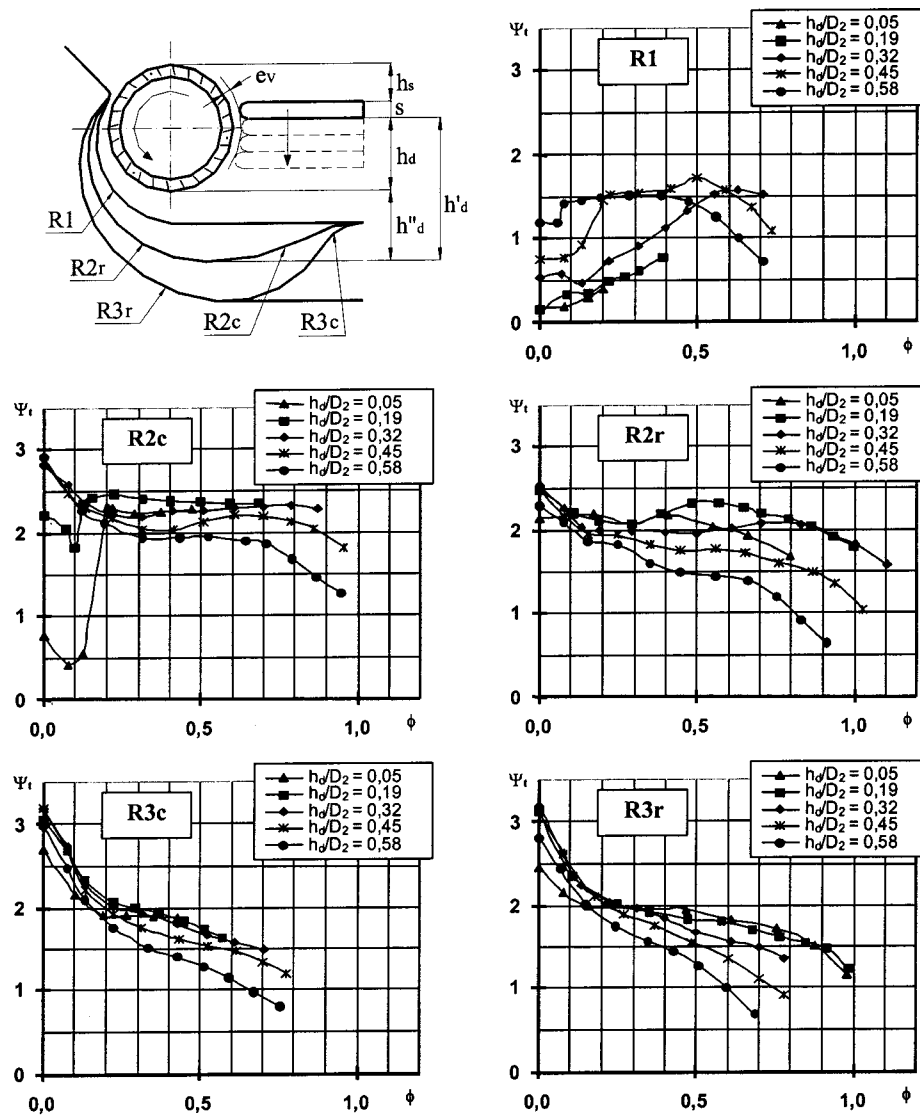


Fig. 8 Results of test program 1: casing shapes featuring thin vortex wall

curved ones (R2c, R3c). Curve stability is not affected by duct shape for R3. Curve instability at low flow rates disappears when R2r is combined with low h_d/D_2 values. On the other hand, the rectilinear duct implies efficiency penalties, especially for the intermediate width rear wall.

Variation of Casing Shape (Modular Vortex Wall)—Program 2. The results of the experimental tests using thick vortex walls of variable thickness are presented in this section. For each rear wall, the ψ_t - ϕ curves are presented in Fig. 9 for constant inflow arc and in Fig. 10 for constant height of the discharge section. The maximum values of total efficiency are shown

Table 1 Test program 1: maximum total efficiencies (%) in Fig. 8

h_d/D_2	R1	R2r	R3r	R2c	R3c
0.05	4,5	20	16,8	22	16
0.19	8,4	26	18,4	28,8	17,7
0.32	18	26,8	17,3	34,1	19
0.45	20	24,3	16,7	32,5	18,6
0.58	21,8	20,3	14	27	17,2

in Tables 2 and 3, respectively. The effects of variations of the geometrical parameters of the casing on fan performance can be summarized as follows.

Vortex Wall Thickness s/D_2 . Thick vortex walls are demonstrated to be effective mainly in raising efficiency for the small width rear wall. In fact, the highest efficiency (42%) is obtained with maximum vortex wall thickness and minimum radial width of the rear wall (R1). This is in agreement with the Eck fan patent, [17], similar to this fan configuration, which shows very high efficiency. Controversial effects appear for R2 and R3: Peak efficiency is obtained for the thickest wall using the rectilinear discharge duct, whereas it is achieved for the single module ($s/D_2 = 0.13$) using the curved discharge duct.

Both at constant inflow arc and at constant height of the discharge section (Figs. 9 and 10), an increase in the vortex wall thickness implies more unstable curves for all the rear walls. For the rear walls R2 and R3, growing thickness seems to create an obstruction to the throughflow, with consequent reduction in maximum flow rate and energy transfer. This effect does not appear for R1 where ψ_t increases with s/D_2 . Instability effects are stronger in the tests with constant height of the discharge section. On the other hand, thin vortex walls at the same low height

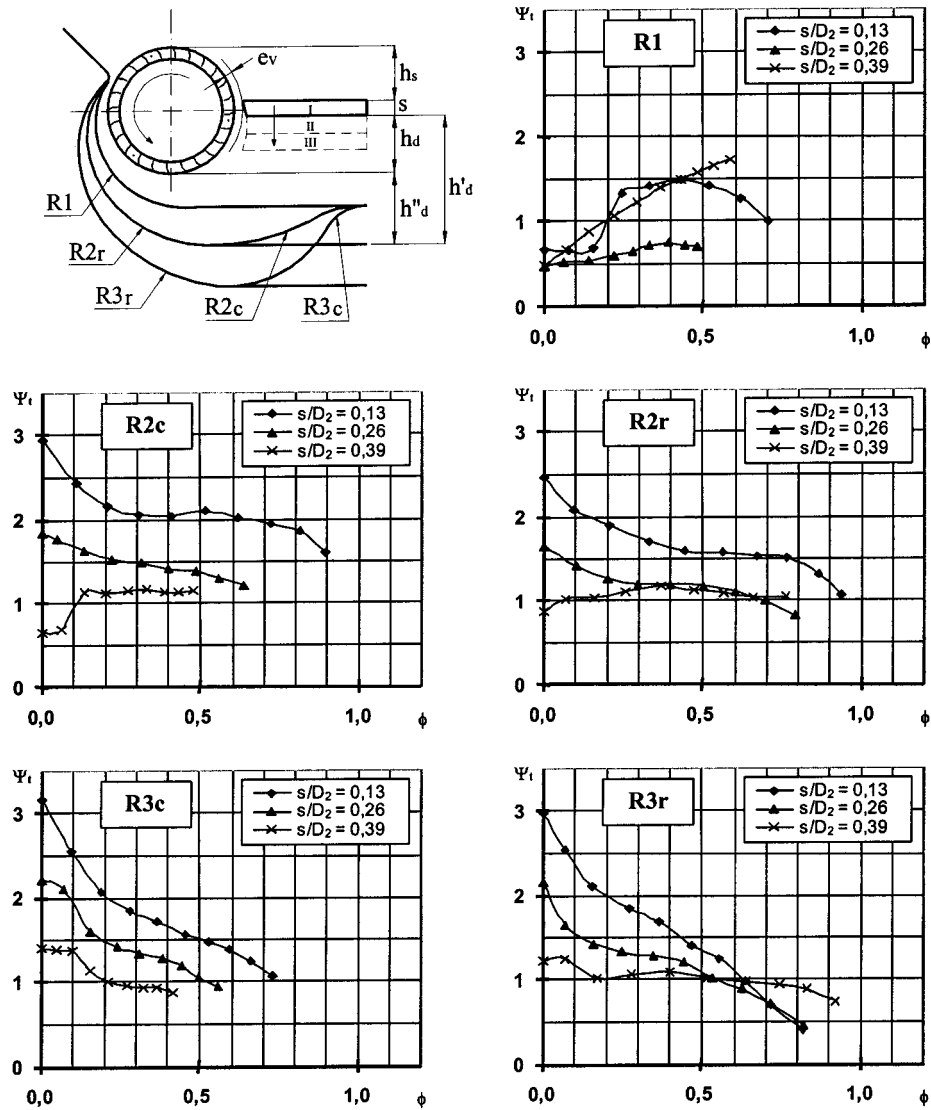


Fig. 9 Results of test program 2: casing shapes featuring modular vortex wall (constant inflow arc)

($h_d/D_2=0.19$) already showed a tendency to instability. Accordingly, stability is strongly determined by the height of the discharge section.

Rear Wall Radial Width θ^* . As for the thin vortex wall, a larger width of the rear wall implies more stable curves and lower efficiencies. Maximum ψ_i is obtained for R2 combined with the thinnest vortex wall, whereas η_i is maximum for R1 combined with the thickest vortex wall, as mentioned above.

Discharge Duct. Higher flow rates are obtained using the rectilinear discharge duct, as for the thin vortex wall, both at constant inflow arc and at constant height of the discharge section. Still, the rectilinear discharge duct increases stability at low flow rates for the R2 rear wall. The combined effects of discharge ducts and vortex wall thickness were already discussed above.

Shape of the Clearance Between Impeller and Vortex Wall. A round-shaped front edge of the vortex wall was used in the experimental tests with thin vortex wall (see Fig. 8), whereas a log spiral law is chosen here for the modular vortex wall. Accordingly, the first module has different radial clearance, the thickness

being the same. This leads to a slight decrease of ψ_i for the same vortex wall height (compare the $\psi_i-\phi$ curves of the thin vortex wall having $h_d/D_2=0.45$ with those of the modular wall having $s/D_2=0.13$ in the tests with constant inflow arc, or the $\psi_i-\phi$ curves of the thin vortex wall having $h_d/D_2=0.18$ with those of the modular wall having $s/D_2=0.13$ in the tests with constant height of the discharge section).

Variation of Impeller Geometry—Program 3. The $\psi_i-\phi$ curves obtained in the experimental tests of the third program are presented in Fig. 11. It appears that the worst performance is obtained either with the larger internal blade angle (110°) or with the rear wall having small radial width (R1). Independent of impeller blade angles, the best performance is achieved by the four configurations having intermediate and large radial width rear walls (R2r and R3r) combined with the two lowest positions of the vortex wall ($h_d/D_2=0.19$ and 0.32). This result confirms the indications about the influence of the casing shape on performance given for the 38070 impeller. The $\psi_i-\phi$ and $\eta_i-\phi$ curves obtained for each of the six impellers are grouped together in Fig. 12 for each of the four best performing casings.

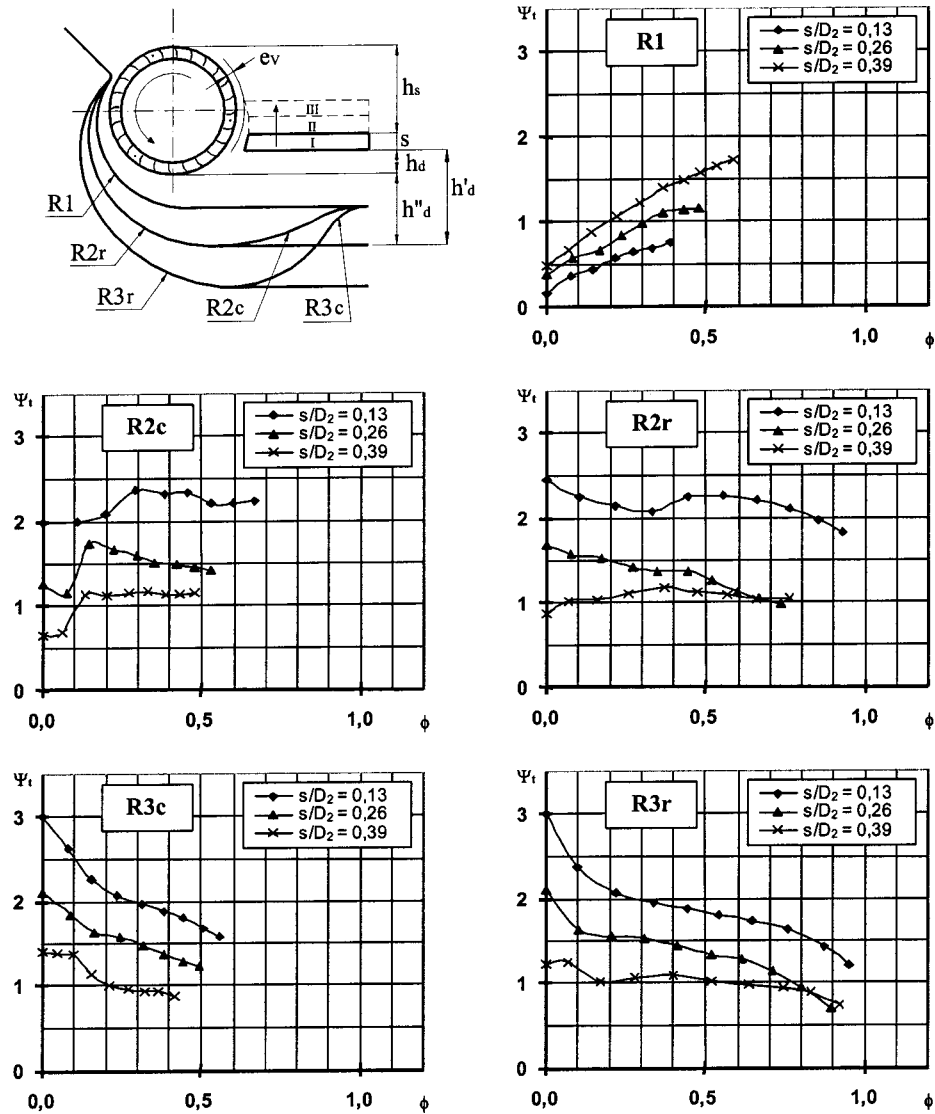


Fig. 10 Results of test program 2: casing shapes featuring modular vortex wall (constant discharge section)

Total Pressure Coefficient. All the ψ_t - ϕ curves show a common characteristic behavior. The total pressure coefficient rapidly decreases from its null-flow-rate value until a discontinuity in the slope of the curve occurs. Both external and internal blade angles affect the location of this point of discontinuity, in terms of ϕ . If β_1 increases, the point moves towards higher flow coefficients; conversely, if β_2 increases, the point moves towards lower flow coefficients. After the slope discontinuity, the behavior of the curves strictly depends on the casing shape. For small discharge sections (casing R2r- $h_d/D_2=0.19$), ψ_t tends to increase as ϕ increases, intermediate values of the discharge section (casings R2r- $h_d/D_2=0.32$ and R3r- $h_d/D_2=0.19$) lead to a fairly constant ψ_t , and when the discharge section is large (casing

R3r- $h_d/D_2=0.32$) ψ_t definitely decreases as ϕ increases. Results of test program 1 can therefore be generalized independently of impeller blade angles.

Maximum Flow Rate. The maximum flow rate at fully open conditions shows a characteristic behavior depending on impeller blade angles. The maximum flow coefficient first increases when β_1 is raised from 70 deg to 90 deg, then it decreases when β_1 is further raised to 110 deg. On the other hand, flow coefficients in fully open conditions for $\beta_2=25$ deg are always higher than those for $\beta_2=38$ deg.

Total Efficiency. Maximum values of total efficiency for all impellers and all casings are obtained in a narrow range of the

Table 2 Test program 2: maximum total efficiencies (%) in Fig. 9

s/D_2	R1	R2r	R3r	R2c	R3c
0.13	23	21,8	16,7	33,4	18,3
0.26	18,7	20,9	16,2	26,7	16,4
0.39	42	28,9	19,1	28,3	16

Table 3 Test program 2: maximum total efficiencies (%) in Fig. 10

s/D_2	R1	R2r	R3r	R2c	R3c
0.13	10,2	26,5	18,4	28,5	17,5
0.26	21,7	19,4	16,3	24	15
0.39	42	28,9	19,1	28,3	16

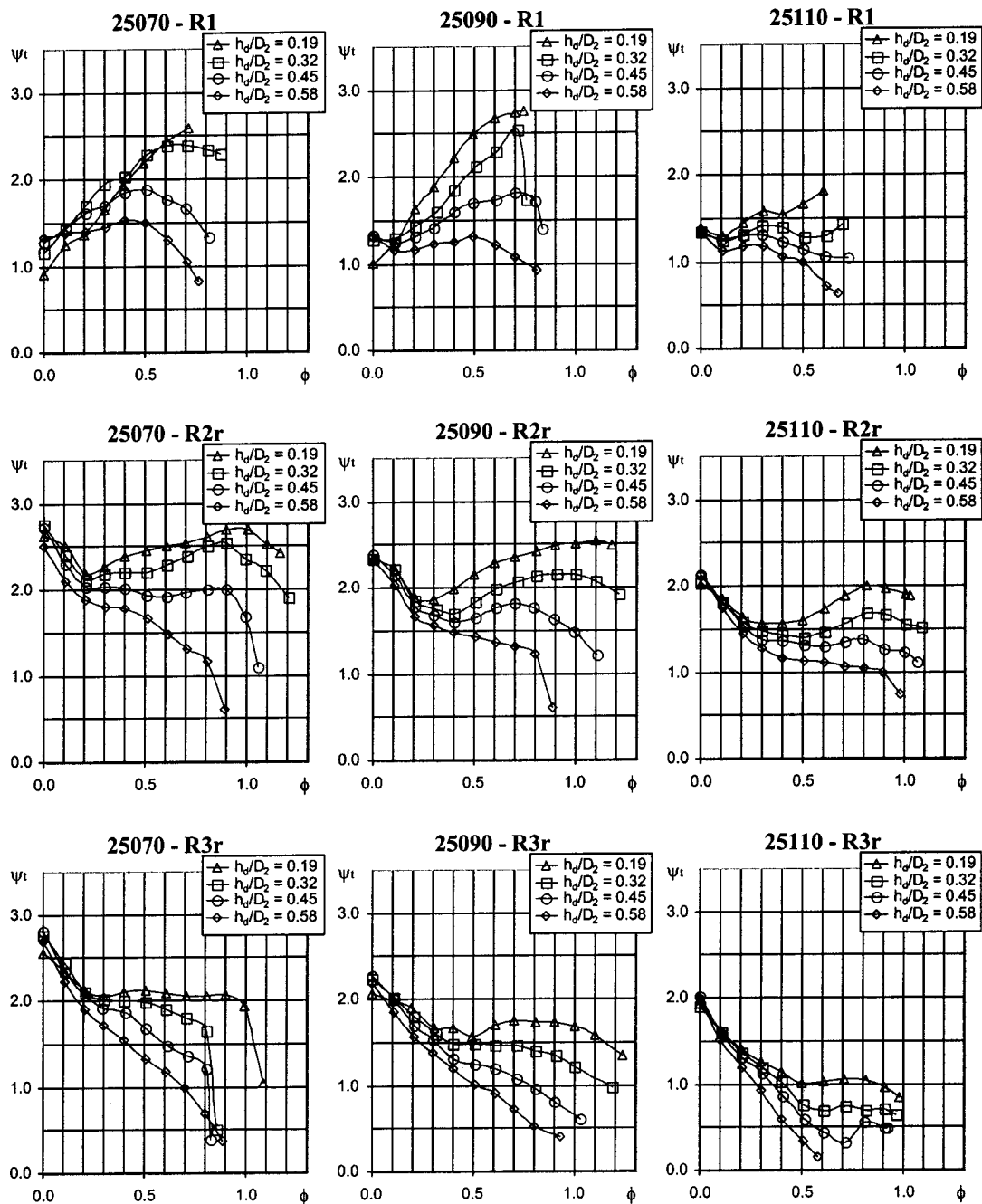


Fig. 11 Results of test program 3: different impellers matched with thin vortex wall casings

flow coefficient, the only exception being the 38,110 impeller, which always leads to performances much worse than those of the other impellers. The range is approximately centered around $\phi = 0.6$. In the same range, except for $\beta_1 = 110$ deg, the total pressure coefficient tends to a common value for each casing, independent of the impeller blade angles. This indicates that impeller blade angles strongly affects the maximum value of η_t , but has almost negligible effects on flow and total pressure coefficients corresponding to the maximum η_t . Efficiencies for $\beta_2 = 25$ deg are always higher than those for $\beta_2 = 38$ deg, the internal blade angle being equal. On the other hand, for the same external blade angle, the maximum efficiencies are achieved by impellers having $\beta_1 = 90$ deg.

Many of these characteristic behaviors were observed also using other casings; results are not presented here because of their poorer performance.

Noise Generation. Noise issues are particularly critical in cross-flow fan design because the flow field is not axial-symmetric and the highest radial velocities are located near the vortex wall edge where rotor-stator interaction is maximum, resulting in large fluctuations of flow quantities. The few experimental measures in the literature show that noise can be lowered by increasing the radial clearance of the vortex wall, [5,18], of course, as well as by reducing the interaction between the eccentric vortex within the impeller and the blade cascade. This can be

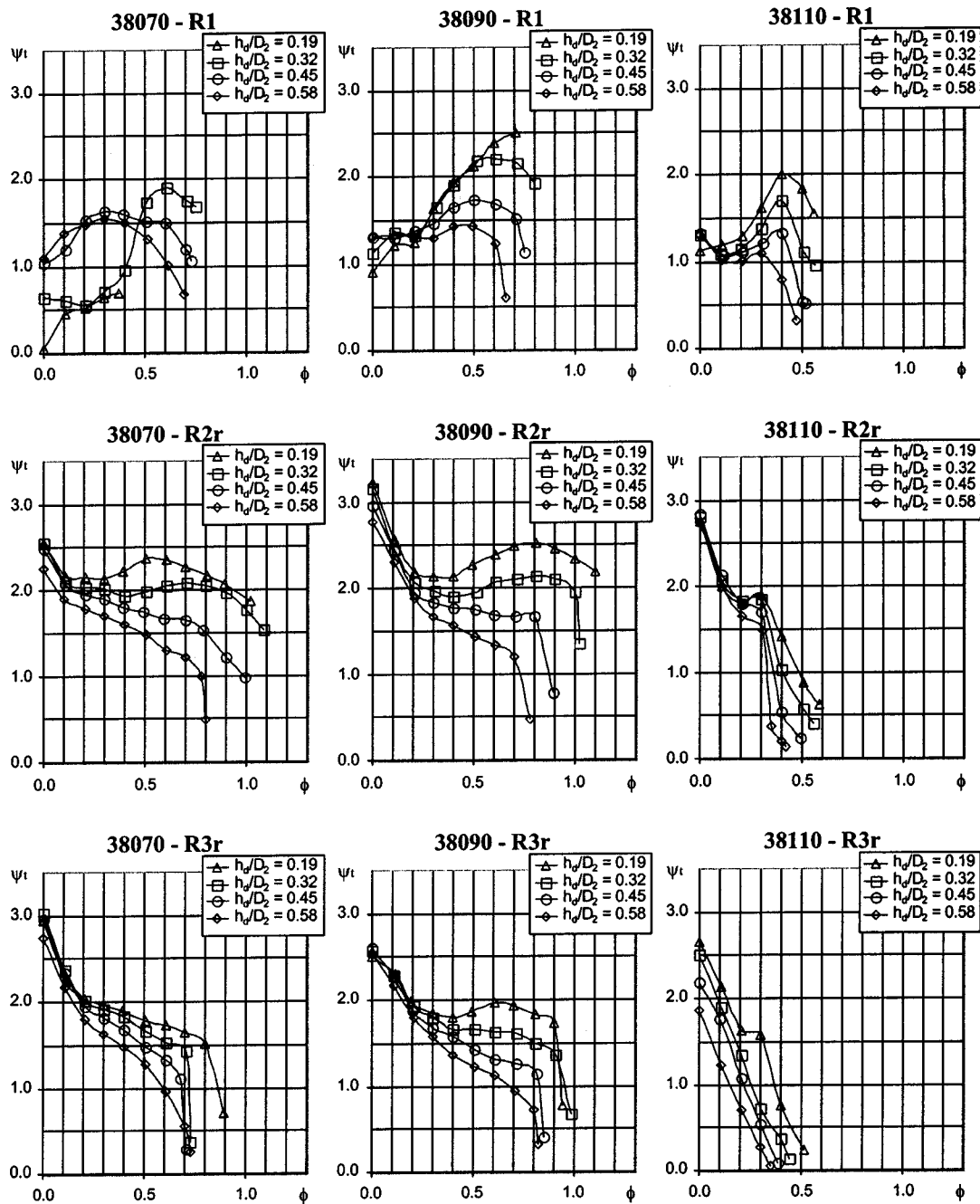


Fig. 11 (continued)

done by reducing the strength and the eccentricity of the vortex itself, increasing vortex wall thickness, [18], or reducing rear wall radial width, [4]. The results of a nonstandard noise measurement performed during test programs 1 and 2 agree with the indication of the literature.

Conclusions

Three experimental test programs have been carried out on the basis of the independent variables chosen in [11] to define fan geometry. All the combinations of values for the selected variables resulting in high performance have been investigated. Test results demonstrated that five variables are the most significant: rear wall radial width, vortex wall height and thickness, and internal and external blade angles of the impeller. Among them, the radial

width of the rear wall appears to be the fundamental parameter to define the fan characteristic curve. Three categories of machines are observed according to a small, large or intermediate radial width of the rear wall. Within each category, the most significant effects on performance are given by variation of the vortex wall height and thickness. In particular,

- small radial width rear walls combined with low height vortex walls lead to unstable characteristic curves, independent of the vortex wall thickness. Curves become more stable by increasing the height of the vortex wall. An increase in vortex wall thickness leads both to higher total pressure and efficiency. The maximum values of flow coefficient are hardly higher than 0.8.
- large radial width rear walls lead to stable curves, independent of the vortex wall height and thickness.

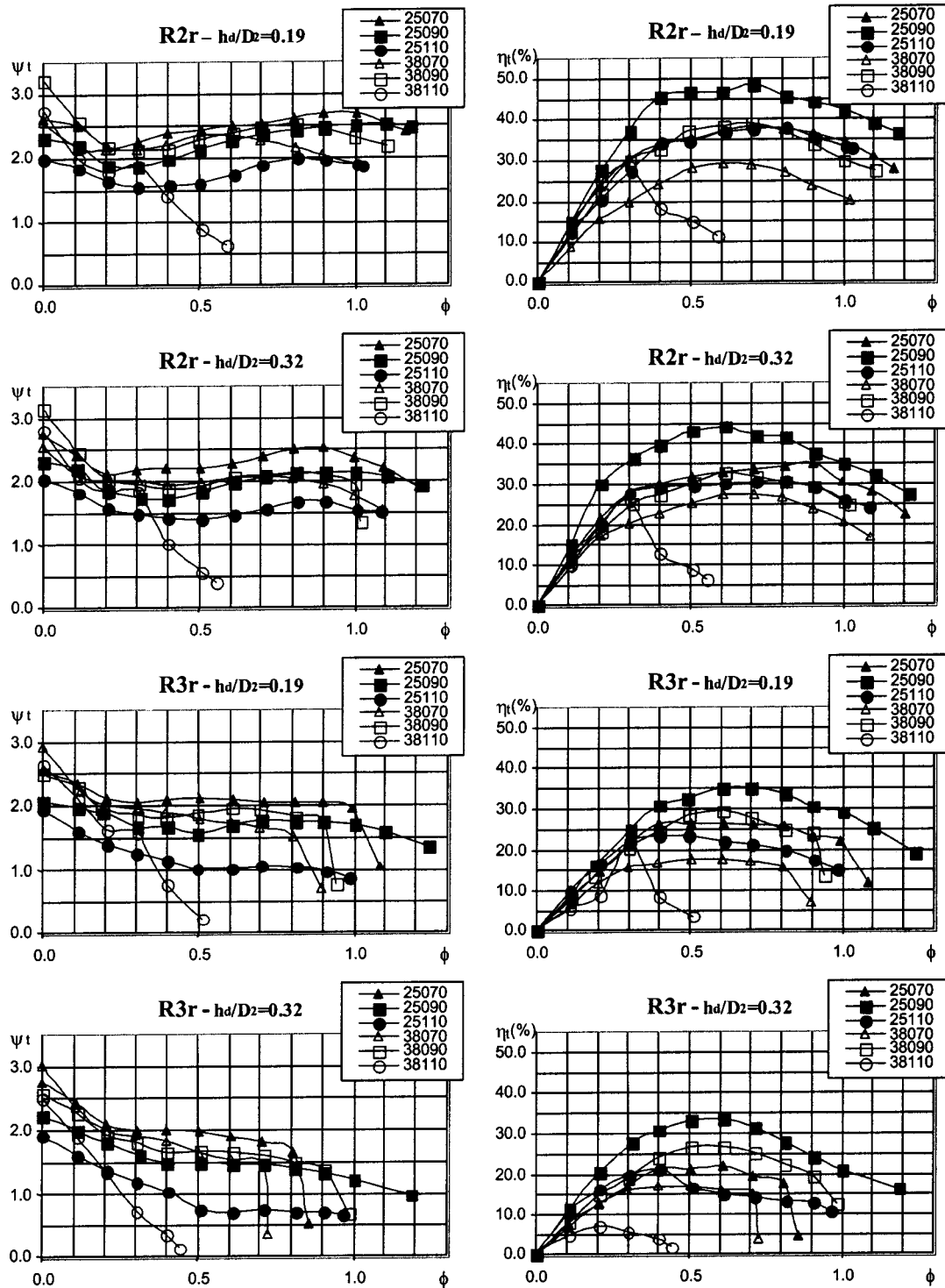


Fig. 12 Results of test program 3: best performing casing configurations

dent of the height of the vortex wall. Higher thickness of the vortex wall has a negative effect on both total pressure and efficiency. The maximum value of flow coefficient is normally around 0.9.

- intermediate radial width rear walls lead to unstable curves for small values of the vortex wall height, and to stable curves for large values of this height, curves being approximately flat for intermediate heights. A higher vortex wall thickness causes a decrease in total pressure and an increase in total efficiency. However, the efficiencies obtained using smaller width rear walls are

not reached. These rear walls lead to the best characteristic and, matched with rectilinear discharge ducts, to the highest values of flow coefficient.

Impeller blade angles do not substantially alter these trends, while generally affecting maximum efficiency and flow rate. In more detail,

- best total efficiencies and highest flow rates are achieved for a 90 deg internal blade angle, the external being equal, and a 25 deg external blade angle, the internal being equal.

- blade angle influence on the total pressure and the flow rate corresponding to maximum total efficiency seems negligible.

Less important effects have been observed for variations of the discharge duct shape and of the radial clearance between impeller and vortex wall:

- the radial clearance between the impeller and a thin vortex wall does not significantly affect fan performance. However, the clearance shape has a marked influence on performance for the thick vortex wall, since decreasing values in the direction of rotation increase both efficiency and total pressure.
- A rectilinear discharge duct generally results in higher values of the flow coefficient and more stable curves.

It is apparent that a choice of casing design parameters is derived from a compromise among the often conflicting needs of high total pressure, high efficiency and high flow rate. In general, if the objective is to maximize efficiency, small width rear walls and high thickness vortex walls are to be preferred. If the objective is to maximize total pressure in a wide range of flow rates, an intermediate width rear wall combined with a thin vortex wall is more suitable. Maximum flow rates are obtained using intermediate to large width rear walls and, preferably, rectilinear discharge ducts. The best tradeoffs among these objectives are usually obtained with internal and external impeller blade angles equal to 90 deg and 25 deg, respectively. Although the validity of these design indications is limited by working assumptions (fixed values for some of the parameters defining impeller and casing shape, fixed rotational speed, flat and horizontal vortex wall, etc.), they can be considered as a good starting point for the definition of cross-flow fan design criteria.

Nomenclature

- D = diameter (m)
 e = radial clearance (m)
 h = height (m)
 L = impeller axial length (m)
 n = rotational speed (rpm)
 p = pressure (Pa)
 P = power (W)
 q = volumetric flow rate (m^3/s)
 R = radial coordinate of the rear wall log spiral arc (m)
 Re = Reynolds number
 s = thickness (m)
 u = peripheral speed (m/s)
 Z = number of blades

Greek

- β = blade angle (deg)
 δ = rear wall suction angle
 η = efficiency
 θ = angle, angular coordinate of the rear wall log spiral arc (rad)

- ϕ = flow coefficient
 ρ = air density (kg/m^3)
 τ = set of design variables
 ψ = pressure coefficient

Subscripts

- 1 = internal
 2 = external
 b = blade
 d = discharge
 s = suction
 t = total
 I = impeller
 R = rear wall
 V = vortex wall

Acknowledgments

The authors wish to thank Prof. Alarico Macor for helpful discussions and suggestions.

References

- [1] Laakso, H., 1957, "Querstromventilatoren mit Druckkennwerten $\psi > 4$," *Heizung-Luftung-Haustechnik*, **8**(12).
- [2] Trampusch, H., 1964, "Cross-Flow Fan," ASME Paper No. 64-WA/FE-25.
- [3] Ilberg, H., and Sadeh, W. Z., 1965–1966, "Flow Theory and Performance of Tangential Fans," *Proc. Inst. Mech. Eng.*, **180**, Part 1(19).
- [4] Porter, A. M., and Markland, E., 1970, "A Study of the Cross Flow Fan," *J. Mech. Eng. Sci.*, **12**(6).
- [5] Preszler, L., and Lajos, T., 1972, "Experiments for the Development of the Tangential Flow Fan," *Proc. of the 4th Conference on Fluid Machinery*, Akademiai Kiado, Budapest, pp. 1071–1082.
- [6] Yamafuji, K., 1975, "Studies on the Flow of Cross-Flow Impellers—1st Report, Experimental Study," *Bull. JSME*, **18**(123).
- [7] Murata, S., and Nishihara, K., 1976, "An Experimental Study of Cross Flow—1st Report, Effects of Housing Geometry on the Fan Performance," *Bull. JSME*, **19**(129).
- [8] Murata, S., and Nishihara, K., 1976, "An Experimental Study of Cross Flow—2nd Report, Movements of Eccentric Vortex inside Impeller," *Bull. JSME*, **19**(129).
- [9] Allen, D. J., 1982, "The Effect of Rotor and Casing Design on Cross-Flow Fan Performance," *International Conference on Fan Design and Applications*, Sept. 7–9, Guilford, England, Paper No. J1.
- [10] Tuckey, P. R., Holgate, M. J., and Clayton, B. R., 1982, "Performance and Aerodynamics of a Cross Flow Fan," *International Conference on Fan Design and Applications*, Sept. 7–9, Guilford, England, Paper No. J3.
- [11] Lazzaretto, A., 2003, "A Criterion to Define Cross-Flow Fan Design Parameters," *ASME J. Fluids Eng.*, **125**, pp. 680–683.
- [12] Bush, E. H., 1972, "Crossflow Fans—History and Recent Developments," *Conference on Fan Technology and Practice*, Apr 18–19, London.
- [13] Clayton, B. R., 1975, "A Review and Appraisal of Crossflow Fans," *Building Services Engineer*, **42**, pp. 230–247.
- [14] UNI 10531, 1995, (in Italian) "Ventilatori Industriali—Metodi di prova e Condizioni di Accettazione," Milan, (in Italian).
- [15] ISO 5801, 1993, "Industrial fans—Performance Testing using Standardized Airways."
- [16] Lazzaretto, L., Lazzaretto, A., Macor, A., and Martegani, A. D., 2001, "On Cross-Flow Fan Similarity: Effects of Casing Shape," *ASME J. Fluids Eng.*, **123**, pp. 1–9.
- [17] Eck B., U.S. Patent 2 942 773.
- [18] Eck B., 1973, *Fans*, Pergamon Press, Oxford, UK.

Fluid Dynamic Aspects of Electrostatic Precipitators: Turbulence Characteristics in Scale Models

Aldo Coghe

Michele Mantegna

Giorgio Sotgia

Dipartimento di Energetica,
Politecnico di Milano,
P. le Leonardo da Vinci, 32,
20131 Milano, Italy

The present work originated in an investigation on fluid dynamic aspects of electrostatic precipitators performed on scale models of an industrial apparatus. The experimental analysis of velocity and turbulence distribution, performed by hot-wire anemometry, confirmed that significant turbulence levels are found inside particle collectors. In fact, components used to spatially smooth the flow and lower its velocity peaks, such as hoods with wide divergence angles, turning vanes, and perforated plates, may also act as sources of turbulence and reduce the efficiency of electrostatic precipitators. These observations prompted a deeper analysis, both analytical and experimental, of the turbulence decay downstream perforated screens. A new simple semi-empirical model of turbulence decay is proposed, which has shown reasonably good agreement with experimental data, even at short downstream distance from the perforated plate, 50 to 250 hydraulic diameters. [DOI: 10.1115/1.1593704]

1 Introduction

Electrostatic precipitators (ESP) are well-known, highly efficient devices applied in power stations and many other large-scale industrial systems in order to reduce fly ash and fine particle emissions. Although the first patent by F. G. Cottrell dates from 1906, it is still difficult to achieve efficiencies higher than 99%. H. J. White [1], in his thorough review concerning the whole physical phenomena of the dust collecting process, stated that: “for the finer particles which are of the greatest interest in electrical precipitation, the nature and properties of the gas flow establish the basic laws and patterns of particle collection.” In the same book are also emphasized the complex effects of several physical properties and operating conditions. They have to be taken into account in order to reach a successful separation process. The more recent literature, [2,3], adds more insights into the processes in electrical precipitation, particularly with reference to “grade efficiency.”

Due to the increase of the number and unit power of industrial plants, combined with the lowering of dust emissions standards, the enhancement of efficiency deserves further investigation, in spite of previous significant R&D studies. One of the most important aspects characterising ESP is the fluid dynamics, since the velocity field throughout the collecting region controls dust deposition. In turn, the velocity field is influenced by several factors, including the geometry of the inlet and outlet hoppers, the inner elements inserted to equalize the flow distribution, the shape of collecting electrodes, the electrical wind, the “leaking” and “snaking” flow pattern [1], the onset of wakes, etc.

Concerning the secondary flow generated by the corona discharge, Leonard et al. [2] examined, by means of different experimental approaches, the turbulence induced by the electrostatic field in single wire and multiwire flat-plate precipitators. More recently, Soldati et al. [4] formulated a CFD model reproducing the flow field and the role of dust deposition in flat plate ESP. Leonard concluded that “for typical ESP conditions, the level of corona-induced turbulence is significantly smaller than that result-

ing from entrance ducting and the wakes of internal structures typical of commercial precipitators.” The shape of inlet and outlet ducts is normally imposed by layout constraints. In some cases guide vanes and perforated plates may prove ineffective or even countereffective as flow-smoothing devices. They may even cause flow instability, [5–7].

Our department has been involved for many years in research on scale models of flue gas cleaning devices, both ESP and catalytic reactors (SCR), according to the customary procedure adopted also by Hamon Research-Cottrell Inc. The studies concern ESP and SCR apparatus in Power Plants of the national electric network of novel and retrofit buildup. The experimental work aims to support a theoretical analysis by means of CFD commercial codes. The main goal was to achieve a time-averaged velocity field as uniform as possible, just upstream from and throughout the cleaning devices. The first approximation parameter to assess the flow uniformity is the percent root mean square Index (% RMS) of the velocity distribution on a given cross section. This parameter is commonly related to the system performance (see Table 1).

Other criteria based on a single statistical parameter are of the same order of approximation. Also in the well-known Deutsch formula, [8], the whole complexity of the problem is brought into the so called “migration velocity,” which characterizes particle transport.

The present investigation is aimed at studying two particular aspects influencing the turbulence inside an ESP: (a) the turbulent kinetic energy generated downstream from a perforated plate and its decay, (b) the mean and turbulent velocity field within the region delimited by a pair of collecting electrodes. The importance of the first item is due to the fact that a perforated plate is frequently inserted at the end of the upstream hopper, very close to the first collecting stage of an ESP, and may influence its performance. Some correlation concerning the decay of nearly isotropic turbulence is available in the literature. Since the application to specific cases is questionable, experiments were performed on the same perforated plates used in the laboratory tests. Moreover, a new simplified model has been developed and checked against our experimental data. The second item mainly concerns the effects of the collecting electrodes on the velocity field. In fact, the onset of local flow detachment is likely to produce tur-

Contributed by the Fluids Engineering Division for publication in the JOURNAL OF FLUIDS ENGINEERING. Manuscript received by the Fluids Engineering Division April 21, 2000; revised manuscript received January 12, 2003. Associate Editor: J. Bridges.

Table 1 ESP system performance based on the percent RMS index

% RMS	≈10%–15%	≈15%–25%	>30%
quality	excellent	satisfactory	poor

bulence close to the plates. Moreover, the evolution of the inlet flow disturbances through a collecting stage appears of some interest. On the scale model we used collecting electrodes of undulated shape, which, according to various patents, are preferred to prevent significant dust re-entrainment during the rapping process.

The final goal is to provide realistic boundary conditions for CFD calculations and to validate the numerical simulations with the experimental data obtained from the dust collecting stages. The knowledge of the mean velocity field and turbulence intensity will also allow predictions of collector efficiency, by means of a particle transport correlation.

2 Turbulent Decay Laws

Turbulence is still one of the great unsolved problems of physics, in spite of the efforts devoted to it over more than a century since the pioneering work of O. Reynolds. The most simplified case is homogeneous isotropic turbulence, approximately satisfied by the flow field downstream from a perforated plate. In fact, grid-generated turbulence is a good approximation to homogeneity at a distance larger than about 50 hydraulic diameters downstream.

No exact law is known for the decay of homogeneous and isotropic turbulence, although many experimental studies of grid-generated turbulence are available in the literature. The difficulty of an exact representation lies above all in the advective terms of Navier-Stokes equations, which are nonlinear and do not cause decay by themselves, but redistribute turbulent kinetic energy across the frequency spectrum, [9]. Unless we are in the final stage of decay, we would expect the advective term to dominate over the dissipative one. At the end of the 1930s, Loytsianski and Milliontchikov [10] deduced an asymptotically correct decay law suitable when turbulent energy is so small that viscous dissipation is predominant. This law does not fit the needs of industrial equipment modeling, because the most interesting stage of turbulence decay happens earlier, when viscous dissipation is confined at the smallest scales.

Hinze [11] reported many experimental results of grid turbulence and those by Comte-Bellot and Corrsin [12] are amongst the most complete. Provided the flow Reynolds number is large, it was found that the decay of grid-generated turbulence may be described by power laws such as

$$k(t) = k(t^*) \left(\frac{t^*}{t} \right)^n \quad (1)$$

where t is the time elapsed since a conventional reference time, t^* . It should be noted that power laws are valid starting at some distance downstream from the grid location, because of near-grid effects that alter the turbulence behavior. Although power laws like Eq. (1) were obtained experimentally for all grid geometry, there is no agreement on the value of the exponent n , which appears to vary significantly from grid to grid, [12]. Power laws have only asymptotic validity and, owing to the unknown origin of the time coordinate, it is difficult to determine the precise value of the exponent n in any particular experiment.

3 A New Model

A new model has been developed assuming that homogeneous turbulence is a good approximation downstream from a perforated plate, in the sense that variations in the flow statistical properties take place over distances larger than the turbulent length scales.

The turbulence is also approximately isotropic. Since there is little mean shear, turbulence energy production is negligible and energy is simply transferred from large to small scales, where it is dissipated. In strictly homogeneous turbulence the diffusive term is zero, too. In this condition we can describe the decay of turbulent energy by the following equation, [13],

$$\frac{dk}{dt} = -\varepsilon \quad (2)$$

where ε represents the turbulent energy dissipation rate. This is the one-dimensional turbulent kinetic energy equation for homogeneous turbulence without mean flow and no mean velocity gradients. It states that, because there is no production, the turbulent energy decreases continuously. Equation (2) gives the time rate of change of turbulent energy per unit mass in a Lagrangian reference frame moving with the mean flow velocity, \bar{U}_z . The time is related to downstream distance by $t = z/\bar{U}_z$. Thus, Eq. (2) transforms into

$$\bar{U}_z \frac{dk}{dz} = -\varepsilon \quad (3)$$

which contains two unknown quantities, k and ε . One needs another equation to solve the problem, namely a model of the turbulent energy dissipation rate. We have resorted to the following relation, which relates k and ε and is based on dimensional considerations, [14,15]:

$$\varepsilon = \alpha k^{3/2} \quad (4)$$

where α is a proportionality constant depending on a characteristic length scale of the system. Substituting Eq. (4) into Eq. (3), writing

$$\beta = \frac{\alpha}{2\bar{U}_z}, \quad (5)$$

and performing an integration, one obtains

$$\frac{1}{\sqrt{k(z)}} - \frac{1}{\sqrt{k(0)}} = \beta z \quad (6)$$

which may be rewritten similarly to a power law

$$k(z) = \left[\beta z + \frac{1}{\sqrt{k(0)}} \right]^{-2} \quad (7)$$

where z is the distance from the perforated plate. Notice that Eq. (7) contains two empirical parameters, $k(0)$ and β , to be assigned experimentally. The proposed law has the advantage of being linear with respect to the auxiliary variable κ , if one assumes $\kappa = 1/\sqrt{k}$

$$\kappa(z) - \kappa(0) = \beta z. \quad (8)$$

This property makes it easier to compute β through a linear fit of the experimental data. Introducing the nondimensional variable $\zeta = z/d$ in place of z , and $(\bar{U}_z)^2/2k$ instead of k , the proposed law for decaying homogeneous turbulence may be written in the following dimensionless form:

$$\frac{\bar{U}_z^2}{2k} = \frac{\bar{U}_z^2}{2} \left[\beta \zeta d + \frac{1}{\sqrt{k(0)}} \right] \quad (9)$$

where d is the hydraulic diameter of the holes in the perforated plate.

4 Experimental Setup

Measurements were obtained using a transparent scale model (Fig. 1) reproducing a catalytic reactor inserted in a research and demonstration power plant (volume flow rate $\approx 20,000$ [m³/h])

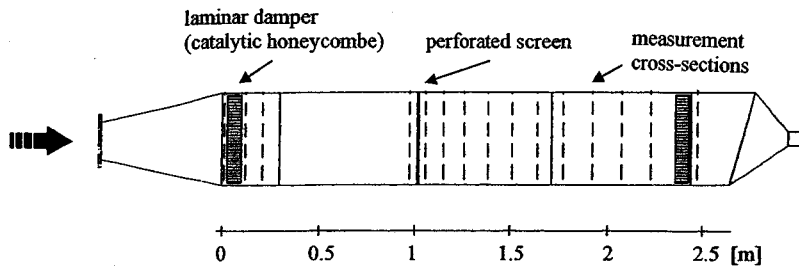


Fig. 1 Schematic of the test section used to measure turbulence decay past a perforated screen

s.c.). The scale model had rectangular cross section (514×278 mm, hydraulic diameter, $D=361$ mm) and a L/D ratio ≈ 7 . Perforated screens were inserted downstream from a laminar damper and the system was operated at $Re \approx 5 \div 6 \times 10^4$. A “plenum” was inserted downstream from the scale model to uncouple it from disturbances. A centrifugal fan with a throttle valve allowed adjustment of the air flow-rate, measured by an orifice flow meter.

Flow velocity was measured by a constant temperature hot-wire anemometer (DISA 55M) with $5\text{-}\mu\text{m}$ -diameter wire probe (mod. P11), which ensured a frequency response adequate to the turbulent spectrum. The probe was calibrated on a potential jet in the velocity range 0.2 to 50 m/s, and installed on a carriage sliding on a steel track and controlled by a computer-driven stepper motor. More than 20,000 data were collected at every measurement point, by means of a dynamical signals analyzer (Hewlett-Packard 35665A) at sampling frequency of 32 kHz, and transferred to a PC for statistical analysis. The sampled voltages were converted into velocities through the calibration function and then processed to determine mean and fluctuating components. The probe wire was aligned normally to the axial flow direction in order to be preferentially sensitive to the longitudinal velocity component.

5 Experimental Results

In the experimental investigation three types of perforated plates were used (Table 2). Their geometry is completely described by two quantities: *hydraulic diameter* d of the holes and *void ratio* (area of the holes to the total plate area). Comparison of experimental data with our model was carried out according to two criteria. First we applied the standard least-squares method to find a linear fit of the data, according to Eq. (8).

Figures 2–4 show some examples of the linear best fits of the experimental data. The numerical values of both coefficients of the model, say $k'(0)$ and β , as deduced by the linear fit, are reported in Table 3. In the same table is reported the measured value of $k(0)$. Adequacy of the fit to experimental data was evaluated by means of the percent root mean square error, which falls in the range 1.37 to 3.86%. Since common sense suggests a monotone decay line, irrespective of the analytical representation, experimental data oscillations should be interpreted as flow irregularities and disturbances.

Table 2 Characteristics of the perforated plates

Grid No.	Hole Shape and Pattern	Hydraulic Diameter (mm)	Void Ratio
1	circular holes, triangular pattern	5	0.35
2	circular holes, triangular pattern	6	0.53
3	square holes, square pattern	8	0.64

Another approach which is closer to the practice of turbulent models in the numerical simulation of flow fields (where mainly upstream boundary conditions are needed), is to impose $k(0)$, by assigning to it the value of k at the first measurement location, and then to apply a least-squares linear regression analysis. With a few symbolic manipulations, one can prove that the new value of β is

$$\beta' = \frac{\sum_{i=2}^N (\kappa_i - \kappa_1)(z_i - z_1)}{\sum_{i=2}^N (z_i - z_1)^2} \quad (10)$$

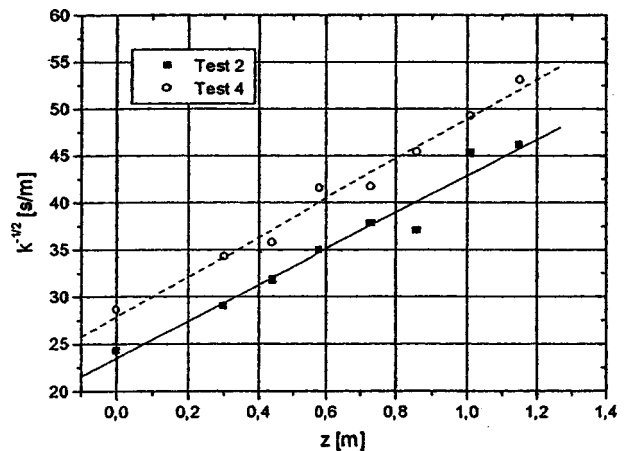


Fig. 2 Measured turbulence decay for test cases 2 and 4 of Table 2: experimental data points and their linear best fit according to Eq. (8)

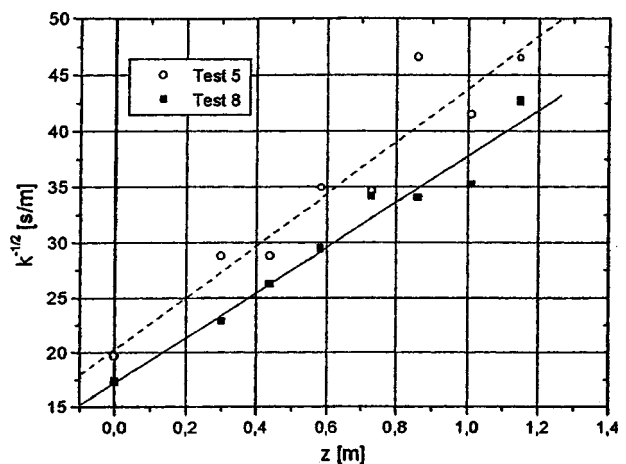


Fig. 3 Measured turbulence decay for test cases 5 and 8 of Table 2: experimental data points and their linear best fit according to Eq. (8)

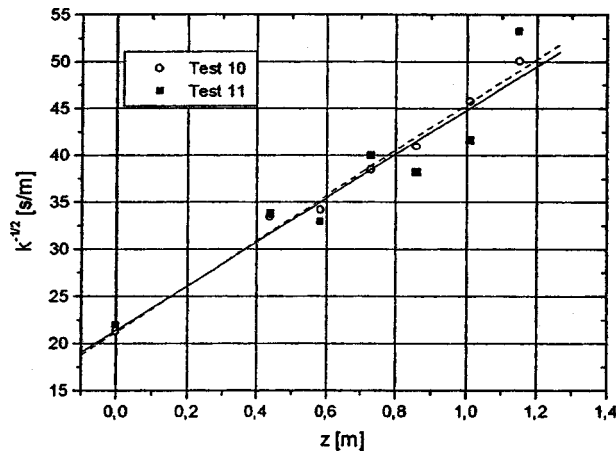


Fig. 4 Measured turbulence decay for test cases 10 and 11 of Table 2: experimental data points and their linear best fit according to Eq. (8)

Notice that summations are restricted to indexes 2 to N , since the first point is now fixed. The values of β' for the modified linear fits and the corresponding RMS errors are reported in the last two columns of Table 3. Typically the error is three to five times larger than before. That is because the modified least-squares method, having imposed the first point, is more severe and less adaptive to experimental data, though closer to the practice of numerical simulation.

It is also interesting to show the complete set of data in one plot, in order to evaluate the turbulence model on the whole, through comparison with the dimensionless form (9), which is an obvious candidate for such a task. Unfortunately, the coefficients depend upon various quantities such as β and \overline{U}_z which are specific to each data set, so Eq. (9) maps each set onto a different curve. However, with a little mathematics one can prove that introducing auxiliary nondimensional coordinates

$$u = \frac{z}{d} + \frac{1}{\beta d \sqrt{k(0)}}; \quad w = \frac{1}{k \beta^2 d^2} \quad (11)$$

Equation (9) transforms onto one parabola of the equation $w = u^2$.

Plotting the experimental data in the (u, w) plane, they form a “cloud” of 92 data points (Fig. 5) around the parabola (solid line), while the least-square parabola (dashed line) fitting the same data is represented by the equation

$$w = 0.98u^2 - 0.083u + 20.16. \quad (12)$$

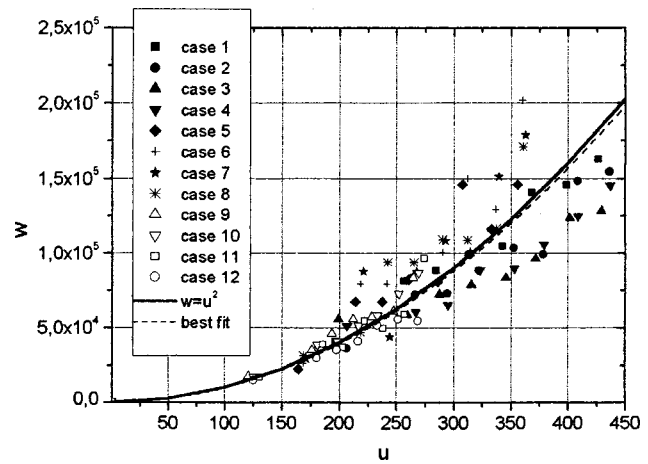


Fig. 5 The complete set of data in dimensionless form. The solid line is the parabola $w = u^2$, while the dashed line represents the best fit of the data.

Theoretical and experimental least-squares parabolas match quite well. The scatter of the data reduces for low u values, which refer to relatively short distances from the turbulence-generating perforated screen, hence to a region where turbulence is likely to be neither homogeneous nor isotropic. Obviously, this is the most critical region for any turbulence model. Concerning the dispersion of experimental points around the curve, it should be noted that the measured values of k refer to a three-dimensional flow field which the suggested model tries to describe with only one spatial coordinate (as a first approach to the problem). Consequently, the accuracy is satisfactory in most cases, since even a full-blown three-dimensional turbulence model (such as the widely used $k-\epsilon$) often misses the experimental values by 20% or more, [16].

6 Flow Nonuniformity

The last remark concerning the intrinsic three-dimensional character of the flow leads to the second subject of this paper, the flow uniformity. Its importance from the standpoint of the efficiency of electrostatic precipitators may be evaluated using the well-known formula by Deutsch [4].

In an approximately two-dimensional velocity field, the overall efficiency of the precipitator may be computed as the spatial average of local efficiencies, weighted with respect to flow velocity:

Table 3 List of test cases

Test No.	Gird No.	$k(0) \times 10^{-3}$ (m ² /s ²) (Measured)	$k'(0) \times 10^{-3}$ (m ² /s ²) (Interpolated)	β (m ⁻² s)	(%) RMS Error	β' (m ⁻² s)	(%) RMS Error
1	1	2.11	2.39	22.2	1.64	21.0	7.20
2	1	1.70	2.67	23.5	2.52	18.5	7.41
3	1	1.40	2.94	26.8	1.58	18.6	4.83
4	1	1.22	2.26	27.9	1.37	20.2	5.27
5	2	2.59	1.82	20.3	3.86	24.2	13.10
6	2	2.87	1.56	18.7	2.74	25.4	11.30
7	2	3.06	1.95	17.8	2.74	22.3	10.50
8	2	3.32	2.38	17.2	2.42	20.4	7.87
9	3	2.42	1.86	21.1	1.75	24.0	7.70
10	3	2.22	1.71	21.2	1.55	24.2	4.82
11	3	2.08	1.83	21.4	2.44	22.8	13.60
12	3	1.93	2.70	22.9	1.99	19.4	6.52

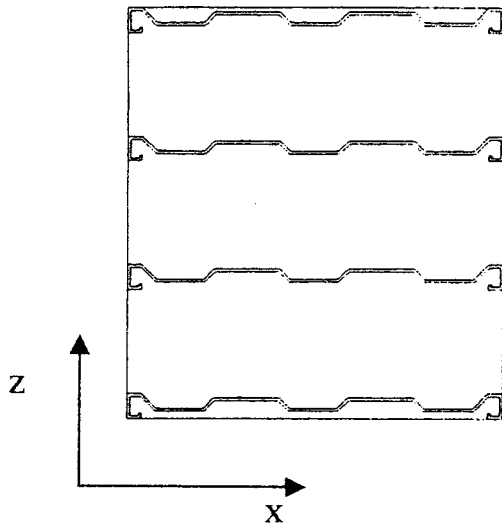


Fig. 6 Schematic of the collecting electrodes used in the present investigation

$$\eta = 1 - \frac{\sum_{i=1}^N U_i \exp\left(-\frac{W_i L}{U_i \delta}\right)}{\sum_{i=1}^N U_i} \quad (13)$$

where W_i are the local particle transverse migration velocities, U_i the local flow mean velocities, and L and δ are the length and spacing of the electrodes.

The experience shows that in standard ESP η decreases monotonically when U_i increases. Ducts having higher U_i dominate the overall efficiency of the precipitator, and the damage caused by regions with U_i above the average is only partially balanced by the improvement in regions where U_i is below the average. The assumption of uniform particle distribution was used in developing the Deutsch formula. This is valid if turbulent mixing is significant. However, theoretical and experimental work, [2], has shown "that for moderate levels of turbulence, e.g., fully developed turbulent channel flow, precipitators should be far more efficient than is predicted by the Deutsch formula." These results suggest that it is desirable to minimize the generation of turbulence for improved precipitator performance, since the largest diffusivities produce the lowest grade efficiency, [3]. The influence of fluid dynamics on precipitator efficiencies is worthy of investigation although the problem is complicated by secondary effects. In real precipitators, efficiencies lower than those predicted by the Deutsch formula may be found, probably caused by the local structure of the electrical field, as suggested by numerical predictions, [3].

7 Experiments on Scale Models

The main aim of the experiments on scale models was to obtain a better knowledge of the flow characteristics in the region of the dust-collecting electrodes. Experimental and numerical results indicate that the mean flow, the electrohydrodynamic flow and the turbulence field undergo significant modifications caused by mutual interaction, in flat-plate-wire or plate-plate collecting systems, [17]. Industrial collecting electrodes have an undulated shape, [1], like those used in the present investigation (Fig. 6), which may induce turbulence. Moreover, hoods with wide divergence angles, turning vanes and perforated plates also generate a turbulent (even recirculating) flow at the inlet of the first stage, because their geometry may not correspond to the optimum configuration, [5,7].

As a first approach, experimental tests were performed on a 1:16 scale model of a dust-separating system including the electrostatic filter, the upstream and downstream hoods and ducts. Due

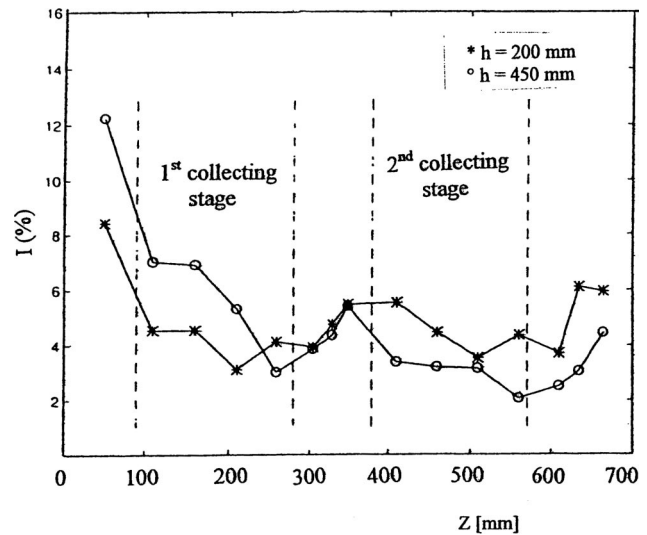


Fig. 7 Axial distribution of the relative turbulence intensity as measured at two different depths from the upper wall of the model

to the short distance between the plate electrodes (≈ 20 mm), mean velocity and turbulence intensity profiles were measured along the centreline of the first two collecting stages. Figure 7 presents the axial distribution of the relative turbulence intensity (defined as the ratio of the local RMS fluctuating component to the flow mean velocity), as measured at two different depths, h , from the upper wall of the model. It is worth noting the relatively high inlet value followed by a rapid decay along the first collecting stage and a further decrease in the second one. The small increase in the lag between the stages is probably due to the sudden, though small, expansion in the cross section. The aforementioned behavior is justified by the existence of a diffuser upstream from the filter, having an obtuse angle (about 100 deg). In spite of the insertion of perforated screens to make the mean flow more uniform, vortices generated by the fluid vein detachment contribute to flow nonuniformity and increased turbulence near the wall. This may reduce the efficiency of collecting electrodes.

These results suggested a more detailed investigation of the two-dimensional turbulence distribution inside a 1:3 scale model of two collecting electrodes. Their shape is shown in Fig. 6 and the operating flow conditions were selected in order to preserve both the geometry and flow similarity with respect to full scale particle collectors. The investigation was aimed at reconstructing the flow field distribution in the volume delimited by the first stage of collecting electrodes. Measurements were carried out considering four different experimental arrangements, in order to ascertain the effect of inserting a perforated plate and its distance upstream from the electrodes:

- Case A: laminar damper 540 mm upstream from the scale model,
- Case B: perforated plate 540 mm ($z/d=54$) upstream,
- Case C: perforated plate 190 mm ($z/d=19$) upstream, and
- Case D: perforated plate 100 mm ($z/d=19$) upstream.

Since preliminary experiments proved the approximate symmetry of the flow field with respect to the median horizontal plane, measurements were carried out in the upper-half section only, on three horizontal planes 40 mm apart, starting 200 mm below the upper wall. Figures 8 and 9 show the isolines of mean velocity and turbulence intensity in a section 280 mm from the top wall, confined by the electrodes shown in Fig. 6.

Figure 8 refers to case A and indicates that the mean flow is almost uniform at the inlet with moderate turbulence intensity, which then increases, close to one electrode, probably due to the corrugated plate geometry. Lower levels are found in the inner region, where turbulence intensity falls under 10%, which is con-

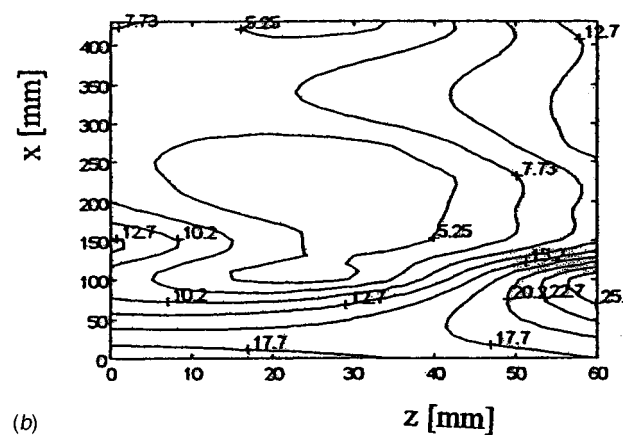
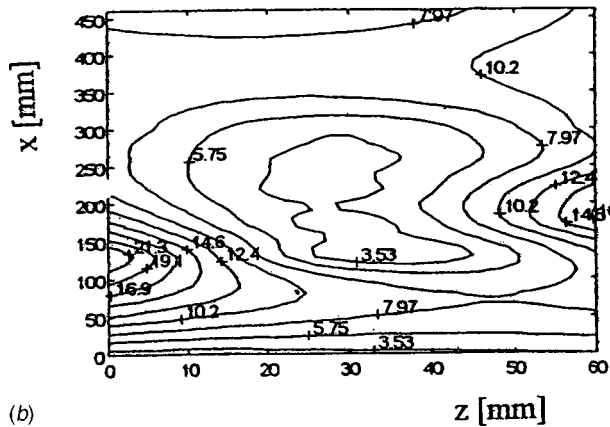
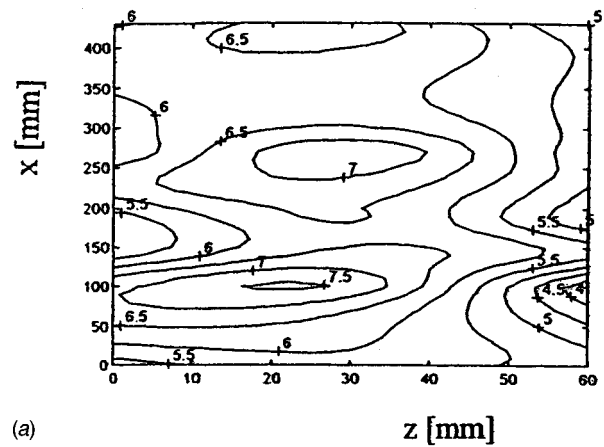
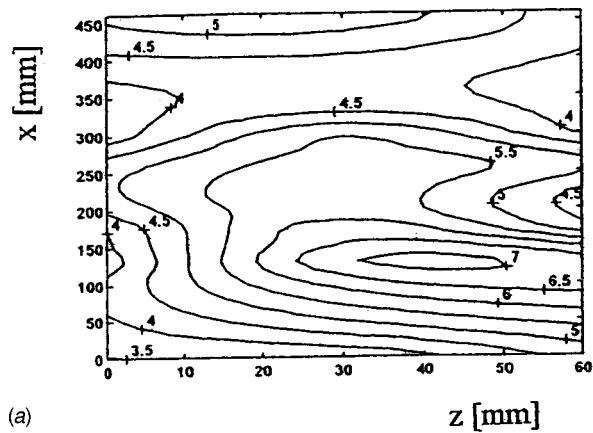


Fig. 8 Mean velocity (a) and turbulence intensity (b) isolines measured in a section 280 mm from the top wall, in a 1:3 scale model of two collecting electrodes. Experimental case A.

Fig. 9 Mean velocity (a) and turbulence intensity (b) isolines measured in a section 280 mm from the top wall, in a 1:3 scale model of two collecting electrodes. Experimental case D.

sidered a standard value in this type of flow. Similar behavior is found in case D (Fig. 9). However, the turbulence level near the wall is higher, because the grid-generated turbulence is not allowed to decay sufficiently before entering the electrode stage.

Table 4 reports, for each arrangement, the average of the local mean velocities over the entire section, together with two dimensionless distribution parameters, the root mean square index (% RMS) and skewness, S , which give indication of the flow uniformity across the section. Positive values of S denounce local high values of the flow velocity. Values close to zero for both RMS and S should guarantee the best configuration.

8 Conclusions

A new semi-empirical model of turbulence decay past a perforated plate was deduced and tested. The proposed model was shown to be in good agreement with experimental data even at relatively short distances from the perforated plate, 50 to 250 hydraulic diameters downstream. Further research is in progress to analyze a wider range of test conditions.

The experimental results on scale models confirmed that significant turbulence levels are found in practical ESP. In fact, in-

dustrial dust-separating systems require perforated plates or other devices to lower the bulk kinetic energy of the main flow across the hood between the upstream ducts and precipitators. The layout of conventional systems has one of the perforated plates close to the entrance of the first collecting stage. As a consequence, the turbulence generated near the grid propagates inside the first part of the stage. Moreover, the electrode geometry itself may further contribute to turbulence production. It is therefore important to optimize the overall system configuration of electrostatic precipitators and particular attention should be paid to the design of the upstream section of the first collection stage.

Experimental investigations on scale models prove useful in achieving a better knowledge of turbulence generation and distribution. The present study was also intended to provide a reliable database for validation of CFD codes and improvement of their predictive capability.

Acknowledgments

The authors wish to thank Mrs. A. Antonini, R. Bassan, C. Cerretelli, G.M. Fiorino, A. Invernizzi, and C. Rinaldi for the valuable cooperation in performing the experiments. The research activity was financially supported by ENEL (Italian Energetic Board), Hamon Research-Cottrell Italia and Termokimik Co.

Nomenclature

- d = hydraulic diameter of the holes in the perforated plates (m)
- D = hydraulic diameter of the scale model (m)
- h = depth from the upper wall (m)

Table 4 Distribution parameters for cases A to D

Quantity	Case A	Case B	Case C	Case D
Mean velocity [m/s]	5.14	5.61	5.83	5.79
% RMS	0.21	0.18	0.17	0.19
S	0.25	-0.14	0.90	-0.17

k = turbulent kinetic energy per unit mass (m^2/s^2)
 L = length of collecting electrodes (m)
 Re = Reynolds number
 RMS = root mean square
 S = dimensionless skewness
 t = time (s)
 t^* = reference time (s), as defined in Eq. (1)
 u, w = nondimensional coordinates, as defined in Eq. (11)
 \bar{U}_z = flow mean velocity (time average) (m/s)
 \bar{W} = transverse migration velocity of the particles
 z = longitudinal coordinate or downstream distance (m)

Greek

α = empirical coefficient (m^{-1}), as defined in Eq. (4)
 β = empirical coefficient (m^{-2}s), as defined in Eq. (5)
 δ = spacing of the collecting electrodes (m)
 ε = dissipation rate of turbulent kinetic energy (m^2s^{-3})
 η = collection efficiency of the precipitator
 κ = auxiliary quantity (m^{-1}s), ($=k^{-1/2}$)

References

- [1] White, H. J., 1963, *Industrial Electrostatic Precipitation*, Addison-Wesley, New York.
- [2] Leonard, G. L., Mitchner, M., and Self, S. A., 1983, "An Experimental Study of the Electro Hydrodynamic Flow in Electrostatic Precipitators," *J. Fluids Mech.*, **127**, pp. 123–140.
- [3] Riehle, C., and Löffler, F., 1995, "Grade Efficiency and Eddy Diffusivity Models," *J. Electrostat.*, **34**, pp. 401–413.
- [4] Soldati, A., Casal, M., Andreussi, P., and Banerjee, S., 1997, "Lagrangian Simulation of Turbulent Particle Dispersion in Electrostatic Precipitators," *AIChE J.*, **43**(6), pp. 1403–1412.
- [5] Sotgia, G., 1982, "The Effect of Fluid Dynamics on the Efficiency of Electrostatic Precipitators," *Ingegneria Ambientale*, **11**(5), Sept. (in Italian).
- [6] Bassan, R., Ferrari, P., Rinaldi, C., and Sotgia, G., 1994, "Flow Velocity Equalization in Flue Gases Industrial Cleaning Devices: Design Criteria and Experimental Tests on Scale Models," *Proceedings of the ATI National Conference*, Perugia, Sept. (in Italian).
- [7] Idel'chick, E., 1991, *Fluid Dynamics of Industrial Equipment: Flow Distribution Design Methods*, Norman A. Decker, ed., Hemisphere, Washington, DC.
- [8] Deutsch, W., 1922, "Bewegung und Ladung der Elektrizitätsträger in Zylinderkondensator," *Ann. Phys. (Leipzig)*, Vierte Folge-Band **68**, pp. 335–344.
- [9] Frisch, U., 1995, *Turbulence*, Cambridge University Press, Cambridge, UK.
- [10] Landau, L., and Lifchitz, E. M., 1971, *Mécanique des Fluides*, Editions MIR, Moscow.
- [11] Hinze, J. O., 1975, *Turbulence*, McGraw-Hill, New York.
- [12] Comte-Bellot, G., and Corrsin, S., 1966, "The Use of a Contraction to Improve the Isotropy of a Grid-Generated Turbulence," *J. Fluids Mech.*, **25**, Part 4, pp. 657–682.
- [13] Mathieu, J., and Scott, J., 2000, *An Introduction to Turbulent Flow*, Cambridge University Press, New York.
- [14] Tennekes, H., and Lumley, J. L., 1985, *A First Course in Turbulence*, The M.I.T. Press, Cambridge, MA.
- [15] Durbin, P. A., and Petterson, Reif B. A., 2001, *Statistical Theory and Modeling for Turbulent Flows*, John Wiley and Sons, New York.
- [16] Ferziger, J. H., and Peric, M., 1999, *Computational Methods for Fluid Dynamics*, 2nd Rev. Ed., Springer-Verlag, Berlin.
- [17] Soldati, A., and Banerjee, S., 1998, "Turbulence Modification by Large-Scale Organized Electro Hydrodynamic Flows," *Phys. Fluids*, **10**(7), pp. 1742–1756.

Experimental Study of the Flow in a Compact Heat Exchanger Channel With Embossed-Type Vortex Generators

F. Dupont
C. Gabillet
P. Bot

e-mail: bot@ecole-navale.fr

Institut de Recherche de l'Ecole-Navale,
F29240 Brest-Naval, France

The isothermal flow in a model channel of plate-fin heat exchanger with periodically arranged embossed-like vortex generators is investigated. Velocity measurements are performed by LDA in the transitional regime (Reynolds number from 1000 up to 5000). Strong longitudinal vortices are observed downstream of each generator. The vortex roll-up process is highlighted by the evolution of the velocity vector field in the cross section of the flow. The modifications of the vortex characteristics after successively encountered generators are investigated. This work shows most of the flow features which are known to produce heat transfer enhancement, and shows that these smooth shaped vortex generators are very promising for enhanced heat exchangers. [DOI: 10.1115/1.1595675]

1 Introduction

To enhance heat transfer in industrial compact heat exchangers, an interesting passive method is to use longitudinal vortices in the flow. An industrial mean to generate such vortices is to place wings or winglets on the transfer surface, called vortex generators (for a review, see [1,2]). It appears that a better knowledge of these vortex flows should enable a better design of optimized compact heat exchangers. A lot of work has been dedicated into analyzing the effect of vortex generators on the boundary layer of a single plate with a uniform flow far above the surface, [3–5]. This enabled an insight into the mechanisms of longitudinal vortex-induced transfer enhancement. It showed the interactions between the vortex and boundary layer, [6], and the increase of turbulence intensity, [7]. For example, Gentry and Jacobi [5] investigated the interactions of a vortex pair generated by delta wings with a boundary layer, and found a 50% to 60% enhancement of averaged transfer over a flat plate. However, for the issue of compact heat exchangers, it is necessary to extend this knowledge to the case of confined channel flows.

Investigation of confined channel flows with rectangular or delta wing and winglet vortex generators has recently motivated numerous numerical studies, [8–11] and a few experimental ones, [12,13]. A recent numerical study, [14], has shown the efficiency of parallelepipedic generators. The strong confinement increases the number of involved parameters and the complexity of the flow. Thus, there is a real need in experimental studies to get a better insight into the transfer enhancement mechanism. In parametric studies, [2,9,10,15], recommendations for the design of vortex generators in compact heat exchangers are given. The geometrical configuration studied here (see Section 2) is chosen according to these recommendations.

In a tube-fin exchanger, vortex generators can be obtained at reasonable manufacturing costs by punching the fins. The obtained triangular winglets perpendicular to the fins are known to give rise to a significant transfer enhancement, [13,15]. In a plate-fin exchanger, however, punching the fins is prohibited so as to avoid the mixing of both fluids. Due to the constraints in manufacturing costs, an acceptable method of obtaining vortex generators is to emboss the plates, which results in a smooth shaped

winglet without sharp edges and of a limited height. The ability of such rounded embossed bodies to generate efficient vortices for transfer enhancement will be discussed.

The present work is an experimental investigation of the flow field in a channel of a vortex enhanced heat exchanger in a geometrical configuration close to industrial applications of plate-fin exchangers, where several vortex generators are periodically arranged. In order to be able to carry out flow measurements, the length scales are chosen to be around five times larger in the present experiment than in practical exchangers.

The aim of this work is to show the ability of embossed vortex generators to produce longitudinal vortices, and to precisely describe the resulting complex flow in a given geometry.

To our knowledge, the present are the first velocity measurements achieved in a channel with smooth obstacles simulating embossed vortex generators in a plate-fin exchanger. The downstream development of a vortex is investigated, as well as the evolution of the flow structure after the fluid successively encounters several vortex generators. The Reynolds number effects are also discussed. After a description of the experimental setup, results of the velocity field and the vortex characteristics are presented. Finally, the expected effects on heat transfer are discussed, as well as how the present results may be of general interest for the issue of vortex enhanced heat exchangers.

2 Experimental Setup

The experiments have been conducted in a hydrodynamic loop made of a volumetric pump, two free surface buffer tanks, a test section, and a bypass system. The test section (label (1), on Fig. 1) consists of a 980 mm long, 860 mm high channel, with a width $H = 27$ mm, delimited by lateral walls made of 25 mm transparent Perspex (2). In the upstream settling tank (3), diffusing plates (4), a honeycomb (5), and a converging section (6) are placed to ho-

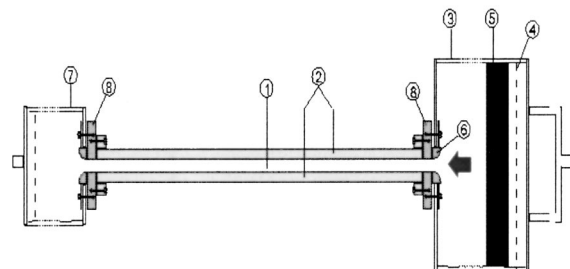


Fig. 1 Top view of the experimental facility

Contributed by the Fluids Engineering Division for publication in the JOURNAL OF FLUIDS ENGINEERING. Manuscript received by the Fluids Engineering Division Apr. 4, 2002; revised manuscript received Mar. 3, 2003. Associate Editor: M. V. Ötügen.

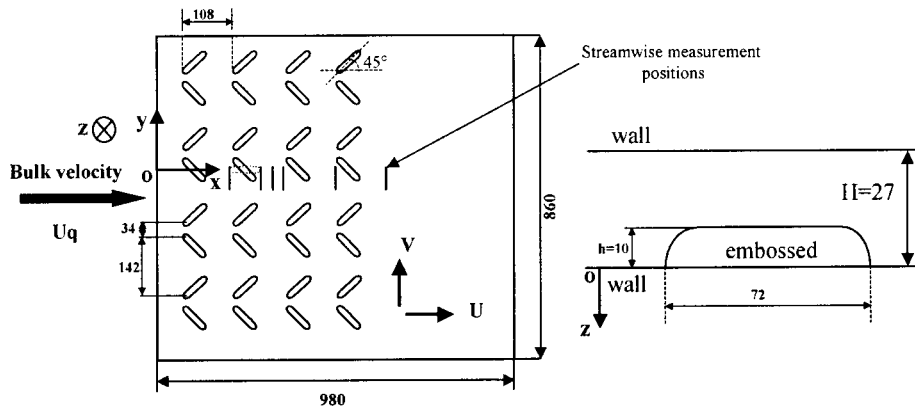


Fig. 2 Geometry of the channel with mounted embossed-like vortex generators. All dimensions are in millimeters. Pairs of generators are arranged in four lines (streamwise horizontal direction: x) and four columns (transverse vertical direction: y).

mogenize the flow at the test section inlet. A mixing tank (7) is placed downstream the test section which is fitted with mounting flanges (8). Flow rates are determined by a magnetic flow meter with a relative accuracy of 2%. The experimental setup enables to achieve a bulk velocity U_q in the range from 0.037 m/s to 0.37 m/s, corresponding to a Reynolds number $Re=U_q H/\nu$ in the range [1000;10000]. The inlet velocity profile cannot be measured because there is no optical access at the entrance of the test section. Measurements in the channel without vortex generators were in reasonable agreement with the theory of developing flows in the entrance of a rectangular channel, [16], and showed that the turbulence intensity was always lower than 5%. At the beginning of the channel, the flow is considered as uniform and boundary layers develop downstream along the plates. In the rectangular test section, the flow in a plate-fin exchanger channel with embossed vortex generators is simulated. The vortex generators are wooden semicylinders which are attached to one of the lateral walls. Their length and height are, respectively, $2.7H$ and $0.37H$, and the ends are rounded with a curvature radius of $0.37H$ in both directions (1/4 of a sphere). Vortex generator pairs are arranged in four lines (streamwise horizontal direction: x) and four columns (transverse vertical direction: y), as shown on Fig. 2. In a pair, generators are symmetrically inclined with a 45° angle of attack, separated by $1.3H$. Lines are separated by $6.5H$, and the distance between columns is $4H$.

Velocity Measurements. To investigate the flow in the channel, the longitudinal u and vertical v velocity components were measured by laser Doppler anemometry (LDA). Measurement of the spanwise velocity component w is not possible in this experiment because of the orientation of the laser beams. A Dantec two-component LDA system with three beams is used in the back scattering mode. A beam expander and a lens of 360 mm focal length provide a probe volume that is 0.5 mm long in the spanwise direction and 0.04 mm wide in the longitudinal and vertical directions. The probe volume is traversed in the flow by a mechanical displacement system of absolute accuracy of 5 microns. Thus, the uncertainty of the measurement position relative to the walls is 0.5 mm. The water flow is seeded with Iridine particles of typical size of one micron. The scattered light signal is processed by two Dantec burst spectrum analyzers. The u and v velocity components have been recorded in a cross section of the flow over a grid of 20 nodes in the spanwise direction and 30 nodes in the vertical direction, with a 1.3 mm step. At each position, a maximum of 2500 data points are collected at a typical data rate of 50 Hz, and the mean (U, V) and rms (u', v') values are computed. U and V are estimated with a relative accuracy of $\pm 2\%$ and $\pm 6\%$, respectively, with a confidence level of 95%. Rms values are obtained with a relative accuracy of $\pm 3\%$.

3 Results

The whole flow is expected to be symmetrical with respect to the streamwise center line of the test section. Moreover, the flow behind each vortex generator pair should be symmetric with respect to the center line of the pair. Velocity measurements are carried out in one cross section downstream of each vortex generator on a single line just above the channel center line. To see the evolution of a vortex downstream of a generator, measurements have also been taken in three different cross sections behind the second column. The location of each measurement section x is shown in Fig. 2 and summarized in Table 1, where the distance downstream of the generator d is also given. Three flow rates have been studied, corresponding to $Re=1000, 2000$ and 5000 (i.e.: $U_q=0.037, 0.074$ and 0.188 m/s).

To have a first insight into the flow structure, a visualization has been made by dye injection just upstream of the first vortex generator (Fig. 3). The dye line first follows the body suction side.

Table 1 Summary of all measurement sections' reduced position x/H , column number and corresponding reduced distance behind the vortex generator trailing edge d/H

$\frac{x}{H}$	Column Number	$\frac{d}{H}$
7.1	1	2.4
9.1		0.4
10.1	2	1.4
11.1		2.4
15.1	3	2.4
19.1	4	2.4



Fig. 3 Vortex visualization by dye injection, for $Re=1000$, behind a generator of the first column

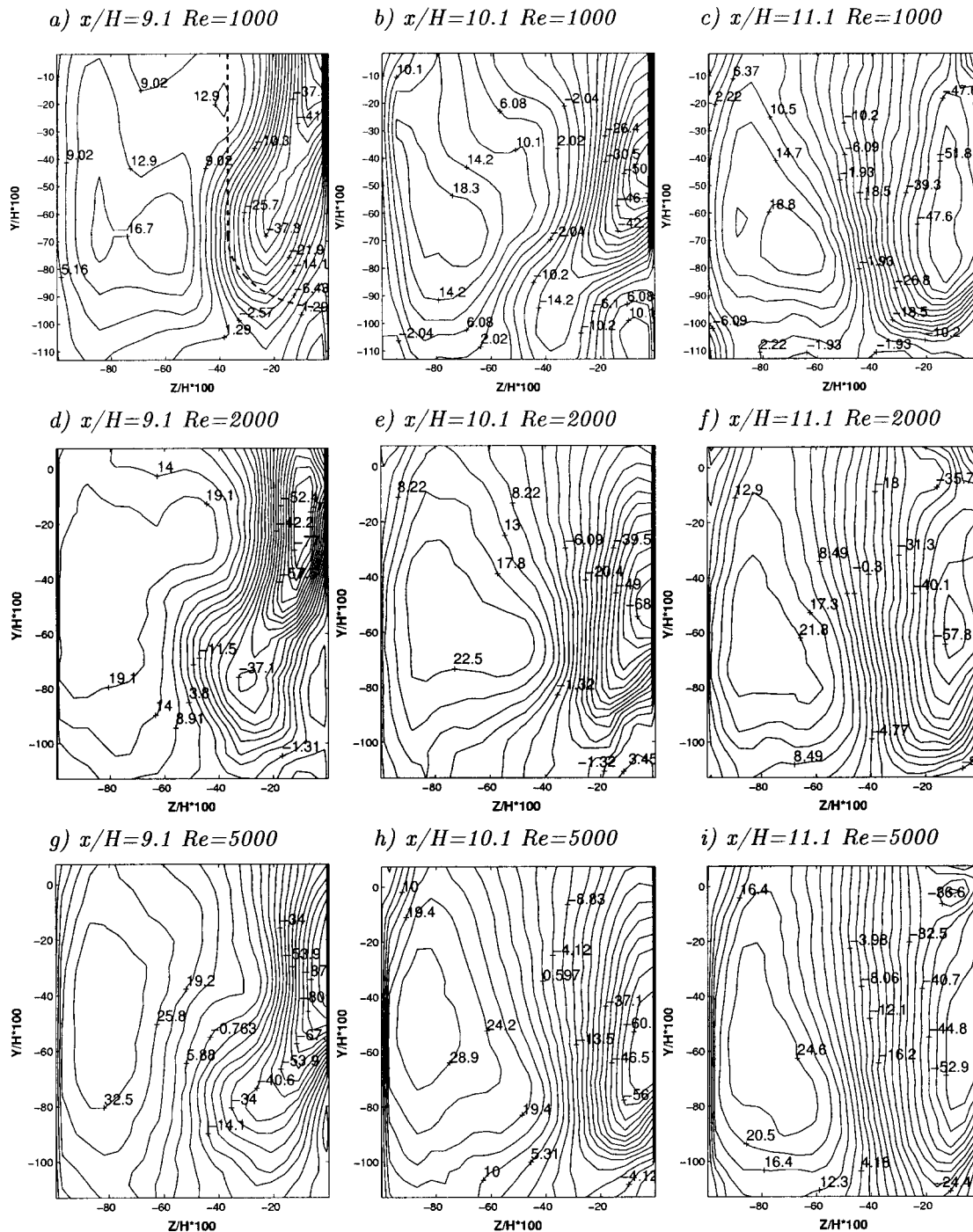


Fig. 4 Iso-values (%) of mean vertical velocity component $V/U_q \times 100$, for $Re=1000$ (a,b,c), $Re=2000$ (d,e,f), and $Re=5000$ (g,h,i) behind the 2nd column at three streamwise cross sections (Oz, Oy)

Then a helical emission line appears after the separation point. This visualization shows the development of a vortex and its trajectory downstream of the vortex generator.

The evolution of the velocity field is investigated in detail behind the second column of vortex generators. Then, global vortex parameters are studied after a succession of generators.

3.1 Velocity Fields. First, the mean velocity components are investigated. Velocities are scaled by the bulk velocity U_q , and lengths are normalized by the channel width H . Using the measurement sections at $x/H=9.1, 10.1, 11.1$, it is possible to

estimate $\partial U/\partial x$ and $\partial V/\partial y$ at the cross sections $x/H=9.6, 10.1, 10.6$, and then to determine the third component W using the continuity equation (Eq. (1)).

$$\frac{\partial U}{\partial x} + \frac{\partial V}{\partial y} + \frac{\partial W}{\partial z} = 0 \quad (1)$$

The derivatives have been computed by a finite difference method with a center scheme, and the W component has been integrated by the trapezoid method. On the domain boundaries, forward and backward schemes have been used. A zero value has

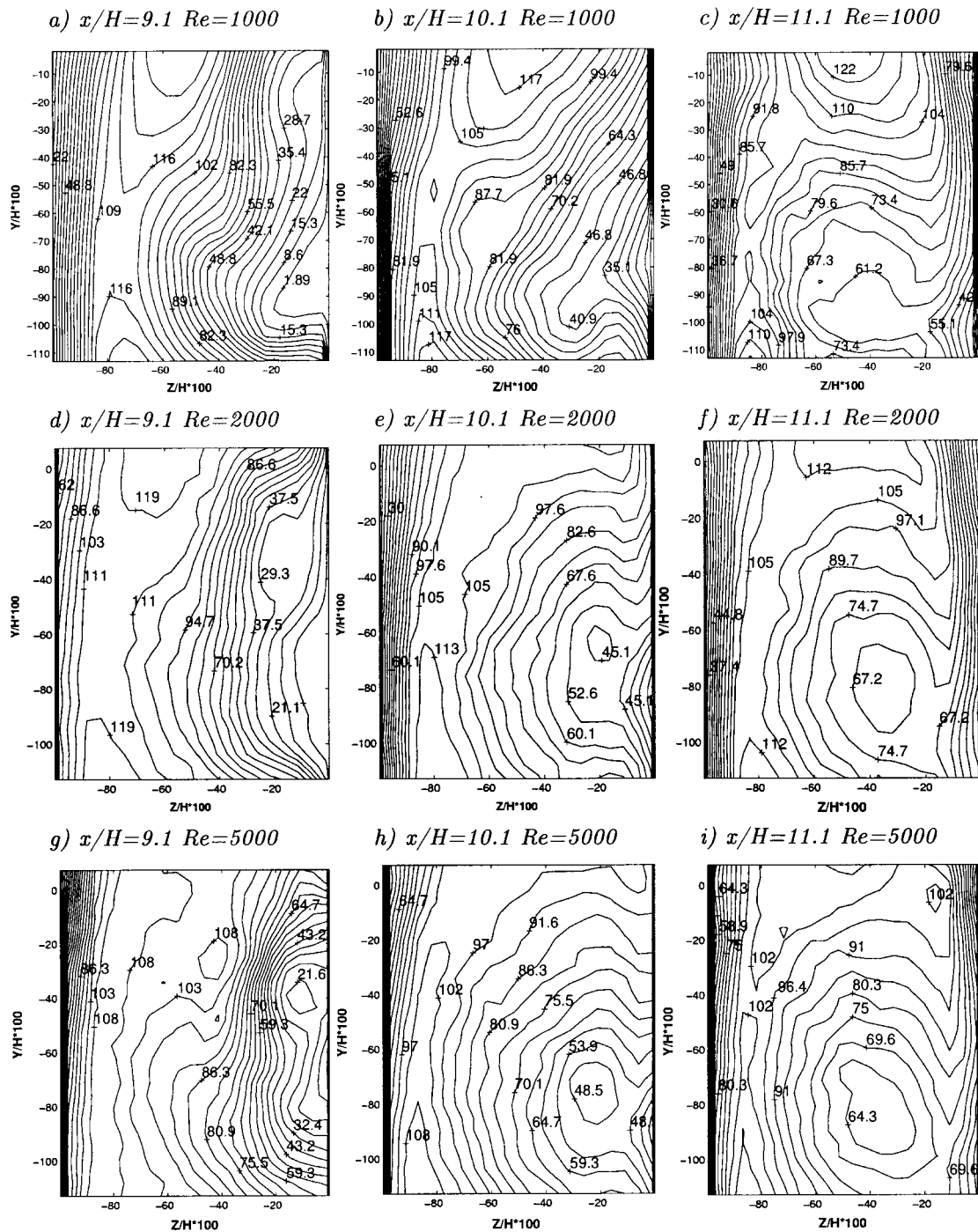


Fig. 5 Iso-values (%) of mean longitudinal velocity component $U/U_q \times 100$, for $Re=1000$ (a,b,c), $Re=2000$ (d,e,f), and $Re=5000$ (g,h,i) behind the 2nd column at three streamwise cross sections (Oz, Oy)

been applied to each velocity component on both walls (no slip no through boundary condition). Within this framework, if U and V measurements are considered as independent random variables, computation of the velocity gradient $\partial W/\partial z$ is assumed to be accurate to within U_q/H . Therefore, W is estimated with an accuracy of $0.05U_q$ near the walls. In the central part of the channel, uncertainty becomes higher, up to the order of U_q , because of integration along the z -direction. In fact, computation of the finite differences should eliminate the systematic errors. Another source of error that cannot be estimated here comes from the estimation of space derivatives by discrete finite differences. Despite this observation of rather poor accuracy, computation of the velocity

component W has been used to get a qualitative idea of the velocity vector field and the vortex structure at three positions downstream of the second vortex generator.

Velocity fields in the three cross sections behind the second generator are shown on Fig. 4 for V and Fig. 5 for U , for the three Reynolds numbers. Figure 6 shows the corresponding mean velocity vector field in the cross section.

The existence of an intense longitudinal vortex developing downstream of the generator is shown in the velocity fields by the positive and negative peaks facing each other in the V distribution (Fig. 4), and by the longitudinal velocity deficit in the U distribution (Fig. 5). The vortex structure is also clearly highlighted by

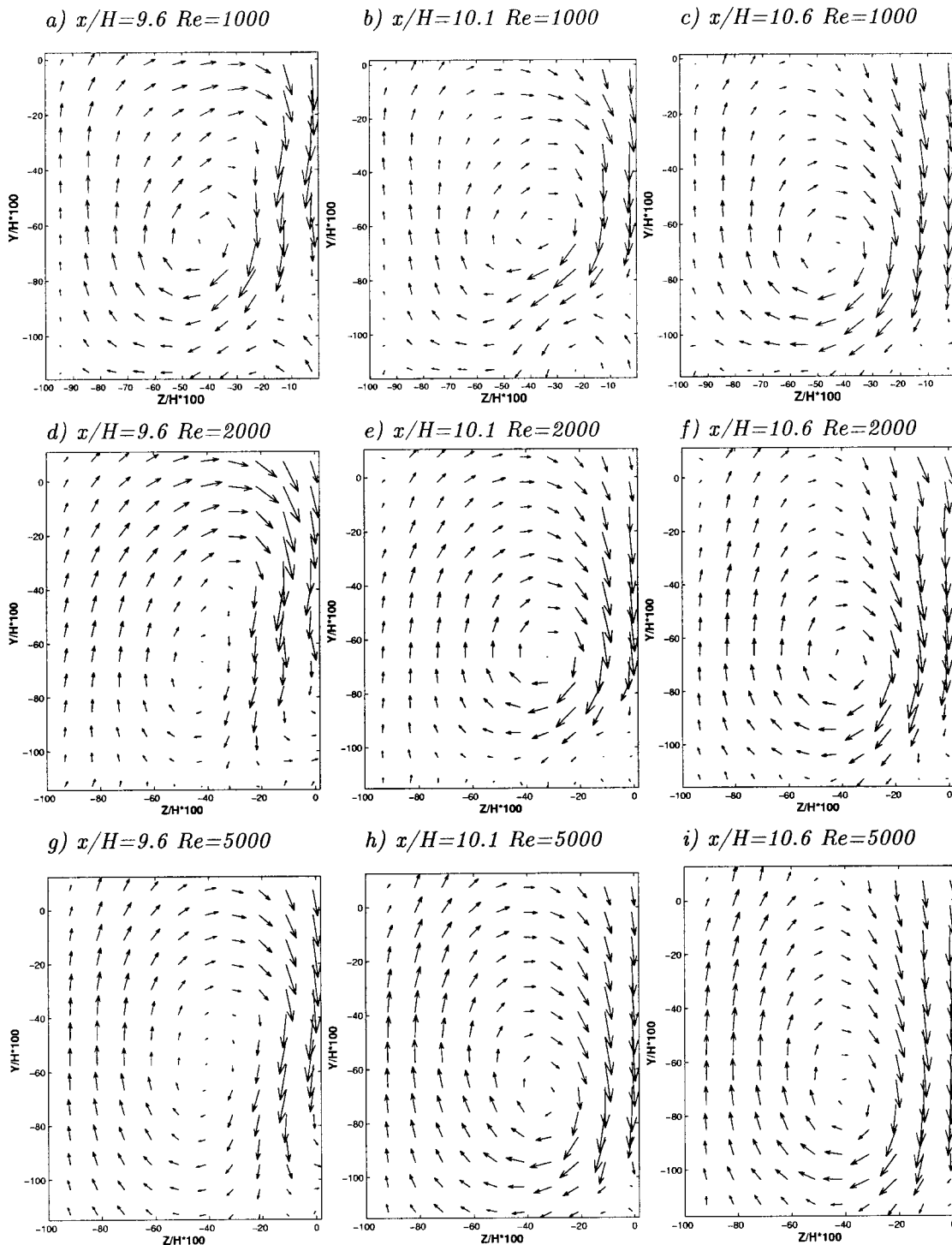


Fig. 6 Mean velocity field in the cross section, for $Re=1000$ (a,b,c), $Re=2000$ (d,e,f), and $Re=5000$ (g,h,i) behind the 2nd column at three streamwise cross sections (Oz, Oy)

the vector fields in the different cross sections (Fig. 6). With a rather circular appearance for the lower Reynolds number, the vortex is elongated in the y -direction for $Re=5000$. Moreover, it is located closer to the wall where the generators are attached ($z/H \approx -0.3$), particularly for the higher Reynolds number values. It is also noticeable that the extrema of transverse velocity are located very close to the walls (Fig. 4). As a result, the velocity gradients on the walls are sharp, which implies a strong momentum transfer in transverse and spanwise directions.

For $Re=1000$ at the first two locations, the top half of another

vortex appears in the bottom-right-hand corner ($z/H \approx -0.1$; $y/H \approx -0.85$). This small secondary vortex, rotating in the opposite direction, is induced by the main vortex in the vicinity of the wall. It is not actually visible for higher Reynolds numbers. This could be because it is out of the measurement area.

An important asymmetry in the z -direction in the V velocity distribution is observed for the three cross sections and for each Reynolds number. The negative peak of V is much stronger than the positive one, with $V_{\min} \approx -0.5U_q$ to $-0.8U_q$ near the wall where the generators are attached, and $V_{\max} \approx 0.2$ to $0.3U_q$ near

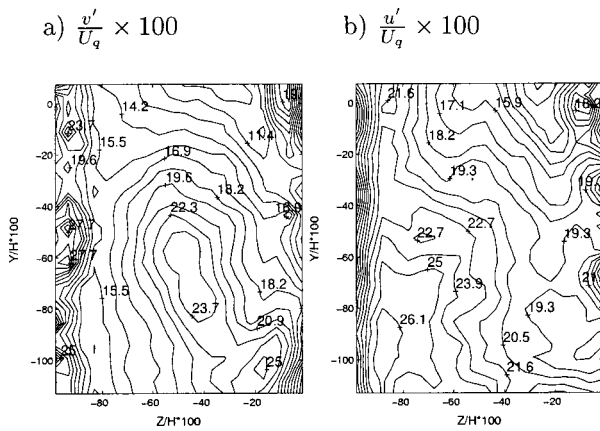


Fig. 7 Iso-values (%) of rms vertical (a) and rms longitudinal (b) velocity components, for $Re=2000$, behind the 2nd column, at $x/H=11.1$

the opposite wall. This asymmetry is stronger for a higher Reynolds number, and may be related to two causes. It results from the interaction between the vortex and the neighboring wall, as predicted by the image theory, [5,17]. But it is also an effect of a downward deviation of the flow due to the body orientation. As shown by Fig. 3 for $Re=2000$, vortices are oriented with an angle approximately equal to half the body angle of attack, showing the flow deviation and vortices drifting along the wall.

In addition, the signature of the longitudinal vortex roll up is shown by the longitudinal, u , velocity field (Fig. 5). At $x/H=9.1$, the longitudinal velocity presents a large area of low velocity near the wall where the bodies are attached. This region corresponds to the wake of the body. The vortex formation progressively appears by the generation of a velocity deficit in the vortex core, which reaches $0.45U_q$. This “wake-like” effect results from the slowing down of the fluid by the body, and from the vortex development from $x/H=9.6$ to $x/H=10.1$. It is noticeable that the higher the Reynolds number, the earlier the vortex development. In fact, the local velocity deficit in the vortex core shows up at $x/H=10.1$ for $Re=2000$ and 5000 , but hardly appears at $x/H=11.1$ for $Re=1000$.

A local acceleration (up to $1.1U_q$) is shown outside the vortex, which verifies the mass conservation. Furthermore, a thinning of the boundary layer shows up where the vortex induced velocities are directed towards the wall, on the middle-right-hand side and bottom-left-hand corner, particularly for $x/H \geq 10.1$. These so-

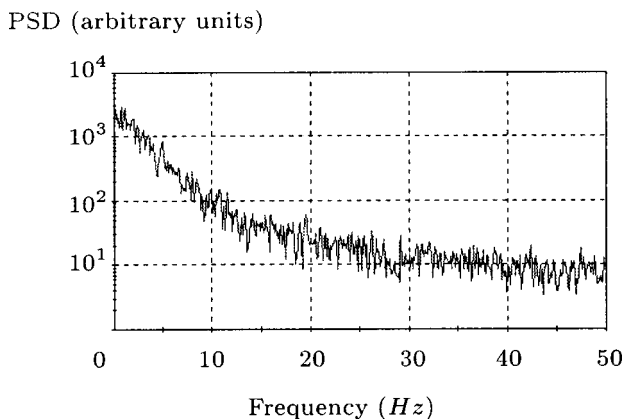


Fig. 8 Example of power spectral density of the transverse velocity fluctuations v' , recorded at $x/H=19.1$, $y/H=-48.1$, $z/H=-82.4$, for $Re=2000$, with a sampling frequency of 100 Hz

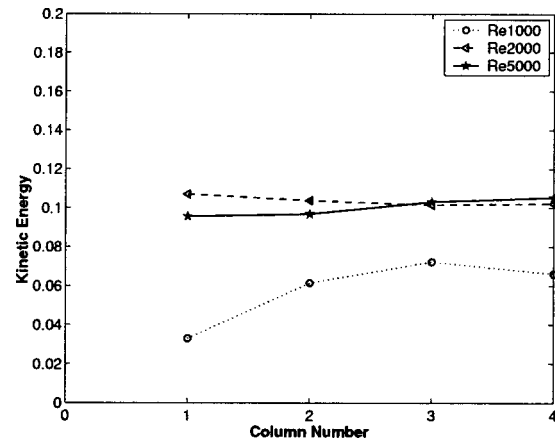


Fig. 9 Average kinetic energy of the fluctuating motion $k/(1/2)U_q^2$ behind successive generators, at $d/H=2.4$ downstream of each generator

called downwash flow regions are responsible for a local increase in the mean momentum transfer with the wall. However, in the regions where the vortex-induced velocities pull the fluid out of the wall (upwash flow regions: on the top left and bottom-right-hand corners), the boundary layer is obviously thicker, leading to a decrease of local momentum transfer.

3.2 Velocity Fluctuations. The iso-values of the rms longitudinal and vertical velocity u' and v' measured at $x/H=11.1$ are shown on Fig. 7. To determine whether or not these fluctuations are associated with a coherent motion in the body wake, a spectral analysis has been performed on the time series of the velocity measurements, using fast Fourier transform, after re-sampling of the LDA signals. As shown for example on Fig. 8, no significant periodicity has been detected in any velocity time series. Then, the rms velocity may be associated with turbulence, in the wide sense of random fluctuations.

An interesting point is the high level of the vertical fluctuating motion in the core of the vortex, $v'/U_q \approx 0.25$ (Fig. 7(a)). Moreover, as a consequence of the blowing effect in the upwash region and a redistribution between the spanwise and vertical fluctuating components, a remarkable increase in v' can be seen (up to $v'/U_q \approx 0.25$). As it is expected in the region where the boundary layer is thinner, the longitudinal fluctuating velocity component is high ($u'/U_q \approx 0.25$, Fig. 7(b)). Thus, an increase in the production of turbulent kinetic energy, due to the shear stresses under velocity

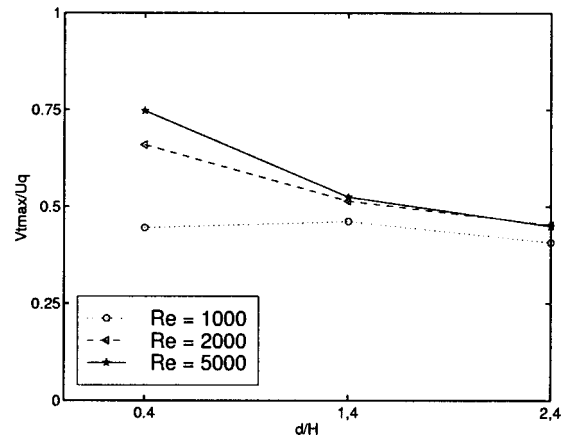


Fig. 10 Vortex maximal tangential velocity downstream of the 2nd column

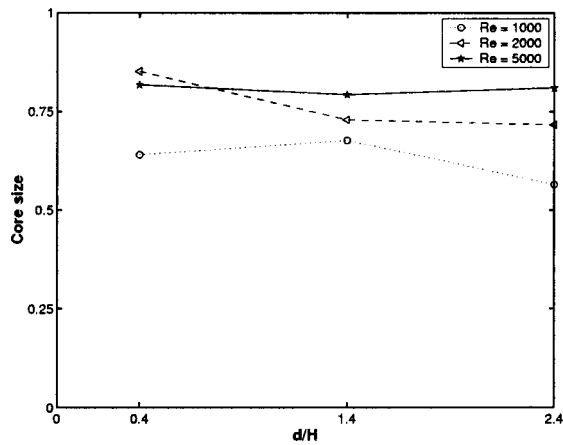


Fig. 11 Vortex core size $2a/H$ downstream of the 2nd column

gradients in these near wall regions, is expected to have a strong influence on the longitudinal component. Focusing our interest on the global influence of the Reynolds number and successive generators on turbulence, we consider the space-averaged turbulent kinetic energy k . With the assumption that $w' \approx v'$, k may be estimated by $k = (1/2(u'^2 + 2v'^2))$, where angular brackets denote a space averaging over the whole measurement cross section. For $Re=1000$, the turbulent kinetic energy increases from $k/1/2U_q^2=0.03$ behind the first vortex generator ($x/H=7.1$) to $k/1/2U_q^2=0.07$ behind the third and fourth vortex generators ($x/H \geq 15.1$) (Fig. 9). For $Re \geq 2000$, the turbulent kinetic energy is neither sensitive to the Reynolds number nor to the successive generators encountered and reaches $k/1/2U_q^2=0.1$. These results demonstrate that the flow turbulence is developed after the first vortex generator for $Re \geq 2000$.

3.3 Vortex Parameters. In this section, the global flow structure is analyzed from the recorded mean velocity fields in terms of the main vortex characteristics. The vortex core size and intensity are deduced from the V velocity component in the following way. The mean vortex core radius a is defined as half the distance between the positions of the maximum V_{\max} and minimum V_{\min} in the V velocity distribution (see Fig. 4). The relative accuracy of a is estimated to $\pm 15\%$. The vortex maximum tangential velocity is estimated as $V_{t \max} = 1/2(V_{\max} - V_{\min})$, and the intensity of the vortex is defined as the circulation $\Gamma = 2\pi a V_{t \max}$, leading to an accuracy of $\pm 6\%$ and $\pm 20\%$, respectively, for these two quantities. This method enables the determi-

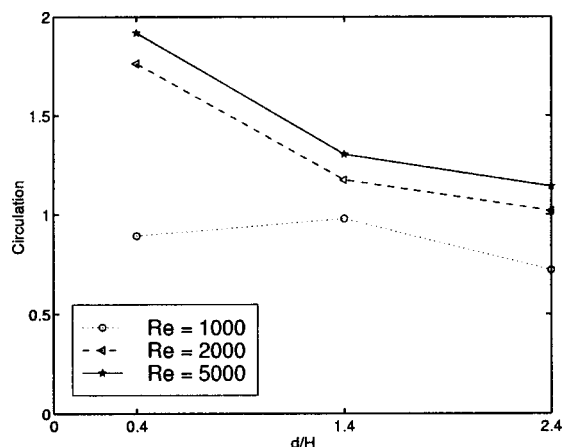


Fig. 12 Vortex intensity $\Gamma/U_q H$ downstream of the 2nd column

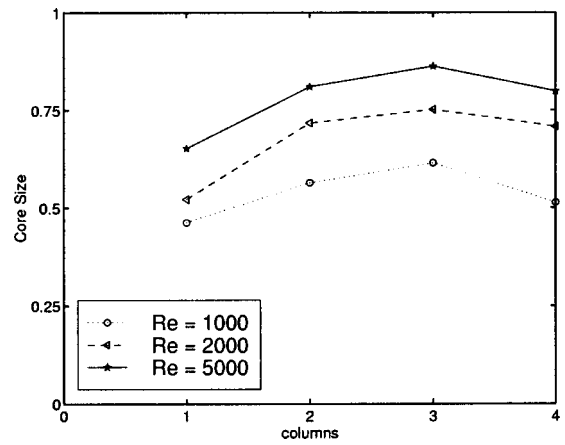


Fig. 13 Vortices core size $2a/H$ behind different columns, at $d/H=2.4$ downstream of each generator

nation of the vortex intensity even when the third velocity component W is not measured. This intensity is related to the large scale mixing effect of the vortex.

The evolution downstream of one vortex generator and the modification of the vortex features with the successive bodies encountered ("column effect") are analyzed for different values of the Reynolds number. The maximum tangential velocity $V_{t \max}$ decreases downstream because of vortex dissipation (Fig. 10). As the transverse velocity extrema are located close to the walls, the dissipation is mainly due to friction on the wall, which results in a high momentum transfer to the wall. This is particularly true for the highest Reynolds number. However, at a distance $d/H=2.4$ behind the vortex generator, the maximal tangential velocity $V_{t \max}/U_q \approx 0.45$ is nearly independent of Re . The vortex core size remains quite constant downstream of a generator, but the higher the Reynolds number, the larger the vortex (Fig. 11). This is a consequence of a stronger flow separation on the vortex generator for an increasing Re . In addition, the thinning of the boundary layer with Re allows a larger vortex to develop. The same conclusion holds for the circulation: It is clearly augmented by the increase of Re and a decrease is observed downstream of each generator, down to $\Gamma/U_q H=0.72$ for $Re=1000$ and $\Gamma/U_q H=1.15$ for $Re=5000$, at $d/H=2.4$ behind the vortex generator (Fig. 12). Considering the successive generators encountered by the flow, there is no evidence of any variation of $V_{t \max}$. However, it is interesting to note that the size of each vortex increases from the first to the third column (Fig. 13). This fact indicates that the

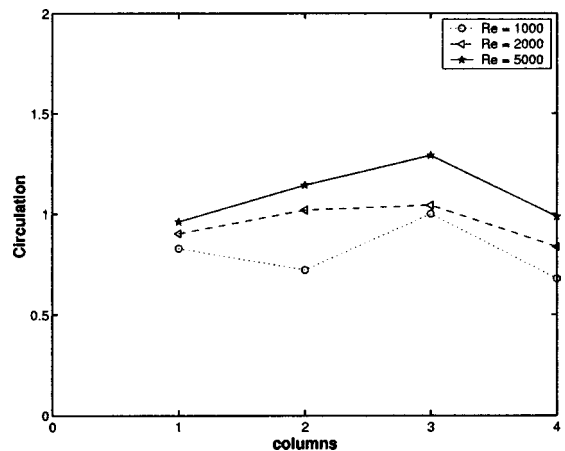


Fig. 14 Vortex circulation $\Gamma/U_q H$ behind different columns, at $d/H=2.4$ downstream of each generator

vortices of successive generators interact with each other, and that a vortex may benefit from vorticity generated upstream. Nevertheless, a decrease of the vortex size shows up beyond the third column. This observation may be attributed to the development of the boundary layer on the flat plate that limits the vortex size. A similar behavior to the vortex size is observed for the circulation (Fig. 14).

4 Discussion

Like any vortex generator, embossed bodies are dedicated to enhance heat transfer. Here, we discuss the possible effects on heat transfer of the vortices observed in the present isothermal flow. The first point is the vortex-induced large-scale mixing, and its role in heat advection. Indeed, the advective heat flux per unit surface q depends on the temperature difference across the vortex ΔT , and the maximum tangential velocity directly linked to the vortex intensity and size: $q = \rho C_p \Gamma / 2\pi a \Delta T$. According to Gentry and Jacobi [5], the location of the vortex core relative to the thermal boundary layer is the key factor for the advective heat transfer across the vortex. The vortex should not remain outside the boundary layer, in order to come across an area of strong temperature difference, leading to a high advected flux. In the present confined geometry, and considering the large size of observed vortices (from 0.5 up to $0.8H$), there is no doubt that it would spread over an area of high temperature difference, in the corresponding heated flow. Hence, the advective flux due to the vortex is likely to be strong.

The second point is the boundary layer thinning observed in the downwash region. Experimental studies have shown that the thinning of the boundary layer is always associated with a local increase of heat transfer on the wall, both for turbulent, [6], and laminar, [7], boundary layers developing over a flat plate. It may be argued that this statement still holds in a confined channel.

The effect of the fluctuating motion on heat transfer is less straightforward. Yanagihara and Torii [7] suggested that the transfer enhancement observed in the upwash flow region may be linked to the increase of turbulence intensity in this region, and that this effect extends far downstream of the generator.

Finally, the isothermal vortex flow investigated here reveals characteristic features which are known to enhance heat transfer. The efficiency of these embossed vortex generators to enhance transfer is supported by some preliminary results of a mass transfer study made by Schulz and Fiebig, with the ammonia absorption method, in a channel with similar embossed generators, [18].

A systematic experimental study for different geometries was not possible at this stage, since geometric parameters are too numerous. Such a parametric study should be achieved either by numerical tools or through global heat transfer measurements. Moreover, searching for an optimized configuration should include pressure loss measurements and other economic considerations which may be different for each application. Nevertheless, the present experimental investigation should provide data for a better understanding of transfer enhancement mechanisms, and for the validation of numerical tools.

5 Conclusion

The flow in a confined channel with periodically arranged smooth-shaped vortex generators is investigated. The experiment is designed to simulate the flow in a channel of industrial plate-fin heat exchanger with embossed vortex generators. The mean and fluctuating velocity fields are characterized by LDA for different values of the Reynolds number. Measurements are performed in several cross sections behind the successive generators. The flow field shows the existence of strong longitudinal vortices behind each vortex generator, which are known to give rise to significant heat transfer enhancement, [5–7]. Indeed, the large-scale mixing is highlighted by the large size and intensity of vortices, and a noticeable thinning of the boundary layer is observed in the downwash flow regions. Moreover, local turbulent mixing is strong,

particularly in the upwash and downwash flow regions and in the core of the vortices. Vortices are characterized by a high tangential velocity (0.5 to $0.8U_q$) and a wake-like deficit of streamwise velocity in the core. The nondimensional vortex intensity increases with the Reynolds number due to a stronger flow separation. As vortices are located closer to the embossed wall, heat transfer is expected to be enhanced preferentially on this wall. An interesting result in the periodical arrangement of the generators is the contribution of the vorticity induced by the upstream generators to the increased vortex sizes and intensities from generators located downstream. However, saturation takes place after the third generator column. Moreover, the turbulence development is accelerated by vortex generators. In fact, for a high enough Reynolds number ($Re \geq 2000$), the flow reaches its maximum turbulence level after the first vortex generator column. Overall, embossed vortex generators are shown to be a promising alternative to punched winglets for a plate-fin type heat exchanger.

Acknowledgments

This work was supported by the E. C. Joule Program contract JOE3-CT97-0056. The authors are grateful to MM. Mitra, Leiner, Fruman, and Billard for valuable discussions, and to the referees for their interesting remarks.

Nomenclature

a	= mean vortex core radius, m
C_p	= heat capacity of the fluid, J/kg·K
d	= distance downstream of the body trailing edge, m
H	= channel width, m
k	= turbulent kinetic energy, m^2/s^2
q	= advective heat flux, W/m^2
Re	= Reynolds number ($= U_q H / \nu$), dimensionless
U	= mean longitudinal velocity component, m/s
U_q	= bulk velocity, m/s
u	= longitudinal velocity component, m/s
u'	= rms longitudinal velocity component, m/s
V	= mean vertical velocity component, m/s
V_{\min}	= minimum of mean vertical velocity in a cross section, m/s
V_{\max}	= maximum of mean vertical velocity in a cross section, m/s
$V_{t\max}$	= maximum of tangential velocity in a cross section, m/s
v	= vertical velocity component, m/s
v'	= rms vertical velocity component, m/s
W	= mean spanwise velocity component, m/s
w	= spanwise velocity component, m/s
w'	= rms spanwise velocity component, m/s
x	= streamwise coordinate, m
y	= vertical coordinate, m
z	= spanwise (normal to plates) coordinate, m

Greek Symbols

ΔT	= temperature difference across the vortex, K
Γ	= vortex circulation, m^2/s
ν	= kinematic viscosity of the fluid, m^2/s
ρ	= density of the fluid, kg/m^3

References

- [1] Jacobi, A. M., and Shah, R. K., 1995, "Heat Transfer Surface Enhancement Through the Use of Longitudinal Vortices: A Review of Recent Progress," *Exp. Therm. Fluid Sci.*, **11**, pp. 295–709.
- [2] Fiebig, M., 1995, "Vortex Generators for Compact Heat Exchangers," *Journal of Enhanced Heat Transfer*, **2**(1–2), pp. 43–61.
- [3] Shabaka, I. M. M. A., Metha, R. D., and Bradshaw, P., 1985, "Longitudinal Vortices Embedded in Turbulent Boundary Layers. Part 1 Single Vortex," *J. Fluid Mech.*, **155**, pp. 37–57.
- [4] Mehta, R. D., and Bradshaw, P., 1988, "Longitudinal Vortices Embedded in Turbulent Boundary Layers. Part 2, Vortex Pair With Common Flow Upwards," *J. Fluid Mech.*, **188**, pp. 529–546.

- [5] Gentry, M. C., and Jacobi, A. M., 1996, "Heat Transfer Enhancement by Delta-Wing Vortex Generators on a Flat Plate: Vortex Interactions With the Boundary Layer," *Exp. Therm. Fluid Sci.*, **14**, pp. 231–642.
- [6] Eibeck, P. A., and Eaton, J. K., 1987, "Heat Transfer Effects of a Longitudinal Vortex Embedded in a Turbulent Boundary Layer," *Trans. ASME*, **109**, Feb..
- [7] Yanagihara, J. I., and Torii, K., 1992, "Enhancement of Laminar Boundary Layer Heat Transfer by a Vortex Generator," *JSME Int. J.*, **35**(3), pp. 400–405.
- [8] Fiebig, M., Mitra, N., and Dong, Y., 1990, "Simultaneous Heat Transfer Enhancement and Flow Loss Reduction of Fin-Tubes," *9th Int Heat Transfer Conf*, **9**, pp. 51–55.
- [9] Biswas, G., and Chattopadhyay, H., 1992, "Heat Transfer in a Channel With Built-In Wing Type Vortex Generators," *J. Heat Mass Transfer*, **35**(4), pp. 803–814.
- [10] Biswas, G., Torii, K., Fujii, D., and Nishino, K., 1996, "Numerical and Experimental Determination of Flow Structure and Heat Transfer Effects of Longitudinal Vortices in a Channel Flow," *J. Heat Mass Transfer*, **39**(16), pp. 3441–3451.
- [11] Fiebig, M., and Mitra, N. K., 1998, *Development in Heat Transfer: Computer Simulation in Compact Heat Exchangers*, B. Sunden and M. Faghri, eds., Computational Mechanics Publications, **1**, pp. 220–254.
- [12] Lau, S., 1995, "Experimental Study of the Turbulent Flow in a Channel With Periodically Arranged Longitudinal Vortex Generators," *Exp. Therm. Fluid Sci.*, **14**, pp. 255–261.
- [13] Fiebig, M., Valencia, A., and Mitra, N. K., 1993, "Wing-Type Vortex Generators for Fin-and-Tube Heat Exchangers," *Exp. Therm. Fluid Sci.*, **7**, pp. 587–595.
- [14] Sohankar, A., and Davidson, L., 2001, "Effect of Inclined Vortex Generators on Heat Transfer Enhancement in a Three-Dimensional Channel," *Numer. Heat Transfer, Part A*, **39**(5), pp. 433–448.
- [15] Valencia, A., Fiebig, M., and Mitra, N. K., 1996, "Heat Transfer Enhancement by Longitudinal Vortices in a Fin-Tube Heat Exchanger Element With Flat Tubes," *ASME J. Heat Transfer*, **118**, pp. 209–211.
- [16] Schlichting, H., 1979, *Boundary-Layer Theory*, 7th Ed., McGraw-Hill, New York.
- [17] Mokry, M., and Rainbird, W. J., 1975, "Calculation of Vortex Sheet Roll-Up in a Rectangular Wind Tunnel," *J. Aircr.*, **12**, pp. 750–752.
- [18] Schulz, K., and Fiebig, M., 2000, "Accurate Inexpensive Local Heat/Mass Transfer Determination by Digital Image Processing Applied to the Ammonia Absorption Method," *private communication*.

The Forced Oscillations of Submerged Bodies

Angel Sanz-Andrés

Professor
e-mail: asanz@idr.upm.es

Gonzalo Tevar

Associate Professor

Instituto Universitario "Ignacio Da Riva,"
Universidad Politécnica de Madrid,
c/o E.T.S.I. Aeronáuticos,
Pza. Cardenal Cisneros, s/n,
E 28040 Madrid, Spain

Francisco-Javier Rivas

Engineer,
Integration and Testing Department,
EADS/CASA Espacio,
Avda. de Aragon 404,
28022 Madrid, Spain
e-mail: jrivas@casa-de.es

The increasing use of very light structures in aerospace applications are given rise to the need of taking into account the effects of the surrounding media in the motion of a structure (as for instance, in modal testing of solar panels or antennae) as it is usually performed in the motion of bodies submerged in water in marine applications. New methods are in development aiming at to determine rigid-body properties (the center of mass position and inertia properties) from the results of oscillations tests (at low frequencies during modal testing, by exciting the rigid-body modes only) by using the equations of the rigid-body dynamics. As it is shown in this paper, the effect of the surrounding media significantly modifies the oscillation dynamics in the case of light structures and therefore this effect should be taken into account in the development of the above-mentioned methods. The aim of the paper is to show that, if a central point exists for the aerodynamic forces acting on the body, the motion equations for the small amplitude rotational and translational oscillations can be expressed in a form which is a generalization of the motion equations for a body in vacuum, thus allowing to obtain a physical idea of the motion and aerodynamic effects and also significantly simplifying the calculation of the solutions and the interpretation of the results. In the formulation developed here the translational oscillations and the rotational motion around the center of mass are decoupled, as is the case for the rigid-body motion in vacuum, whereas in the classical added mass formulation the six motion equations are coupled. Also in this paper the nonsteady motion of small amplitude of a rigid body submerged in an ideal, incompressible fluid is considered in order to define the conditions for the existence of the central point in the case of a three-dimensional body. The results here presented are also of interest in marine applications. [DOI: 10.1115/1.1593706]

Introduction

There are an increasing interest in the determination of the rigid-body properties (RBP) of an article by using the results of model testing experiments at low frequencies (the rigid-body motion range) in such a way that the elastic modes are not excited, [1–5]. This is due to that the realization of modal tests is nowadays easier than the “classical” methods (e.g., trifilar pendulum, etc.) in a significant number of technical applications.

These new methods are based on system identification techniques, which employs the rigid-body dynamic equations and the measurements obtained during testing. In these tests several accelerometers placed on the body are used together with load cells that measure the force applied by the shaker, [5]. The effect of the surrounding air can be neglected in most of these applications, because the articles are massive enough and their exposed surface is not significant. However, the surrounding media can remarkably modify the oscillation dynamics of light structures, and therefore this effect should be taken into account in the mathematical models that the above-mentioned methods are based on.

The general problem of the surrounded body dynamics can be very complex, [6,7]. However, there is a way of simplification in the case that the external shape of the body is such that there is a central point for the aerodynamic force loading, and the motion amplitude is small (so that nonlinear terms can be neglected).

The existence of this central point in a number of technically interesting bodies (e.g., large and light spacecraft antennae) can be shown, provided that their external shape fulfills some symmetry conditions. In such a case the 6×6 generalized mass matrix can be split into two 3×3 matrices, the added mass and the added inertia matrices, which constitutes an extremely useful simplification for the study of the submerged rigid-body dynamics.

The aim of the study reflected in this paper is to contribute to the development of the analysis of the dynamics of rigid bodies submerged in a fluid, by considering bodies whose external shape are such that some simplifications of the equations can be obtained. These shapes should show some symmetries, which is not a very restrictive condition, and are very common in industrial applications (e.g., satellite antennae, solar panels, etc.).

In the first section (Section 1) the submerged body problem formulation is presented, then (Section 2) the equations are rearranged in order to obtain a more compact expression, similar to the ones applicable to a body in vacuum. In order to show some specific results some particular kinds of bodies whose shape allows for further reduction of the equations (central point coincident with the center of mass, diagonal added mass and inertia matrices, plates) are analyzed in the following sections (Section 3 and Section 4).

In Section 5, in line with the classical presentation of the problem [8], the expressions for the calculations of the net pressure force and moment on a moving rigid body (generalized forces) as a function of the generalized mass matrix and the generalized speed of the body, with the simplification of small amplitude motions, are presented together with the central point concept and its properties.

The expressions for the added mass can be obtained in a straightforward way, [8], if the fluid motion can be considered as derived from a potential function (that is both, viscosity effects can be neglected, and irrotational conditions hold). In what follows the flow created by the body oscillations of small amplitude is considered as a potential flow which is valid in the cases where the condition $St \cdot Re \gg 1$ is satisfied (St is the Strouhal number and Re is the Reynolds number).

1 Submerged Body Motion Problem Formulation

Let us consider the configuration shown in Fig. 1. A body of surface Σ is performing both translational and rotational oscilla-

Contributed by the Fluids Engineering Division for publication in the JOURNAL OF FLUIDS ENGINEERING. Manuscript received by the Fluids Engineering Division July 11, 2001, revised manuscript received January 23, 2003. Associate Editor: J. Katz.

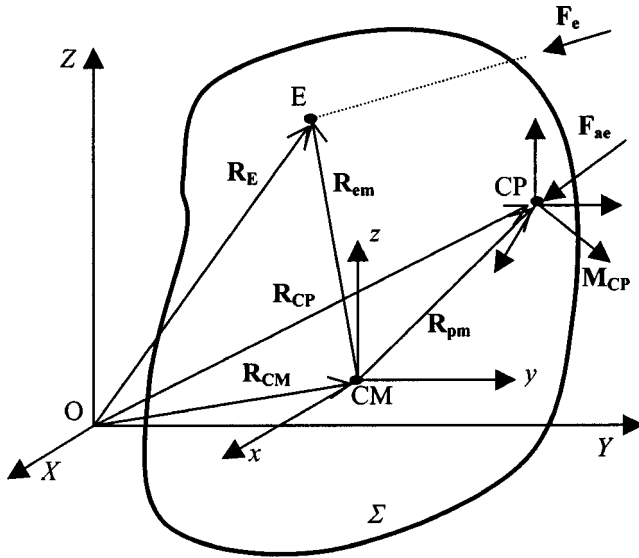


Fig. 1 Geometry of the body and definition of reference systems (CM: center of mass; E: point where F_e is applied; CP: central point; O; X, Y, Z): inertial reference system; (CM; x, y, z): body fixed reference system

tions of small amplitude around a reference position. Let us define an inertial reference system (X, Y, Z) and a moving reference system fixed to the body (x, y, z) (body reference frame) with the origin at the center of mass (CM) and with the axes parallel to the inertial axes when the body is placed at its reference position.

The force that creates the motion, F_e , is applied to a point E. It is assumed that the geometry of Σ is such that a central point (CP) exists for the aerodynamic forces acting on the body, and therefore, as shown in Eq. (5), the distributed aerodynamic loading can be reduced to a net force, F_{ae} , applied in the CP and a net moment M_{CP} .

The dynamics of the body is described by both the equations of the center of mass motion in an inertial reference system and the rotational dynamics around the center of mass. The first equation is

$$m\{\ddot{R}_{CM}\} = \{F_e\} + \{F_{ae}\} \quad (1a)$$

where $\{R_{CM}\}$ is the position of the center of mass, m is the mass of the body, $\{F_e\}$ is the net applied external force which produces the motion, $\{F_{ae}\}$ is the net force due to the body motion and acting at the central point.

The equations of rotational motion in the moving system fixed to the body (x, y, z) are

$$[I_p]\{\dot{\omega}\} = \{M_e\} + \{M_{ae}\} \quad (1b)$$

where $\{M_e\}$ and $\{M_{ae}\}$ are the net moments due to the applied force and the aerodynamic loading, respectively, calculated with regard to the mass center, $[I_p]$ is the body inertia tensor, and $\{\dot{\omega}\}$ is the angular acceleration.

The existence of a central point (see Section 5) implies that

(1) the linear acceleration of the central point just produces force (and not net moment), that is

$$\{F_{ae}\} = -[m_r]\{\ddot{R}_{CP}\} \quad (2)$$

where $\{R_{CP}\}$ is the central point position and $[m_r]$ is the added mass matrix, and

(2) the angular acceleration only gives rise to an aerodynamic moment (and not net force), with regard to the central point, $\{M_{CP}\}$.

Therefore, the aerodynamic moment referred to the mass center $\{M_{ae}\}$, neglecting higher order terms, are given by

$$\{M_{ae}\} = \{M_{Ra}\} + \{M_{CP}\} \quad (3)$$

where $\{M_{Ra}\}$ is the moment of the net aerodynamic force, $\{F_{ae}\}$, applied at the central point with regard to the mass center:

$$\{M_{Ra}\} = (R_{CP} - R_{CM}) \wedge F_{ae} = [R_{CP} - R_{CM}]^* \{F_{ae}\} = [R_{PM}]^* \{F_{ae}\} \quad (4)$$

where $[X]^*$ is the matrix notation for the cross product. The aerodynamic force moment with regard to the central point, $\{M_{CP}\}$, as shown in Eq. (5) is

$$\{M_{CP}\} = -[I_r]\{\dot{\omega}\} \quad (5)$$

where $[I_r]$ is the added inertia matrix.

The expressions (1b) and (3) implies that the added inertia matrix is expressed in axes parallel to the moving axes.

2 Submerged Body Motion Equations

Let us substitute the above expression for the aerodynamic forces and moments and the central point position in the basic expression of the formulation (1). Considering that

$$\{R_{PM}\} = \{R_{CP}\} - \{R_{CM}\} \quad (6)$$

then

$$\{\ddot{R}_{CP}\} = \{\ddot{R}_{CM}\} + [\dot{\omega}]^* \{R_{PM}\}. \quad (7)$$

Substituting (7) in (1a) one obtains

$$[m_T]\{\ddot{R}_{CM}\} + [m_r][\dot{\omega}]^* \{R_{PM}\} = \{F_e\} \quad (8)$$

where $[m_T]$ is the total mass matrix

$$[m_T] = m[1] + [m_r], \quad (9)$$

[1] being the identity matrix.

By substituting (3) and (5) in (1b) and taking into account that

$$\{M_e\} = [R_{em}]^* \{F_e\} \quad (10)$$

where

$$\{R_{em}\} = \{R_e\} - \{R_{CM}\}$$

the following expression is obtained:

$$[I_{pa}]\{\dot{\omega}\} - m[R_{PM}]^* \{\ddot{R}_{CM}\} = [R_{em} - R_{PM}]^* \{F_e\} \quad (11)$$

where $[I_{pa}]$ is the combination of body and added inertia matrices

$$[I_{pa}] = [I_p] + [I_r]. \quad (12)$$

The motion is therefore defined by (8) and (11). However, the motion of the mass center and the rotational motion around it appear coupled to each other. We will try to obtain a decoupled formulation. In order to eliminate $\{\ddot{R}_{CM}\}$ in the equation of rotational motion (11) let us calculate it from (8),

$$\{\ddot{R}_{CM}\} = -[m_T]^{-1}[m_r][\dot{\omega}]^* \{R_{PM}\} + [m_T]^{-1}\{F_e\}, \quad (13)$$

and substitute it in (11) to obtain

$$[I_{pa}]\{\dot{\omega}\} + [R_{PM}]^* [m_r] ([1] - [\delta_m]) [\dot{\omega}]^* \{R_{PM}\} = (-[R_{PM}]^* [\delta_m] + [R_{em}]^*) \{F_e\} \quad (14)$$

where the added mass coefficient matrix $[\delta_m]$ is given by

$$[\delta_m] = [m_T]^{-1}[m_r] = [1] - m[m_T]^{-1} \quad (15)$$

It can be shown that $[\delta_m] = [\delta_m]$. If $[m_r]$ is diagonal then also the added mass coefficient matrix $[\delta_m]$ is diagonal.

Equation (14) can be written in a more compact form by using the following relation, derived from the properties of the cross vector product

$$[X]^* \{A\} = -[A]^* \{X\}. \quad (16)$$

Then, from (14) one can obtain

$$\{\dot{\omega}\} = [I_T]^{-1} [R'_{em}] \{F_e\} \quad (17)$$

where

$$[I_T] = [I_{pa}] + [I_{pm}] \quad (18a)$$

$$\begin{aligned} [I_{pm}] &= -[R_{PM}]^* [m_r] ([1] - [\delta_m]) [R_{PM}]^* \\ &= -m [R_{PM}]^* [\delta_m] [R_{PM}]^* \end{aligned} \quad (18b)$$

$$[R'_{em}] = [R_{em}]^* - [R_{PM}]^* [\delta_m] \quad (18c)$$

$[I_T]$ is the total inertia matrix, $[I_{pm}]$ is a matrix representing an effect similar to an inertia tensor due to the displacement of the central point from the mass center (it can be shown that $[I_{pm}]$ is symmetrical), $[R'_{em}]$ is like the cross product with a kind of corrected position action point of the applied force.

Introducing (17) in (8) the following result is obtained:

$$\{\ddot{R}_{CM}\} = [m_T]^{-1} ([1] + [D]) \{F_e\} \quad (19a)$$

where the force correction term, $[D]$ is given by

$$[D] = [m_r] [R_{PM}]^* [I_T]^{-1} [R'_{em}]. \quad (19b)$$

This equation shows that the motion of the center of mass is equivalent to that of a body which has a larger mass, but both its mass is different along each axis (note that the equivalent mass is structured as a matrix $[m_T]$), and the equivalent force is the original but enlarged by a factor $([1] + [D])$. Observe that $[D]$ is zero if the central point coincides with the center of mass ($[R_{PM}]^* = 0$). However, $[D]$ is not zero in general, even if the force is applied at the mass center ($[R'_{em}]^* = 0$), because this is not a necessary condition for making $[R'_{em}] = 0$. In fact, for $[R'_{em}]$ to be zero, according to (18c), it is required also that $[R_{PM}]^* [\delta_m] = 0$, expression which involves both the position of the central point and the added mass matrix.

Summarizing, the dynamics of the forced motion of a body when surrounded by a fluid, has been shown to be described by two equations (1.17) and (1.19) which have the same structure as the classical equations of the body motion in vacuum, although substituting the classical mass, inertia tensor and position of the point of application of the force by the respective generalized matrix equivalents, $[m_T]$, $[I_T]$, $[R'_{em}]$. The similarity of the structure of the equations allows one to take advantage of the results obtained and the methods employed to solve for the case of the oscillations of body in vacuum.

In order to better understand the meaning of $[R'_{em}]$, let us assume $\{R_{em}\} = (x_f, y_f, z_f)$ and $\{R_{PM}\} = (x_{CP}, y_{CP}, z_{CP})$, and $[m_r]$ be a diagonal matrix. Then

$$[R'_{em}] = \begin{bmatrix} 0 & -z_f + \delta_{my} z_{CP} & y_f - \delta_{mz} y_{CP} \\ z_f - \delta_{mx} z_{CP} & 0 & -x_f + \delta_{mz} x_{CP} \\ -y_f + \delta_{mx} y_{CP} & x_f - \delta_{my} x_{CP} & 0 \end{bmatrix}. \quad (20a)$$

If $[\delta_m] = \delta_m [1]$ then the matrix $[R'_{em}]$ represents the cross product with the vector $\{R'_{em}\}$ defined as follows:

$$\{R'_{em}\} = \{R_e\} - \delta_m \{R_{PM}\} = \begin{Bmatrix} x_f - \delta_m x_{CP} \\ y_f - \delta_m y_{CP} \\ z_f - \delta_m z_{CP} \end{Bmatrix}. \quad (20b)$$

Observe that, in this case, the effect of the surrounding fluid is to modify the moment produced by the applied force by modifying the distance from the point of action of the applied force to the mass center by the quantity $\delta_m \{R_{PM}\}$.

In a general case the solution of the dynamics represented by Eqs. (17) and (19) is easy to obtain, as far as it is a set of linear equations on the driving force, whose solution can be obtained by using Fourier or Laplace transform methods. However, in some cases the interpretation of the results may be not so easy, mainly if the structure of the displacement inertia matrix, $[I_{pm}]$, is complex due to the aerodynamic effects. Therefore, as no general interpretation can be explained, in the following sections some simplified cases of practical interest are presented.

3 Central Point Coincident With the Center of Mass

If the central point coincides with the center of mass, $\{R_{PM}\} = 0$, then $[D] = 0$, $[R'_{em}] = [R_{em}]$, $[I_{pm}] = 0$, $[I_T] = [I_{pa}] = [I_p] + [I_r]$ and there are only changes both in $\{\ddot{R}_{CM}\}$, due to the matrix $[m_T]^{-1}$, and in $\{\dot{\omega}\}$ due to $[I_T]^{-1}$. In this case the physical interpretation is clear, the motion of the center of mass is as in vacuum, but with a different combination, along each axis, of responses to force due to the product $[m_T]^{-1} \{F_e\}$. The rotational motion around the center of mass is as in vacuum although now the total inertia tensor must include the added inertia tensor coming from the aerodynamic forces.

4 Diagonal Added Mass and Inertia Matrices

Let us assume that the added mass and inertia matrices are diagonal when referred to a reference frame whose axes are parallel to the body reference frame. The fulfillment of these assumptions can be easily deduced in some cases when the external shape of the body shows appropriate symmetry planes (see Section 5).

If the added mass tensor is diagonal, then $[\delta_m]$ is also diagonal and the displacement inertia matrix $[I_{pm}]$ is reduced to the following expression:

$$[I_{pm}] = [I_{pms}] = m \begin{bmatrix} \delta_{my} z_{CP}^2 + \delta_{mz} y_{CP}^2 & -\delta_{mz} x_{CP} y_{CP} & -\delta_{my} x_{CP} z_{CP} \\ -\delta_{mz} x_{CP} y_{CP} & \delta_{mx} z_{CP}^2 + \delta_{mz} x_{CP}^2 & -\delta_{mx} z_{CP} y_{CP} \\ -\delta_{my} x_{CP} z_{CP} & -\delta_{mx} z_{CP} y_{CP} & \delta_{mx} y_{CP}^2 + \delta_{my} x_{CP}^2 \end{bmatrix}. \quad (21)$$

Although the displacement inertia matrix $[I_{pm}]$ is now somehow simplified to the form $[I_{pms}]$, it is not diagonal, unless some of the factors in the matrix elements outside of the main diagonal are null. These factors have the form $x_i x_j \delta_{mxi}$ ($x_1 = x, x_2 = y, x_3 = z$). For instance, as in a plate the added mass coefficients are $\delta_{mx} = \delta_{my} = 0$ (only $\delta_{mz} \neq 0$), if in addition, one coordinate of the central point is zero (e.g., $x_{CP} = 0$), then the matrix $[I_{pms}]$

becomes diagonal and therefore its contribution is reduced to just a modification of the elements of inertia matrix in the main diagonal.

The structure of $[I_{pms}]$ is typical of the contribution to the inertia tensor of a point mass placed in (x_{CP}, y_{CP}, z_{CP}) but the difference is that the value of the inertia to be considered in each direction ($m \delta_{mxi}$ along axis x_i) is not the same.

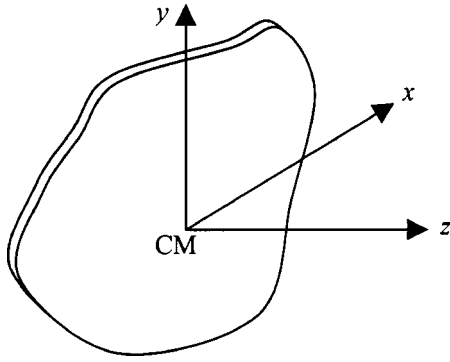


Fig. 2 Problem geometry for the plate dynamic analysis. (CM; x, y, z): body fixed reference system.

In some cases, if x_{CP} , y_{CP} , and z_{CP} are small enough, $[I_{pms}]$ could be neglected when compared to $[I_p]$ or $[I_{pa}]$.

4.1 Plate With Diagonal Inertia Matrix and Excitation Along a Coordinate Axis. Let us consider the body depicted in Fig. 2, with diagonal inertia matrix. Let us assume that $\delta_{mx} = \delta_{my} = x_{CP} = 0$, then one obtains

$$[m_T] = \begin{bmatrix} m & 0 & 0 \\ 0 & m & 0 \\ 0 & 0 & m + m_{rz} \end{bmatrix} \quad (22a)$$

$$[I_{pms}] = m \delta_{mz} y_{CP}^2 \begin{bmatrix} 1 & 0 & 0 \\ 0 & 0 & 0 \\ 0 & 0 & 0 \end{bmatrix} \quad (22b)$$

$$[I_T] = \begin{bmatrix} I_{Tx} & 0 & 0 \\ 0 & I_{Ty} & 0 \\ 0 & 0 & I_{Tz} \end{bmatrix} \quad (22c)$$

where

$$I_{Tx} = I_{pax} + m \delta_{mz} y_{CP}^2; \quad I_{Ty} = I_{pay}; \quad I_{Tz} = I_{paz}. \quad (22d)$$

If the position of the force is $x_f = z_f = 0$, then

$$[R'_{em}] = \begin{bmatrix} 0 & 0 & y_f - y_{CP} \delta_{mz} \\ 0 & 0 & 0 \\ -y_f & 0 & 0 \end{bmatrix} \quad (23a)$$

$$[D] = - (y_f - y_{CP} \delta_{mz}) \frac{m_{rz}}{I_{Tx}} y_{CP} \begin{bmatrix} 0 & 0 & 0 \\ 0 & 0 & 0 \\ 0 & 0 & 1 \end{bmatrix}. \quad (23b)$$

The motion equations are then

$$\ddot{R}_{CMx} = \frac{F_{ex}}{m} \quad (24a)$$

$$\ddot{R}_{CMy} = \frac{F_{ey}}{m} \quad (24b)$$

$$\ddot{R}_{CMz} = \frac{F_{ez}}{m + m_{rz}} \left[1 - (y_f - y_{CP} \delta_{mz}) \frac{m_{rz}}{I_{Tx}} y_{CP} \right] \quad (24c)$$

$$\dot{\omega}_x = \frac{F_{ez}}{I_{Tx}} (y_f - y_{CP} \delta_{mz}) \quad (24d)$$

$$\dot{\omega}_y = 0 \quad (24e)$$

$$\dot{\omega}_z = - \frac{F_{ex}}{I_{Tz}} y_f. \quad (24f)$$

Observe the corrections due to the surrounding fluid effect in the simple dynamics considered: the increasing of both the mass (for the translation along z -axis) and the moment of inertia (for the rotation around x -axis). If $y_f > y_{CP} \delta_{mz}$ (with $y_{CP} > 0$) both the effective force component along z and moment component along x decrease and vice versa.

4.2 Circular Plate. In the case of a circular plate of radius b , made of homogeneous material with density ρ_m and thickness t_p , the added mass and inertia matrices are diagonal and the elements in the main diagonal are as follows:

$$m_{rx} = m_{ry} = 0; \quad m_{rz} = \frac{8}{3} \rho_a b^3 \quad (25a)$$

$$I_{rx} = I_{ry} = \frac{16}{45} \rho_a b^5; \quad I_{rz} = 0. \quad (25b)$$

The displacement inertia matrix, $[I_{pm}] = [I_{pms}] = [0]$, as deduced from (22b) as the position of the central point and the center of mass coincides, $\{R_{pm}\} = \{0\}$. The force correction term is $[D] = [0]$, as $[R_{em}]^* = [0]$.

The body inertia tensor is diagonal, and the elements in the main diagonal are given by

$$I_{px} = I_{py} = \frac{\pi}{4} \rho_m b^4 t_p; \quad I_{pz} = \frac{\pi}{2} \rho_m b^4 t_p \quad (26)$$

The motion equations, if the force is applied at $\{R_{em}\} = \{x_f, y_f, z_f\}$, are

$$\{\ddot{R}_{CM}\} = [m_T]^{-1} \{F_e\} = \frac{1}{m} \begin{bmatrix} 1 & 0 & 0 \\ 0 & 1 & 0 \\ 0 & 0 & \frac{1}{1 + \nu_{mz}} \end{bmatrix} \{F_e\} \quad (27a)$$

$$\{\dot{\omega}\} = [I_T]^{-1} [R_{em}]^* \{F_e\} \quad (27b)$$

where

$$[I_T] = \begin{bmatrix} I_{px} + I_{rx} & 0 & 0 \\ 0 & I_{py} + I_{ry} & 0 \\ 0 & 0 & I_{pz} \end{bmatrix} = \begin{bmatrix} I_{px}(1 + \nu_{Ix}) & 0 & 0 \\ 0 & I_{py}(1 + \nu_{Iy}) & 0 \\ 0 & 0 & I_{pz} \end{bmatrix} \quad (27c)$$

$$[R_{em}]^* = \begin{bmatrix} 0 & -z_f & y_f \\ z_f & 0 & -x_f \\ -y_f & x_f & 0 \end{bmatrix} \quad (27d)$$

$$\nu_{mz} = \frac{m_{rz}}{m} = \frac{8}{3\pi} \frac{\rho_a}{\rho_m} \frac{b}{t_p} \quad (27e)$$

$$\nu_{Ix} = \frac{I_{rx}}{I_{px}} = \frac{64}{45\pi} \frac{\rho_a}{\rho_m} \frac{b}{t_p}. \quad (27f)$$

The motion of the center of mass along axes x and y is identical as in vacuum, but along the z -axis the response of the body corresponds to one of mass increased by the factor $(1 + \nu_{mz})$.

The rotational motion around the center of mass is similar to that in vacuum with increased moment of inertia around axes x and y by a factor $(1 + \nu_{Ix})$.

In the case that there is not coincidence of the center of mass with the central point, as in Section 4.1, and also the force is applied at $x_f = z_f = 0$, $y_f \neq 0$, the following equations are obtained:

$$\ddot{R}_{CMx} = \frac{F_{ex}}{m} \quad (28a)$$

$$\ddot{R}_{CMy} = \frac{F_{ey}}{m} \quad (28b)$$

$$\ddot{R}_{CMz} = \frac{F_{ez}}{m(1+\nu_{mz})} \left[1 - \left(y_f - y_{CP} \frac{\nu_{mz}}{1+\nu_{mz}} \right) \frac{m\nu_{mz}}{I_{p11}(1+\nu_{Ix})} y_{CP} \right] \quad (28c)$$

$$\dot{\omega}_x = \frac{F_{ez}}{I_{px}(1+\nu_{Ix})} \left(y_f - y_{CP} \frac{\nu_{mz}}{1+\nu_{mz}} \right) \quad (28d)$$

$$\dot{\omega}_y = 0 \quad (28e)$$

$$\dot{\omega}_z = -\frac{F_{ex}}{I_{pz}} y_f \quad (28f)$$

Observe that the rotational dynamics around the z -axis is not changed, as well as translations along the x and y -axes. Rotation around the x -axis and translations along the z -axis are modified, both due to the increase of mass and moment of inertia and to the displacement of the central point from the center of mass.

The values of the parameters that control the influence of the surrounding fluid, ν_{mz} and ν_{Ix} , in a case with technological interest (disk antenna of 2 m diameter, of "sandwich" material, of aluminum, $\rho_m = 2.8 \times 10^3 \text{ kg/m}^3$, with total skin thickness $t_p = 2 \text{ mm}$, oscillating in air, $\rho_a \approx 1.1 \text{ kg/m}^3$) are

$$\nu_{mz} = 0.15 \text{ and } \nu_{Ix} = 0.08 \quad (29)$$

which shows the relevance of taking into account the effect of the air when analyzing solid-body oscillations of light structures. In the most simplified case (the central point and the mass center coincides, $y_{CP} = 0$) the effect amounts to a 15% increase of the effective mass along the z -axis and an 8% in the moment of inertia around x -axis.

5 Central Point

Let us consider the motion of a body in an ideal incompressible fluid. The net pressure load on a body, \mathbf{F}_{ae} , and the net pressure moment with regard to a point O, \mathbf{M}_o , are given by [8] for small-amplitude motions (the nonlinear terms are neglected)

$$-\mathbf{F}_{ae} \cong \frac{d' \mathbf{Q}}{dt} = \sum_{\substack{i=1 \dots 6 \\ k=1 \dots 3}} M_{Rik} \dot{U}^i \mathbf{e}_k \quad (30)$$

$$-\mathbf{M}_o \cong \frac{d' \mathbf{K}}{dt} = \sum_{\substack{i=1 \dots 6 \\ k=1 \dots 3}} M_{Ri(k+3)} \dot{U}^i \mathbf{e}_k \quad (31)$$

where the dot above the symbols represents derivation with respect to time. U^i are the components of the generalized speed projected in moving axes (U^i , if $i=1,2,3$ are the origin speed components in moving axes, $\mathbf{U}_o = (U^1, U^2, U^3)$, and if $i=4,5,6$ are the components of the angular rotation speed, $\boldsymbol{\omega} = (U^4, U^5, U^6)$), \mathbf{e}_k are the moving axes base vectors fixed to the body, M_{Rik} are the components of the generalized added mass matrix $[M_R]$, which can be obtained as explained in [8].

In the case of small amplitude motions these results allow one to see M_{Rik} as an added mass or moment of inertia, that is, as the component k of the force or moment produced by the action of a unitary generalized acceleration \dot{U}^i . The symmetry of $[M_R]$ helps in the interpretation of the results.

Note that in a general case every component of the generalized speed contributes to the three force components and to the three moment components.

In a general case the matrix $[M_R]$ has 36 elements, although, as it is very well known, due to symmetry conditions ($M_{Rik} = M_{Rki}$) only 21 are independent and nonzero. However, this fig-

ure is reduced if the body surface presents symmetries. One symmetry plane reduces the number of nonzero elements to 12. Two symmetry planes reduce the number to eight elements and three planes to six elements (just the ones belonging to main matrix diagonal).

Equations (30) and (31) can be expressed together in a generalized form, $\{F_i\}$

$$\{F_i\} = -[M_{Rik}] \{\dot{U}_i\} \quad (32)$$

where $\{F_i\}$ is defined as follows:

$$\mathbf{F}_{ae} = \{F_1, F_2, F_3\}; \quad \mathbf{M}_o = \{F_4, F_5, F_6\} \quad (33)$$

which is the classical expression employed in the study of small amplitude oscillations, [6]. Let us assume that the moments with regard to a point caused by a pure accelerated translation motion are zero. This point is called the central point (CP). Vice versa, pure accelerated rotation around CP does not produce net pressure force. In other words, with regard CP, unsteady translations generate just only forces, and rotations just only moments.

The existence of the central point is not a general property of bodies, although its existence can be demonstrated in some cases, e.g., in the potential bidimensional flow, [9].

In case of a body with central point the generalized added mass matrix $[M_R]$ of the motion in axes with the origin at the central point can be split in four boxes, 3×3 elements each, \tilde{M}_{Rij} , defined as

$$[M_R] = \begin{bmatrix} \tilde{M}_{R11} & \tilde{M}_{R12} \\ \tilde{M}_{R21} & \tilde{M}_{R22} \end{bmatrix} \quad (34)$$

where $\tilde{M}_{R12} = \tilde{M}_{R21} = 0$. By using (30), (31), and (32) one obtains

$$-\{F_{ae}\} = [m_r] \{\dot{U}_{CP}\}; \quad [\tilde{M}_{R11}] = [m_r]; \quad m_{rij} = M_{Rij}, \quad i, j = 1, 2, 3 \quad (35)$$

$$-\{M_{CP}\} = [I_r] \{\dot{\omega}\}; \quad [\tilde{M}_{R22}] = [I_r];$$

$$I_{rij} = M_{R(i+3)(j+3)}, \quad i, j = 1, 2, 3 \quad (36)$$

where $[m_r]$ and $[I_r]$ are the added mass and inertia matrices (with regard to the reference system used to calculate $[M_R]$), U_{CP} is the central point speed.

The existence of central point can be shown in the case of a body with at least two symmetry planes (like a spacecraft antenna) and a plate (as a spacecraft solar panel). Results concerning the added mass matrix of several geometrical shapes can be found in the classical literature, [7–11].

Conclusions

In this paper uncoupled equations of the translational and rotational dynamics for the small-amplitude motions of a submerged body has been obtained in the case that a central point exists for the aerodynamic forces loading generated by the surrounding fluid. In the classical solution the six degrees-of-freedom are coupled. The structure of the equations obtained is similar to the ones of the motion in vacuum. In the translational motion, instead of the usual scalar mass it appears a mass matrix $[m_T]$ and a new forcing term proportional to the applied external force through a matrix, $[D]$. The structure of the matrices shows that the effect is in general not the same for all the directions, as it is in the case of vacuum.

Concerning the rotational motion two main changes arise. The first one is that the inertia tensor is substituted by another matrix that is the composition of the body inertia tensor, the added inertia matrix, and another inertia matrix due to the distance between the central point and the center of mass. The second one is that the point where the external force is applied is substituted by a new term that resembles something like a corrected position (it is not strictly a corrected position except in a particular case).

Due to the complexity that the presence of the new matrices arise in a general case, the interpretations of the dynamics has not been attempted in a general case. Instead, a few but technologically interesting cases have been analyzed (plates, bodies showing symmetries).

Also, the existence of a central point in the case of three-dimensional bodies, with appropriate external shape, performing small-amplitude nonsteady motions inside an ideal, incompressible fluid, has been considered.

The results obtained are of special interest in the field of the design and testing of comparatively light structures (e.g., aerospace structures when tested in air, marine structures, etc.).

Acknowledgments

This study has been partially supported by the Spanish "Centro para el Desarrollo Tecnológico Industrial," of the Ministerio de Ciencia y Tecnología, Project PNE-001/2000-C3. This paper resulted from the cooperation between the Instituto Universitario "Ignacio Da Riva" of the Universidad Politécnica de Madrid and EADS-CASA, División Espacio, Integration and Testing Department. The authors wish to thank to Luis Muñoz-Sevilla for his support, and to J. Meseguer and J. M. Perales for fruitful discussions.

Nomenclature

$[D]$	= force correction term, dimensionless
$\mathbf{F}_e, \{F_e\}$	= applied external force, N
$\mathbf{F}_{ae}, \{F_{ae}\}$	= net aerodynamic force, N
F_i	= components of the generalized force, N if $i = 1,2,3$; N.m if $i = 4,5,6$
$[I_{pms}]$	= displacement inertia matrix, $[I_{pm}]$, in simplified form, kg.m^2
$[I_p]$	= body inertia tensor, kg.m^2
$[I_{pa}]$	= body plus added inertia matrix (see (12)), kg.m^2
$[I_{pm}]$	= inertia matrix due to central point to center of mass displacement, kg.m^2
$[I_r]$	= added inertia matrix, kg.m^2
$[I_T]$	= total inertia matrix, kg.m^2
\mathbf{K}	= fluid angular momentum, N.m.s
$\{M_{ae}\}$	= net moment of aerodynamic forces with regard to the center of mass, N.m
$\mathbf{M}_{CP}, \{M_{CP}\}$	= net moment of aerodynamic forces with regard to central point, N.m
$\{M_e\}$	= net moment of applied external forces with regard to the center of mass, N.m
\mathbf{M}_o	= net aerodynamic torque with regard to point O, N.m
$\{M_{Ra}\}$	= moment of the net aerodynamic force applied at the central point with regard to the center of mass, N.m
$[M_R]$	= generalized mass matrix, kg
$[\tilde{M}_{Rij}]$	= submatrix of the generalized mass matrix, $[M_R]$ (see (6c)), kg if $i=j=1$; kg.m^2 if $i=j=2$
M_{Rik}	= components of the generalized mass matrix, kg
\mathbf{Q}	= fluid momentum, N.s
$\mathbf{R}_{CM}, \{R_{CM}\}$	= position of the center of mass, m
$\mathbf{R}_{CP}, \{R_{CP}\}$	= central point position, m
$\{R_E\}$	= position of the point where the external force is applied, m
$\{R_{em}\}$	= position where the external force is applied, with regard to the center of mass, m

$[R'_{em}]$	= kind of cross product with a corrected position of the applied force application point, m
$\{R_{PM}\}$	= central point position with regard to the center of mass, m
\mathbf{U}_{CP}	= central point speed, m/s
U^i	= components of the generalized speed of the origin of the moving body axes, m/s if $i = 1,2,3$; rad/s if $i = 4,5,6$
\mathbf{U}_o	= generalized speed of the origin of the moving body axes, see U^i for dimensions
\mathbf{V}	= fluid velocity field, m/s
(X, Y, Z)	= inertial reference system
b	= circular plate radius, m
\mathbf{e}_k	= vector base of the moving reference system, fixed to the body
m	= mass, kg
$[m_r]$	= added mass matrix, kg
$[m_T]$	= total mass matrix, kg
n	= coordinate along the normal to the body surface
\mathbf{n}	= normal to the surface of the body, Σ , dimensionless
p	= pressure, Pa
\mathbf{r}	= vector traced from O to $d\sigma$, m
\mathbf{r}_{CP}	= central point position in the initial reference system, m
t	= time, s
t_p	= plate thickness, m
(x,y,z)	= body reference system (origin at the center of mass)
$[\delta_m]$	= added mass coefficient matrix, dimensionless
ρ_a	= density of surrounding fluid, kg/m^3
ρ_m	= density of material, kg/m^3
v_{mi}	= added mass component "i" to body mass ratio, dimensionless
$\{\dot{\omega}\}$	= angular acceleration, rad/s^2
ω	= rotation speed of the moving axes relative to inertial axes, rad/s

References

- [1] Bretl, J., and Conti, P., 1987, "Rigid Body Mass Properties From Test Data," *Proceedings of the 5th International Modal Analysis Conference*, Apr. 6–9, London, I, Society for Experimental Mechanics, Bethel, CT, pp. 655–659.
- [2] Fregolent, A., Sestieri, A., and Falzetti, M., 1992, "Identification of Rigid Body Inertia Properties From Experimental Frequency Response," *Proceedings of the 10th International Modal Analysis Conference*, Feb. 3–7, San Diego, CA, I, Society for Experimental Mechanics, Bethel, CT, pp. 219–225.
- [3] Pandit, S. M., Yao, Y.-X., and Hu, Z.-Q., 1994, "Dynamic Properties of the Rigid Body and Supports From Vibration Measurements," *ASME J. Vib. Acoust.*, **116**, pp. 269–274.
- [4] Wolcott, K. R., Graham, T. A., and Doty, K. L., 1994, "Innovative Mechanism for Measuring the Mass Properties of an Object," *28th Aerospace Mechanism Symposium*, NASA Lewis Research Center, pp. 107–121.
- [5] Sanz-Andres, A., Tevar, G., and Rivas, F. J., 2001, "ODISEA—A Method for Measurement of Mass Properties of an Element Based on Its Rigid Body Dynamics," *Proceedings of the 4th International Symposium on Environmental Testing for Space Programmes*, Liege, Belgium, European Space Agency Publications Division, ESA SP-467.
- [6] Blevins, R. D., 1993, *Formulas for Natural Frequency and Mode Shape*, Krieger, Malabar, FL, Chapter 14.
- [7] Lamb, H., 1916, *Hydrodynamics*, 4th Ed., Cambridge Univ. Press, Cambridge, UK, Chapter 5.
- [8] Newman, J. N., 1977, *Marine Hydrodynamics*, 6th Ed., M.I.T. Press, Cambridge, MA, Chap. 4.
- [9] Sedov, L. I., 1965, *Two-Dimensional Problems in Hydrodynamics and Aerodynamics*, Wiley Interscience, New York, pp. 29–30.
- [10] Sedov, L. I., 1975, *Mecanique des milieux continus*, II, Mir, Moscow, pp. 194–196.
- [11] Kochin, N. E., Kibel, I. A., and Roze, N. V., 1964, *Theoretical Hydromechanics*, Wiley Interscience, New York, pp. 404–411.

Analysis of Transient Flow in Pipes With Expanding or Contracting Sections

[DOI: 10.1115/1.1593703]

Introduction

The classical theory of liquid transient flow in pipelines (waterhammer) usually draws on the following basic assumptions, [1–4]:

- The liquid flow is one-dimensional, that is the characteristic quantities are cross-section averaged, remaining functions of distance (longitudinal coordinate) and time.
- The liquid undergoes elastic deformations under pressure surges, assuming that relative changes of the liquid density are insignificant (low-compressible fluid).
- The dynamic fluid-pipe interaction is neglected and a quasi-steady pipe response to pressure surges is assumed according to the elastic theory of deformation.
- Hydraulic losses are of a quasi-steady character that is the same losses are assumed for a steady and transient flow at given mean velocity of the liquid.
- The liquid velocity is small compared to the pressure wave speed.

The governing equations of conservation of mass and momentum describing the transient flow in closed conduits, corresponding to the above assumptions, take the well-known forms [3,4]:

- continuity equation

$$\frac{\partial H}{\partial t} + \frac{a^2}{g} \frac{\partial V}{\partial x} = 0, \quad (1)$$

dynamics equation (equation of motion)

$$\frac{\partial H}{\partial x} + \frac{1}{g} \frac{\partial V}{\partial t} + \frac{\lambda}{2gD} V|V| = 0. \quad (2)$$

The survey of the literature and the author's experience, [5,6], indicate that the above mentioned assumptions and the corresponding Eqs. (1) and (2) can be useful for prediction of many typical cases of unsteady flow in pipelines. However, the assumptions of quasi-steady character of hydraulic losses (friction losses) and quasi-steady response of the pipeline structure to pressure surges are often debated. These assumptions, for some types of pipes and occurring flow disturbances, can give rise to excessive discrepancies between the theory and experiment. Therefore, further investigations are in progress in order to extend the classical theory of transient flow by better recognition and improvement of the mathematical description of the following phenomena:

- dynamic interaction between the liquid and a pipeline structure, [7–11],
- unsteady dissipation of energy in the liquid and pipe structure, [1,7,12–15],
- transient cavitation or liquid column separation, [16–18].

There are also other problems not successfully explained and solved in the classical theory of waterhammer. An example is the

treatment of conduits with expanding or contracting cross sections, presented in this paper. Equations (1) and (2) are used in most cases, although it is worthwhile to notice that they, mainly due to the continuity Eq. (1), are valid for pipes with constant cross sections. Application of these equations for multipipe systems requires the use of so-called “junction boundary conditions.” These conditions describe the relationship between the flow parameters across the joints between pipe segments of different size. Sometimes pipelines of variable cross section are approximated by use of an equivalent uniform pipeline elements, according to the generally accepted similarity laws (conditions)—see Appendix A. Practically, such approach is mostly used for spanning the size changes of serially connected pipes along the pipeline length. For pipe element whose cross-sectional area is a continuous function of the length, for example a cone-shaped section, a more general model can be implemented. A continuity equation for conduits whose shapes can be described by differentiable functions was derived by Bednarczyk [19]. A less general form of the continuity equation for cone-shaped pipes can be found in monographs, [3,4]. For conical pipes, the numerical solution presented by Bednarczyk [19] gives lower—whereas that presented by Wylie and Streeter [3,4] higher—pressure amplitudes than the solution based on the model that assumes an equivalent element of constant cross section.

In the present paper, the problem of transient flow of liquid in tapered or expanding pipes is discussed. A mathematical model based on the one-dimensional theory of the unsteady flow is proposed. The paper explains also the differences in methods of computation of the considered problem found in the literature.

Basic Equations

The equations describing the transient liquid flow in conduits with variable cross sections written below can be obtained drawing on the basic assumptions presented in the Introduction of this paper.

Continuity Equation. The equation of continuity derived by Bednarczyk [19] contains a term that can take into account pipes with variable cross sections. It may be written as follows (Appendix B):

$$\frac{\partial H}{\partial t} + \frac{a^2}{g} \frac{\partial V}{\partial x} + \frac{a^2}{g} V \frac{\partial \ln A}{\partial x} = 0. \quad (3)$$

The convective acceleration of pressure was left out in this equation as negligible, compared to the local time derivative, and the relationship $p = \rho g(H - z)$ was introduced. The last left-hand side term of this equation is an extension of Eq. (1). Although the model of liquid flow is one-dimensional, the form of this additional term is of a general character and should not be questioned. The continuity equation for a cone-shaped pipe, [3,4], is a particular case of Eq. (3).

Let us now modify Eq. (3) by introduction of the volume flow rate Q . By setting $V = Q/A$ and performing appropriate transformation of Eq. (3), we obtain

Contributed by the Fluids Engineering Division for publication in the JOURNAL OF FLUIDS ENGINEERING. Manuscript received by the Fluids Engineering Division Apr. 5, 2000; revised manuscript received Feb. 11, 2003. Associate Editor: U. Ghia.

$$\frac{\partial H}{\partial t} + \frac{a^2}{gA} \frac{\partial Q}{\partial x} = 0. \quad (4)$$

Equation (4) is of a much simpler form than Eq. (3). The additional term with the derivative $\partial \ln A / \partial x$ disappears, as a result of introduction of the quantity Q and calculation of the derivative $\partial V / \partial x = \partial(Q/A) / \partial x$. This term is present only if the continuity equation is expressed in terms of V , not Q . It should also be noticed that Eq. (4) has the same form as the continuity equation known from the theory of waterhammer for pipes of constant diameter, [1–4].

Equation of Motion. Besides hydraulic losses due to shear stress (friction), there are other sources of loss in pipes with variable cross-sections, namely additional losses due to the pipe expansion or contraction. The total hydraulic losses are approximately proportional to the square of the flow rate. The equation of liquid motion can therefore be written in the form

$$\frac{\partial H}{\partial x} + \frac{1}{gA} \frac{\partial Q}{\partial t} + r_Q Q |Q| = 0, \quad (5)$$

where the last left-hand side term represents hydraulic losses in a general way ($r_Q = \lambda / (2gDA^2)$ for pipes of constant diameter). The approximate method of determining the hydraulic losses is proposed in Appendix C.

Equations (4) and (5) form a closed system of partial differential equations where the unknowns are the pressure head $H(x, t)$ and flow rate $Q(x, t)$. Solving these equations requires determination of the boundary conditions as well as introduction of the function $A(x)$ describing variation of the cross-sectional area with the pipe length. The formulation of the boundary conditions will not be a subject of the present paper.

Numerical Solution

The system of Eqs. (4) and (5) can be solved by different numerical methods, among others, [3,4]:

- method of characteristics,
- finite difference method,
- finite element method.

The method of characteristics is the most popular for solving hydraulic transient problems. According to this method the hyperbolic partial differential equations are first converted into ordinary differential equations, which are then solved by the finite difference technique.

In order to enable a comparison with the works of Bednarczyk [19] and Wylie and Streeter [3,4] let us apply the method of characteristics. The system of Eqs. (4) and (5) can be then transformed into the following set of ordinary differential equations:

$$\frac{dH}{dt} + \frac{a}{gA} \frac{dQ}{dt} + ar_Q Q |Q| = 0 \quad (6)$$

along the characteristic lines

$$C^+ \quad \frac{dx}{dt} = +a \quad (7)$$

$$\frac{dH}{dt} - \frac{a}{gA} \frac{dQ}{dt} + ar_Q Q |Q| = 0 \quad (8)$$

along the characteristic lines

$$C^- \quad \frac{dx}{dt} = -a. \quad (9)$$

Let us also apply the method of characteristics to transform the system of Eqs. (2) and (3). Then, the following equations corresponding to Eqs. (6) and (8) can be derived:

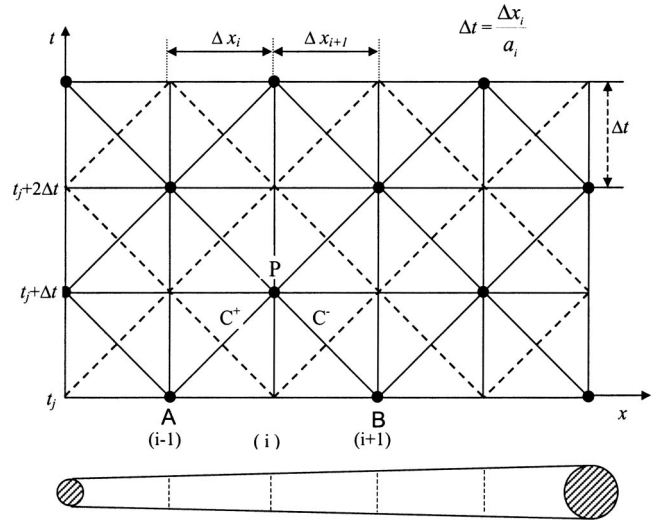


Fig. 1 Grid of characteristic lines described by equations $dx/dt = a$ and $dx/dt = -a$ for the assumed time step Δt

$$\text{for } C^+: \quad \frac{dH}{dt} + \frac{a}{g} \frac{dV}{dt} + \frac{a^2}{g} V \frac{\partial \ln A}{\partial x} + ar_V V |V| = 0 \quad (10)$$

$$\text{for } C^-: \quad \frac{dH}{dt} - \frac{a}{g} \frac{dV}{dt} + \frac{a^2}{g} V \frac{\partial \ln A}{\partial x} + ar_V V |V| = 0, \quad (11)$$

where the last left-hand side term represents hydraulic losses in a general way ($r_V = \lambda / (2gD)$ for pipes of constant diameter).

The system of Eqs. (6), (7), (8), and (9) or (7), (10), (9), and (11) can be integrated approximately for differentiable functions $A = A(x)$. The trapezoid method can be utilized even if the pressure wave speed a does not remain constant in cases where the ratio of the pipe diameter to the pipe wall thickness varies along the pipe length. Let us assume that its value for the given computational pipe segments can be calculated based on the principle of conservation of the pressure wave propagation time—see Appendix A, Eq. (A2). Let us assume further that the quantity a is independent of the flow parameters, mainly the pressure. The presented model concerns only the single-phase flow. Therefore, for the assumed integration step, a grid of characteristic lines can be found from Eqs. (7) and (9)—Fig. 1.

As an example, let us integrate Eqs. (6) and (8), or Eqs. (10) and (11), in consistence with the above assumptions, between points A and P as well as B and P, lying on the characteristic lines C^+ and C^- , respectively (see Fig. 1). The following functions of the pipe cross-sectional area will be adopted for an unpressurized pipeline

$$A(x) = 0.25\pi [D_i + K_d(x - x_i)]^2, \quad \text{where}$$

$$K_d = (D_{i+1} - D_i) / (x_{i+1} - x_i) \quad (12)$$

$$A(x) = A_i + K_a(x - x_i), \quad \text{where } K_a = (A_{i+1} - A_i) / (x_{i+1} - x_i) \quad (13)$$

$$A(x) = A_i \times \exp(K_e(x - x_i)), \quad \text{where}$$

$$K_e = \ln(A_{i+1}/A_i) / (x_{i+1} - x_i). \quad (14)$$

As a result of integration, Eqs. (6) and (8) or (10) and (11) can be presented in the following difference form:

$$H_P - H_A + \frac{a_{A-P}}{g} \frac{Q_P - Q_A}{A_{zA-P}} + R_{A-P} Q_P |Q_A| = 0 \quad (15)$$

$$H_P - H_B - \frac{a_{B-P}}{g} \frac{Q_P - Q_B}{A_{zB-P}} + R_{B-P} Q_P |Q_B| = 0 \quad (16)$$

where constants A_z and R assume values resulting from the given function $A(x)$. These constants can be evaluated between the points A and P on the characteristic line C^+ from the following relationships (Appendix C):

- for $A(x) = 0.25\pi[D_A + K_d(x - x_A)]^2$

$$A_{zA-P} = (A_P A_A)^{0.5}, \quad (17)$$

$$R_{A-P} = \frac{\lambda_{A-P}(x_P - x_A)}{8g(D_P - D_A)} \left(\frac{1}{A_A^2} - \frac{1}{A_P^2} \right) + \frac{\xi_{A-P}}{2gA_P^2} \quad (18)$$

- for $A(x) = A_A + K_d(x - x_A)$

$$A_{zA-P} = \frac{A_P - A_A}{\ln(A_A/A_P)}, \quad (19)$$

$$R_{A-P} = \frac{\lambda_{A-P}\pi^{0.5}(x_P - x_A)}{6g(A_P - A_A)} \left(\frac{1}{A_A^{1.5}} - \frac{1}{A_P^{1.5}} \right) + \frac{\xi_{A-P}}{2gA_P^2} \quad (20)$$

- for $A(x) = A_A \times \exp[K_e(x - x_A)]$

$$A_{zA-P} = \frac{A_A \ln(A_P/A_A)}{(1 - A_A/A_P)}, \quad (21)$$

$$R_{A-P} = \frac{\lambda_{A-P}(x_P - x_A)}{5g(\ln A_P - \ln A_A)} \left(\frac{1}{D_A A_A^2} - \frac{1}{D_P A_P^2} \right) + \frac{\xi_{A-P}}{2gA_P^2}. \quad (22)$$

Similar relationships, for computing the A_{zB-P} and R_{B-P} values, can be found by integration of Eq. (8) or Eq. (11) along the characteristic line C^- between points B and P .

Comparison of the Methods

Let us first compare the above presented method with the method of equivalent pipe segments. It is easy to show that the obtained relationships Eqs. (17)–(22) are the same as those to be found from Eqs. (A1), (A3), and (A4) for equivalent pipe segments—Appendix A. The same principle of conservation of pressure wave propagation time has been also used—Appendix A, Eq. (A2). Therefore, for the given assumptions the above presented method yields identical results as the method of equivalent segments. In what follows these methods will be compared with the methods presented by Bednarczyk [19] and Wylie and Streeter [3,4]. They also assumed a constant wave speed in a given pipe segment, and one can suppose that it is computed based on the conservation of pressure wave propagation time. No explicit statement on this assumption is to be found in either. We shall neglect hydraulic losses in our further considerations. Appropriate representation of inertia forces has a greater effect on the prediction of pressure variations than modelling of friction forces. Moreover, due to the lack of a general theory of hydraulic resistances, the prediction of hydraulic losses during transient liquid flows is still an approximation.

Making use of the relationship $(\partial \ln A / \partial x) dt = 1/a (\partial \ln A / \partial x) dx = (1/a) d \ln A$, Bednarczyk [19] has substituted Eq. (10) with the equation

$$dH + \frac{a}{g} dV + \frac{aV}{g} d \ln A = 0, \quad (23)$$

which can be written in the difference form obtained after integration applied by [19] along the characteristic line C^+ between points A and P :

$$H_P - H_A + \frac{a_{A-P}}{g} \left(\frac{Q_P}{A_P} - \frac{Q_A}{A_A} \right) + \frac{a_{A-P}}{2g} \left(\frac{Q_P}{A_P} + \frac{Q_A}{A_A} \right) \ln \frac{A_P}{A_A} = 0. \quad (24)$$

Equations (10) and (23) are equivalent. Their integration yields different results, depending upon the manner of treating the non-linearity. The appropriate treatment of the nonlinear term should

be guided by physical requirements. In the integration presented above, Eq. (24), the form of the $A(x)$ function was excluded from consideration. Independently of the pipe segment shape, the average liquid velocity $V_m = 0.5(Q_P/A_P + Q_A/A_A)$ was assumed and the increment of the pipe cross-sectional area within the integration limits—computational ends of the pipe segment—was taken into account. As a result, Eq. (24) was obtained, which, as it can be easily noticed, is not valid for steady flow as a particular case of the transient flow. (When we omit hydraulic losses and velocity head for steady flow, $Q_P = Q_A$, we cannot get $H_P = H_A$ from Eq. (24).)

The compatibility equation along the characteristic line C^+ given in [3,4], after elimination of a likely error in print (the units in the last term of Eqs. (16–8), p. 403, are inconsistent, and likely Δx should be replaced by 1) can be written as follows:

$$H_P - H_A + \frac{a_{A-P}}{g} \left[\frac{Q_P}{A_P} - \frac{Q_A}{A_A} - \frac{1}{2} (Q_P + Q_A) \left(\frac{1}{A_P} - \frac{1}{A_A} \right) \right] = 0. \quad (25)$$

The above equation can be derived by integration of Eqs. (6) or (10) between points A and P for a cone-shaped pipe, assuming the average flow rate $Q_m = 0.5(Q_P + Q_A) = 0.5(V_P A_P + V_A A_A)$. It should be stressed here that by assuming a linear change of the flow rate (according to the trapezoidal rule of integration) between points A and P , one can get Eq. (15) with A_z determined from the relationship Eq. (17). It can be therefore supposed that integration based on the average flow rate yields less accurate approximation.

Equations (15), (24), and (25) differ considerably from each other, independently of the method of accounting for hydraulic losses. This is not due to different forms of differential equations assumed for description of the transient flow in pipes with variable cross sections, but only due to the applied methods of integration. The integration presented in this paper leads to the relationships consistent with the method of equivalent pipes based on the generally accepted similarity conditions. By introducing the flow rate Q , instead of velocity V , the equations governing unsteady flow in a pipeline with variable cross section obtain simple forms, and, therefore, their integration, with correct accounting for the $A(x)$ function, is easier than that of earlier equations, [3,4,17]. Additionally, it can be worthy to stress that the assumption of a constant equivalent pressure wave speed based on conservation of wave propagation time allows for simpler solutions. However, one can imagine a more general approach—with account of pressure wave speed variation along the pipe length taken directly in integration of the governing equations. Such an approach would be very complicated and could be a subject of a separate paper.

In order to better illustrate the differences between the compared methods, let us consider a case of an immediate flow shutdown in a cone-shaped pipe. Because of neglecting the hydraulic resistance, it is easy to determine the waterhammer pressure rises based on the considered methods and to relate the obtained values to the pressure rises calculated for an equivalent pipe segment. The results of these calculations are presented in Fig. 2, showing the pressure changes as a function of the conical pipe contraction or expansion ratio D_2/D_1 (D_1 and D_2 are the diameters of the pipe segment at its ends). The graphs illustrate differences between the compared methods. It is clear that the method described by Bednarczyk [19] yields lower, whereas that presented by Wylie and Streeter [3,4] higher values of the computed pressure rises than the method of equivalent pipe segments with a constant substitute cross section, and also the method described in the present contribution. From a practical point of view, it can be also interesting to compare the results of pressure rises obtained by means of the proposed method (and also according to the method of equivalent pipes) for pipes described by Eqs. (12)–(14), with the pressure rises for pipes whose diameter or cross-section area is an arithmetic average of diameters or cross section areas at their ends, respectively. It can be expected that replacing of cone-

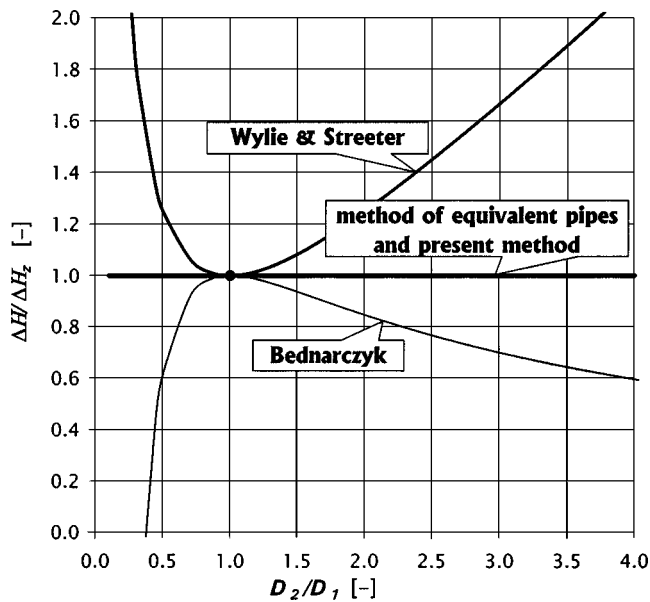


Fig. 2 Differences in the prediction of pressure rises in cone-shaped pipes with different expanding coefficients obtained by means of the methods under comparison

shaped pipeline segments with segments of averaged diameters or external cross section areas is a common practice in pipeline calculations performed for engineering purposes.

The results referring to the first case are displayed in Fig. 3, the second case is illustrated in Fig. 4. The presented results show that appropriate representation of variations in the pipe cross-sectional area has a great effect on the accuracy of computed flow transients. For example, if a cone-shaped pipe with diameter ratio $D_2/D_1 = 2$ is replaced by a pipe of arithmetical average diameter the discrepancy in prediction of the pressure rise can be as high as 12%—Fig. 3.

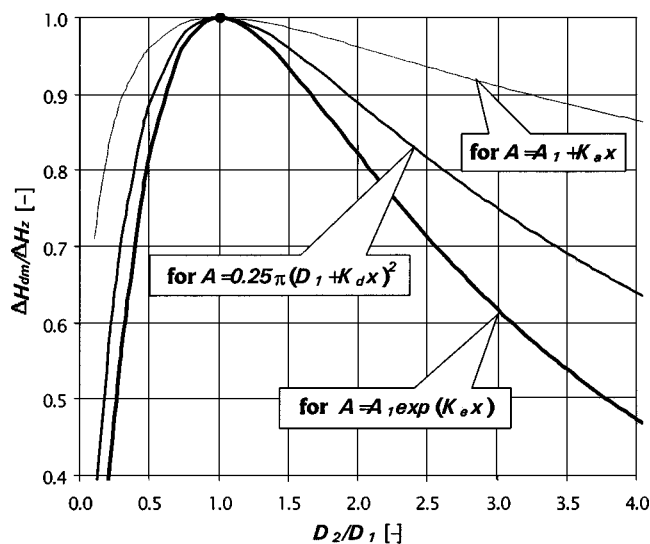


Fig. 3 Comparison of pressure rises (ΔH_2) obtained using the method of equivalent pipes for different pipe geometries (linear variation of diameter, linear variation of cross section area, and exponential variation of cross section area) and calculated (ΔH_{am}) for a uniform pipe with diameter equal to the arithmetical average of diameters at both ends of the segment under consideration

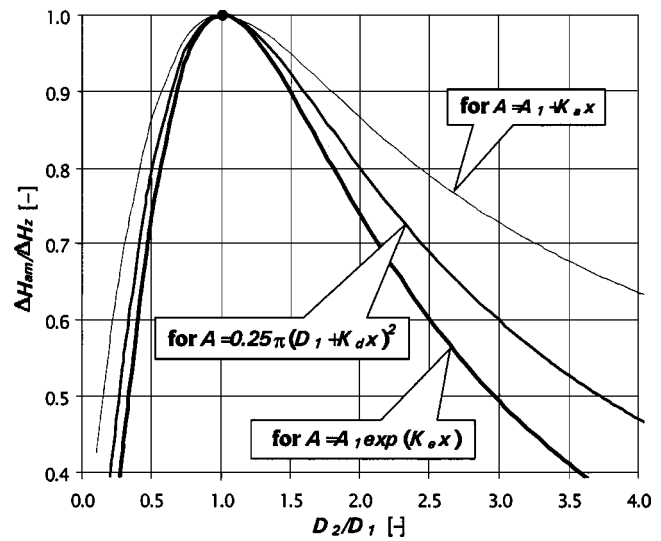


Fig. 4 Comparison of pressure changes (ΔH_2) obtained using the method of equivalent pipes for different pipe geometries (linear variation of diameter, linear variation of cross section area, and exponential variation of cross section area) and calculated (ΔH_{am}) for a uniform pipe with cross section area equal arithmetic average of cross-section areas at both ends of the segment under consideration

Conclusions

The considerations conducted in this paper prove that the continuity equation of one-dimensional unsteady liquid flow, expressed in terms of the flow rate, assumes the same form for pipes with constant and variable cross sections. This result is not true for the continuity equation written in terms of the liquid velocity. According to the classical theory of waterhammer, the latter remains valid only for pipes of a constant cross-sectional area. Extending the validity of this equation on pipes with expanding or contracting sections requires introduction of an additional term.

It has been shown that, assuming an equivalent wave speed in computational pipe segments, the analysis of waterhammer based on the direct solution of the equations governing one-dimensional transient liquid flows in pipes with variable cross sections gives identical results to those following from the analysis based on equivalent pipe segments. The above-mentioned conclusion is in contradiction with the treatments given by Bednarczyk, [19], and Wylie and Streeter [3,4]. For conical pipes, the numerical method presented by Bednarczyk [19] yields a lower, whereas the method presented by Wylie and Streeter, [3,4], higher pressure rises than the method of equivalent pipe segments of constant cross sections. The discrepancies increase with the degree of pipe expansion or contraction. The reason for these discrepancies has been explained.

It has been also proved that the degree of pipe expansion or contraction as well as the type of function describing changes in the pipe shape have a considerable effect on the inaccuracy in computations made while the pipe with expanding or contracting sections is replaced by a uniform pipe whose diameter or cross-section area are arithmetic averages of the respective values at the pipe ends.

Nomenclature

- a = pressure wave speed
- A = pipe cross-sectional area
- c = pipe constraint coefficient (dimensionless parameter that describes the effect of pipe constraint condition on the wave speed)
- C^+ , C^- = name of the characteristics equations

D = pipe inner diameter
 e = pipe wall thickness
 E = pipe wall modulus of elasticity
 E_ρ = liquid bulk modulus of elasticity
 g = gravitational acceleration
 H = pressure (piezometric) head
 K = pipe expansion (contraction) coefficient
 L = pipe length
 p = pressure
 r_V = hydraulic loss coefficient defined by the formula $r_V = \Delta H_r / (V|V|\Delta x)$; ($r_V = \lambda / (2gD)$ for pipes of constant diameter)
 r_Q = hydraulic loss coefficient defined by the formula $r_Q = \Delta H_r / (Q|Q|\Delta x)$; ($r_Q = \lambda / (2gDA^2)$ for pipes of constant diameter)
 Re = Reynolds number
 Q = volumetric flow rate
 V = liquid mean velocity
 x = distance along the pipe (longitudinal coordinate)
 t = time
 z = elevation of centerline of pipe above datum
 λ = Darcy-Weisbach friction factor
 ν = Poisson's ratio
 ρ = liquid mass density
 ξ = coefficient of hydraulic losses due to pipe expansion or contraction

Subscripts and Superscripts

$1, 2$ = internal cross sections of a pipe segment at its ends
 A, B, P = nodes of characteristic lines grid
 a = pipe with a linear change of the inner cross-sectional area
 d = conical pipe (with a linear change of the inner diameter)
 e = pipe with an exponential change of the inner cross-sectional area
 r = hydraulic losses
 i = pipe cross section
 m = average value
 z = equivalent (substitute) value
 λ = friction losses

Appendix A

Transformation of Real Pipes With Expanding or Contracting Sections to Equivalent Pipe Segments of Constant Dimension. The similarity conditions should be preserved in order to transform a pipe with expanding or contracting sections to an equivalent uniform pipe segment. These conditions imply that the following properties should not change in the equivalent pipe segment, compared to the real pipe of the same length L :

- (1) inertia forces due to the same way of flow shutdown,
- (2) pressure wave propagation time, and
- (3) hydraulic losses.

Condition (1) leads to the following formula for the equivalent cross-sectional area A_z of the pipe segment:

$$A_z = \frac{L}{\int_0^L \frac{dx}{A(x)}} \quad (A1)$$

The equivalent pressure wave speed a_z can be found from the condition (2):

$$a_z = \frac{L}{\int_0^L \frac{dx}{a(x)}} \quad (A2)$$

Condition (3) for the hydraulic losses can be rewritten as

- for losses due to friction

$$\frac{\lambda_z L}{D_z^5} = \int_0^L \frac{\lambda}{D^5} dx \quad \left(\frac{\lambda_z L Q^2}{2g D_z A_z^2} = \int_0^L \frac{\lambda Q^2}{2g D A^2} dx \right) \quad (A3)$$

- for losses due to shape changes

$$\frac{\xi_z}{D_z^4} = \frac{\xi}{D^4} \quad \left(\frac{\xi_z Q^2}{2g A_z^2} = \frac{\xi Q^2}{2g A^2} \right) \quad (A4)$$

Appendix B

Continuity Equation. The principle of mass conservation in the pipe flow leads to the following equation:

$$\frac{\partial(\rho A V)}{\partial x} + \frac{\partial(\rho A)}{\partial t} = 0 \quad (B1)$$

or, after a simple expanding the derivative of the product of terms, to

$$\frac{\partial V}{\partial x} + \frac{1}{\rho} \left(\frac{\partial \rho}{\partial t} + V \frac{\partial \rho}{\partial x} \right) + \frac{1}{A} \left(\frac{\partial A}{\partial t} + V \frac{\partial A}{\partial x} \right) = 0 \quad (B2)$$

Making use of the definition of the modulus of elasticity, one can get

$$\frac{1}{\rho} \left(\frac{\partial \rho}{\partial t} + V \frac{\partial \rho}{\partial x} \right) = \frac{1}{E_\rho} \left(\frac{\partial p}{\partial t} + V \frac{\partial p}{\partial x} \right) \quad (B3)$$

In the case under consideration, changes in A take place not only due to pressure rise, but also due to longitudinal changes in the shape of the pipe shell. Therefore we can write as follows:

$$\frac{1}{A} \left(\frac{\partial A}{\partial t} + V \frac{\partial A}{\partial x} \right) = \frac{V}{A} \frac{\partial A}{\partial x} + \frac{1}{A} \frac{\partial A}{\partial p} \left(\frac{\partial p}{\partial t} + V \frac{\partial p}{\partial x} \right) \quad (B4)$$

The quantity $1/A \partial A / \partial p$ can be determined from the Hooke's law for a pipe shell elastically deformed under pressure. Setting Eqs. (B3) and (B4) into Eq. (B2), we get

$$\frac{\partial p}{\partial t} + V \frac{\partial p}{\partial x} + \rho a^2 \frac{\partial V}{\partial x} + \rho a^2 V \frac{\partial \ln A}{\partial x} = 0 \quad (B5)$$

where the quantity a —the pressure wave speed—is defined by the formula

$$a = \left(\frac{E_\rho}{\rho} \right)^{0.5} \left(1 + \frac{E_\rho}{A} \frac{\partial A}{\partial p} \right)^{-0.5} \quad (B6)$$

In case of a cylindrical pipe Eq. (B6) takes the form

$$a = \left(\frac{E_\rho}{\rho} \right)^{0.5} \left(1 + \frac{c D E_\rho}{e E} \right)^{-0.5} \quad (B7)$$

The coefficient c depends on the pipe constraints and after Wylie and Streeter [3,4] can be found from one of the following relationships:

- for a pipe anchored against longitudinal movement

$$c = 1 - \nu^2, \quad (B8)$$

- for a pipe anchored at one end only

$$c = 1 - 0.5\nu, \quad (B9)$$

- for a pipe anchored with expansion joints throughout

$$c = 1. \quad (B10)$$

Appendix C

Integration Method. The expressions obtained as a result of integration of terms in Eq. (6) along the characteristic line C^+ between points A and P (Fig. 1) are presented below. The integra-

tion has been carried out by means of the trapezoid method, i.e., assuming linear variation of the flow quantities Q and H along the integrating lines.

Term I.

$$\int_{t_A}^{t_P} \frac{dH}{dt} dt = \frac{H_P - H_A}{t_P - t_A} \int_{t_A}^{t_P} dt = H_P - H_A$$

Term II. A constant equivalent pressure wave speed based on conservation of wave propagation time has been assumed. Such assumption, applied also by Bednarczyk [19] and Wylie and Streeter, [3,4], allows to simplify the integration as presented below and to derive exact results.

Cone-shaped pipe. $D = D_A + K_d \times (x - x_A)$, where $K_d = (D_P - D_A)/(x_P - x_A)$

$$\begin{aligned} \int_{t_A}^{t_P} \frac{a}{gA} \frac{dQ}{dt} dt &= \frac{4}{\pi g} \frac{Q_P - Q_A}{t_P - t_A} \int_{x_A}^{x_P} \left(D_A + \frac{D_P - D_A}{x_P - x_A} (x - x_A) \right)^{-2} dx \\ &= - \left(D_A + \frac{D_P - D_A}{x_P - x_A} (x - x_A) \right)^{-1} \Big|_{x_A}^{x_P} \\ &\quad \times \frac{x_P - x_A}{D_P - D_A} \frac{4}{\pi g} \frac{Q_P - Q_A}{t_P - t_A} \\ &= \frac{4a}{\pi g} \left(\frac{1}{D_A} - \frac{1}{D_P} \right) \frac{Q_P - Q_A}{D_P - D_A} \\ &= \frac{4a}{\pi g} \frac{Q_P - Q_A}{D_A D_P} = \frac{a}{g} \frac{Q_P - Q_A}{A_z} \end{aligned}$$

Pipe with a linear change of the cross-sectional area.

$A = A_A + K_a \times (x - x_A)$ where $K_a = (A_P - A_A)/(x_P - x_A)$

$$\begin{aligned} \int_{t_A}^{t_P} \frac{a}{gA} \frac{dQ}{dt} dt &= \frac{1}{g} \frac{Q_P - Q_A}{t_P - t_A} \int_{x_A}^{x_P} \left(A_A + \frac{A_P - A_A}{x_P - x_A} (x - x_A) \right)^{-1} dx \\ &= \frac{1}{g} \frac{Q_P - Q_A}{t_P - t_A} \frac{x_P - x_A}{A_P - A_A} \\ &\quad \times \ln \left(A_A + \frac{A_P - A_A}{x_P - x_A} (x - x_A) \right) \Big|_{x_A}^{x_P} \\ &= \frac{a}{g} \frac{Q_P - Q_A}{A_P - A_A} \ln \left(\frac{A_P}{A_A} \right) = \frac{a}{g} \frac{Q_P - Q_A}{A_z} \end{aligned}$$

Pipe with an exponential change of the cross-sectional area.

$A = A_A \times \exp[K_e(x - x_A)]$ where $K_e = \ln(A_P/A_A)/(x_P - x_A)$

$$\begin{aligned} \int_{t_A}^{t_P} \frac{a}{gA} \frac{dQ}{dt} dt &= \frac{1}{g} \frac{Q_P - Q_A}{t_P - t_A} \\ &\quad \times \int_{x_A}^{x_P} \left(A_A \exp \left(\frac{\ln A_P - \ln A_A}{x_P - x_A} (x - x_A) \right) \right)^{-1} dx \\ &= \frac{1}{g} \frac{Q_P - Q_A}{t_P - t_A} \frac{x_P - x_A}{\ln A_P - \ln A_A} \\ &\quad \times \left(-A_A \exp \left(\frac{\ln A_P - \ln A_A}{x_P - x_A} (x - x_A) \right) \right) \Big|_{x_A}^{x_P} \\ &= \frac{a}{g} \frac{Q_P - Q_A}{\ln(A_P/A_A)} \left(\frac{1}{A_A} - \frac{1}{A_P} \right) = \frac{a}{g} \frac{Q_P - Q_A}{A_z} \end{aligned}$$

Term III. The prediction of hydraulic losses occurring during transient flows still draws on approximation. This is not only due

to the lack of a general theory of turbulent pipe friction, but also due to the nonlinear form of the last term in Eqs. (6) and (8). According to Wylie and Streeter [4], friction losses can be fairly predicted with the aid of the relationship $\Delta H_r = R^* Q_P |Q_A|$, where Q_P and Q_A denote the flow rates at the ends of the computational pipe segment. In pipes with variable cross sections, besides friction losses, losses due to the pipe expansion or contraction should be also taken into account. Let the total losses in a pipe segment be expressed as follows:

$$\begin{aligned} \Delta H_r &= \int_{t_A}^{t_P} a r_Q Q |Q| dt \\ &= \int_{x_A}^{x_P} r_Q Q |Q| dx \\ &= \Delta H_\lambda + \Delta H_\xi \\ &= \int_{x_A}^{x_P} \frac{\lambda}{2gDA^2} Q |Q| dx + \frac{\xi}{2gA_P^2} Q_P |Q_A|. \end{aligned}$$

In order to integrate the friction loss term, let us assume the friction coefficient λ from the preceding step of integration. For a pipe with internal diameter described by $D = D_A + K_d(x - x_A)$, we can get the friction loss expressed as follows:

$$\begin{aligned} \Delta H_\lambda &= \int_{x_A}^{x_P} \frac{\lambda}{2gDA^2} Q |Q| dx \\ &= \frac{8\lambda_{A-P} Q_P |Q_A|}{\pi^2 g} \int_{x_A}^{x_P} \left(D_A + \frac{D_P - D_A}{x_P - x_A} (x - x_A) \right)^{-5} dx \\ &= - \frac{2\lambda_{A-P} Q_P |Q_A|}{\pi^2 g} \frac{x_P - x_A}{D_P - D_A} \left(D_A + \frac{D_P - D_A}{x_P - x_A} (x - x_A) \right)^{-4} \Big|_{x_A}^{x_P} \\ &= \frac{\lambda_{A-P} (x_P - x_A)}{8g(D_P - D_A)} \left(\frac{1}{A_A^2} - \frac{1}{A_P^2} \right) Q_P |Q_A| = R_\lambda Q_P |Q_A| \end{aligned}$$

whereas the total losses in the computational pipe segment can be presented in the form

$$R = R_\lambda + R_\xi = \frac{\lambda_{A-P} (x_P - x_A)}{8g(D_P - D_A)} \left(\frac{1}{A_A^2} - \frac{1}{A_P^2} \right) + \frac{\xi_{A-P}}{2gA_P^2}.$$

We can obtain in a similar way

- for a pipe with linear cross section area variation, $A = A_A + K_a(x - x_A)$:

$$R = \frac{\lambda_{A-P} \pi^{0.5} (x_P - x_A)}{6g(A_P - A_A)} \left(\frac{1}{A_A^{1.5}} - \frac{1}{A_P^{1.5}} \right) + \frac{\xi_{A-P}}{2gA_P^2}$$

- for a pipe with an exponential cross section area variation, $A = A_A \exp[K_e(x - x_A)]$:

$$R = \frac{\lambda_{A-P} (x_P - x_A)}{5g(\ln A_P - \ln A_A)} \left(\frac{1}{D_A A_A^2} - \frac{1}{D_P A_P^2} \right) + \frac{\xi_{A-P}}{2gA_P^2}.$$

It is worthwhile to notice that the empirical coefficient ξ of losses due to shape changes can assume different values depending on the flow direction. It is generally known that hydraulic resistance in diverging pipes is considerably higher than that in converging pipes for the same ratio of the inlet to outlet or outlet to inlet cross-sectional area, respectively.

References

- [1] Betamio de Almeida, A., and Koelle, E., 1992, *Fluid Transients in Pipe Networks*, CMP Elsevier Applied Science, New York.
- [2] Chaudhry, M. H., 1979, *Applied Hydraulic Transients*, Van Nostrand Reinhold, New York.

- [3] Wylie, E. B., and Streeter, L. V., 1978, *Fluid Transients*, McGraw-Hill, New York.
- [4] Wylie, E. B., and Streeter, L. V., 1993, *Fluid Transients in Systems*, Prentice-Hall, Englewood Cliffs, NJ.
- [5] Adamkowski, A., 1988, "Transient Flow in Pipeline Systems of Hydraulic Turbomachines," Ph.D. thesis, Institute of Fluid Flow Machinery of the Polish Academy of Sciences (in Polish).
- [6] Adamkowski, A., 1996, "Theoretical and Experimental Investigations of Waterhammer Attenuation by Cut-Off and By-Pass Valves in Pipeline Systems of Hydraulic Turbomachines," Copybooks of the Institute of Fluid Flow Machinery of the Polish Academy of Sciences, No. 461/1423/96, Gdańsk (in Polish).
- [7] Budny, D. D., Wiggert, D. C., and Hatfield, F. J., 1991, "The Influence of Structural Damping on Internal Pressure During a Transient Pipe Flow," *ASME J. Fluids Eng.*, **113**, pp. 424–429.
- [8] Fan, D., and Tijsseling, A., 1992, "Fluid-Structure Interaction With Cavitation in Transient Pipe Flows," *ASME J. Fluids Eng.*, **114**.
- [9] Tijsseling, A. S., 1996, "Fluid-Structure Interaction in Liquid-Filled Pipe Systems: A Review," *J. Fluids Struct.*, **10**, pp. 109–146.
- [10] Wiggert, D. C., Hatfield, F. J., and Stuckenbruck, S., 1987, "Analysis of Liquid and Structural Transients by the Method of Characteristics," *ASME J. Fluids Eng.*, **109**, pp. 161–165.
- [11] Wan, Zhang-Min, and Tan, Soon Keat, 1997, "Coupled Analysis of Fluid Transients and Structural Dynamic Responses of a Pipeline Systems," *J. Hydraul. Res.*, **35**(1), pp. 119–131.
- [12] Elansary, A. S., Chaudhry, M. H., and Silva, W., 1994, "Numerical and Experimental Investigation of Transient Pipe Flow," *J. Hydraul. Res.*, **32**(5).
- [13] Vardy, A. E., and Hwang, Kuo-Lun, 1991, "A Characteristics Model of Transient Friction in Pipes," *J. Hydraul. Res.*, **29**(5).
- [14] Vardy, A. E., Brown, J. M. B., and Hwang, Kuo-Lun, 1994, "A Weighting Function Model of Transient Turbulent Pipe Friction," *J. Hydraul. Res.*, **31**(4).
- [15] Zarzycki, Z., "Hydraulic Resistance of Unsteady Liquid Flow in Pipes," Copybooks of Technical Univ. Szczecin, No. 516/1994 (in Polish).
- [16] Bergant, A., and Simpson, A. R., 1999, "Pipeline Column Separation Flow Regimes," *J. Hydraul. Res.*, **125**(8).
- [17] Moody, F. J., 1991, "A Survey of Fluid Transient Studies—1991," *ASME J. Pressure Vessel Technol.*, **113**.
- [18] Simpson, A. R., and Bergant, A., 1994, "Numerical Comparison of Pipe-Column Separation Models," *J. Hydraul. Eng.*, **120**(3).
- [19] Bednarczyk, S., 1974, "Unsteady Fluid Flow in Pressure Pipelines," *Archives of Hydraulic Engineering*, **XXI**(4) (in Polish).

Application of an Angular Momentum Balance Method for Investigating Numerical Accuracy in Swirling Flow

H. Nilsson
L. Davidson

Department of Thermo and Fluid Dynamics,
Chalmers,
SE-412 96 Göteborg, Sweden

This work derives and applies a method for the investigation of numerical accuracy in computational fluid dynamics. The method is used to investigate discretization errors in computations of swirling flow in water turbines. The work focuses on the conservation of a subset of the angular momentum equations that is particularly important to swirling flow in water turbines. The method is based on the fact that the discretized angular momentum equations are not necessarily conserved when the discretized linear momentum equations are solved. However, the method can be used to investigate the effect of discretization on any equation that should be conserved in the correct solution, and the application is not limited to water turbines. Computations made for two Kaplan water turbine runners and a simplified geometry of one of the Kaplan runner ducts are investigated to highlight the general and simple applicability of the method.
[DOI: 10.1115/1.1595673]

1 Background

The use of computational fluid dynamics (CFD) in industry has increased dramatically in recent decades and is now used in many fields as a complement to model testing. Computational results obtained in industrial applications are usually claimed to be qualitatively correct, i.e., they can be used to identify trends but not to establish the quantitatively correct values. There are several reasons why the industrial computational results are not quantitatively correct. First, the physics of the applications and the boundary conditions are approximated using more or less sophisticated methods. Secondly, the resulting approximated physical application is computed by a numerical method that uses further approximations and computational limitations.

To study the accuracy of the numerical method, an assumption can be made that the physics of the application and the boundary conditions are approximated consistently. The accuracy of a computation then depends on the resolution of the discretized problem. A sufficiently fine resolution will thus give the correct solution to the approximated problem if the iterative convergence and round-off errors are small. Fine resolutions cannot be used in industrial applications, however, because of restrictions on computational power and time limitations. The resolutions used in industrial applications are usually not even close to a sufficiently fine resolution. This has led to an increased interest in methods for studying the accuracy of CFD results, [1,2], and many scientific journals have adopted statement policies about this, [3,4].

When CFD is applied to turbulent flow in complex geometries it is often difficult to obtain an iteratively converged solution, i.e., a solution that satisfies the discretized equations, for the reason that the preferred higher order discretization schemes are highly unstable when the computational grid has very skewed and thin control volumes. One way of dealing with this is to use stable discretization schemes. A number of discretization schemes of varying stability are available in the literature. Depending on the complexity of the flow and the geometry, a discretization scheme that gives an iteratively converged solution usually has an ob-

served discretization order that lies between the first and second order. Figure 1 shows the computed flow above and below a Kaplan runner using the first-order hybrid scheme and the second-order Van Leer scheme. The influence of the discretization scheme is striking.

Stable discretization schemes introduce discretization errors that must be investigated before it is possible to achieve reliable computational results.

One approach to studying the accuracy of CFD results is to look at the sensitivity to grid refinement using the Richardson extrapolation method, [5–7]. The Richardson method uses results from three grids of different refinement to estimate the grid convergence error. If h is a geometric discretization parameter representative of the grid spacing of the finest grid ($h_1 = h$), the subsequent grids are coarsened according to $h_2 = rh$ and $h_3 = r^2h$. The refinement parameter can for instance be chosen to be $r = 2$. The main requirement of the Richardson method is that the solutions at all the grids must be in the asymptotic range. This requirement can be met in some cases. In general three-dimensional industrial computations, however, where it is difficult to get even the finest solution in the asymptotic range, the method cannot be used to its full extent, [8,9]. Another major drawback of the method is that time constraints do not allow computations on several grids in industry. The original Richardson paper, [10], examined the difference between a low-order solution and a high-order solution on the same grid. This requires computations of two solutions, which is time-consuming, and makes it necessary to obtain a high-order computation, which is not always the case in industrial CFD. A fast and simple method that investigates the discretization error of a single solution on a single (coarse) grid is therefore needed.

The present method uses a single computational result from a single grid to investigate the accuracy of that computational result. Most CFD codes use conservation of mass and linear momentum to compute the flow. Hence, imbalances in angular momentum, kinetic energy and higher moments reflect the numerical accuracy, [11,12]. The CFD codes may be rewritten to conserve other than mass and linear momentum, but, in any numerical approach, there will be nonconserved quantities that can serve as candidates for numerical accuracy assessment. Since all quantities of the flow cannot be investigated, it is necessary to choose quantities that are

Contributed by the Fluids Engineering Division for publication in the JOURNAL OF FLUIDS ENGINEERING. Manuscript received by the Fluids Engineering Division Nov. 15, 2001; revised manuscript received Feb. 23, 2003. Associate Editors: G. Karniadakis.

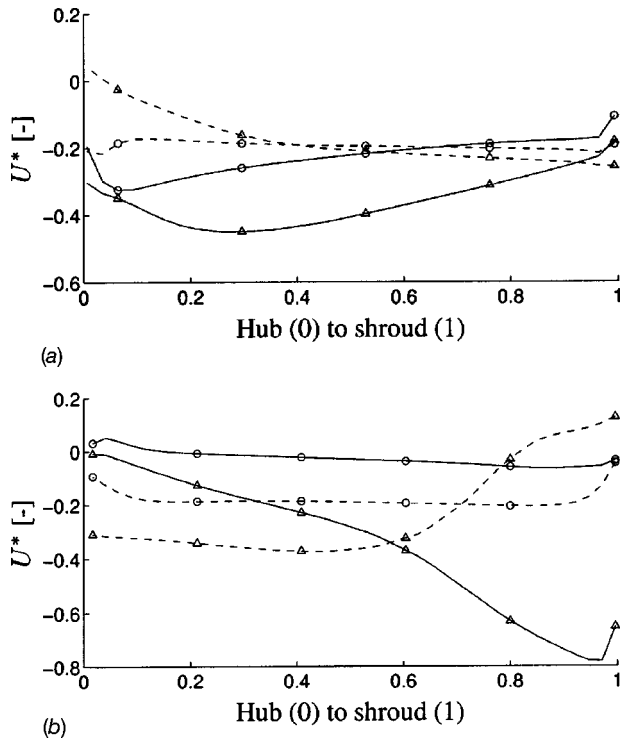


Fig. 1 Circumferentially averaged velocity coefficients above and below a Kaplan runner (Kaplan 1). Solid lines: tangential velocity; dashed lines: axial velocity. Markers: Δ : first-order hybrid scheme; \circ : second-order Van Leer scheme. The velocities are normalized by the runner radius and the runner angular velocity. (a) Above the runner, (b) below the runner.

particularly important to the flow. A set of important quantities can be specified for each industrial application. The method described in this work can be used to estimate the accuracy with respect to those quantities. When all important quantities of the flow are conserved, the computational results can be considered correct. Angular momentum is one important quantity in swirling flow in water turbines, which is studied in the present work.

2 Derivation of the Angular Momentum Balance

The derivation of the angular momentum balance starts with the Reynolds transport theorem for an arbitrarily moving deformable control volume, [13,14],

$$\frac{dB_{\text{sys}}}{dt} = \frac{d}{dt} \left(\int_{CV} \beta \rho dV \right) + \int_{CS} \beta \rho (\mathbf{U}_r \cdot \mathbf{n}) dA$$

where B is a property of the fluid, $\beta = dB/dm$ is the intensive value or B per unit mass, and dB_{sys}/dt is the rate of change of B of a system (material region) confined in a control volume that instantaneously comprises the system. This expression is thus a conversion formula between a system and a control volume that instantaneously occupies the same space and, in other words, is a coupling between the Lagrangian and Eulerian descriptions. The velocity relative to that of the control volume surface is $\mathbf{U}_r = \mathbf{U}(\mathbf{r}, t) - \mathbf{U}_s(\mathbf{r}, t)$, where $\mathbf{U}(\mathbf{r}, t)$ is the fluid velocity and $\mathbf{U}_s(\mathbf{r}, t)$ is the control volume surface velocity. The Reynolds transport theorem can be used to write all the basic laws in integral form and can thus be used to derive the mass balance ($B=m$, $\beta = dm/dm=1$), the linear momentum balance (Navier Stokes, $\mathbf{B} = m\mathbf{U}$, $\beta = dm\mathbf{U}/dm = \mathbf{U}$), the energy balance ($B=E$, $\beta = dE/dm = e$), and the angular momentum balance ($\mathbf{B} = \mathbf{H}_o$, $= \int_{\text{sys}} (\mathbf{r} \times \mathbf{U}) dm$, $\beta = d\mathbf{H}_o/dm = \mathbf{r} \times \mathbf{U}$).

The angular momentum balance for an arbitrarily moving deformable control volume is

$$\frac{d\mathbf{H}_o}{dt} \Big|_{\text{sys}} = \frac{d}{dt} \left(\int_{CV} (\mathbf{r} \times \mathbf{U}) \rho dV \right) + \int_{CS} (\mathbf{r} \times \mathbf{U}) \rho (\mathbf{U}_r \cdot \mathbf{n}) dA. \quad (1)$$

According to the laws of mechanics, the rate of change of the angular momentum of the system is equal to the sum of all the moments about an arbitrary point o acting on a control volume that instantaneously comprises the system, yielding an expression for the left-hand side of Eq. (1) as ([15])

$$\frac{d\mathbf{H}_o}{dt} \Big|_{\text{sys}} = \int_{CS} \mathbf{r} \times \mathbf{F}_s dA + \int_{CV} \mathbf{r} \times \mathbf{F}_b \rho dV - \int_{CV} (\mathbf{r} \times \mathbf{a}) \rho dV, \quad (2)$$

where \mathbf{F}_s is the surface force (both viscous, turbulent shear, and normal forces) per unit area acting on the control volume surface and \mathbf{F}_b is the body force per unit mass acting inside the control volume. The vector, \mathbf{a} , is the acceleration of the coordinate system, [14],

$$\mathbf{a} = \frac{d^2 \mathbf{R}}{dt^2} + \frac{d\boldsymbol{\Omega}}{dt} \times \mathbf{r} + 2\boldsymbol{\Omega} \times \mathbf{U} + \boldsymbol{\Omega} \times (\boldsymbol{\Omega} \times \mathbf{r}), \quad (3)$$

where \mathbf{R} is the position vector of the origin of the noninertial coordinate system relative to an inertial coordinate system, \mathbf{r} is the position vector relative to the non-inertial coordinate system, and $\boldsymbol{\Omega}$ is the angular velocity of the noninertial coordinate system. The terms on the right hand side in the equation correspond to system acceleration, system angular acceleration, Coriolis acceleration and centripetal acceleration.

If the control volume is nondeformable and the flow is steady, the time derivative of the volume integral in Eq. (1) vanishes. Further, if the control volume is rotating at a constant $\boldsymbol{\Omega}$ about a stationary origin, the angular momentum balance (Eqs. (1)–(3)) reads

$$\int_{CS} \mathbf{r} \times \mathbf{F}_s dA + \int_{CV} \mathbf{r} \times \mathbf{F}_b \rho dV - \int_{CV} \mathbf{r} \times (2\boldsymbol{\Omega} \times \mathbf{U}) \rho dV - \int_{CV} \mathbf{r} \times (\boldsymbol{\Omega} \times (\boldsymbol{\Omega} \times \mathbf{r})) \rho dV = \int_{CS} (\mathbf{r} \times \mathbf{U}) \rho (\mathbf{U} \cdot \mathbf{n}) dA. \quad (4)$$

This is an extremely complicated relation that contains all the features of the linear momentum balance. In addition, it should be recalled that it was derived from the change in angular momentum about point o , which has not yet been specified. Relation (4) is obviously valid for all possible choices of o !

If the position vector, \mathbf{r} , can be approximated as constant over the volume of integration, the angular momentum and linear momentum balances are equivalent in continuum mechanics, [13], and the angular momentum balance can be derived from the vector product of \mathbf{r} and the linear momentum balance. However, since the computational control volumes are not infinitesimal, the discretized angular momentum balance is not necessarily satisfied simply because the discretized linear momentum balance is satisfied. It is thus up to the discretization scheme to conserve both angular and linear momentum.

2.1 Angular Momentum Balance in Turbomachinery. In turbomachinery, the axial component of the angular momentum balance about the axis of rotation transfers torque to the rotating shaft. Assuming that $\boldsymbol{\Omega} = \Omega \mathbf{e}_z$ (\mathbf{e}_z is the unit vector in the z -direction) is aligned with the shaft, the axial component of the angular momentum balance (Eq. (4)) about the axis of rotation reads

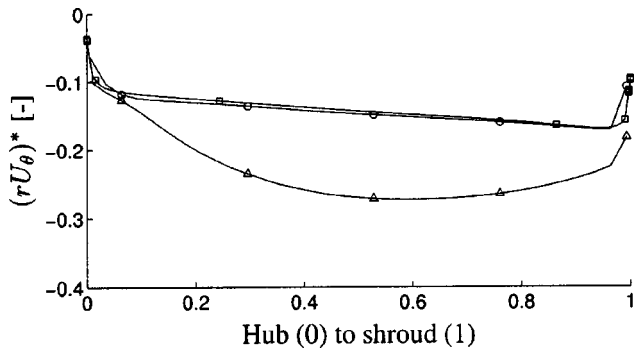


Fig. 2 Angular momentum distributions at the inlet and a section before the runner of a Kaplan runner (Kaplan 1). The distribution at the inlet should be approximately conserved at the section before the runner in a correct solution, i.e., the curves should coincide. Markers: \square : inlet distribution; \triangle : first-order hybrid scheme, before the runner; \circ : second-order Van Leer scheme, before the runner. The angular momentum is normalized by the runner radius and the runner angular velocity.

$$\int_{CS} rF_{s\theta}dA + \int_{CV} rF_{b\theta}dV + \int_{CV} 2r\Omega U_r\rho dV = \int_{CS} rU_\theta\rho(\mathbf{U}\cdot\mathbf{n})dA \quad (5)$$

where r is the cylindrical radial direction and θ is the tangential direction. The term involving Ω originates from the Coriolis term of the angular momentum balance. There is no effect of the centripetal term, however, since the coordinate system rotation vector, Ω , is aligned with the axial component of the balance. Further, if gravity, as in the present work, is the only body force, $\int_{CV} rF_{b\theta}dV=0$. Equation (5) is the central equation in the present work.

Equation (5) can be further reduced for simple investigations of the flow in turbomachines. This is done in the remainder of this section. When applied to a thin stationary axisymmetric stream tube ($r \approx \text{const}$ at inlet and outlet) with uniform inlet (index 1) and outlet (index 2) velocities and negligible surface forces, Eq. (5) is reduced to

$$\int_{CV} rF_{b\theta}dV = \Delta\dot{m}(r_2U_{\theta 2} - r_1U_{\theta 1})$$

where $\Delta\dot{m}$ is the mass flow through the stream tube. If $F_{b\theta}$ includes all the tangential body forces from the blades in a turbomachine, we obtain the power balance for the stream tube, [15],

$$-\Delta P_{\text{shaft}} = \Delta\dot{m}\Omega(r_2U_{\theta 2} - r_1U_{\theta 1}). \quad (6)$$

This is the *general Euler equation for turbomachinery*, [15], relating the input shaft power to the change in angular momentum for a thin axisymmetric stream tube, which highlights the importance of the angular momentum balance in this kind of flow.

Equation (6) can be used to verify the numerical results to some extent. One can assume that the thicknesses of the stream tubes through the domain are proportional to the channel width, and that the mass flow through all the stream tubes is the same, [16]. These are not accurate assumptions, which is one of the reasons that this simplified method is not complete. Further, the shaft power in each stream tube is difficult to obtain, and thus the general Euler equation is not easily applicable in the region where the runner blades are located. However, the distribution of rU_θ should be approximately conserved in each stream tube in regions where there are no runner blades ($\Delta P_{\text{shaft}}=0$). Figure 2 shows the angular momentum distribution of the circumferentially averaged flow at the inlet and a section above the runner of a Kaplan runner

(the Kaplan 1 runner described later) for both the first-order hybrid and the second-order Van Leer discretization schemes (using the tangential velocities in Fig. 1(a)). It is obvious that the hybrid computation does not satisfy the general Euler equation while the Van Leer computation works well. The Van Leer computations were carried out and analyzed by Nilsson and Davidson [17] (the k15 case), which gives detailed information on the analysis in Fig. 2.

The present work uses Eq. (5), without further assumptions, to investigate numerical accuracy of the computational results.

3 The Computational Method

The computations used for the investigations in the present work were made using the CALC-PMB finite volume CFD code. The main features of the CALC-PMB CFD code are its use of conformal block structured boundary fitted coordinates, a pressure correction scheme (SIMPLEC [18]), Cartesian velocity components as the principal unknowns, and a collocated grid arrangement together with Rhie and Chow interpolation. The computational blocks are solved in parallel with Dirichlet-Dirichlet coupling using PVM (parallel virtual machine) or MPI (message passing interface). The parallel efficiency is excellent, with super scalar speed-up for load balanced applications, [19]. The ICFM CFD/CAE grid generator is used for grid generation, and Enight and Matlab are used for post-processing.

Coriolis and centripetal effects are included in the momentum equations when the computational domain is rotating, but the low-Reynolds $k-\omega$ turbulence model of Wilcox [20], which can be integrated all the way to the wall, is used without terms for rotational effects. This is common in turbomachinery computations for reasons of numerical stability and the small impact of such terms in these kinds of industrial applications.

This work investigates the computational results obtained using two different discretization schemes, the hybrid scheme, and the Van Leer scheme. Equations and discretization schemes are described in the following sections.

3.1 Equations. The steady Reynolds time-averaged continuity and Navier-Stokes equations for incompressible flow in a rotating frame of reference read ([21,22])

$$\begin{aligned} \frac{\partial \rho U_i}{\partial x_i} &= 0 \\ \frac{\partial \rho U_i U_j}{\partial x_j} &= -\frac{\partial P}{\partial x_i} + \frac{\partial}{\partial x_j} \left((\mu + \mu_i) \frac{\partial U_i}{\partial x_j} \right) \\ &\quad + \rho g_i - \rho \epsilon_{ijk} \epsilon_{klm} \Omega_j \Omega_l x_m - 2\rho \epsilon_{ijk} \Omega_j U_k \end{aligned}$$

where $-\epsilon_{ijk}\epsilon_{klm}\Omega_j\Omega_l x_m$ is the centripetal term and $-2\epsilon_{ijk}\Omega_j U_k$ is the Coriolis term, owing to the rotating coordinate system. Because of the potential nature of the pressure, gravitational and centripetal terms, [22], they are put together during the computations in what is often referred to as a *reduced* pressure gradient

$$-\frac{\partial P^*}{\partial x_i} = -\frac{\partial P}{\partial x_i} + \rho g_i - \rho \epsilon_{ijk} \epsilon_{klm} \Omega_j \Omega_l x_m.$$

Thus, a relation for the *reduced* pressure is

$$P^* = P - \rho g_i x_i + \rho \epsilon_{ijk} \epsilon_{klm} \Omega_j \Omega_l x_m x_i.$$

In post-processing, the variation of the gravity term is assumed to be negligible and the centripetal term is simply subtracted from the *reduced* pressure.

The $k-\omega$ model of Wilcox [20] for the turbulent kinetic energy, k , and the specific dissipation rate, ω , reads

$$\frac{\partial \rho U_j k}{\partial x_j} = \frac{\partial}{\partial x_j} \left[\left(\mu + \frac{\mu_t}{\sigma_k} \right) \frac{\partial k}{\partial x_j} \right] + P_k - \rho \beta^* \omega k$$

$$\frac{\partial \rho U_j \omega}{\partial x_j} = \frac{\partial}{\partial x_j} \left[\left(\mu + \frac{\mu_t}{\sigma_\omega} \right) \frac{\partial \omega}{\partial x_j} \right] + \frac{\omega}{k} (c_{\omega 1} P_k - c_{\omega 2} \rho k \omega)$$

where the turbulent viscosity, μ_t , is defined as

$$\mu_t = \rho \frac{k}{\omega}$$

The production term reads

$$P_k = \mu_t \left(\frac{\partial U_i}{\partial x_j} + \frac{\partial U_j}{\partial x_i} \right) \frac{\partial U_i}{\partial x_j}$$

and the closure coefficients are given by

$$\beta^* = 0.09, \quad c_{\omega 1} = \frac{5}{9}, \quad c_{\omega 2} = \frac{3}{40}, \quad \sigma_k = 2 \quad \text{and} \quad \sigma_\omega = 2.$$

A no-slip wall boundary condition is applied for the velocities and $k=0$ at the walls. The specific dissipation at the first node normal to the wall (at $y^+ < 2.5$) is set to $\omega = 6\nu / (C_{\omega 2} n^2)$, where n denotes the normal distance to the wall. For the pressure, $\partial^2 P / \partial n^2 = 0$ at all boundaries. Dirichlet boundary conditions are applied at the inlet and Neumann boundary conditions are applied at the outlet for the velocity components and for the turbulent quantities.

3.2 Discretization Schemes. To solve the discretized linear momentum equations, the fluxes through the faces of the computational control volumes must be known. Since all variables are calculated at the nodes, some kind of interpolation must be used to obtain the fluxes through the computational control volume faces. A number of ways of doing this are described in the literature. This work studies the numerical solutions obtained when using the hybrid and the Van Leer [23] discretization schemes. Both discretization schemes are bounded and use upwinding for the convective terms. They are briefly described in the following sections.

3.2.1 The Hybrid Scheme. The hybrid scheme is a combination of the central and the first-order upwind schemes. It uses central differencing if the magnitude of the Peclet number is below two and first-order upwind differencing otherwise, i.e.,

$$\Phi_e = \Phi_P \quad \text{for } U_e > 0 \quad \text{and} \quad |\text{Pe}_e| \geq 2$$

$$\Phi_e = \Phi_E \quad \text{for } U_e < 0 \quad \text{and} \quad |\text{Pe}_e| \geq 2$$

$$\Phi_e = f_e \Phi_E + (1 - f_e) \Phi_P \quad \text{for } |\text{Pe}_e| < 2.$$

The Peclet number reads

$$\text{Pe}_e = \frac{F_e}{D_e}$$

where F_e is the convective mass flux and D_e is the diffusion flux at the computational control volume faces. The factor f_e that appears in the central scheme is a linear interpolation factor that allows the grid to be nonuniform; for uniform grids, $f_e = 0.5$. The hybrid scheme thus uses the first-order upwind scheme if convection is dominant and the central scheme if diffusion is not negligible. The diffusion is discretized using central differencing for $|\text{Pe}_e| < 2$ and is neglected otherwise.

The major drawback of the hybrid scheme is that convection is dominant in most flows, and the scheme can thus be regarded as a first-order upwind scheme.

3.2.2 The Van Leer Scheme. The scheme of Van Leer [23] is of second-order accuracy except at local minima or maxima, where its accuracy is of the first order. One advantage of this scheme is that it is bounded. For the east face, it can be written

$$U_e > 0 \Rightarrow \begin{cases} \Phi_e = \Phi_P & \text{if } |\Phi_E - 2\Phi_P + \Phi_W| \geq |\Phi_E - \Phi_W| \\ \Phi_e = \Phi_P + \frac{(\Phi_E - \Phi_P)(\Phi_P - \Phi_W)}{\Phi_E - \Phi_W} & \text{otherwise} \end{cases}$$

$$U_e < 0 \Rightarrow \begin{cases} \Phi_e = \Phi_E & \text{if } |\Phi_P - 2\Phi_E + \Phi_{EE}| \geq |\Phi_P - \Phi_{EE}| \\ \Phi_e = \Phi_E + \frac{(\Phi_P - \Phi_E)(\Phi_E - \Phi_{EE})}{\Phi_P - \Phi_{EE}} & \text{otherwise} \end{cases}$$

The diffusion is discretized using central differencing.

This scheme is thus a bounded first-order upwind scheme with a correction term, which makes it second-order accurate.

3.3 Convergence, Verification, and Validation. An iteratively converged solution is assumed to have been reached when the largest normalized residual of the momentum equations, the continuity equation and the turbulence equations is reduced to 10^{-3} , [24]. The residuals of the momentum equation are normalized by the sum of the mass flow through the turbine and the mass flow through the periodic surfaces multiplied by the largest velocity component in the computational domain. The residual of the continuity equation is normalized by the sum of the mass flow through the turbine and the mass flow through the periodic surfaces. The residuals of the turbulence equations are normalized by the largest residual during the iterations.

The iteratively converged results of a correctly implemented finite volume method should be conservative with respect to the computed equations. The computational results of the continuity and linear momentum equations have been verified by the method described in this work. The result from this verification corresponds to the iterative convergence limit. The information obtained from the angular momentum balance can not be obtained from the mass or linear momentum balances, however, since the finite volume formulation conserves mass and linear momentum when the residuals are small.

The CALC-PMB CFD code has been extensively validated against the GAMM Francis runner, the Hölleforsen (Turbine 99-II) Kaplan runner, the Hölleforsen distributor and academic test cases, [25]. The code has also been used and validated in other industrial applications, such as: LES of the flow around a simplified bus, LES of a high-lift air foil and heat transfer in gas turbines.

The code uses double precision real numbers to avoid numerical cancellation.

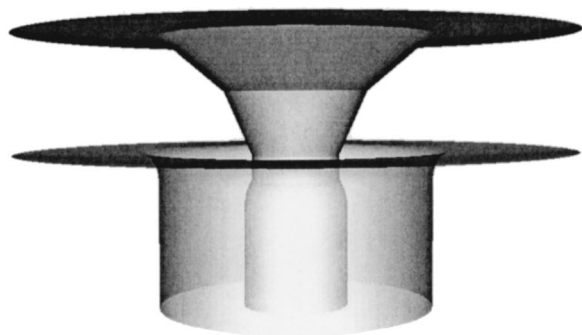
4 Cases

The angular momentum balance method described in the present work is applied to the flow in water turbines. There are numerous types and configurations of water turbines, each optimized for the conditions of the specific power plant. The water turbines studied in this work are low-head Kaplan turbines, which are the most common water turbines in Sweden.

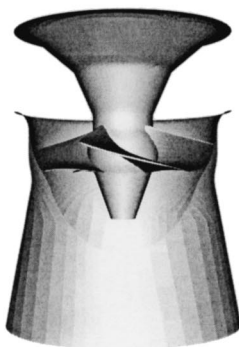
The geometry and flow features in the vicinity of a Kaplan water turbine runner comprises an axisymmetric duct with radial swirling inflow above the runner and axial (ideally nonswirling) flow through a short axisymmetric diffusor below the runner. The angular momentum balance method is applied to two Kaplan runners and a simplified geometry of the axisymmetric duct of one of the Kaplan runners without the runner blades (see Fig. 3).

The cases are briefly described in the following sections.

4.1 Simplified Geometry. Figure 4 shows the meridional contour of the simplified geometry and two computational grids with 14,378 and 31,521 control volumes. The complete geometry is the axisymmetric volume obtained from revolving this geometry around the Z-axis. The grids have different grid density in the through-flow direction and similar grid distributions in the other two directions. There are seven computational control volumes in the periodic direction, covering 10 deg of the total circumference. Periodic boundary conditions are used in the circumferential di-



(a)



(b)



(c)

Fig. 3 The three geometries studied in this work. In all cases the flow is swirling radially inwards at the top and axially downwards at the bottom. (a) The simplified geometry, (b) Kaplan 1, (c) Kaplan 2.

rection. The velocity profile at the inlet is a turbulent 1/7 profile with a swirling component, [24], and the steady axisymmetric flow in the inertial coordinate system is computed.

4.2 Kaplan Runners. Two different Kaplan runners are investigated in the present work. For both cases, the steady flow is computed in a single rotating blade passage employing periodic boundary conditions. Inlet boundary conditions are taken from separate computations of the flow in the upstream guide vane passage.

Detailed information on the first Kaplan runner case (denoted Kaplan 1) can be found in the literature, [24,25], where it is denoted case k15. The simplified geometry in this work is the same as the upper part of the duct of this Kaplan runner, where the error is greatest for the hybrid discretization scheme.

The computational results of the flow in the Hölleforsen Kaplan

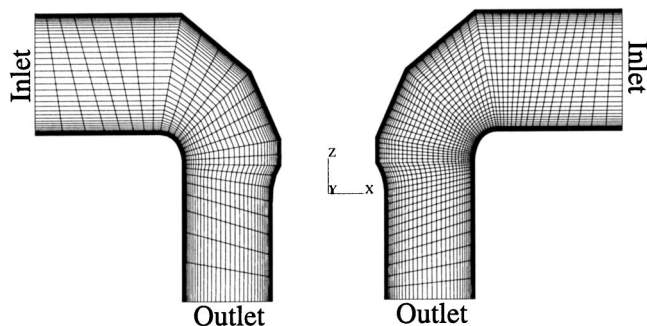


Fig. 4 Meridional view of the coarse (left) and fine (right) grid of the simplified geometry. The grid densities and distributions differ mainly in the through-flow direction.

runner (denoted Kaplan 2) were thoroughly investigated and validated against measurements at the Turbine 99-II workshop. The investigations included in the present work use the computation that was denoted the standard case in the workshop paper, [26], which used the Van Leer discretization scheme. A computation with the hybrid discretization scheme has also been made to show the difference in the angular momentum balance between the two schemes.

Both Kaplan cases include the clearance between the runner blade tips and the shroud, which makes structured multiblock grid generation very complicated.

5 The Angular Momentum Balance Method

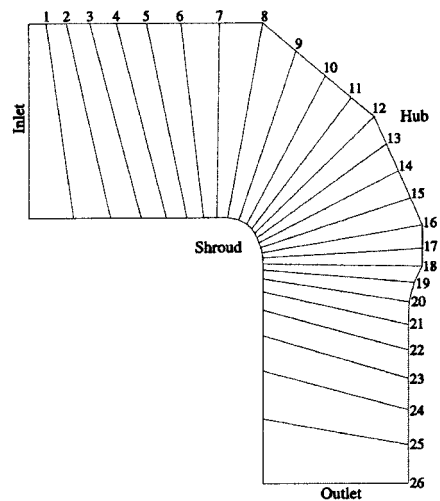
5.1 Implementation. The fundamental idea of the angular momentum balance method is to compute the flux of angular momentum through the computational control volume faces using exactly the same discretization scheme as was used for the flux of linear momentum in the CFD solver (see Section 3.2). It is very important that this implementation is made correctly since small errors in computing the fluxes make it impossible to investigate the balance error. The angular momentum fluxes are used to compute a control volume angular momentum balance error by summing up the flux into the control volume and generation inside the control volume, and normalizing by the flux into the computational domain, i.e., (c.f. Eq. (5))

$$\epsilon = \left(\int_{CS} r F_{s\theta} dA + \int_{CV} r F_{b\theta} dV + \int_{CV} 2r\Omega U_r \rho dV - \int_{CS} r U_{\theta} \rho (\mathbf{U} \cdot \mathbf{n}) dA \right) / \int_{INLET} r U_{\theta} \rho (\mathbf{U} \cdot \mathbf{n}) dA.$$

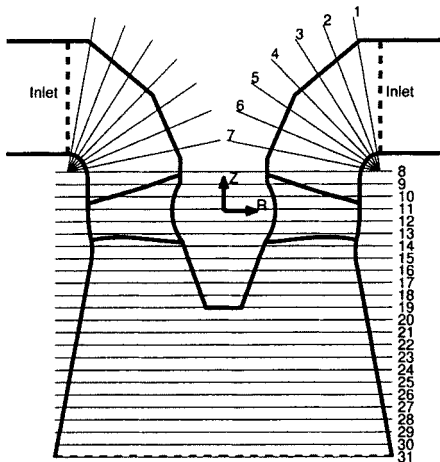
The control volume investigated can be a computational control volume or a control volume that comprises several of the computational control volumes. When computing a balance error over several computational control volumes, a summation of the balance errors over the computational control volumes cancels the fluxes through internal faces, which results in a balance error of the composite control volume.

In the present work the angular momentum balance method is applied to through-flow investigations, [27]. Applying the method between two cross-flow planes (axisymmetric in turbomachine runners) yields the angular momentum balance error between those planes. Placing the first cross-flow plane at the inlet and moving the second cross-flow plane from the inlet to the outlet (from plane 1 to plane 26 in Fig. 5(a)) yields the global angular momentum balance error evolution along the flow path. This can be easily done in the CFD code if there are cross-flow grid planes that can serve as boundaries for the control volumes investigated.

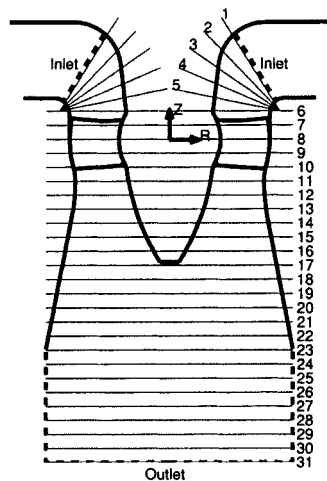
A more general method for summing the balance error over a subdomain of the computational domain is to save the computational control volume balances as an element-based (constant in



(a)

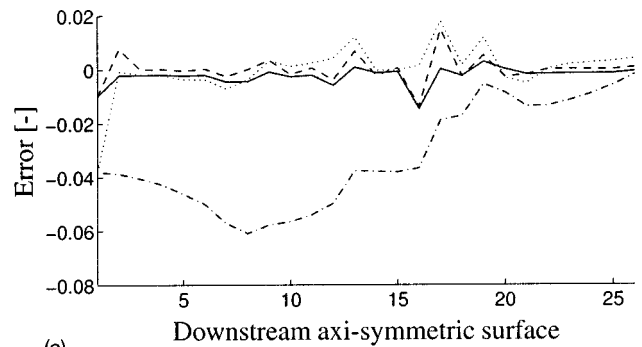


(b)

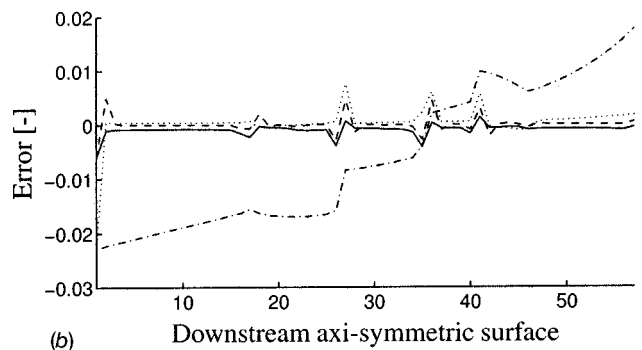


(c)

Fig. 5 Definitions of the cross-flow axisymmetric surfaces. The numbered surfaces (represented by thin lines) are grid surfaces for the simplified case and general control surfaces for the Kaplan cases. (a) The simplified geometry with numbered axisymmetric cross-flow grid surfaces corresponding to the coarse grid. (b) The meridional contour of the Kaplan 1 runner (thick lines). The dashed lines show the computational domain. (c) The meridional contour of the Kaplan 2 runner (thick lines). The dashed lines show the computational domain.



(a)



(b)

Fig. 6 Local and cumulative error distributions from inlet to outlet of the simplified geometry. Dashed line: Van-Leer, local error; dotted line: hybrid, local error; solid line: Van-Leer, cumulative error; dashed-dotted line: hybrid, cumulative error. (a) Coarse grid, (b) fine grid.

each computational control volume) error density, i.e., the balance divided by the volume of the computational control volume. Using a post-processing tool such as Enight, the sum over any subdomain can be derived by an element-based volume integral of the error density over the subdomain. There is then no need for explicit grid planes at the cross-flow surfaces, and they can cut arbitrarily through the geometry (see Figs. 5(b,c)). The only requirements on the post-processing tool are that it can cut out arbitrary parts of the computational domain and compute the volumes of the computational control volumes correctly. The element-based volume integral is then obtained by multiplying the volume of the computational control volume by the local balance, which is constant in each computational control volume. The overall balance and volume of the computational domain were conserved in the analysis by Enight, and the investigation of the simplified geometry gave the same result in both the analysis by the CFD code and in the analysis by Enight. This shows that no significant errors are introduced in the post-processing by Enight.

5.2 Results. Figure 6 shows the local (between two neighboring axisymmetric surfaces) and cumulative (from the inlet) angular momentum balance error distributions from inlet to outlet (see Section 5.1) in the simplified geometry. The overall balance (from inlet to outlet) is obviously not necessarily representative of the accuracy of the computations since the errors in different parts of the domain might cancel each other. The coarse grid hybrid analysis in Fig. 6(a) highlights this problem, where the total error of the domain is small but the error in different subdomains is large.

Both the hybrid and the Van Leer discretization schemes yield small local errors. The cumulative errors show, however, that the hybrid scheme accumulates the local errors while the Van Leer scheme cancels the local errors. Both schemes have problems at

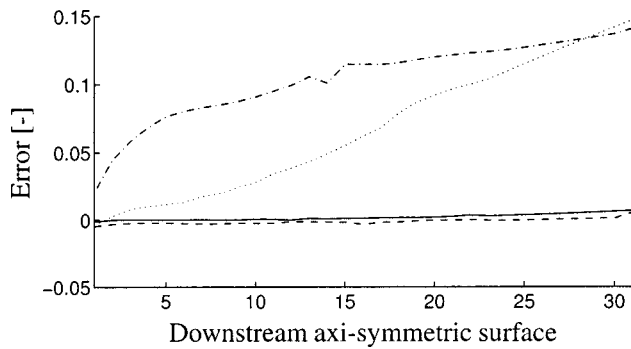


Fig. 7 Cumulative error distributions from inlet to outlet of the Kaplan cases. Dashed line: Van-Leer, Kaplan 1; dashed-dotted line: hybrid, Kaplan 1; solid line: Van-Leer, Kaplan 2; dotted line: hybrid, Kaplan 2.

the inlet and at sharp geometric corners (located at computational control volume planes 8, 12, 16, and 18 for the coarse grid and 17, 26, 35, and 40 for the fine grid).

Figure 7 shows the cumulative angular momentum balance error distributions in the Kaplan runners from inlet to outlet (see Section 5.1). The angular momentum balance method clearly shows the difference between the Van Leer scheme and the hybrid scheme. The hybrid scheme accumulates the local errors while the Van Leer scheme cancels the local errors.

The analysis shows that the hybrid scheme performs worst in the first part of the Kaplan 1 computational domain and best in the first part of the Kaplan 2 computational domain (from the inlet to axisymmetric surface 5).

Table 1 shows the global estimations of the angular momentum balance error, which correspond to the overall cumulative values in Figs. 6 and 7. The global angular momentum balance error of the hybrid scheme are about 30 times larger than that of the Van Leer scheme in the Kaplan cases.

It may seem that a 0.7% angular momentum balance error (Table 1, Van Leer, Kaplan 2) is rather good, but there are at least two reasons why the error should be reduced: (1) the linear momentum is better predicted, (2) water turbine efficiencies are very high (about 95%) and the improvements that can be made are in the range of 0.1% in efficiency. Since the efficiency of water turbines is closely related to the angular momentum balance (see Section 2.1) it is interesting to further investigate the angular momentum balance for the Van Leer scheme. Figure 8 shows iso-surfaces of the largest angular momentum balance error magnitude for the Kaplan 2 Van Leer computations. This gives an indication of where to start the quest for improved results with the Van Leer scheme and the present grid.

6 Conclusion

This work presents a method of investigating the discretization error in swirling flow computations. The method is based on the fact that the discretized angular momentum equations are not necessarily conserved when the discretized linear momentum equations are solved. The method is applied to the first-order hybrid

Table 1 Global angular momentum balance error estimations

Simplified Case	Van Leer		Hybrid	
	Coarse	Fine	Coarse	Fine
Overall balance	$-6.93 \cdot 10^{-4}$	$-4.79 \cdot 10^{-4}$	$-1.92 \cdot 10^{-3}$	$1.77 \cdot 10^{-2}$
Kaplan Cases	Van Leer		Hybrid	
	Kaplan 1	Kaplan 2	Kaplan 1	Kaplan 2
Overall balance	$5.41 \cdot 10^{-3}$	$6.86 \cdot 10^{-3}$	$1.41 \cdot 10^{-1}$	$1.47 \cdot 10^{-1}$

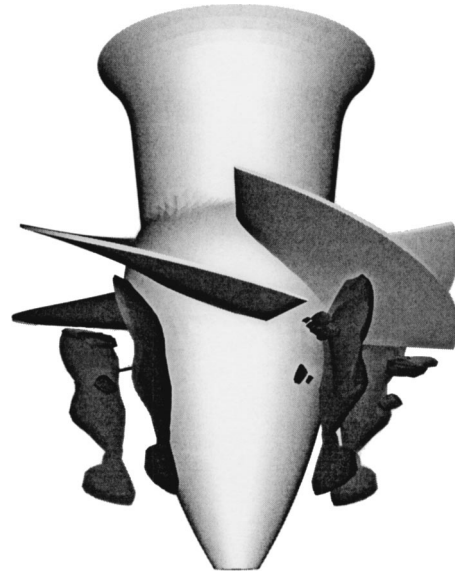


Fig. 8 Iso-surfaces of the absolute value of the computational control volume angular momentum balance indicating where the largest errors are located. The Kaplan 2 case with the Van Leer scheme.

and the second-order Van Leer discretization schemes in swirling flow in water turbines. The angular momentum balance method is applied to through-flow investigations. It is shown that the hybrid scheme cannot be used and that the Van Leer scheme needs improvement to give quantitatively correct results for these kinds of applications. The global angular momentum balance errors of the hybrid scheme are shown to be about 30 times larger than for the Van Leer scheme.

This work has studied only a small part of the angular momentum balance that is important to a single vortex with known features. There are, however, several vortices of unknown features in turbomachinery flow (and most other flows as well) that must also be resolved. A discretization scheme that simultaneously preserves both the linear momentum balance and the *general* angular momentum balance is needed.

Acknowledgments

This work is financed and supported by ELFORSK (Swedish Electrical Utilities Research and Development Company), the Swedish National Energy Administration and GE Energy (Sweden) AB.

GE Energy (Sweden) AB and its staff, particularly Bengt Nauclér, are gratefully acknowledged for information on geometry and support.

Professor F. Avellan and the staff at IMHEF-EPFL in Lausanne are gratefully acknowledged for their influence during the preliminary stages of this work.

The computational resources used at UNICC, Chalmers, are gratefully acknowledged.

References

- [1] Karniadakis, G. E., 2002, "Quantifying Uncertainty in CFD," *ASME J. Fluids Eng.*, **124**, pp. 2–3.
- [2] Mehta, U. B., 1998, "Credible Computational Fluid Dynamics Simulations," *AIAA J.*, **36**(5).
- [3] AIAA, 1994, "Editorial Policy Statement on Numerical Accuracy and Experimental Uncertainty," *AIAA J.*, **32**.
- [4] *Journal of Fluids Engineering*, 1993, "Editorial Policy Statement on the Control of Numerical Accuracy," *ASME J. Fluids Eng.*, **115**.
- [5] Cadafalch, J., Pérez-Segarra, C. D., Cònsul, R., and Oliva, A., 2002, "Verifi-

- cation of Finite Volume Computations on Steady-State Fluid Flow and Heat Transfer," *ASME J. Fluids Eng.*, **124**, pp. 11–21.
- [6] Celik, I., and Zhang, W. M., 1995, "Calculation of Numerical Uncertainty Using Richardson Extrapolation: Application to Some Simple Turbulent Flow Calculations," *ASME J. Fluids Eng.*, **117**, pp. 439–445.
- [7] Roache, P. J., 1998, "Verification of Codes and Calculations," *AIAA J.*, **36**(5).
- [8] Bergström, J., 2000, "Approximations of Numerical Errors and Boundary Conditions in a Draft Tube," *Proceedings from Turbine 99-Workshop on Draft Tube Flow*.
- [9] Bergström, J., and Gebart, R., 1999, "Estimation of Numerical Accuracy for the Flow Field in a Draft Tube," *Int. J. Numer. Methods Heat Fluid Flow*, **9**(4), pp. 472–486.
- [10] Richardson, L. F., 1908, "The Approximate Arithmetical Solution by Finite Differences of Physical Problems Involving Differential Equations, With an Application to the Stresses in a Masonry Dam," *Transactions of the Royal Society of London*, **210**, pp. 307–357.
- [11] Chang, S., and Haworth, D. C., 1997, "Adaptive Grid Refinement Using Cell-Level and Global Imbalances," *Int. J. Numer. Methods Heat Fluid Flow*, **24**, pp. 375–392.
- [12] Haworth, D. C., El Tahry, S. H., and Huebler, M. S., 1993, "A Global Approach to Error Estimation and Physical Diagnostics in Multidimensional Computational Fluid Dynamics," *Int. J. Numer. Methods Heat Fluid Flow*, **17**(1), pp. 75–97.
- [13] Panton, R. L., 1996, *Incompressible Flow*, John Wiley and Sons, New York.
- [14] White, F. M., 1994, *Fluid Mechanics*, 3rd Ed., McGraw-Hill, New York.
- [15] Lakshminarayana, B., 1996, *Fluid Dynamics and Heat Transfer of Turbomachinery*, John Wiley and Sons, New York.
- [16] Krivchenko, G., 1994, *Hydraulic Machines: Turbines and Pumps*, 2nd Ed., CRC Press, Boca Raton, FL.
- [17] Nilsson, H., and Davidson, L., 2000, "A Numerical Comparison of Four Operating Conditions in a Kaplan Water Turbine, Focusing on Tip Clearance Flow," *Proceedings of the 20th IAHR Symposium, Hydraulic Machinery and Cavitation*.
- [18] Van Doormaal, J. P., and Raithby, G. D., 1984, "Enhancements of the SIMPLE Method for Predicting Incompressible Fluid Flows," *Numer. Heat Transfer*, **7**, pp. 147–163.
- [19] Nilsson, H., Dahlström, S., and Davidson, L., 2001, "Parallel Multiblock CFD Computations Applied to Industrial Cases," *Parallel Computational Fluid Dynamics—Trends and Applications*, C. B. Janssen et al., ed., Elsevier, Amsterdam, pp. 525–532.
- [20] Wilcox, D. C., 1988, "Reassessment of the Scale-Determining Equation for Advanced Turbulence Models," *AIAA J.*, **26**(11), pp. 1299–1310.
- [21] Davidson, L., 1997, "An Introduction to Turbulence Models," Internal Report, Thermo and Fluid Dynamics, Chalmers University of Technology, Gothenburg Feb.
- [22] Kundu, P. K., 1990, *Fluid Mechanics*, Academic Press, San Diego, CA.
- [23] van Leer, B., 1974, "Towards the Ultimate Conservative Difference Scheme. Monotonicity and Conservation Combined in a Second Order Scheme," *J. Comput. Phys.*, **14**, pp. 361–370.
- [24] Nilsson, H., 1999, "A Numerical Investigation of the Turbulent Flow in a Kaplan Water Turbine Runner," thesis for the degree of Licentiate of Engineering, May, Department of Thermo and Fluid Dynamics, Chalmers University of Technology, Gothenburg.
- [25] Nilsson, H., 2002, "Numerical Investigations of Turbulent Flow in Water Turbines," thesis for the degree of Doctor of Philosophy, Department of Thermo and Fluid Dynamics, Chalmers University of Technology, Gothenburg.
- [26] Nilsson, H., and Davidson, L., 2001, "A Numerical Investigation of the Flow in the Wicket Gate and Runner of the Hölleforsen (Turbine 99) Kaplan Turbine Model," *Proceedings from Turbine 99 II*.
- [27] Santal, O., and Avellan, F., 1992, "Hydraulic Analysis of Flow Computation Results," *Proceedings of the 16th IAHR Symposium*, **2**, pp. 545–554.

Conservatism of the Grid Convergence Index in Finite Volume Computations on Steady-State Fluid Flow and Heat Transfer

Patrick J. Roache

Consultant, 1215 Apache Drive, Socorro, NM 87801
e-mail: hermosa@swcp.com

This note presents observations on [1] relevant to the evaluation of the adequacy of the conservatism of my grid convergence index (GCI) method of uniform reporting of grid convergence studies for verification of calculations, [2]. This is a timely issue, pertinent to current interest in revised publication standards for JFE in computational fluid dynamics.

The authors, [1], present a uniquely far-ranging application of the GCI. They treat the following seven problems, any one of which would constitute a study worthy of publication: two-dimensional driven cavity (laminar), variants with two-dimensional inclined walls, with five levels of grid refinement; three-dimensional driven cavity (laminar), with four levels of grid refinement; axisymmetric turbulent flow (low $Re\ k-\epsilon$) through a compressor valve, \tanh stretching, zonal refinement, power-law advection differencing, with five levels of grid refinement; three-dimensional premixed methane/air laminar flat flame on a perforated burner, with seven levels of grid refinement; free convection heat transfer from isothermal cylinder in a square duct, three zones, \tanh stretching of body-fitted grid, with five levels of grid refinement; two-dimensional linear advection-diffusion model problem, rotated one-dimensional exact solution, with six levels of grid refinement. Both global and local GCI are calculated. Cartesian staggered and boundary-fitted nonstaggered grids are used, with two numerical schemes (upwind differencing and SMART or power-law differencing). As recommended, [2], when three or more grid solutions are used to calculate an observed rate of convergence p , the authors use GCI with factor of safety $F_s = 1.25$. They test all nodes for monotone or oscillatory convergence (as observed over the grid set used). A global observed p is used in the local GCIs. (Using local p is erratic, [3].) The authors present local observed p and local volume-weighted GCI, deviations from global values, and fraction of nodes that are oscillatory versus (observed) monotone. (Boundary nodes are excluded.) As many as 1/3 of the nodes are determined to be oscillatory. The exact solutions being unknown, the benchmark or reference solutions are those obtained using the highest order method on the finest grid. As in all such exercises, this makes the GCI evaluation less conclusive for the finest grid sequences, but the evaluations from the other grid sequences should not be significantly affected.

Contributed by the Fluids Engineering Division for publication in the JOURNAL OF FLUIDS ENGINEERING. Manuscript received by the Fluids Engineering Division June 25, 2002; revised manuscript received Feb. 3, 2003. Associate Editor: I. Celik.

The authors' conclusions include the following. For the linear model problem with exact solution: "The GCI has predicted the real absolute discretization error for all the studied situations quite well." For all problems: "The certainty of the error band estimators has been checked by comparing its value to the "exact" [reference value, highest-order method on finest grid] absolute error of the numerical solutions, always obtaining very reasonable values."

Here, I summarize some conclusions obtained from examination of the results in [1] which shed light on the question of the conservative (or nonconservative) character of the GCI in the engineering sense. That is, how often is the actual error greater than that banded by the GCI? My stated goal has been the 95% certainty (5% uncertainty, what would be roughly a 2σ error band if the distribution were Gaussian) error band typical of experimentalists, i.e., ~19 out of 20 cases produce $GCI < \text{actual error}$, over an ensemble of CFD problems, including physical problem, grid sequence, and numerical methods. The results are most encouraging for my recommended factor of safety $F_s = 1.25$ for three or more grids. (A more detailed summary is available from the author.)

Briefly, the net result is 14 NC (nonconservative) of 176 entries, or 8.0%. Restricting the count to the SMART algorithm, the net result is 2 NC of 88 entries, or 2.3%. For the UDS algorithm, the net result is 12 NC of 88 entries, or 13.6%. This justifies the claim in [2] and elsewhere that lower order methods are not only less accurate, but their error estimates (and error bands) are less reliable. Neglecting all cases with $p < 1$, which *might* arguably be considered, we would obtain a net 13/127 for 10.2%. It is seen that discarding $p < 1$ cases discards proportionately more conservative results. This probably is due to the fact that p is increasing as convergence is approached, so that the lag effect makes the estimator and error band more conservative. That is, the fine grid calculation has a p larger than the average (observed) p over the three grids.

In summary, from the limited perspective and interest of determining the conservativeness of using the GCI with $F_s = 1.25$, the results of Cadafalch et al. [1] lead to the following conclusions.

1. Confirm that the recommended $F_s = 1.25$ used with three-grid studies to determine the observed p is roughly compatible with the target error band (5% uncertainty).
2. Confirm that UDS is not only less accurate than higher order methods but is less reliable, i.e., the error estimates and error bands are not as reliable (or "credible").
3. Suggest that reliable GCI may be calculated using a global observed p even though as many as ~1/3 of the node values are known to be converging nonmonotonically.
4. Suggest that there is no necessity to discard results with observed $p < 1$, probably because p is increasing as convergence is approached, so that the lag effect makes the estimator and error band more conservative. This leads to excessively conservative GCI for SMART calculations, but this is not an impediment to publication standards. These conclusions from the seven different physical problems computed in Cadafalch et al. agree

with my own experiments on the Burgers equation and with other papers cited in [2], provided that those papers also use careful multigrid studies with experimental determination of observed p .

References

- [1] Cadafalch, J., Pérez-Segarra, C. C., Cónsul, R., and Oliva, A., 2002, "Verification of Finite Volume Computations on Steady State Fluid Flow and Heat Transfer," *ASME J. Fluids Eng.*, **124**, pp. 11–21.
- [2] Roache, P. J., 1998, *Verification and Validation in Computational Science and Engineering*, Hermosa Publishers, Albuquerque, NM.
- [3] Cadafalch, J. 2002, private communication.

Criticisms of the "Correction Factor" Verification Method

Patrick J. Roache

Consultant, 1215 Apache Drive, Socorro, NM 87801
e-mail: hermosa@swcp.com

This note presents criticisms of the verification methods presented in [1,2] and modified in [3]. Therein, the "correction factor" verification procedure of the authors is contrasted to my grid convergence index (GCI) method first presented in [4] and later refined to include a more general factor of safety, [5]. In [1–3] the authors refer to the GCI as the "factor of safety" method, but here I retain the original descriptor, already well established in the literature.

Details and several additional minor points are available from the author.

1 50% Uncertainty

By the authors' design, the correction factor $C_k \rightarrow 1$ as $\Delta x \rightarrow 0$. This means the method reverts to Richardson Extrapolation, which, being the best estimate possible with the available information, produces (by definition) $\sim 50\%$ uncertainty estimate. This violates the intention explicitly stated in [1–3] and shared in [4,5] of achieving a 95% certainty (or 5% uncertainty, what would be roughly a 2σ error band if the distribution were Gaussian). It is a mistake to think that the goal of 95% certainty is appropriate only outside the asymptotic regime; "asymptotic range" does not imply zero error.

2 Use of Theoretical Rather Than Observed Convergence Rate

The authors use "at least three" grid solutions to experimentally determine the order of convergence p , but then often use a theoretical value for the estimated asymptotic p ; this negates the value of performing three-grid studies and determining observed p .

3 Equivalence of the C_k and GCI Methods

The authors' correction factor procedure, [1,2], is in fact equivalent to the GCI method, with a different procedure for choosing the factor of safety. This equivalence has since been acknowledged by the authors in [3]. Unfortunately, as noted under #1, their method gives $\sim 50\%$ uncertainty, which is not acceptable.

4 Claims of Excessive Conservatism of GCI

The authors' claims that the GCI with $F_s = 1.25$ is excessively conservative compared to their own method are not justifiable. In

fact, in two of their own cases, their C_k methods are more conservative than the GCI. (See discussion of Table 3 of [2] on page 807, and discussion of Table 4 of [3] on page 8. In the first case, their correction factor produces an equivalent $F_s = 6.4$, hence the excessive conservatism.) This occurs again for a third problem by Ebert and Gorski [6]. (In this work, the C_k method was excessively conservative compared even to the very conservative GCI using $F_s = 3$ for a minimal two-grid study.) At the very worst, with their uncertainty estimator using $C_k = 1$, the reported GCI using $F_s = 1.25$ would be 25% larger. To put this into perspective, a $C_k = 1$ best estimate for grid convergence of 2% would be reported as a GCI = 2.5%. This is hardly excessive conservatism, and produces something more like the desired 5% uncertainty rather than the $\sim 50\%$ uncertainty of $C_k = 1$.

5 Uncertainty Estimates for the Corrected (Richardson-Extrapolated) Solutions

The authors claim to have extended their own correction factor method and the GCI to cover the case when the corrected (Richardson Extrapolated) solution is actually used as the final solution (rather than RE just being used to estimate the error for the fine grid solution). This extension is not correct in its asymptotic behavior, is grossly unconservative, and ignores my heuristic but more conservative formulation previously suggested two decades earlier, [7]; see Eq. (5.6.4) of [5] and discussion therein. (As L. Eça (pers. comm.) has recently pointed out, that equation is limited to $r = 2, p = 2$.) The poverty of their concept is shown by the fact that, in the asymptotic regime wherein by their design $C_k = 1$, their extensions yield the meaningless uncertainty estimates $U_c = 0$. (Eça and Hoekstra [8] have described the performance of these uncertainty estimates as "a complete fiasco." See also [9].)

Aside from the evident failure of this procedure, the authors have simply claimed that their use of the corrected solution addresses the criticisms of Oberkampf and Trucano [10] by making the treatment of the numerical error stochastic rather than deterministic. This claim is unsupported.

6 Determining Conservatism

Attempts to assess the adequacy of the conservatism of the GCI or the C_k in [1–3] and elsewhere by looking at the "conservatism" of GCI for a single problem miss the point. The only way to assess this is to consider an ensemble of problems, as in [5]. The new data by Cadafalch et al. [11], which covers seven physical problems from laminar planar flows to turbulent axisymmetric flows, are still supportive of the conclusion given in [5] that the GCI method with $F_s = 1.25$ correlates roughly with the desired 5% uncertainty.

7 Apparent Monotone Convergence

The papers [1–3] ignore the possibility that observed monotone grid convergence may only be apparent, due to sampling error. This is common, almost universal practice, and is not much of a criticism, except for the fact that (some of) the same authors elsewhere, [12], have pointed out the possibility. This issue, and more generally nonconstant p , has been addressed seriously only by Eça and Hoekstra [8,9] who use a least-squares approach to evaluate observed p over a minimum of a four-grid set. (Note that more than a three-grid set is required to detect variable observed p .) The unique Eça and Hoekstra method is recommended for noisy data far from the asymptotic regime.

Final Comment

The present criticisms and those given earlier by Oberkampf [13], even if taken at face value, should not detract from the many valuable aspects of the papers [1–3]. These include (a) candid presentation of many numerical details for a real and difficult engineering problem which are often glossed over in similar papers, including issues of maintaining a near-constant grid refine-

Contributed by the Fluids Engineering Division for publication in the JOURNAL OF FLUIDS ENGINEERING. Manuscript received by the Fluids Engineering Division June 25, 2000; revised manuscript received Feb. 3, 2003. Associate Editor: I. Celik.

ment ratio with nonorthogonal boundary-fitted grids, (b) consideration of the interaction of iterative convergence criteria with the grid convergence study, and (c) incorporation of modifications in the validation metric of [14] to include a programmatic tolerance as recommended in [15] and/or validation at E level when $E > U_V$ where E is the discrepancy between simulation and experiment. (See Case 4 of Section 4.1 of [1].)

References

- [1] Stern, F., Wilson, R. V., Coleman, H. W., and Paterson, E. G., 2001, "Comprehensive Approach to Verification and Validation of CFD Simulations—Part I: Methodology and Procedures," *ASME J. Fluids Eng.*, **123**, pp. 793–802.
- [2] Wilson, R. V., Stern, F., Coleman, H. W., and Paterson, E. G., 2001, "Comprehensive Approach to Verification and Validation of CFD Simulations—Part II: Application for RANS Simulation of a Cargo/Container Ship," *ASME J. Fluids Eng.*, **123**, pp. 803–810.
- [3] Wilson, R., and Stern, F., 2002, "Verification and Validation for RANS Simulation of a Naval Surface Combatant," AIAA Paper No. 2002-0904.
- [4] Roache, P. J., 1993, "A Method for Uniform Reporting of Grid Refinement Studies," *Quantification of Uncertainty in Computational Fluid Dynamics*, I. Celik, C. J. Chen, P. J. Roache, and G. Scheurer, eds., ASME, New York, ASME FED-Vol. 158, pp. 109–120.
- [5] Roache, P. J., 1996, *Verification and Validation in Computational Science and Engineering*, Hermosa Publishers, Albuquerque, NM.
- [6] Ebert, M. P., and Gorski, J. J., 2001, "A Verification and Validation Procedure for Computational Fluid Dynamics Solutions," NSWCCD-50-TR-2001/0006, Hydromechanics Directorate Report, NSWC, Carderock Division, West Bethesda MD.
- [7] Roache, P. J., 1982, "Scaling of High Reynolds Number Weakly Separated Channel Flows," *Numerical and Physical Aspects of Aerodynamic Flows*, T. Cebeci, ed., Springer-Verlag, New York, pp. 87–98.
- [8] Eça, L., and Hoekstra, M., 2000, "An Evaluation of Verification Procedures for Computational Fluid Dynamics," IST Report D72-7, Instituto Superior Tecnico (Lisbon), June 2000.
- [9] Eça, L., and Hoekstra, M., 2002, "An Evaluation of Verification Procedures for CFD Applications," 24th Symposium on Naval Hydrodynamics, Fukuoka, Japan, July 8–13.
- [10] Oberkampf, W. L., and Trucano, T. G., "Validation Methodology in Computational Fluid Dynamics," AIAA Paper No. 2549.
- [11] Cadafalch, J., Pérez-Segarra, C. C., Cónsul, R., and Oliva, A., 2002, "Verification of Finite Volume Computations on Steady State Fluid Flow and Heat Transfer," *ASME J. Fluids Eng.*, **124**, pp. 11–21.
- [12] Coleman, H. W., Stern, F., Di Mascio, A., and Campana, E., 2001, "The Problem With Oscillatory Behavior in Grid Convergence Studies," *ASME J. Fluids Eng.*, **123**, pp. 438–439.
- [13] Oberkampf, W. L., discussion, and Coleman, H. W., and Stern, F., 2002, authors' closure, *ASME J. Fluids Eng.*, **124**, pp. 809–811.
- [14] Coleman, H. W., and Stern, F., 1997, "Uncertainties in CFD Code Validation," *ASME J. Fluids Eng.*, **119**, pp. 795–803.
- [15] Roache, P. J., discussion, and Coleman, H. W., and Stern, F., 1998, authors' closure, *ASME J. Fluids Eng.*, **120**, pp. 635–636.

Some Observations on Uncertainties and the Verification and Validation of a Simulation

Hugh W. Coleman

Professor, Propulsion Research Center, Mechanical and Aerospace Engineering Department, University of Alabama in Huntsville, Huntsville, AL 35899
e-mail: coleman@mae.uah.edu. Fellow ASME

In this note, my objectives are to clarify the ideas in a previously published quantitative verification and validation (V&V) approach that is based on experimental uncertainty analysis concepts; to suggest a new viewpoint (and nomenclature) for assessment of the results of V&V efforts; and to discuss an inherent ambiguity in the interpretation of results of grid refinement studies that are used in verification approaches.

[DOI: 10.1115/1.1588694]

Contributed by the Fluids Engineering Division for publication in the JOURNAL OF FLUIDS ENGINEERING. Manuscript received by the Fluids Engineering Division July 8, 2002; revised manuscript received Feb. 9, 2003. Associate Editor: I. Celik.

To my knowledge, the only published verification and validation (V&V) approach, [1–3], for computational mechanics simulations that produces quantitative validation results is based on the concepts and definitions used in experimental uncertainty analysis. Since these are generally not familiar to those who have no occasion to apply experimental uncertainty analysis in their work, I have noted a number of misconceptions in V&V discussions in papers, articles, and reports in the past several years. My objectives in this note are to clarify the ideas in this quantitative V&V approach; to suggest a new viewpoint (and nomenclature) for assessment of the results of V&V efforts; and to discuss an inherent ambiguity in the interpretation of results of grid refinement studies that are used in verification approaches.

Verification and Validation (V&V) From an Experimental Uncertainty Analysis Perspective

The schematic in Fig. 1 shows my view of the V&V process from the perspective of the definitions and concepts used in experimental uncertainty analysis, [4–6]. The sources of errors are shown in the ovals, and the corresponding symbols for the errors (δ) and the uncertainties (U) are indicated adjacent to them. Pertinent definitions are, [5,6]: (A) error (of measurement): result of a measurement minus a true value of the measurand; and (B) uncertainty (of measurement): parameter, associated with the result of a measurement, that characterizes the dispersion of the values that could reasonably be attributed to the measurand (also, from the 1984 first edition of [6]: an estimate characterizing the range of values within which the true value of a measurand lies). As first presented by Coleman and Stern [1], these concepts were extended to apply to a simulation result as well as an experimental result, and the definitions include both random errors/uncertainties and systematic errors/uncertainties (which are the type affecting the simulation result in most instances).

The "truth" is the real value of a quantity of interest defined by the observer and, as pointed out by a reviewer, is an abstraction. As an example for this note, define the reality of interest (the truth) as the drag force on a perfectly made, perfectly smooth specific aircraft model suspended without support in a uniform, infinite flow of specified velocity of a designated fluid at designated thermodynamic conditions, etc. This truth is independent of experiment or simulation; however, incomplete definition of the quantity gives rise to an additional uncertainty, [5]. (As discussed later, in the special case of the experiment as run being defined as the reality of interest, the truth is obviously not independent of the experiment.)

In the Coleman and Stern V&V approach [1–3,7], we defined three categories into which all of the errors (δ) in a simulation result, S , were assigned. The categories are those errors (δ_{SMA}) due to modeling assumptions, those (δ_{SPD}) due to the use of previous experimental data (which contains errors), and those (δ_{SN}) due to the numerical solution of the equations. The corresponding uncertainties are designated U_{SMA} , U_{SPD} , and U_{SN} , respectively, and are interpreted such that the interval $\pm U_{SN}$ (for example) contains δ_{SN} 95 times out of 100.

Examples of possible contributors to U_{SMA} are uncertainties due to the turbulence model used and those due to assumptions of incompressibility, two-dimensionality, etc.

Contributors to U_{SPD} are the uncertainties in code inputs such as material properties. To estimate U_{SPD} for a case in which the simulation uses previous data d_i in m instances, [1], one must evaluate

$$U_{SPD}^2 = \sum_{i=1}^m \left(\frac{\partial S}{\partial d_i} \right)^2 (U_{d_i})^2 \quad (1)$$

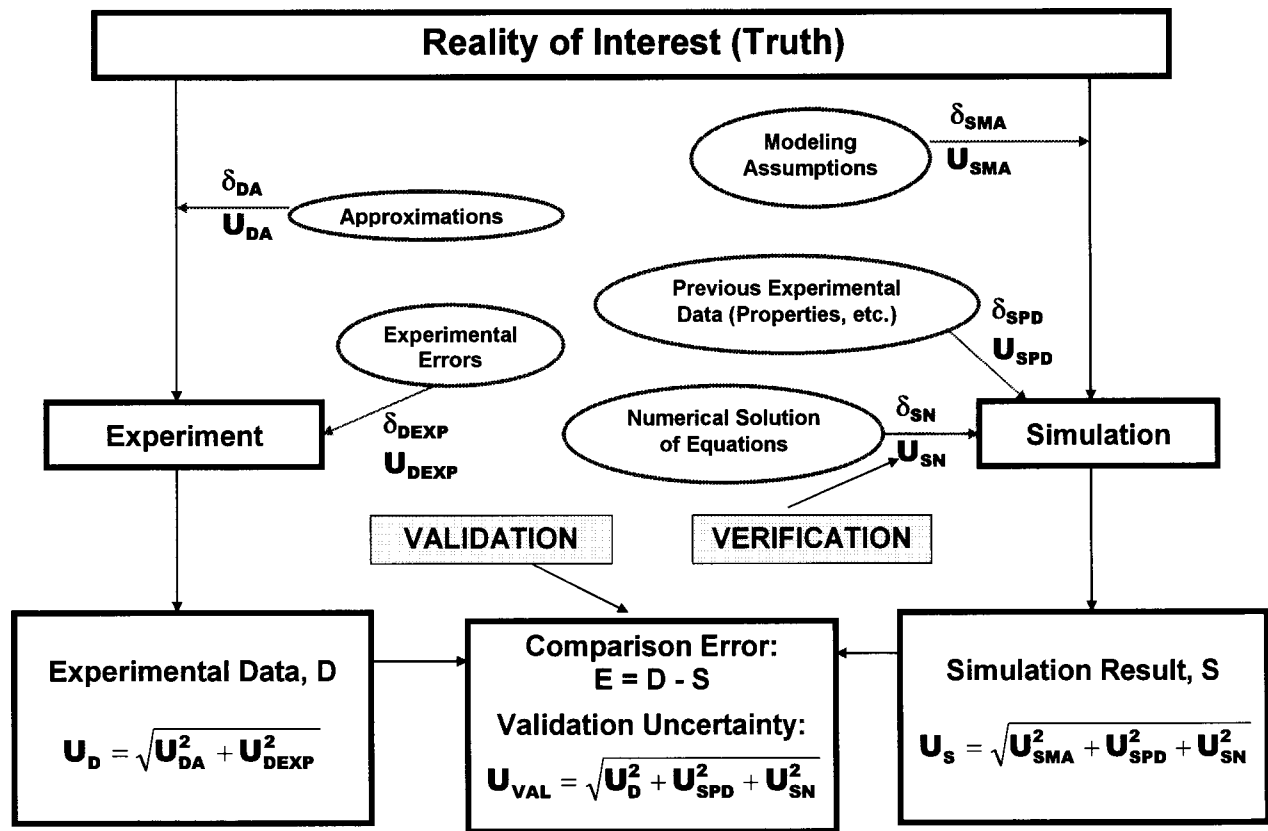


Fig. 1 A view of the verification and validation process (sources of error shown in ovals)

where the U_{d_i} are the uncertainties in the input data. Note that a sensitivity coefficient must be determined for each d_i —in complex cases (with combustion and heat transfer, for example) this might require more resources than those required by multigrid convergence studies.

For U_{SN} , an important contributor is usually the uncertainty arising from the size and type of grid used in solving the discretized equations, along with other contributors such as iterative convergence, etc.

The experimental result is D , and its associated uncertainty U_D is estimated using experimental uncertainty analysis procedures that have been well established, [4,5]. U_D is the uncertainty estimate appropriate for D —it includes all effects of averaging, includes all random and systematic uncertainty components, and includes any correlations of errors/uncertainties (nonzero covariances) and any other factors that influence D and U_D . In some instances, [8–10], D and U_D have mistakenly been assumed as pertaining to a single experimental result or measurement and not including the possibility of averaged results or systematic errors/uncertainties or correlated uncertainty effects—leading then to a misinterpretation of the basic ideas in the approach, [1–3].

In the schematic, I have divided the errors in D into categories of (1) errors δ_{DA} due to the actual experiment approximating the reality of interest (truth) and (2) experimental errors δ_{DEXP} occurring in the actual test as it is constructed and executed. The corresponding uncertainties are designated U_{DA} and U_{DEXP} . If the aircraft model is tested in a wind tunnel, then the uncertainty in D arising from effects of the finite extent, nonuniform flow in the actual experiment could be assigned to the U_{DA} category, while the uncertainty in the simulation due to actually solving the equations on a finite domain would be assigned to the U_{SMA} category. Uncertainty due to measurement error is one of the contributors to the U_{DEXP} category.

If truth is defined as the drag force on the model *in the experiment as run*, then $U_{DA}=0$ and the “Experiment” and “Reality of Interest” boxes in the figure are one and the same. This is the only case in which the experiment as run and the defined “truth” are the same. As pointed out by Roache [12], in the sense used here the experiment is always a reality but is not always the reality of interest.

Three metrics (E , U_{VAL} , and U_{reqd}) are used in the Coleman and Stern V&V approach, [1–3,7]. The comparison error E is the difference between the experimental result D and the simulation result S —it is the resultant of all of the errors that influence D and S . The validation uncertainty U_{VAL} (originally designated U_V) is the combination of all of the experimental uncertainties (U_D) and the uncertainties in the simulation due to the use of previous experimental data (U_{SPD}) and due to the numerical solution of the equations (U_{SN}). U_{VAL} can be viewed as the noise level imposed by all of the uncertainties in D and those uncertainties in S due to the use of previous experimental data and due to the numerical solution of the equations—this means that E would lie in the range $\pm U_{VAL}$ 95 times out of 100 if $\delta_{SMA}=0$. Thus, if $|E| \gg U_{VAL}$ then the sign and magnitude of E can be taken as indicative of the modeling error δ_{SMA} . On the other hand if $|E| < U_{VAL}$ or $|E| \approx U_{VAL}$, then from an uncertainty point of view nothing definitive can be concluded about the sign or magnitude of δ_{SMA} (other than observing that the combination of δ_{SMA} with all of the other errors is less than U_{VAL}).

(I know of no way of estimating U_{SMA} (or δ_{SMA}) before implementation of the validation process, so the U_s in Fig. 1 cannot be estimated a priori.)

The third metric U_{reqd} is the level of validation required from a programmatic standpoint. If, for example, one must be able to compute the drag force to within 1% for the simulation to be useful in a design process, then $U_{reqd}=1\%$. The V&V process

does not require specification of a value for U_{reqd} , but if a value of U_{reqd} is known it can be used to establish maximum allowable uncertainties during the planning and design of the validation experiment.

An alternate viewpoint and approach to V&V, [8,9,11], uses the definitions: “Uncertainty: A potential deficiency in any phase or activity of the modeling process that is due to lack of knowledge” and “Error: A recognizable deficiency in any phase or activity of modeling and simulation that is not due to lack of knowledge.” Use of these definitions to estimate uncertainties or to achieve quantification of the result of a V&V effort has not yet been published.

Comments on the Assessment of V&V Results

Definitions of verification that are in current use are: “verification is the process of determining that a model implementation accurately represents the developer’s conceptual description of the model and the solution to the model,” [8,9,11], and “verification is defined as a process for assessing simulation numerical uncertainty . . .,” [7]. Definitions of validation that are in current use are: “validation is defined as the process of determining the degree to which a model is an accurate representation of the real world from the perspective of the intended uses of the model,” [8,9,11], and “validation is defined as a process for assessing simulation modeling uncertainty by using benchmark experimental data and, when conditions permit, estimating the sign and magnitude of the modeling error itself.” [7]. (The words “from the perspective of the intended uses of the model” should be interpreted, [12], as referring to the variable(s) and set point chosen for the validation effort—a different interpretation of the phrase than had been made previously by myself and others.)

More succinct but conceptually descriptive definitions were given by Roache [13]: verification—solving the equations right; and validation—solving the right equations. These can be paraphrased in a syntax similar to the definitions in the previous paragraph: Verification is the process of assessing how correctly the equations are solved; and validation is the process of assessing how closely the equations model the reality of interest.

The verification process does not require nor use experimental data and can be performed in the absence of a validation effort. The validation process does require experimental data with which simulation results can be compared, and, as formulated in [1] and viewed in Fig. 1, completion of the validation process also requires that verification has been performed and an estimate of U_{SN} has been made.

In recent V&V efforts, [1–3,7–9,11,13,14], for example], workers in the area (myself included) have used phraseology indicating that a simulation or code had been or had not been “validated” or that validation had been or had not been “achieved.” In the original Coleman and Stern publication, [1], we proposed to call a simulation validated or not validated based on the relative magnitudes of E and U_{VAL} . I now believe that a more logical interpretation that is consistent with the meanings of the definitions in the preceding paragraphs is the following.

A validated simulation is simply one that has undergone the validation process. As a result of that process, a level of validation (the larger of $|E|$ and U_{VAL}) is established for a variable at a given set point, and that level is independent of whether a U_{reqd} is specified or not. The phrase “validated simulation” is thus not an indicator of the degree of goodness of the simulation.

The validation uncertainty U_{VAL} sets the best (tightest, lowest) level of validation possible under the circumstances that exist, so it must be estimated if any informed statement about the level of validation is to be made. If $|E|$ is less than U_{VAL} then the level of validation can be said to be U_{VAL} but not $|E|$, since $|E|$ is below the noise level set by the existing uncertainties. If $|E|$ is

greater than U_{VAL} then the level of validation is $|E|$. So, in a sense, a validation effort can be considered successful if $|E|$ and U_{VAL} are determined, regardless of their values. As a result of the validation effort, one knows “how good” the simulation is (for particular variables and for a particular set point, of course). Whether or not the result of the effort is good enough is influenced by U_{reqd} and is considered by some to be a part of certification rather than validation, [12].

The Ambiguity Problem in Grid Refinement Studies

Grid refinement studies have been and continue to be used and/or cited, [7–9,11,13,14], for example] as a means to demonstrate convergence and assess the numerical uncertainty U_{SN} . In [15], however, it was shown that grid refinement studies can erroneously indicate monotonic convergence when the real (but unknown) behavior is actually oscillatory. In fact, monotonic convergence can also be indicated when the real (but unknown) behavior is oscillatory divergence. To use results of a three-grid refinement study to show monotonic convergence, one must assume a priori that the real behavior is monotonic convergence. Monotonic convergence indications from refinement studies using four or more grids may make one feel more confident, but in principle the ambiguity still remains.

I suggest that as results of grid refinement studies are used in the future to evaluate convergence and assess U_{SN} , the ambiguity must at least be acknowledged to exist when results are reported. I also think that this ambiguous trait inherent in grid refinement methods emphasizes the need for development of other defensible, economically feasible approaches for demonstrating convergence and estimating U_{SN} as we strive to develop V&V approaches that can actually be useful in science and engineering applications.

References

- [1] Coleman, H. W., and Stern, F., 1997, “Uncertainties in CFD Code Validation,” *ASME J. Fluids Eng.*, **119**, pp. 795–803.
- [2] Roache, P. J., 1998, discussion *ASME J. Fluids Eng.*, **120**, p. 635.
- [3] Coleman, H. W., and Stern, F., 1998, authors’ closure, *ASME J. Fluids Eng.*, **120**, pp. 635–636.
- [4] Coleman, H. W., and Steele, W. G., 1999, *Experimentation and Uncertainty Analysis for Engineers*, 2nd Ed., John Wiley & Sons, New York.
- [5] *Guide to the Expression of Uncertainty in Measurement* (corrected and reprinted, 1995), International Organization for Standardization, Geneva, Switzerland.
- [6] *International Vocabulary of Basic and General Terms in Metrology*, 1993, 2nd Ed., International Organization for Standardization, Geneva, Switzerland.
- [7] Stern, F., Wilson, R. V., Coleman, H. W., and Paterson, E. G., 2001, “Comprehensive Approach to Verification and Validation of CFD Simulations—Part 1: Methodology and Procedures,” *ASME J. Fluids Eng.*, **123**, pp. 793–802.
- [8] Oberkampf, W. L., and Trucano, T. G., 2000, “Validation Methodology in Computational Fluid Dynamics,” AIAA Paper No. 2000–2549.
- [9] Oberkampf, W. L., and Trucano, T. G., 2002, “Verification and Validation in Computational Fluid Dynamics,” Sandia National Laboratories Report SAND2002-0529, Mar.
- [10] Oberkampf, W. L., 2002, discussion, *ASME J. Fluids Eng.*, **124**, pp. 809–810.
- [11] *Guide for the Verification and Validation of Computational Fluid Dynamics Solutions*, 1998, AIAA Guide G-077-1998 (www.aiaa.org).
- [12] Roache, P. J., 2002, private e-mail communications.
- [13] Roache, P. J., 1998, *Verification and Validation in Computational Science and Engineering*, Hermosa, Albuquerque, NM (www.hermosa-pub.com/hermosa)
- [14] Wilson, R., and Stern, F., 2002, “Verification and Validation for RANS Simulation of a Naval Surface Combatant,” AIAA Paper No. 2002-0904.
- [15] Coleman, H. W., Stern, F., Di Mascio, A., and Campana, Emilio, 2001, “The Problem With Oscillatory Behavior in Grid Convergence Studies,” *ASME J. Fluids Eng.*, **123**, pp. 438–439.

Water Hammer Phenomena in Gas-Water Two-Phase Bubbly Flow Through a 90-Degree Bend Tube

Wang Shuli

Li Zhuo

Department of Mechanical Engineering,
Jiangsu Institute of Petrochemical Technology, Jiangsu,
People's Republic of China

1 Introduction

The water hammer phenomena caused by a sudden valve closure in gas-liquid or vapor-liquid two-phase flows must be clarified for the safety analysis in chemical plants, power plants, and pipeline transport of fluids such as petroleum and natural gas. It is well known that when a valve is closed suddenly, the upstream pressure rises sharply owing to the inertia of the fluid and the pressure wave propagates through the fluid, which causes transient flows through a straight pipe have been investigated in detail for many years, [1,2]. There are none on such a gas-liquid two-

phase flow through a 90 deg bend pipe that must be common in the pipeline system. This investigation is intended to make it clear.

In general, the factors affecting the flow characteristics of the water hammer through a 90 deg bend pipe such as pressure potential surge and propagation speed are as follows: superficial velocity, void fraction, and valve closing time.

The experiments were conducted in a horizontal tube of 25.4 mm in inner diameter and 2.5 in ratio of the curvature radius to the inner diameter of the bend tube in the ranges of superficial velocity j_L from 0.2 to 1.64 m/s and of void fraction from 0.036% to 0.96%, using air and water as the working fluid under the general temperature. The profiles of transient pressure, the value of potential surge and its attenuation, and propagation velocity of the compression waves were obtained and discussed, comparing them with those in single-phase water flow.

2 Experimental Apparatus and Procedure

The schematic diagram of the experimental apparatus is shown in Fig. 1 and Fig. 2. It is composed of a horizontal test tube (5), a sudden closure valve (6), downstream and upstream tanks (3,8), with size $2.0 \times 0.8 \times 0.8 \text{ m}^3$, a circulation pump (1), a laser source with lens assembly, a CCD camera to measure the void fraction α . The sudden closure valve (6) was a ball valve. The duration of valve closure was about 14 ms.

For two-phase flow, the propagation speed of compression wave in uniform bubbly flow is given by the following equation, [3]:

$$C_{TP} = \left\{ \frac{1}{\left[\alpha^2 + \alpha(1-\alpha) \frac{\rho_L}{\rho_g} \right] + \left[(1-\alpha)^2 + \alpha(1-\alpha) \frac{\rho_g}{\rho_L} \right] \frac{\Delta p_{TP}}{\rho_g C_L^2}} \cdot \frac{\Delta p_{TP}}{\rho_g} \right\}^{1/2} \quad (1)$$

where Δp_{TP} is the magnitude of the initial maximum pressure rise (that is, potential surge).

To observe the flow pattern and measure the void fraction α with PIV, a 50-cm glass pipe in length was installed in the pipeline (Fig. 1, (7)).

The experimental procedure was as follows. The pressure, the flow rate, and the air input were set to five values for a steady-state. Next, after closing the end valve (6) suddenly and operating the solenoid valves (2 and 9), the pressures p_1 to p_{10} were measured. The pressures were recorded on an oscillograph (SC20/16) via a strain-gauge-type pressure transducer and an amplifier which links with a microcomputer. In this study, void fraction α were measured using the particle image velocimetry (PIV) system developed by Chen and Fan [4]. This PIV technique consists of laser sheeting, video recording, and image processing as the three major parts. It is able to measure the full-field flow information including void fraction, velocity vectors, and acceleration, [5].

3 Experimental Results

3.1 The Pressure Rise in Single-Phase Flow. First experiments on the water hammer in the liquid single-phase flow were carried out to verify the experimental accuracy and to compare it

with the case of two-phase flows at a constant initial temperature of about 18° C and an initial superficial water velocity of j_L from 0.23 m/s to 1.64 m/s. At the locations 1, 2, 5, 6, 7, 10 shown in Fig. 2, the initial potential surge Δp_{SP} agrees well with the results calculated by Joukowsky's equation:

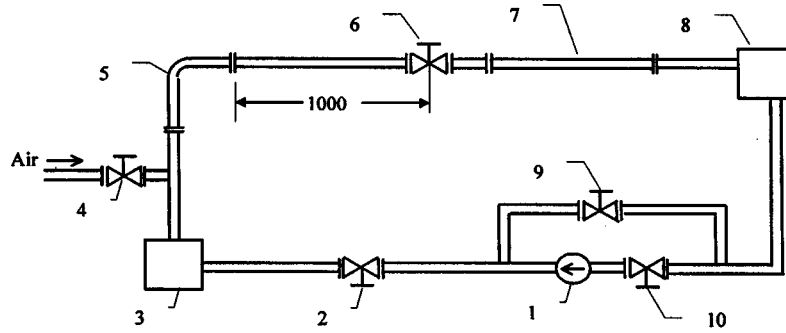
$$\Delta p_{SP} = c_L \rho_L j_L \quad (2)$$

where c_L is the propagation speed of the pressure wave in the water, ρ_L is working fluid density, and j_L is the superficial liquid velocity. In the bend tube, the initial potential surge using the following equation:

$$\Delta p_{SP} = c_L \rho_L j_L (1 + \lambda j_L) \quad (3)$$

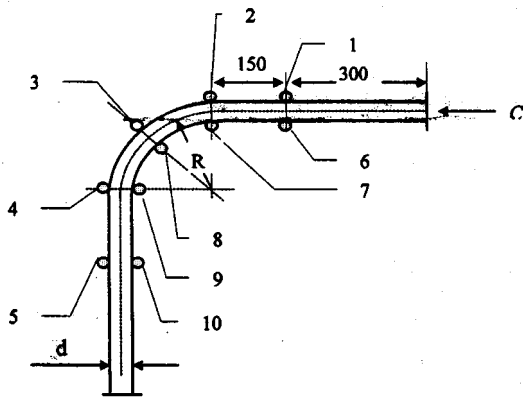
Coefficient λ is relevant with the locations in the bend tube, and at location 3, $\lambda = 0.072$, and at the location 8, $\lambda = -0.056$. The pressure wave through a bend tube, on the centrifugal effect, the initial potential surge is obviously different.

Contributed by the Fluids Engineering Division for publication in the JOURNAL OF FLUIDS ENGINEERING. Manuscript received by the Fluids Engineering Division Sept. 26, 2001; revised manuscript received Jan. 7, 2003. Associate Editor: Y. Matsumoto.



1- Pump 2,4,6,9,10-Valves 3,8 -Water Tank 5 -Test section(bend tube) 7- Glass Pipe

Fig. 1 Schematic of experimental facility



1 to 10 Pressure transducer of strain gauge type, $R/d=2.5$

Fig. 2 Schematic of the test section

3.2 The Potential Surge in Two-Phase Flow

3.2.1 Effect of Void Fractions and Superficial Liquid Velocities. Experiments were conducted for void fractions were 0.035% to 0.96% under a constant temperature of 18°C, superficial liquid velocities were in the range from 0.2 m/s to 1.63 m/s ($\alpha=0.16\%$, -0.85%).

The initial pressure rise at locations 1 and 2 can be calculated with the following equation:

$$\Delta p_{TP} = C_{TP} \rho_{TP} j_{TP} \quad (4)$$

where C_{TP} is the propagation speed of the pressure wave as given by Eq. (2), ρ_{TP} is the mean density of two-phase flow $\{\approx(1-\alpha)\rho_L\}$, and j_{TP} is the mean velocity of two-phase flow $\{\approx j_L/(1-\alpha)\}$.

The initial pressure rise in bend pipe is correlated by the following equation:

$$\Delta p_{TP} = C_{TP} \rho_{TP} j_{TP} (1 + \kappa j_{TP}). \quad (5)$$

Coefficient κ is only relevant with the locations in the bent tube, and at the location 3 $\kappa=0.058$, at the location 8, $\kappa=-0.042$.

3.2.2 Attenuation of the Potential Surge. The initial pressure rise Δp_{PS} caused by a sudden valve closure decreased through a 90 deg bend tube. The attenuating rate φ ($\varphi = \Delta p_{TP} / \Delta p_{SP}$) with void fraction is correlated by

$$\varphi = 0.987 - 0.274\alpha^{0.558}. \quad (6)$$

4 Conclusions

The water hammer phenomena caused by a rapid valve closure in a two-phase flow were investigated experimentally using air and water as working fluids. The results are summarized as follows:

- The profile of the pressure transients is characterized by the existence of a sharp initial pressure rise and the value of potential surge at location 3 (Fig. 2) is bigger than the value of potential surge at location 1 or 2 (inlet), and the value of potential surge at the location 8 is less than the value of potential surge at the location 1 or 2.
- In a straight line, the potential surge can be calculated using Eq. (2) for single-phase flow and Eq. (4) for two-phase flow. In the bend pipe Eq. (3) can be used for single-flow, and Eq. (5) for two-phase flow.
- The value of the attenuating rate φ can be calculated by Eq. (6)
- That can be figured out the effect of the curvature radius of a bend tube on the pressure rise is prominent. Under the same conditions, the smaller the curvature radius of the bend tube, the bigger the pressure rise.

Nomenclature

- j = superficial velocity (m/s)
- c = propagation speed of compression wave (m/s)
- Δp = potential surge (Pa)
- ρ = density (kg/m^3)
- α = void fraction
- φ = decayed rate of potential surge
- TP = two-phase flow
- SP = single phase flow
- L = liquid phase

References

- [1] Akagawa, K., Fujii, T., Ito, Y., and Yamaguchi, T., 1982, "Studies on Shock Phenomena in Two-Phase Flow," *Bull. JSME*, **25**, pp. 387-394.
- [2] Fujii, T., and Akagawa, K., 1985, "An Analysis of Water Hammer Phenomena in Bubbly Flow," *ASME*, New York, *ASME-FED-29*, pp. 147-154.
- [3] Hsu, Y. Y., and Graham, R. W., 1976, *Transport Processes in Boiling and Two-Phase System*, McGraw-Hill, New York.
- [4] Chen, R. C., and Fan, L. S., 1992, "Particle Image Velocimetry for Character the Flow Structure in Three-Dimensional Gas-Liquid-Solid Fluidized Beds," *Chem. Eng. Sci.*, **47**, pp. 3615-3620.
- [5] Bachalo, W. D., 1994, "Experimental Methods in Multiphase Flow," *Int. J. Multiphase Flow*, **20**, pp. 261-295.

On the Linear Encroachment in Two-Immiscible Fluid Systems in a Porous Medium

Kambiz Vafai

Department of Mechanical Engineering, University of California, Riverside, Riverside, CA 92521.
Fellow ASME

Bader Alazmi

Department of Mechanical Engineering, The Ohio State University, Columbus, OH 43210. Mem. ASME

A careful review to the previous study of Srinivasan and Vafai on the linear encroachment in two-immiscible fluid systems in a porous medium reveals some typos in their analytical solution. In the present study, an accurate analytical solution, which accounts for boundary and inertia effects, is obtained to predict the movement of the interfacial front and corrections to previous results are provided wherever necessary. Despite the similarity in the general behavior of the present accurate solution and the previous one, the existence of an accurate analytical solution is essential for future numerical and experimental studies.

[DOI: 10.1115/1.1588696]

Introduction

Linear encroachment of two-immiscible fluid systems is an important problem in many engineering applications such as die filling and injection molding. Muskat [1] considered a one-dimensional Darcy's flow model to study the linear encroachment of two fluids in a narrow channel. An analytical solution for linear encroachment in two-immiscible fluid systems in a porous material was presented in Srinivasan and Vafai [2] where boundary and inertia effects are accounted for. It is found that using this analytical solution is required in the vicinity of solid boundaries and/or faster moving flows where Muskat's model fails to predict the necessary time for the encroaching fluid to completely displace the second fluid. In addition, Srinivasan and Vafai [2] show that implementing their analytical solution is essential for cases of low mobility ratio as well as higher values of permeability.

A schematic diagram of the flow configuration and the coordinate system is shown in Fig. 1. Governing equations and boundary conditions for the problem under consideration are provided in Srinivasan and Vafai [2]. Unfortunately a small typo in the exact solution caused a deflection in some of the results. The purpose of this note is to correct these typos and adjust the dependent results accordingly.

Results

The same procedures used in [2] are used here to correct the analytical solution. As mentioned earlier, all governing equations and boundary conditions given in [2] are correct. The first typo is found in Eq. (21), which should read as follows:

$$u_D = \frac{K_1}{\mu_1} \frac{P_{in} - P_e}{(1 - \epsilon)X_0^M - L} \quad (1)$$

Contributed by the Fluids Engineering Division for publication in the JOURNAL OF FLUIDS ENGINEERING. Manuscript received by the Fluids Engineering Division Jan. 6, 2003; revised manuscript received Jan. 12, 2003. Associate Editor: J. Katz.

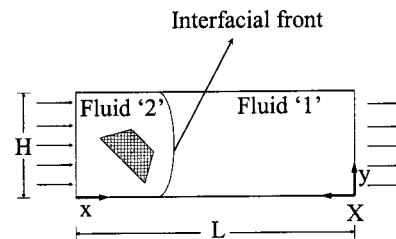


Fig. 1 Schematic diagram of the problem

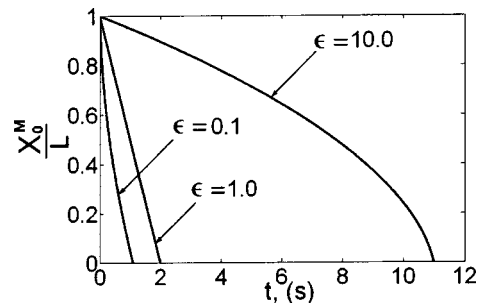


Fig. 2 Prediction of the location of interface using Darcy's model for different mobility ratios " ϵ " with $\delta=0.45$, $\Delta P=2.25 \times 10^7$, $\mu_1=0.01002$, $K=1 \times 10^{-10}$, and $L=1$ m

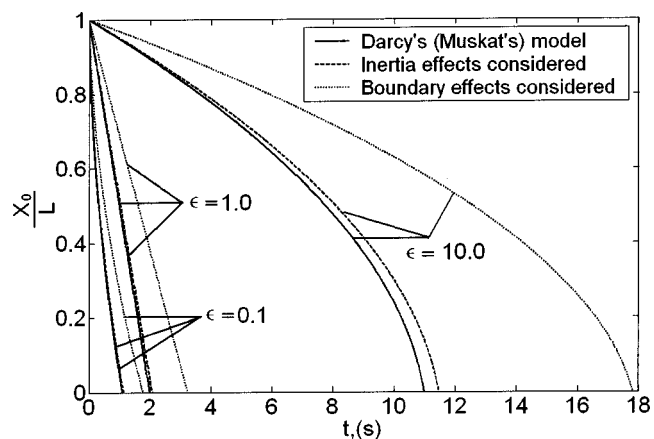


Fig. 3 Progress of the interfacial front at $y=\sqrt{Kl\delta}$ ($\eta=1$), $\delta=0.45$, $\Delta P=2.25 \times 10^7$, $\mu_1=0.01002$, $K=1 \times 10^{-10}$, and $L=1$ m using different models

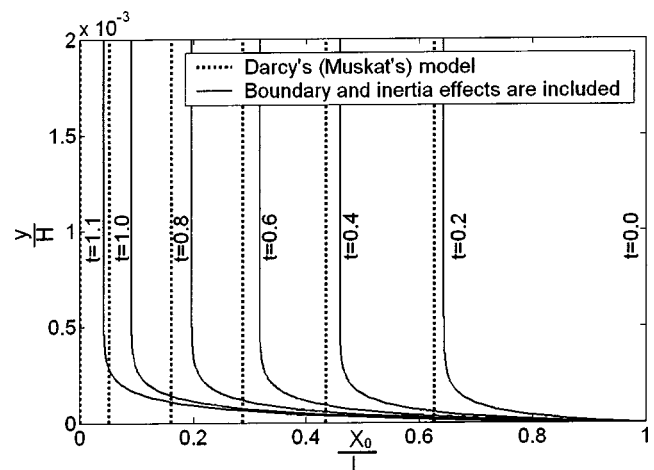


Fig. 4 Progress of the interfacial front, $\epsilon=0.1$, $\delta=0.45$, $\Delta P=2.25 \times 10^7$, $\mu_1=0.01002$, $K=1 \times 10^{-10}$, and $L=1$ m

Table 1 Summary of the corrections

Present	Srinivasan and Vafai [2]
$\frac{X_0^M}{L} = \frac{1 - \sqrt{\epsilon^2 + (1-\epsilon) \left\{ \frac{2K_1}{\mu_1 \delta} \frac{P_{in} - P_e}{L^2} t \right\}}}{(1-\epsilon)}$	$\frac{X_a^M}{L} = \frac{-\epsilon + \sqrt{1 - (1-\epsilon) \left\{ \frac{2K_1}{\mu_1 \delta} \frac{P_{in} - P_e}{L^2} t \right\}}}{(1-\epsilon)}$
$u_D = \frac{K_1}{\mu_1} \frac{P_{in} - P_e}{(1-\epsilon)X_0^M - L}$	$u_D = \frac{K_1}{\mu_1} \frac{P_{in} - P_e}{(1-\epsilon)X_0^M + \epsilon L}$

There are two typos in Eq. (23), which should read as follows:

$$\left(\frac{X_0^M}{L} - 1 \right) \left(\frac{X_0^M}{L} (1-\epsilon) - (1+\epsilon) \right) - \frac{2K_1}{\mu_1 \delta} \frac{(P_{in} - P_e)}{L^2} t = 0. \quad (2)$$

As a result, the obtained analytical solution in [2] (Eq. (24)) should be replaced by

$$\frac{X_0^M}{L} = \frac{2 - \sqrt{4 + 4(1-\epsilon) \left\{ \frac{2K_1}{\mu_1 \delta} \frac{P_{in} - P_e}{L^2} t - (1+\epsilon) \right\}}}{2(1-\epsilon)}. \quad (3)$$

The singular perturbation used to find the inertial and boundary effects in [2] are found to be accurate. This makes it easy to incorporate the expression of the velocity in the boundary region as well as the expression of the velocity in the core region to the analytical solution in Eq. (3). Using these expressions along with the analytical solution for the Darcian free-surface front position, the analytical solution inside the boundary layer region and the analytical solution in the core region, respectively, are

$$(1-\epsilon) \left(\frac{X_0^M}{L} \right)^2 - 2 \left(\frac{X_0^M}{L} \right) - \left\{ \frac{2K_1}{\mu_1 \delta} \frac{(P_{in} - P_e)}{L^2} (u_b^0 + \delta u_b^1 + \delta^2 u_b^2 + \dots) t - (1+\epsilon) \right\} = 0 \quad (4)$$

$$(1-\epsilon) \left(\frac{X_0^M}{L} \right)^2 - 2 \left(\frac{X_0^M}{L} \right) - \left\{ \frac{2K_1}{\mu_1 \delta} \frac{(P_{in} - P_e)}{L^2} (1 - \beta \delta + 2\beta^2 \delta^2 - 5\beta^3 \delta^3) t - (1+\epsilon) \right\} = 0. \quad (5)$$

The above two equations (4), (5) are to replace Eqs. (25) and (26) in [2]. Figures 2–4 are to replace Figs. 2, 4, and 5 in [2], respectively. Other Figs. in [2] are not corrected here for the sake of brevity. In fact, Figs. 6, 7 in [2] are similar to Fig. 5 while results in Fig. 3 can be deduced from Eq. (1). Finally, a summary of the main findings is shown in Table 1.

Conclusions

Analytical solution for the problem of linear encroachment in two-immiscible fluid systems in a porous material is obtained. The main characteristics of the previous results in [2] are unaffected. However, it is believed that the existence of an accurate analytical solution is essential for future numerical and experimental studies.

Nomenclature

- H = width of the channel (m)
- K = permeability of the porous structure (m^2)
- L = horizontal extent of the channel (m)
- P = pressure (Nm^{-2})
- P_e = pressure at exit (Nm^{-2})
- P_{in} = pressure at inlet (Nm^{-2})
- t = time (s)
- u_b = dimensionless velocity field in the boundary layer region (ms^{-1})
- u_D = Darcian convective velocity (ms^{-1})
- x = coordinate along the horizontal length of the channel from left to right as shown in Fig. 1 (m)
- X = coordinate along the horizontal length of the channel from right to left as shown in Fig. 1 (m)
- X_0 = location of the interface using the generalized model (m)
- X_0^M = location of the interface using the Muskat's model (m)
- y = coordinate along the vertical length of the channel (m)
- β = parameter defined as the product of the Reynolds number and the empirical function F
- δ = porosity of the porous medium
- η = dimensionless vertical coordinate
- μ = fluid viscosity ($kg\ m^{-1}\ s^{-1}$)
- ϵ = mobility ratio

References

[1] Muskat, M., 1937, *The Flow of Homogeneous Fluids Through Porous Media*, 1st Ed., Edwards, Ann Arbor, MI.
 [2] Srinivasan, V., and Vafai, K., 1994, "Analysis of Linear Encroachment in Two-Immiscible Fluid Systems in a Porous Medium," *ASME J. Fluids Eng.*, **116**, pp. 135–139.